RUPRECHT-KARLS-UNIVERSITÄT HEIDELBERG

DOCTORAL THESIS

Perspectives of the Radial Velocity Method: Physical Modeling of the Wavelength Solution & Exoplanetary Detections around Giant Stars

---

Author:
Marcelo Said TALA PINTO

Supervisor:
Prof. Dr. Andreas QUIRRENBACH
Second Referee:
Prof. Dr. Thomas HENNING

Thesis submitted in fulfillment of the requirements
for the degree of Doctor of Natural Sciences

in the

Extrasolar Planet Research Group
Landessternwarte Königstuhl

June 4, 2019

Dissertation in Astronomy
submitted to the
Combined Faculties of the Natural Sciences and Mathematics
of the Ruperto-Carola-University of Heidelberg, Germany
for the degree of
Doctor of Natural Sciences

M.Sc. Marcelo Said **Tala Pinto**
Born in **Antofagasta**, Chile
Oral Examination: 16.07.2019

Perspectives of the Radial Velocity Method:
Physical Modeling of the Wavelength Solution & Exoplanetary Detections around Giant Stars

Referees: Prof. Dr. Andreas Quirrenbach
Prof. Dr. Thomas Henning

"Even if all life on our planet is destroyed, there must be other life somewhere which we know nothing of. It is impossible that ours is the only world; there must be world after world unseen by us, in some region or dimension that we simply do not perceive.
Even though I can't prove that, even though it isn't logical - I believe it, he said to himself"

The Man in the High Castle - Philip K. Dick, 1962

Abstract

First, I present the design and construction of the Front-end of the Waltz Spectrograph. I designed upgrades in the system to optimize its mechanical stability and light coupling efficiency. To improve the instrument performance, I changed the original spectrograph fiber for one with slightly larger core and better focal ratio degradation, providing a spectral resolving power of 60.000, a mean spectral sampling of 2.6 pixels and only 5 % losses due to focal ratio degradation.

In the second part I present a ray tracing software that calculates the optical path of individual rays through an echelle spectrograph from the slit to the detector. By including the effects of the environment on the physical properties of the optical elements that compose the spectrograph, I am able to reproduce some of the trends observed in the time series of the spectral line positions of the calibration data.

Finally, I report the discovery of two planets orbiting the stars HD 25723 and 17 Sco and two planet candidates orbiting 3 Cnc and 44 Uma. Also, I investigate the planet occurrence rates as a function of evolutionary stage for two surveys, Lick and EXPRESS, concluding that there is no strong effect of stellar evolution in planet occurrence rates.

Zusammenfassung

Als erstes präsentiere ich das Design und die Konstruktion des Waltz Spektrografen Frontends. Ich entwarf Verbesserungen im System seine mechanische Stabilität und Lichtkopplungseffizienz zu optimieren. Mit dem Ziel die Leistung des Instruments zu erhöhen, habe ich die ursprüngliche Glasfaser des Spektrografen gegen eine mit einer geringeren Degradierung des Fokusverhältnisses und einem etwas größeren Kern ausgetauscht. Das neue Design erreicht eine spektrale Auflösung von 60.000, eine spektrale Abtastrate von durchschnittlich 2.6 Pixeln sowie lediglich 5% Verlust durch die Degradierung des Fokusverhältnisses.

Im zweiten Teil präsentiere ich eine Lichtstrahlverfolgungssoftware, welche den Weg einzelner Lichtstrahlen durch einen Gitterspektrografen vom Spalt bis zum Detektor berechnet. Indem ich die Umwelteinflüsse auf die physikalischen Eigenschaften der optischen Elemente des Spektrografen miteinbeziehe, kann ein ein paar der Verläufe reproduzieren, welche in Zeitreihen der Spektrallinienpositionen der CARMENES Kalibrationsdaten vorhanden sind.

Zuletzt gebe ich die Entdeckung zweier Planeten um die Sterne HD 25723 und 17 Sco sowie zweier Planetenkandidaten um 3 Cnc und 44 UMa bekannt. Zusätzlich untersuche ich die Planetenhäufigkeit in Abhängigkeit des evolutionären Status zweier Beobachtungsprogramme: Lick und EXPRESS. Mittels der abgeleiteten Planetenhäufigkeit kann ich schlussfolgern, dass die Evolutionsphase des Sterns keinen starken Einfluss auf die Planetenhäufigkeit hat.

Acknowledgements

Long time ago, when my mother took me to the Paranal Observatory, close to my home city Antofagasta, I never thought that I was going to end up doing my PhD in the observatory that built the first optical instrument for the VLT[1]. Learning Astronomy at the Landessternwarte Königstuhl is one of the greatest treasures of my life, and I will always be thankful to my supervisors, Prof. Dr. Andreas Quirrenbach and Priv.-Doz. Sabine Reffert, for giving the opportunity to pursue my doctoral studies in such a rich scientific environment. Just in the LSW it would have been possible to become the best astronomer I can be, and this is mostly because of your support and the freedom you gave me to explore the nature of my scientific work.

I would like to thank to all the people who contributed with their work to the completion of this thesis: Anantha Chanumolu who guided me through the construction of the RAMSES code by giving me parts of her code and providing feedback during the course of this investigation, Lutz Geuer and Ludwig Schäffner for their excellent work at the LSW Workshop building the parts for the Waltz and for the excellent feedback provided when I had to improve my mechanical designs, Walter Seifert and Conchi Cárdenas for providing the optical designs of the CARMENES VIS and NIR spectrographs as built, Otmar Stahl for the discussions about the environment control system of CARMENES and for solving all most my IT issues during the last four years, Julian Stürmer and Christian Schwab for the discussions that helped improving the original design of the Waltz Spectrograph, and Matthias Zechmeister and Florian Bauer for providing the data I used to analyze the behaviour of CARMENES and for all the fruitful discussions that helped me understand what really a wavelength solution is.

The progress in science has never been a task of one, as the cornerstone of a succesful learning process is the exchange of knowledge and ideas with our friends and colleagues. As far as I am from home now, curiously, home never really felt far away and this is thanks to the Exoplanets and Astrophotonics Research Groups at the LSW: Theodorus Anagnos, Paz Bluhm, Stefan Brems, Robert Harris, Paul Heeren, Philip Hottinger, Adrian Kaminski, Jonas Kemmer, Sepideh Sadegi, Dane Späth, Stephan Stock, Thomas Stuber, Trifon Trifonov, Vera Wolthoff and Steffi Yen.

A special tribute deserves Steffi and Rob, as we started our respective science trips in Heidelberg more or less at the same time and have played an important role in my doctoral studies, but also in the quality of the english of this thesis. Without their friendship the days in Heidelberg would have not been so colorful. A special tribute goes to Vera and Stefan for their contribution in the german translation of the abstract.

It is the time to put the final points to this thesis. Before doing so I must emphasize that most of what I am as a scientist and human being was learned from

[1] Appenzeller et al. 1998, "Successful commissioning of FORS1 - the first optical instrument on the VLT."

my family, my mother Ana María Pinto Castillo and my brothers, Maximiliano Tala Pinto and Marco Tala Pinto. Even though none of them is a scientist, they planted in me the seed of curiosity, but more important, the seed of honesty and kindness. And those are, in my opinion, the three qualities that a good scientist must have. To be curious, to be honest, and to be kind.

To you, who are reading these words now.

Thank you.

Contents

List of Figures

List of Tables

List of Abbreviations

HZ	Habitable Zone
MS	Main Sequence
RGB	Red Giant Branch
HB	Horizontal Branch
RV	Radial Velocity
PRV	Precise Radial Velocity
MIR	Mid infrared
VIS	Visible
NIR	Near infrared
CCD	Charged Coupled Device
HF	Hydrogen Fluoride
I2	Molecular Iodine
S/N	Signal-to-Noise
LED	Light-Emitting Diode
PSF	Point Spread Function
FP	Fabry-Perot
CAT	Coudé Auxiliary Telescope
LSW	Landessternwarte Königstuhl
HCL	Hollow Cathode Lamp
WS	Wavelength Solution
FWHM	Full Width at Half Maximum
NZP	Nightly Zero Point
FFU	Fiber Feeding Unit
FF	Far Field
FRD	Focal Ratio Degradation
FOV	Field Of View
FSR	Free Spectral Range
SA	Simulated Annealing
NS	Nested Sampling
MJD	Modified Julian Date
ThAr	Thorium Argon
UAr	Uranium Argon
UNe	Uranium Neon
ThNe	Thorium Neon
CTE	Coefficient of Thermal Expansion

Physical Constants

Speed of Light	$c = 2.997\,924\,58 \times 10^{8}\,\mathrm{m\,s^{-1}}$
Parsec	$pc = 3.0857 \times 10^{16}\,\mathrm{m}$
Astronomical Unit	$AU = 1.496 \times 10^{11}\,\mathrm{m}$
Earth mass	$m_{\oplus} = 5.972 \times 10^{24}\,\mathrm{kg}$
Jupiter mass	$m_{J} = 1.898 \times 10^{27}\,\mathrm{kg}$
Solar Mass	$M_{\odot} = 1.98 \times 10^{24}\,\mathrm{kg}$
Solar Radius	$R_{\odot} = 6.957 \times 10^{8}\,\mathrm{m}$
Gravitational Constant	$G = 6.674 \times 10^{-11}\,\mathrm{m^{3}\,kg^{-1}\,s^{-2}}$

A mi madre, la profesora Ana María Pinto Castillo

Chapter 1

Introduction

1.1 Exoplanets

'Is there anybody out there?', I asked myself once, while stargazing in the heart of the Atacama Desert where I grew up. It is said that there are 10 times more stars in the Universe than grains of sand on the Earth. The riddle seems to gain a special meaning in the most arid place on Earth, where the horizon is cut by the silouette of the Andes to the East and the Pacific Ocean to the West, making it one of the best place to observe the sky in the world. It feels a natural question to ask, when billions of stars shine all over the sky.

The Milky Way has between 500 - 700 billion stars (Eadie and Harris, 2016), and recent studies suggests that there is at least one planet per star in the Milky Way (Cassan et al., 2012). Planets like the Earth could be found orbiting their host star in the Habitable Zone (HZ), which is defined as the region around the star in which the surface temperature of the planet is such that it could host liquid water, making these stars ideal targets for studying the possibility of life on other planets. Moreover, Petigura, Howard, and Marcy, 2013 suggest that at least one in five Main-Sequence (MS) stars host Earth-like planets in the HZ, and planet occurrence rates of low mass stars populations, the most abundant type of star in the Milky Way, are possibly even higher (Burke et al., 2015). The first steps in the hunt for planets orbiting other stars, a.k.a. exoplanets, were performed by Belorizky, 1938, who theorized about their detection by measuring the change in the stellar radial velocity due to the presence of a planetary companion with the use of spectroscopic measurements, and Strand, 1943 reported the firsts observational insights of a planet orbiting another stars infering the presence of a third body in the binary system 61 Cygni by calculating their orbital motion using astrometric measurements. However, their instrumental precision was too low to detect such weak signals. The astrometric motion of the Sun star due to the presence of Jupiter as seen from a distance of 5 pc is 2 mas, while the change in the radial velocity of the Sun due to the presence of Jupiter is 12.7 m/s, making it an impossible goal to pursue with the instrumentation available in those years[1]. Almost a decade later, Otto Struve proposed that high precision stellar radial

[1] Milliarsecond astrometric precision was reached for the first time by the Hipparcos mission (Høg, 2017) and Doppler velocimeters provide high precision RVs since the early 90s.

velocities could be used to search for planets orbiting nearby stars. He predicted that Jupiter-like planets could be found as close as 0.02 AU from their host stars (Struve, 1952).

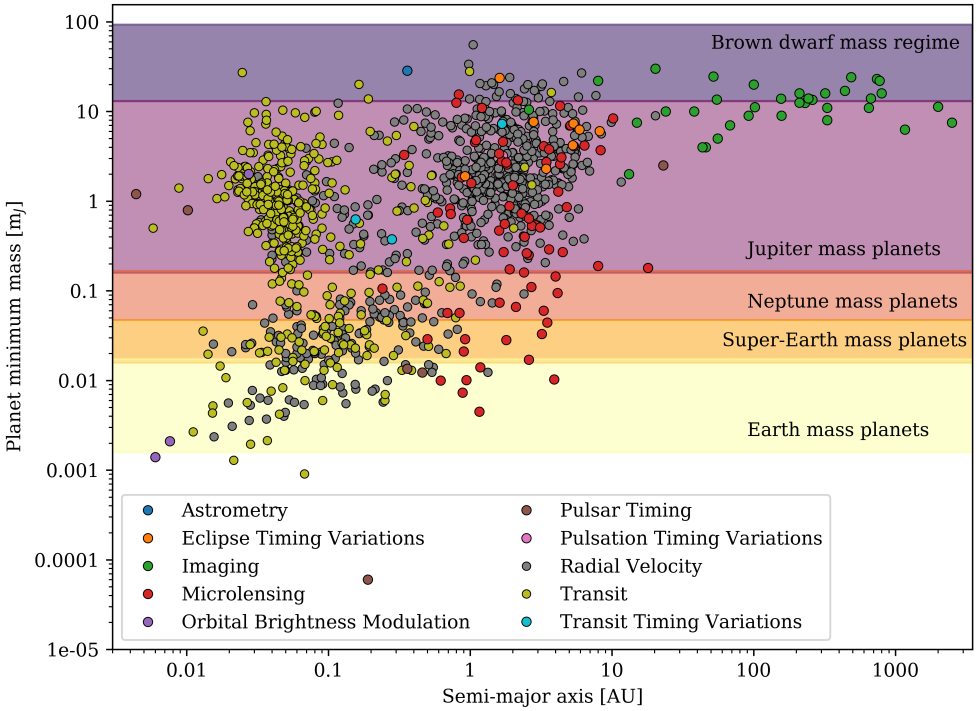

FIGURE 1.1: Planets detected so-far with all the different detection methods developed up-to-date. Data obtained from the NASA Exoplanet Archive.

The planetary detections around a milisecond pulsar and a MS star by Wolszczan and Frail, 1992 and Mayor and Queloz, 1995, respectively, allowed us, for the first time in human history, to investigate the properties of planets orbiting stars other than the Sun. Since then, by pushing the boundaries of technology to improve the precision in photometrical, spectroscopic and astrometric measurements, more than 1500 exoplanets have been detected using different detection methods. Thanks to high precision spectrographs, one can detect unseen companions to stars with the radial velocity method. High precision photometry from the space, specially with the Kepler mission, enables us to detect exoplanets when they transit their stars and dim the stellar light by merely one percent or smaller. Wide field, high-cadence, continuous monitoring of the Galactic bulge from different sites around the southern hemisphere provides unique observations of microlensing events caused by planetary systems from the solar neighbourhood, all the way to the Milky Way center. State-of-the-art Adaptive Optics imaging from ground-based large telescope, coupled with high-contrast coronagraph, capture the photons directly emitted by planets around other stars (Lee, 2018). The variety of planets detected goes from hot jupiters to giant planets orbiting evolved giant stars, including super-earth like

planets orbiting M-dwarf stars, and even an Earth analog, Kepler-69c, a planet with 0.98 $m_\oplus$ orbiting its host star at a distance of 0.64 AU.

Figure 1.1 show all the detected and confirmed planets so far. Most of them have been detected with the Transit method, mainly from Kepler and K2 missions, and the Radial Velocity (RV) method. Different methods are sensitive to different types of planets. While the transit method has been very effective in the search of close-in planets, the direct imaging method is more sensitive to planets at large orbital distances, for example.

The great progress in exoplanetary research, since its early beginning until the last succesful decade, has been possible thanks to the advances in technology that enabled high-precision measurements. With an increasing number of exoplanets and exoplanetary research facilities, space and ground-based, the community efforts are focused in refining the statistics on exoplanet occurrence rates, their origin and evolution, including physical and chemical properties of individual planets.

1.2 The Radial Velocity Method

The RV method is the founding method of planetary detection, and one of the most succesful to date, detecting several hundreds of planets orbiting around nearby stars. This method is also complements transit searches by providing the planetary mass to calculate the bulk density of the exoplanet needed to determine its structure (gas, icy or rocky planet).

The basic principle behind the RV method for the detection of exoplanets is rather simple. One measures the line-of-sight (radial) velocity component of a star as it moves around the center of mass of the star-planet system. This velocity is measured using the Doppler effect, that corresponds to the shift in the wavelength of spectral lines due to the motion of the star. The relative shift in wavelength of a spectral line is given by

$$\frac{\Delta\lambda}{\lambda_0} = \frac{RV}{c} \tag{1.1}$$

Where $\Delta\lambda = (\lambda - \lambda_0)$, λ is the wavelength of the spectral line in the observed spectra, λ_0 is the wavelength of the same line if the star is at rest with respect to Earth, RV is the radial velocity and c is the speed of light. To achieve a precision better than 1 m/s, one must be able to resolve drifts in the wavelength space of the order of 10^{-9}, putting strong contraints to the precision and stability of Precise Radial Velocity (PRV) instruments. In general, a star's radial velocity usually does not change sufficiently during a set of observations, so it can be assumed as constant (absolute radial velocity). However, when a star has an unseen companion in a non face-on orbit with respect to the observer, periodic variations on the star's radial velocity will occur. Figure 1.2 shows the periodic RV variations of 51 Pegasi, the host star of the first exoplanet confirmed. The orbital motion of 51 Peg is due to the presence of a Jupiter-like companion (Mayor and Queloz, 1995). Newton's form of

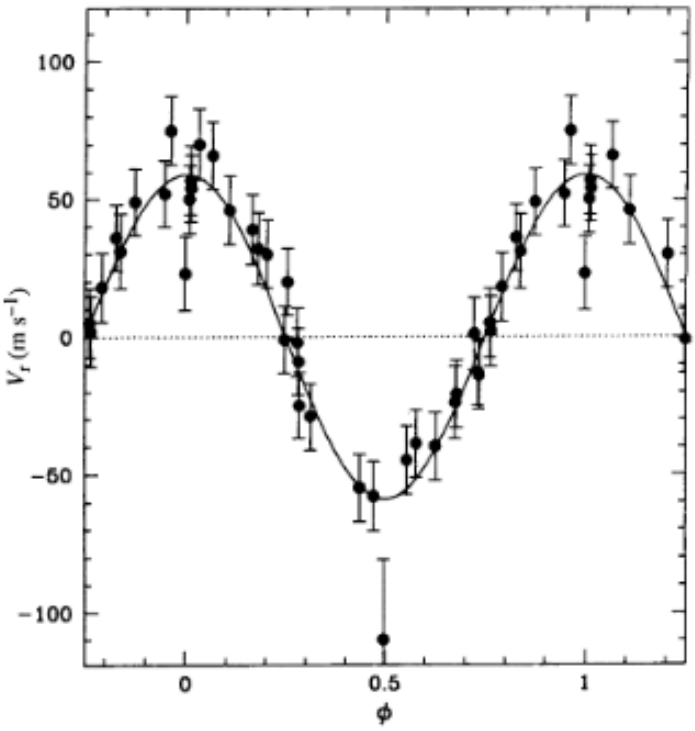

FIGURE 1.2: Orbital motion of 51 Peg due to a Jupiter-like companion. The solid line represents the best Keplerian fit to the data. *Credit*: Mayor and Queloz, 1995.

Kepler's third law is written

$$P^2 = \frac{4\pi^2\, a^3}{G(M_s + M_p)} \tag{1.2}$$

Where M_s is the mass of the star, M_p is the mass of the planet, P is the orbital period and a the semi-major axis. By considering that $M_p \times a_p = M_s \times a_s$, where a_s and a_p are the semi-major axes of the star and planet, respectively, the reflex motion of a star due to the presence of planet is given by

$$K[m\ s^{-1}] = \frac{28.4329}{\sqrt{1-e^2}} \left(\frac{P}{1\ yr}\right)^{-1/3} \left(\frac{M_p\ sin\ i}{M_{Jup}}\right) \left(\frac{M_s + M_p}{M_\odot}\right)^{-2/3} \tag{1.3}$$

Where i is the inclination of the orbital axis to the line of sight. Alternatively, I can use Kepler's third law to replace the orbital period P with the semi-major axis a:

$$K[m\ s^{-1}] = \frac{28.4329}{\sqrt{1-e^2}} \left(\frac{a}{1\ AU}\right)^{-1/2} \left(\frac{M_p\ sin\ i}{M_{Jup}}\right) \left(\frac{M_s + M_p}{M_\odot}\right)^{-1/2} \tag{1.4}$$

In the case of exoplanetary searches, only the RV of the host-star is measured, as the contrast in flux between the planet and its host star is rather small (the contrast between reflected like of Jupiter with respect to the Sun is of the order of 10^{-9}). Hence, RV measurements covering the complete orbital phase allows to measure the

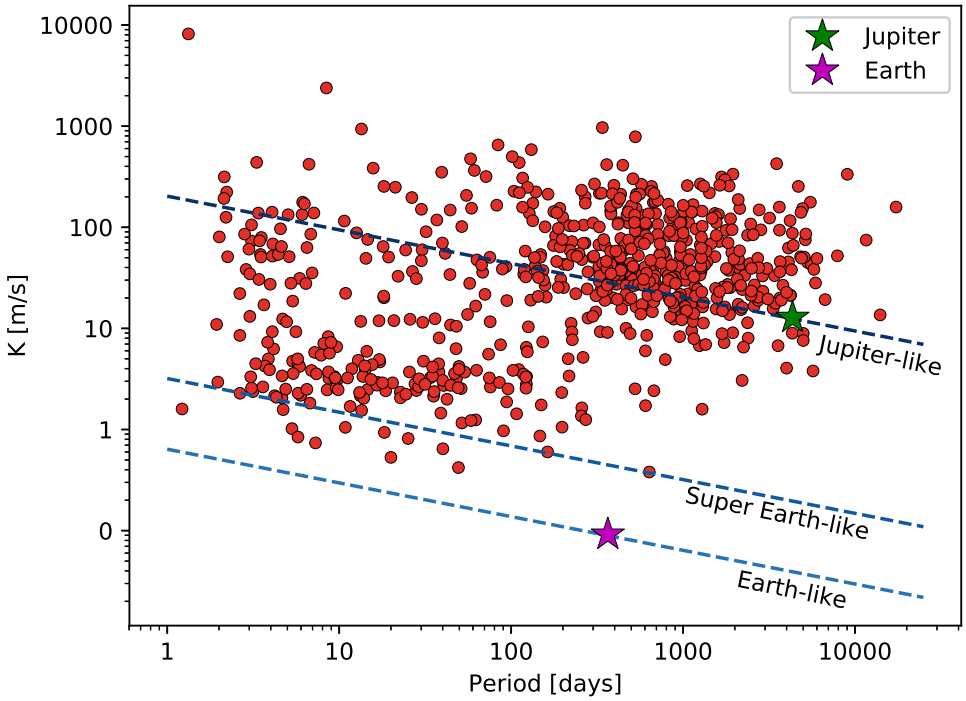

FIGURE 1.3: Planets detected with the radial velocity method. Data obtained from the NASA Exoplanet Archive.

period P, the eccentricity e and the semi-major amplitude K, and the stellar mass can be obtained by comparing spectroscopic, photometric and astrometric observables to grids of stellar evolutionary models. With these observables, one can compute the companion minimum mass $M_p \; sin \; i$ and the semi-major axis a from equation 1.4. Figure 1.3 show the planets detected with the radial velocity method, together with the reflex motion of a solar mass star due to three different planets at different orbital radii calculated with equation 1.4. While a Jupiter analog at a distance of 5.2 AU in a 12 years orbit induces a reflex motion of 11.2 m/s, an Earth analog induces a reflex motion of only 10 cm/s. State-of-the-art instruments are able to measure RVs with a precision of about 1 m/s, allowing to detect planets with masses 5 times the mass of the Earth, the so-called Super-Earths. The success of planetary detections with the radial velocity method over a wider range of periods and planetary masses strongly relies in the improvement of the precision and long-term stability of the measurements.

1.2.1 High Resolution Spectroscopy for Precise Radial Velocities

High precision RV measurements rely on the ability to accurately resolve as many spectral features in the stellar spectrum as possible. Stars emit most of their electromagnetic radiation between the intraviolet (UV) and mid infrared spectral range, however the UV and the MIR ranges are inaccesible from ground-based facilities.

Hence, most of precision RVs instruments work in the visible (VIS) and in the near infrared (NIR) spectral range. In addition, stellar spectra are very diverse, i.e. the spectrum of a O-type star might differ considerably from the spectrum of an M−dwarf, as the nature of the processes and the conditions in which spectral lines are formed are different. In very hot stars (T_eff < 10,000 K) most of the chemical elements are ionized and the atomic energy levels that produce transitions in the optical and in the near infrared are very weakly populated, so the stellar spectrum looks like a continuum with almost no spectral lines to measure precise RVs. Moreover, hot stars are also very fast rotators, blending stellar spectral lines due to rotational broadening. In contrast, in very cool stars (T_eff < 3,500 K) most of the lines are densely packed, less contrasted and overlapping, due to the presence of complex molecule bands. In addition, from a purely instrumental point of view, it becomes more challenging to achieve the required high SN due to the faintness of the stars, plus the fact that cool stars emit most of their radiation in the IR, putting additional constrains to the technical requirements of a PRV instrument (e.g. cryogenic components, background substraction, telluric lines corrections, etc.). Cool stars with spectral types from F5 to M5 are therefore best suited for exoplanetary searches with the RV method.

The main requirements to achieve high precision RVs, from the instrumental point of view, are a broad spectral range, high S/N and high resolving power (R = $\lambda/\Delta\lambda$). By considering also the constrains imposed by the nature and spectral type of the star, a rough estimate of the RV precision is given by

$$\sigma_{RV} = C\ (S/N)^{-1}\ R^{-3/2}\ \Delta\lambda^{-1/2}\ f(Spectral\ type)^{-1/2}\ (v\ sin\ i)^{-1} \tag{1.5}$$

Where σ_{RV} refers to the RV precision, *S/N* is the S/N of the spectrum, *R* is the resolving power, $\Delta\lambda$ is the wavelength coverage of the stellar spectrum, *f(Spectral type)* is a function that describes the density of spectral lines for a given spectral type, *v sin i* is the projected rotational velocity of the star, and *C* is a constant of proportionality (Hatzes, Cochran, and Endl, 2010).

The main tool to measure precise RVs is the cross-dispersed echelle spectrograph. This type of instrument is based in the use of an echelle grating as the main dispersion element. Echelle gratings are a special type of grating characterised by a low groove density and a groove shape optimized to be used at high incidence angles, providing high dispersion - and hence high resolving power - at high diffraction orders. However, the spectral orders overlap, requiring an additional dispersion element to separate the orders in the direction perpendicular to the echelle dispersion. This cross-dispersion element can be a prism, a grating, a grism or a Volume Phased Holographic (VPH) grating. Because of this, an echelle spectrograph produces a 2D spectrum that can be recorded by a typical CCD array, as shown in Figure 1.4. Figure 1.5 shows the basic optical layout of an astronomical fiber-fed spectrograph. Starlight is collected by the telescope and passes through an optical fiber towards the spectrograph. In this case the fiber acts as a pseudo-slit and at the same time as a

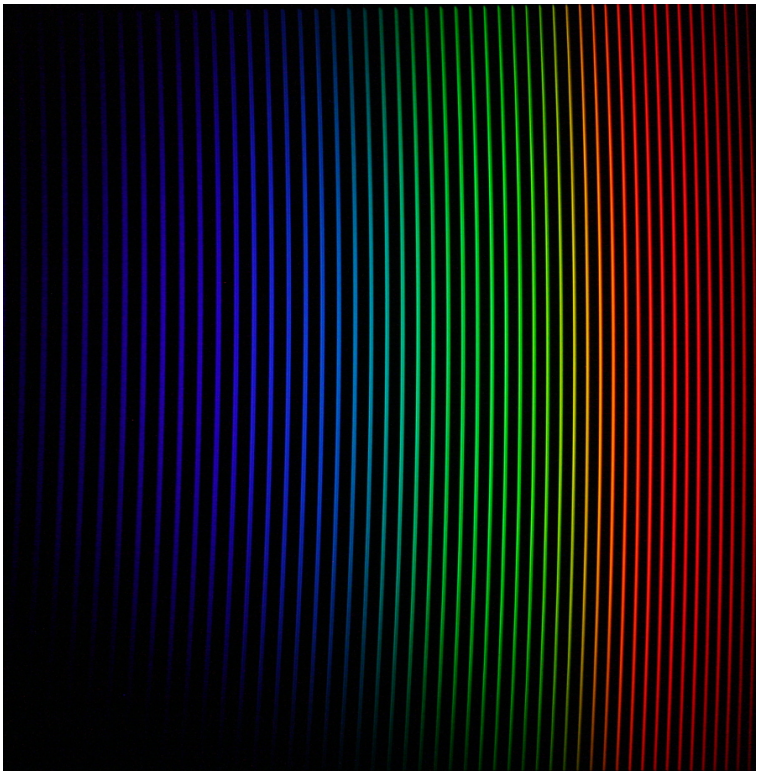

FIGURE 1.4: Echelle spectrum of a continuum source obtained with a DSLR camera attached to the Waltz spectrograph. *Credit*: Paul Heeren.

spatial filter, catching just the light of the star that one desires to observe. The spectrograph itself consist of, basically, a collimator, that makes the light rays parallel before they hitting the dispersion element, a dispersion element, that disperses the incoming beam and creates a spectrum, a camera, to focus the beam, and a detector, to finally record the spectrum. In reality, there are a wide variety of different configurations and combinations of these optical elements, depending on the scientific purpose of the instrument.

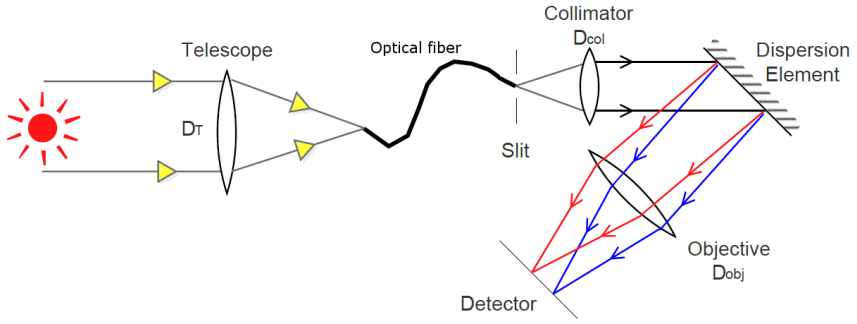

FIGURE 1.5: Basic optical layout of a fiber-fed spectrograph

The resolving power R of a spectrograph is the ability to resolve features in the electromagnetic spectrum as a function of wavelength, and is defined as

$$R = \frac{\lambda}{\Delta\lambda} \tag{1.6}$$

where λ is the wavelength, and $\Delta\lambda$ is the spectral resolution. The main dispersion element of modern astronomical spectrographs is the diffraction grating. A diffraction grating is an optical component with a periodic structure that splits and diffracts light into several beams travelling in different directions as a function of the wavelengths of the beams. In the case of a grating-based astronomical spectrograph, if the incidence and diffraction angle are equal to θ, its resolving power is given by

$$R = \frac{2\ D\ tan\ \theta}{\phi\ D_T} \tag{1.7}$$

where D is the beam diameter, θ is the diffraction angle, ϕ is the sky aperture and D_T the telescope diameter. Most PRV instruments use optical fibers, as they allow to detach the instruments from the telescope focal plane to mount them in a controlled environment, to optimise stability. In these cases, the sky aperture corresponds to the projection of the optical fiber in the sky and the spectrograph slit is defined by the geometry of optical fiber. Hence, the spectral resolving power of a fiber fed spectrograph is

$$R = \frac{2\ f_{col}\ tan\ \theta}{w} \tag{1.8}$$

where f_{col} is the focal length of the collimator, and w is the fiber width. To achieve high precision radial velocities one needs to resolve as many spectral features as possible, and not only to measure the radial velocity of the star with high precision, but also to reduce possible instrumental errors in the RV measurements and in the calibrations. Usually, a spectral resolving power over 40,000 is required to achieve precisions of the order of 10 m/s, and over 100,000 if the objective is to look for planets in which the semi-amplitude of the RV shift produced by the companion is of the order of 1 m/s. Figure 1.6 shows a table of current and future Doppler velocimeters, as well as their spectral resolution and the precision they reach (Pepe, Ehrenreich, and Meyer, 2014).

Currently, radial velocities are measured by one of two methods: the I2 cell technique or the cross-correlation technique. While the first one is based in the observation of a reference spectrum that is superimposed to the stellar spectrum, the second uses a high S/N template of a stellar spectrum to measure the RV drift in observed spectra and a secondary spectrum of a calibration source obtained simultaneously with the stellar spectrum to correct for instrumental drifts. Both techniques have shown great success and how these techniques work is the topic of the next section.

Instrument/technique	Telescope/observatory	Start of operations	Band (μm)	Spectral resolution	Efficiency (%)	Precision (m s^{-1})
Hamilton[180]/self-calibration	Shane 3 m/Lick	1986	0.34–1.1	30,000–60,000	3–6	3
UCLES[181]/self-calibration	3.9-m AAT/AAO	1988	0.47–0.88	~100,000	NA	3–6
HIRES[12]/self-calibration	Keck I/Mauna Kea	1993	0.3–1.0	25,000–85,000	6	1–2
CORALIE[13]/sim. reference	EULER/ESO La Silla	1998	0.38–0.69	60,000	5	3–6
UVES[182]/self-calibration	UT2–VLT/ESO Paranal	1999	0.3–1.1	30,000–110,000	4–15	2–2.5
HRS[183]/self-calibration	HET/McDonald	2000	0.42–1.1	15,000–120,000	6–9	3–6
HDS[184]/self-calibration	Subaru/Mauna Kea	2001	0.3–1.0	90,000–160,000	6–13	5–6
HARPS[18]/sim. reference	3.6 m/ESO La Silla	2003	0.38–0.69	115,000	6	< 0.8
FEROS-II[185]/sim. reference	2.2 m/ESO La Silla	2003	0.36–0.92	48,000	20	10–15
MIKE[186]/self-calibration	Magellan II/Las Campanas	2003	0.32–1.00	65,000–83,000 and 22,000–28,000	20–40	5
SOPHIE[187]/sim. reference	1.93 m/OHP	2006	0.38–0.69	39,000 and 75,000	4 and 8	2
CRIRES[188]/self-calibration	UT1–VLT/ESO Paranal	2007	0.95–5.2	~100,000	15	5
PFS[189]/self-calibration	Magellan II/Las Campanas	2010	0.39–0.67	38,000–190,000	10	1
PARAS[190]/sim. reference	1.2 m/Mt. Abu	2010	0.37–0.86	63,000	NA	3–5
CAFE[191]/sim. reference	2.2 m/Calar Alto	2011	0.39–0.95	~67,000	25	20
CHIRON[192]/self-calibration	1.5 m/CTIO	2011	0.41–87	80,000	15	<1
HARPS-N[54]/sim. reference	TNG/ORM	2012	0.38–0.69	115,000	8	<1
LEVY[193]/self-calibration	APF/Lick	2013	0.37–0.97	114,000–150,000	10–15	<1
EXPERT-III[194]/NA	2-m AST/Fairborn	2013	0.39–0.9*	100,000*	NA	NA
GIANO[71]/self-calibration	TNG/ORM	2014	0.95–2.5	50,000	20	NA
SALT–HRS[195]/self-calibration	SALT/SAAO	2014	0.38–0.89*	16,000–67,000*	10–15*	3–4*
FIRST[194]/NA	2-m AST/Fairborn	2014	0.8–1.8*	60,000–72,000*	NA	NA
IRD[73]/sim. reference	Subaru/Mauna Kea	2014	0.98–1.75*	70,000*	NA	1*
NRES/NA	6 × 1-m/LCOGT	2015	0.39–0.86*	53,000*	NA	3*
MINERVA/self-calibration	4 × 1-m/Mt. Hopkins	2015	0.39–0.86*	NA (Kiwispec)*	NA	1*
CARMENES[72]/sim. reference	Zeiss 3.5-m/Calar Alto	2015	0.55–1.7*	82,000*	10–13*	1*
PEPSI[196]/sim. reference	LBT/Mt. Graham	NA	0.38–0.91*	120,000–320,000*	10*	NA
HPF[74]/sim. reference	HET/McDonald	NA	0.98–1.40*	50,000*	4*	1–3*
CRIRES+/self-calibration	VLT/ESO Paranal	2017	0.95–5.2*	~100,000*	15*	<5*
ESPRESSO[42]/sim. reference	All UTs–VLT/ESO Paranal	2017	0.38–0.78*	60,000–200,000*	6–11*	0.1*
SPIROU[76]/sim. reference	CFHT/Mauna Kea	2017	0.98–2.35*	70,000*	10*	1*
G-CLEF[43]/sim. reference	GMT/Las Campanas	2019	0.35–0.95*	120,000*	20*	0.1*

FIGURE 1.6: Non-exhaustive table of present (active) and future (approved) high-precision Doppler velocimeters (Pepe, Ehrenreich, and Meyer, 2014).

1.2.2 The Iodine Cell Technique

Griffin, 1973 proposed inserting an absorbing medium in the optical path before entry into the spectrograph, superimposing medium absorption features that experience the same instrumental shifts and distortions as the stellar spectrum. He achieved radial velocity precisions of the order of 100 m/s by using the local atmosphere as a medium and its telluric absorption lines to correct for the non-uniformity of the spectrograph illumination. This significant improvement in the RV precision boosted the idea of recording absorption features simultaneously with the stellar spectrum, and Campbell and Walker, 1979 reported a radial velocity precision of ∼13 m/s by installing a gas cell filled with Hydrogen Fluoride (HF) in the telescope beam. The main constrains of the HF cell technique are the limited bandwidth coverage of its absorption spectrum in the optical and the toxicity of the component, that has deadly effects upon contact. Because of this, it was necessary to find a non-deadly chemical component that provided a vast amount of absorption features in the optical wavelength range. *"After 6 months in chemistry libraries, chemistry laboratories, and day-time tests at the Hamilton spectrometer, we settled on using molecular*

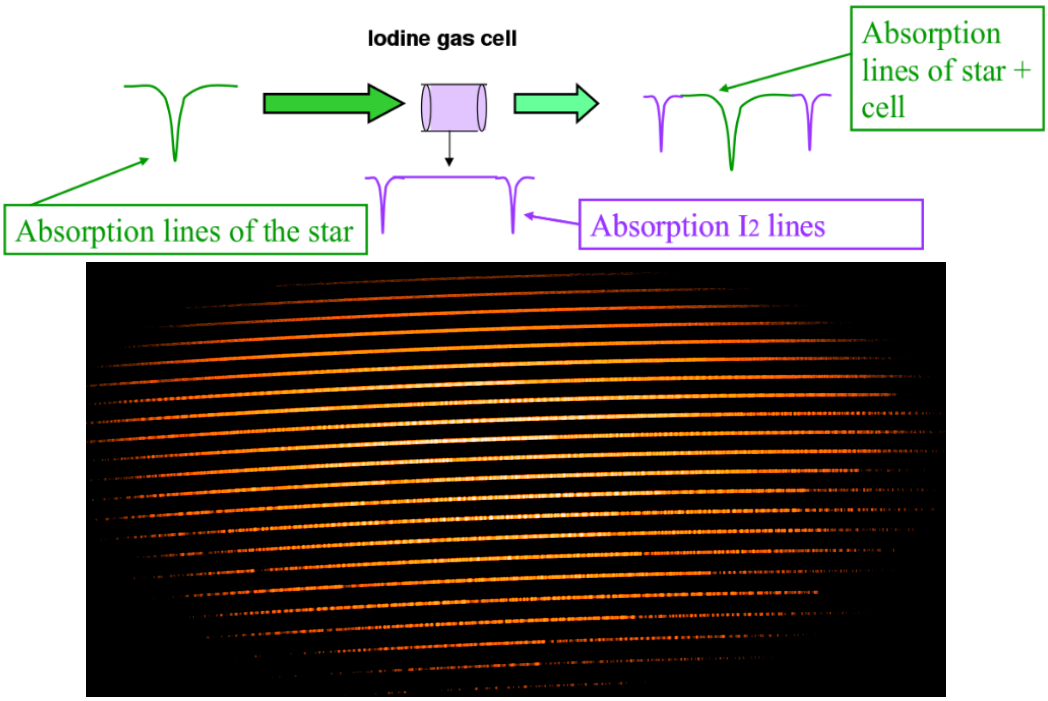

FIGURE 1.7: *Top panel*: Basic description of the I2 cell method. Stellar spectrum is obtained simultaneously with the superimposed I2 spectrum used as a reference. *Credit*: Artie Hatzes lecture notes. *Bottom panel*: Spectrum of an I2 cell taken with the Waltz spectrograph.

iodine)", writes Dr. Paul Butler[2], a pioneer of the iodine technique. The molecular iodine (I2) spectrum provides thousands of absorption features in the spectral range between 5000 Å(green) and 6200 Å(red) that can be used to measure precise radial velocities. Typical cells contain $\sim$ 0.001 Atm of I2, and are thermally stabilized at 50°C, the temperature at which I2 its in gaseous state. The cell is placed in the telescope beam, so starlight passes through the cell before entering the spectrograph. The I2 cell works as a transmission filter, imposing thousands of extremely sharp absorption lines on the stellar spectrum. Figure 1.7 shows the working principle of the I2 method. Starlight passes through a gas cell filled with I2, so that the I2 spectrum is superimposed on top of the stellar spectrum. The bottom panel in Figure 1.7 shows a spectrum of a light-emitting diode (LED) obtained simultaneously with the I2 spectrum.

In order to mitigate purely instrumental effects, such as drifts in the wavelength zero-point or changes in the spectrograph Point Spread Function (PSF), the observations are modeled as a product of two functions, the intrinsic stellar spectrum, I_s, and the transmission function of the I2 cell, T_{I2}. This product is convolved with the spectrograph PSF and binned to the wavelength extent of the CCD pixels. Spectra taken with the I2 cell are modeled as

$$I_{obs}(\lambda) \; = \; k \, [T_{I2} \; I_s(\lambda \; + \; \Delta\lambda)] * PSF \tag{1.9}$$

[2]https://palereddot.org/a-brief-personal-history-of-exoplanets-by-paul-butler/

where k is a normalization factor, $\Delta\lambda$ is the Doppler shift and $*$ refers to convolution. The transmission function of the I2 spectrum, T_{I2}, is directly measured at extreme high resolution (R$\sim 10^6$) and high S/N with a Fourier Transform Spectrometer. The intrinsic stellar spectrum is typically obtained from stacking a large quantity of high S/N observations and creating a template from these spectra. The instrumental PSF can be obtained from observing the sharp features of the I2 spectrum superimposed to a continuum spectrum - it can be the spectrum of a continuum lamp, or the spectrum of a star with almost no absorption features, i.e. a very young and massive star. The PSF is then used to deconvolve it from the template created to model I_s. The Doppler shift is measured by comparing the deconvolved stellar spectrum template with the Doppler-shifted wavelength scale of the observations (Butler et al., 1996).

Initially, Marcy and Butler, 1992 reported a precision of 15 - 20 m/s, but after several hardware and software improvements, Butler et al., 1996 achieved a RV precision of 3 m/s. The first exoplanet detected with the I2 cell method was a Jupiter-like planet orbiting almost every 3 years the star 47 UMa (Butler and Marcy, 1996). Since then, many observatories have adopted the I2 technique to measure precise stellar radial velocities. Current instruments are capable to reach instrumental precisions better than 1 m/s in the spectral range where the I2 lines are present. Some of the instruments that use this technique are listed in the table in Figure 1.6. The main drawback of this technique is the limited wavelength range of the I2 features, which only cover the spectral range between 500 nm - 600 nm.

1.2.3 The Simultaneous Calibration Technique

In parallel to the development of the I2 technique, in 1971 the Marseille Observatory and the Geneve Observatory started a collaboration to build CORAVEL (Baranne, Mayor, and Poncet, 1979), an instrument dedicated to obtaining high precision radial velocities by comparing the stellar spectrum with a reference spectrum. The reference was a template with about 3000 holes matching the absorption lines of Arcturus and that was located in the focal plane of the spectrograph. The stellar velocity was derived from the how well the stellar spectrum matched the template, with the zero point of the velocity determined by the spectrum of iron produced by a hollow-cathode lamp. By achieving accuracies of about 250 m/s[3], CORAVEL built the foundations of the leading technique to detect exoplanets with the radial velocity method, the simultaneous calibration technique.

This technique was pioneered by ELODIE (Baranne et al., 1996), an instrument that was built as an updated version of CORAVEL, but with major hardware improvements. The problem of the illumination at the entrance slit was eliminated by the use of optical fibers to feed the spectrograph (Heacox, 1986), allowing placement of the spectrograph in a gravity invariant and thermally controlled environment, to

[3]https://www.eso.org/public/spain/teles-instr/lasilla/danish154/coravel/

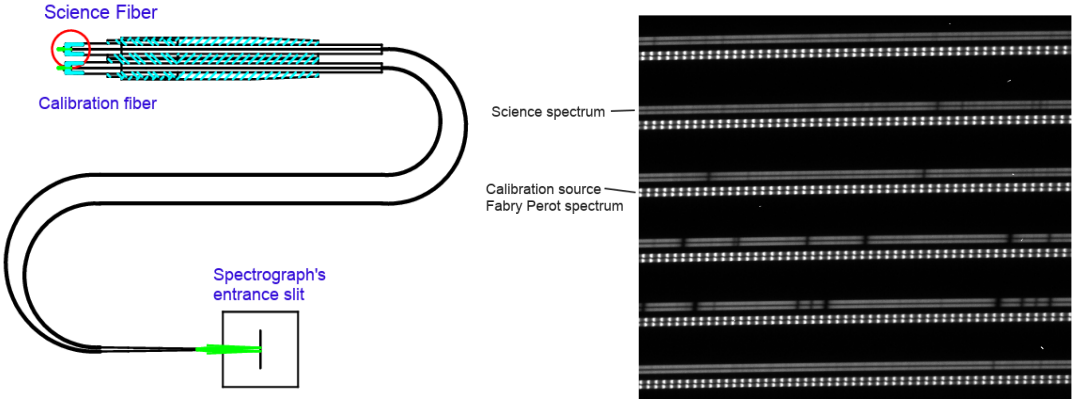

FIGURE 1.8: *Left*: Basic description of the simultaneous calibration technique. *Right*: The spectrograph is fed with two fibers, one for the science spectrum and one of a calibration source. *Credit*: Andreas Kaufer, 1998, modified by the author. Left: section of a science observation frame taken with CARMENES VIS channel. The science and FP calibration spectra are shown.

maximize the instrument stability. The condition of almost identical path for star and calibration is also provided by the high stability and scrambling effect of the optical fibers. ELODIE was fed with two optical fibers, one for the stellar spectrum and one for the sky. During the first year of operation the correlation of the relative drift between the sky spectrum and the star spectrum was noticed. To correct for this effect, the decision was taken to illuminate the secondary fiber with the thorium-argon (ThAr) lamp during stellar exposures to monitor the spectrograph calibration variation. The high precision radial velocities are achieved by cross-correlating the observed spectra with a high S/N template of the observed star (Zucker and Mazeh, 1994). By feeding the spectrograph with a secondary calibration source, observed simultaneously with the science observations, one can correct for additional instrumental drifts that could be present during the time the observation was made. This principle is shown in Figure 1.8.

The efficiency and long-term stability of the instrument allows the measurements of RVs with an accuracy better than 15 m/s over a wide spetral range (3900 Å-6800 Å), while also providing simultaneous measurements of calcium (Ca) H and K lines and Hα, which are interesting from the stellar activity point of view (Cincunegui, Díaz, and Mauas, 2007). After several years of observations, ELODIE detected the first exoplanet orbiting a sun-like star (Mayor and Queloz, 1995), opening an entire new research field in modern astronomy: the detection and characterization of exoplanets.

CORALIE, an improved version of ELODIE, was installed in 1997 in the 1.2m Euler in La Silla Observatory, and it reaches precisions of about 10 m/s (Queloz et al., 2001), and HARPS, one of the most succesful exoplanet hunters, is installed in the 3.6m telescope in La Silla Observatory and reach precisions better than 1 m/s, setting a new standard in terms of RV precision (Mayor et al., 2003). Many instruments have adopted the simultaneous calibration technique, as shown in Figure 1.6,

and the development of new technologies have pushed the limit towards the few meters per second precision regime. The use of the scrambling properties of octagonal fibers have succesfully mitigated the effects of the non-uniformity of the slit illumination. Vacuum conditions and temperature stabilized to a few mK are essential, and state-of-the-art wavelength calibrators, namely Fabry-Perot (FP) etalons (Steinmetz et al., 2009; Wildi et al., 2010; Bauer, Zechmeister, and Reiners, 2015) and Laser Frequency Combs (Osterman, 2007; Li et al., 2008; McCracken, Charsley, and Reid, 2017), provide a regular and stable wavelength reference to calibrate the stellar spectra over a wide spectral range, pushing the limit of the instrumental precision to only a few cm/s.

1.3 The Lick Survey of Giant Planets around Giant Stars

The Lick survey started in the 1999 at the UCO/Lick Observatory using the 0.6 m Coudé Auxiliary Telescope (CAT) together with the Hamilton Echelle Spectrograph (Vogt, 1987) with the main science objective of identifying and characterizing a sample of stars, astrometrically stable at the microarcsecond level, for its use in the Space Interferometric Mission astrometric grid.

Based in various criteria, K giants are the best type of stars for the grid. To reject possible multiple systems and other sources of astrometric jitter, the radial velocities of the sample of stars were monitored with precisions of 5 - 8 m/s. The original sample of giant stars was a selection of 86 K giants brighter than V = 6, with no signs of variability or multiplicity. From this sample, the maximum intrinsic RV variability observed was around 20 m/s, which is small enough to not affect the possible identification of stellar companions around this sample of K giants (Frink et al., 2001). In June 2000, 93 stars were added to the sample, considering less stringent constrains for the stellar variability. From the original sample, and its subsequent extension, the first detection of a planet around a giant star was reported by Frink et al. 2002. In 2004, 194 G- and K-giants were added to the sample. The selection criteria was then larger masses and bluer colors on average as the original sample. The reason for the extension of the sample was to study the dependence of the stellar mass with the presence of a planetary companion, but also the fact that bluer stars tend to have less intrinsic jitter, in comparison to redder stars. The survey stopped taking data with the Hamilton spectrograph in 2011, collecting 12 - 13 years of data for the 373 stars of the Lick sample. Since the detection of the first exoplanet orbiting a K giant star (Frink et al., 2002), about 120 planets around G and K giant stars have been discovered.

The discovery of planets orbiting giant stars allow us to probe the effects of stellar evolution on planetary systems and to test planetary formation theories in the intermediate mass regime (1–3 $M_{\odot}$). This is mainly because massive main-sequence stars have fewer spectral lines and higher rotation velocities, making it harder to

measure precision radial velocities. In contrast, intermediate mass stars on the giant branch are cool and have many spectral lines and small rotation rates. Hence, evolved giant stars are ideal targets for exoplanet searches using the RV method, and many surveys have been looking for planets around these stars in the last decades (Setiawan et al., 2003; Döllinger et al., 2007; Johnson et al., 2007; Sato et al., 2008a; Niedzielski and Wolszczan, 2008; Wittenmyer et al., 2011; Jones et al., 2011; Lee et al., 2012). However, the interpretation of precise radial velocities of G and K giant stars can be a bit ambiguous at times, as the recent examples of γ Draconis (Hatzes et al., 2018) and Aldebaran (Hatzes et al., 2015; Farr et al., 2018; Reichert et al., 2019) have shown. For both K giants the periodic radial velocity signal remained stable over many years, but later disappeared and apparently came back with a phase shift, inconsistent with the signal being due to an orbiting planet. Similarly, Delgado Mena et al., 2018 present evidence for a correlation of radial velocities with the full width at half maximum or the inverse slope of the bisector of the cross correlation function for three K giant stars in open clusters, two of which had been considered planet hosts previously (Lovis and Mayor, 2007a). These studies show that one must be extremely cautious when claiming exoplanet detections around these stars, especially for the more evolved stars with relatively large luminosities and radii, or late K spectral types.

In our Lick sample, we have identified secure planets around several stars (Frink et al., 2002; Reffert et al., 2006; Liu et al., 2008; Mitchell et al., 2013; Trifonov et al., 2014; Sato et al., 2008a; Wittenmyer et al., 2016; Ortiz et al., 2016; Quirrenbach et al., 2019). There are planet candidates around another twenty stars; four of these have an additional planet candidate. Two stars display a linear trend in the RVs on top of the planet candidate periodicity, which could be indicative of sub-stellar objects in very long orbits, but are not considered here further. Two secure planets and four planet candidates are found in spectroscopic binaries. Altogether, this adds up to 43 (candidate) planets in 35 systems.

Motivated by the success of the first phase of the Lick survey (1999 - 2011), I am currently working in the construction a high-resolution spectrograph that will be dedicated to the continuation of the Lick survey. This new PRV facility, the Waltz spectrograph, will be installed in the Waltz telescope, a 72 cm reflector located at the Landessternwarte Königstuhl (LSW) in Heidelberg, Germany. By providing a spectral resolving power of about 60,000 and using the I2 technique, it will provide radial velocities with a precision better than 7 m/s.

1.4 CARMENES: a search for Super-Earths around M-dwarfs

CARMENES is the achronym for **C**alar **A**lto high-**R**esolution search for **M** dwarfs with **E**xoearths with **N**ear-infrared and optical **E**chelle **S**pectrographs, an instrument

built for the 3.5 m Telescope at the Calar Alto Observatory by a consortium of Germans and Spanish institutions [4], with the main science objective of carrying out a precision RV survey of about 300 late-type main-sequence stars to detect low-mass planets in the habitable zone (Quirrenbach et al., 2010).

The Earth induces a reflex motion of about 9 cm/s in the Sun, based in equation 1.3, so Earth-like planets around Sun-like stars will induce reflex motions of that order of magnitude. Signals of this order of magnitude are beyond the detection capabilities of current instrumentation, that can measure RVs with an accuracy of 1 m/s. As the semi-amplitude of the RV variation is a function of stellar mass, the RV variations induced by a planet on less massive star are higher. Just as an example, the reflex motion of an Earth-like planet around a 0.3 $M_\odot$ star orbiting it at a distance of 1 AU is of about 160 cm/s, almost 20 times larger than for a Sun-like star. Therefore one must look for planets around less massive stars, if one aims to detect Earth analogs using the RV method. In addition, planets in close-in orbits induce a larger reflex motion compared to planets orbiting further away, so looking for close-in and short-period planets increase even more the detection limits of Earth-like planets. While a planet around a Sun-like star will be heavily irradiated when in a close-in orbit, the HZ is considerably reduced when observing less massive stars, as the luminosity - and by analogy, the stellar radiation power - increases with stellar mass. Hence, the observation of cooler and less massive stars is the best niche to look for Earth analogs with the RV method.

It has been estimated that at least 70 % of the stars in the Milky Way are M-dwarfs. Hence, the detection of low-mass planets around this type of star is important, as the characterization of planetary companions in this mass range will provide better constraints to theories of planet formation and evolution. M-dwarfs are one of the smallest type of star, with masses ranging from 0.06 $M_\odot$ to 0.9$M_\odot$, and one of the coolest ones, with surface temperatures ranging between 2300 - 4200 K. For late type M-dwarfs (M4-5, M < 0.2 $M_\odot$), a radial velocity precision of 1 m/s is required to detect a super-Earth with 5 $m_\oplus$.

The measurement of precision RVs in M-dwarfs is quite challenging, as these stars are in general fainter than their solar counterparts and they emit most of their radiation in the near-infrared region of the electromagnetic spectrum. In addition, the stellar jitter of few m/s present in these stars could hide the presence of a planetary companion, in the case there is one. To overcome the limitations imposed by the nature of the M-dwarfs, one could obtain high-resolution spectra over a wide spectral range. To maximize the collection of photons from the star and maximize the S/N of the observations, the instrument must be optimized to observe in the NIR spectral range. In addition, by observing in the VIS and in the NIR simultaneously

[4]Landessternwarte Königstuhl (LSW), Max-Planck Institut für Astronomie (MPIA), Instituto de Astrofísica de Andalucía (IAA), Institut de Ciències de l'Espai(ICE), Institut für Astrophysik Göttingen (IAG), Universidad Complutense de Madrid (UCM), Thüringer Landessternwarte Tautenburg (TLS), Instituto de Astrofísica de Canarias (IAC), Hamburger Sternwarte (HS), Centro de Astrobiología (CAB), Centro Astronómico Hispano-Alemán (CAHA)

one can disentangle the signals produced by purely instrinsic stellar effects with the planetary signal and avoid possible false detections (Benatti, 2018).

The CARMENES instrument consist of two separate echelle spectrographs, one VIS and one NIR, covering the spectral range between 0.52 - 1.7 μm in one single exposure at a spectral resolution of 93,400 in the VIS channel and 81,400 in the NIR channel. Both spectrographs are fed with starlight by optical fibers from the Cassegrain focus of the telescope, and they are housed in temperature-stabilized vacuum tanks. CARMENES makes use of Hollow-Cathode Lamps (HCL) spectra, together with spectra of a FP interferometer, to calibrate the stellar spectra with high accuracy. Using the position of the HCL and FP lines, the CARMENES reduction pipeline is able to map from the pixel space in the detector to the wavelength space in the stellar spectra. This is done by performing a polynomial fit in direct regression with $x(\lambda)$, where x is the position, in pixels, of a spectral line with wavelength λ in the detector (Bauer, Zechmeister, and Reiners, 2015). The function that maps from pixel to wavelength space is called the Wavelength Solution (WS).

The instrument first light with the two NIR and VIS channels working simultaneously occurred in November 2015, and the science observations started the 1st of January of 2016. Since then on, more than 10,000 spectra have been obtained in the VIS and NIR channels. During the early phases of CARMENES operations, a number of instrumental effects and calibration issues were identified, which affect the data from the VIS arm on the m s^{-1}. Therefore, for each night dedicated to the CARMENES Survey an instrumental nightly zero point (NZP) of the RVs is calculated by using all the stars with small RV variability (RV-quiet stars) observed in that night. Then each RV measurement is corrected for its NZP and propagated the NZP error into the measurement uncertainty (Quirrenbach et al., 2018; Trifonov et al., 2018).

Reiners et al., 2018a and Trifonov et al., 2018 presented the first exoplanetary systems characterized with CARMENES, and Reiners et al., 2018b derived basic spectroscopic information about radial velocity, Hα-emission, and projected surface rotation for the 324 stars of the survey, so the survey is already providing scientific results, according to what was planned in the design of the project. However, the RV precision to detect low-mass planets highly depends on the value of computed NZPs, whose nature is still unclear.

1.5 Objectives and Outline

The objective of this thesis is to investigate the RV technique from three different perspectives: hardware, data processing and actual exoplanets detections. The thesis is divided into three parts that are independent from each other.

In Chapter 2 I describe my contribution to the Waltz project, a new PRV instrument for the Waltz Telescope in the LSW, that consists of the development of the opto-mechanical design and assembly of the Front-end that links the Waltz Telescope with the spectrograph, and the upgrade of the spectrograph fiber and the pre-slit system of the spectrograph, to enhance the efficiency of the instrument while optimizing the resolving power and spectral sampling.

In Chapter 3 I present **RA**y tracing **M**odeling **S**oftware of **E**chelle **S**pectrographs (RAMSES), a python package that computes the ray tracing of any spectral feature from slit to detector, and its application to CARMENES as case study. By using an optimization routine, I can fit RAMSES to the CARMENES calibration data, and estimate the physical parameters of the instrument that best describe the calibration observations. In addition, I present a detailed characterization of the time series of the spectral line positions used for creating the wavelength solution with two main objectives: study when and how the external interventions to instrument affected its overall performance, and investigate a possible explanation for the NZP, a daily RV offset that must be corrected to achieve the required precision to detect low mass planets.

Chapter 4 is dedicated to the detection of exoplanets around giant stars with the RV method. I present two new confirmed exoplanets and two new candidates from the Lick survey, together with a study of the dependancy of the planet ocurrecence rates in surveys of giant stars as a function of the stellar evolutionary stage.

Chapter 5 summarizes the main conclusions after exploring the different perspectives of the RV method presented in this thesis.

Chapter 2

Front-end opto-mechanical design of the Waltz Telescope

Some of the results presented in this chapter have been published in Tala et al., 2016. Unless stated otherwise, all figures presented are based on own calculations or measurements.

2.1 Introduction

The Lick Doppler survey of giant stars ended when the iodine cell at the Hamilton spectrograph was damaged (Fischer, Marcy, and Spronck, 2014). Since then, the Exoplanet Group at LSW has been looking for alternatives to continue the Lick survey of giant planets around giant stars, especially to confirm long-term trends that are seen in the data which may hint sub-stellar companions with periods of a decade or more. The 72 cm Waltz Telescope located at the LSW Königstuhl in Heidelberg, Germany, seems perfectly suited for the task if equipped with a high resolution spectrograph. The Waltz spectrograph at the Waltz Telescope compares well with the Hamilton echelle spectrograph coupled to the CAT telescope in several aspects: the telescope and throughput of the spectrograph are slightly larger than at Lick, leading to shorter exposure times. The weather conditions and sky conditions are worse, but if the instrument is used during every good night, then it has been estimated that it would be possible to obtain as many or slightly more spectra than during the 1999 - 2011 phase of the survey, with the same cadence as before, 5 nights/month. At the same time of carrying out the scientific survey, the telescope and spectrograph will also be used for student education, serving a double purpose.

An early prototype was built based on a layout with a grating in an off-plane angle: this instrument was a replica of the Yale Doppler Diagnostic Facility laboratory spectrograph at Yale (Schwab et al., 2012). The design was modified to a full white-pupil layout for improved image quality. The spectrograph covers the spectral range between 450 - 800 nm and provides a resolving power of about 60,000. It is fed by a rectangular optical fiber, providing mechanical and illumination stability, and is installed in a separate room, to minimize temperature fluctuations that could lead to mechanical flexures. The instrument will use an iodine cell in the telescope

beam as a stable reference for the measurement of high precision RVs. A ThAr lamp can be used for wavelength calibrations when not working in the high precision RVs regime.

In this chapter I will briefly describe the design of a new PRV instrument, the Waltz Spectrograph, highlighting in particular my contribution to the project, the development of the opto-mechanical design of the Front-End.

2.2 Instrument description

This Waltz Telescope is a F/20.4 reflector with a plate scale of 14.04 arcsec/mm used in Nasmyth focus. The instrument consists of three different modules: the front-end module, the calibration unit and the spectrograph. These are connected with optical fibers. In this section I will briefly describe the spectrograph and the calibration unit, as I will describe the details of my front-end design in §2.4.

2.2.1 Spectrograph optical design

The spectrograph is based on a white-pupil cross-dispersed echelle optical design, with the echelle grating in a quasi-Littrow mode. The spectrograph is fed by a 33 $\times$132 μm rectangular fiber. It covers the spectral range between 450 - 800 nm with a resolving power of 60,700 and a mean sampling of 2.6 pixels.

The output of the optical fiber is imaged into the focus of the collimator. The beam emerges from the fiber core at F/5.5 and it is transformed by the FN-system into the working F/10 of the spectrograph. The image projected in the slit of the spectrograph has a size of 52μm $\times$ 224 μm. The beam is collimated off-axis by a sub-aperture of a 300 mm diameter parabolic mirror with focal length 900 mm, from SpaceWalk instruments. The mirror substrate is Supremax. The off-axis angle is 4.8°. The main dispersion element is an off-the-shelf echelle grating with 31.6 lines/mm and blaze angle of 63.5° from Richardson Gratings. The size of the grating is 200mm $\times$ 100mm $\times$35mm, being completely under-filled with the collimated beam. Due to the white-pupil design of the spectrograph, the beam is reflected back to the collimator after the echelle-dispersion. After the second reflection in the collimator, the beam is focused on the transfer mirror, a flat silver-coated mirror that reflects the beam back to the collimator, for a second collimation. The cross-dispersion is provided by a 130 mm tall prism made of Schott F2 glass with a 60° apex angle working in minimum deviation. All prism surfaces are coated with a silica Sol-Gel anti-reflection coating optimized for the 55° incidence angle. Prism characteristics were chosen to provide a minimum order separation of 25 pixels between the reddest orders, in order to prevent contamination between adjacent orders. The objective camera is a modified Petzval quadruplet apochromat with an aperture of 106 mm and a focal length of 530 mm, hence a F/5, from Takahashi Corporations (FSQ106 ED). It is optimized for wide-field imaging, providing a high quality image over the entire

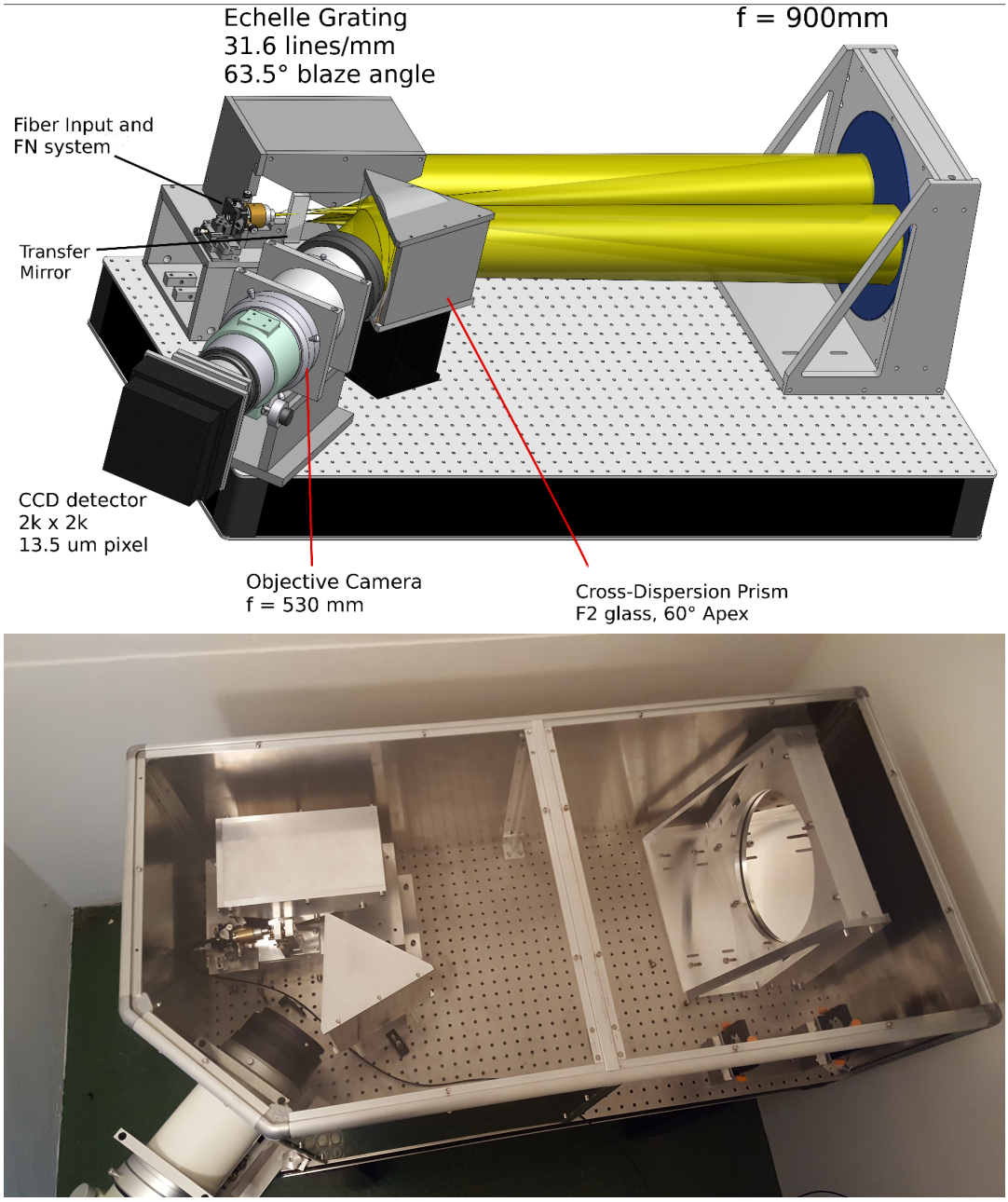

FIGURE 2.1: *Top panel*: Opto-mechanical design of the Waltz spectrograph. *Bottom panel*: Picture of the spectrograph in its enclosure in the coudé room of the Waltz Telescope building.

spectrum. The detector is an Andor iKon-L 936 back-illuminated CCD detector, a 2048 $\times$ 2048 pixel array with 13.5μm pixel size. Read-out noise and dark current values are 2.9e$^-$ and 4$\cdot$10^{-4}e$^-$/pix/sec at -70°C, respectively. A photon counter from Hamamatsu Corporations model H9319-11 is used as an exposure meter and it will observe the zeroth order of the echelle spectrum to estimate the photon-weighted mid-point of the observations for an accurate barycentric correction.

The optical axis height is 192 mm above the optical bench. All reflective elements are mounted on mechanical mounts that provide small tilt adjustments for precise alignment of the optics. There are no movable parts in the spectrograph unit

other than the CCD shutter. The optical bench is a 1200 mm×600 mm rectangular steel breadboard with M6 mounting holes and excellent thermal stability. All the elements of the spectrograph are mounted directly onto the optical bench except for the detector, which is connected to the objective camera through a special mount that allows precise aligment. The bench is mounted on legs with a damping system using compressed air to compensate small mechanical vibrations from the environment, optimizing the instrument stability. Figure 2.1 shows the opto-mechanical design of the instrument.

2.2.2 Calibration Unit

The Calibration Unit is the module of the instrument that contains the calibration lamps: a continuum lamp for order tracing and flat fielding, and a Thorium-Argon (ThAr) Hollow Cathode Lamp (HCL) for wavelength calibration. ThAr lamps provide a vast forest of spectral emission lines within the spectral range of the spectrograph, with strong Ar lines above 650 nm. Figure 2.2 show the layout of the calibration unit. All the optical elements are at the same height, and aligned on-axis. The beams coming out of the continuum and emission lines lamps are collimated using off-the-shelf achromat doublets from Thorlabs. In the case of the ThAr lamp, the collimated beam goes straight into the lens that focuses the beam onto the tip of the fiber that takes the light from the calibration sources to the front-end to be re-injected in the fiber that feeds the spectrograph. As shown in Figure 2.2, the optical axis of the continuum lamp, and of the lens that collimates its beam, is perpendicular to the fiber optical axis. A flat fold mirror is used to redirect the light and focus it onto the tip of the calibration fiber. This fold mirror is mounted on a movable platform, in order the place it in or out of the continuum lamp beam, when observing (or not) continuum spectra. As a continuum source, I have proposed the simultaneous use of two continuum sources: a quartz-tungsten halogen lamp and a LED whose spectrum is centered at 550 nm. This is to enhance the efficiency of the continuum source in the spectral region of the iodine spectrum, as the quartz-tungsten halogen lamp light intensity considerably decreases in this wavelength range. To join the light of both sources, a beam-splitter is mounted between the quartz-tungsten lamp and the LED, as shown in Figure 2.2. In this case, the light of the halogen lamp goes straight through the splitter. The LED is mounted perpendicular to the halogen lamp axis, but the splitter aligns the LED beam with the halogen lamp axis. The beam splitter is a 90:10, meaning that 90% of the LED light is conserved after passing through it while only 10% of the halogen lamp light is conserved after the splitter. The reason for this is that the halogen lamp is much more intense than the LED, so by using the 90:10 beam splitter, the intensity of both sources is better balanced.

The only movable part is the mount for the fold mirror. The motor that moves the platform is controlled by an Arduino micro-controller coupled with a motor-shield that provides a suitable interface to control the motion of this motor, and therefore the platform that moves the fold mirror. There are two limit switches installed in the

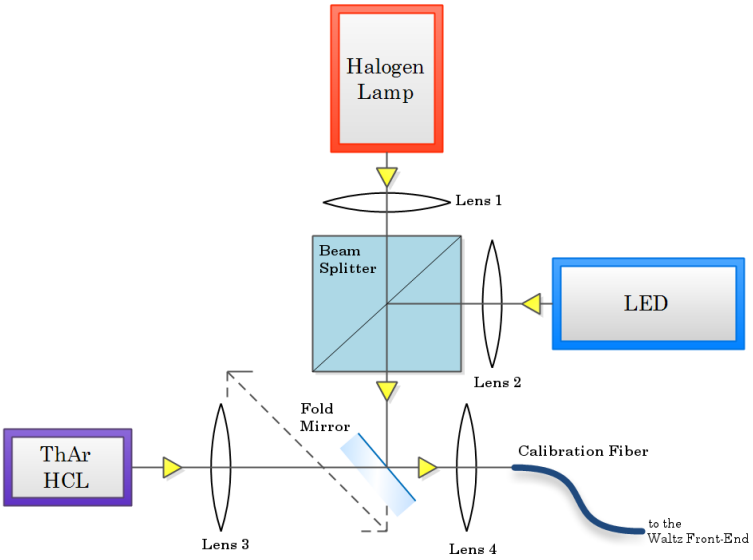

FIGURE 2.2: Diagram of the optical layout of the Calibration Unit.

fold mirror mount, to prevent the from moving further than the physical limits of the mount. The functionality of these limit switches is enabled by the same microcontroller that controls the motor of the fold mirror mount.

All the light sources are plugged to a multi-plug extension socket that is connected to an internet server which controls the functioning of the sockets via a web interface.

2.3 FN-system and Spectrograph Fiber upgrade

The original optical design of the instrument was presented in Tala et al., 2016. This original design considered the use of a 25μm$\times$100μm rectangular core fiber for the spectrograph fiber. The output focal ratio of this fiber is F/4.46, which is transformed by the FN-system into the F/10 of the collimator. The echelle grating aperture is 100 mm, and in the optical design the beam size is 90 mm to avoid issues with scattered light from the grating frame. Hence, there is not much room for a larger beam, and all the rays emerging from the fiber with focal ratio < 4.46 are lost. Focal ratio degradation (FRD) measurements of this fiber show that the light loses are about 20% due to the size of the beam diameter at the grating plane, which is consistent with the measurements of the spectrograph efficiency done by Heeren, 2016.

One additional, and relevant, fact about this fiber is that the manufacturer (Ceramoptec) decided to stop the manufacturing this particular fiber. Hence, it was not possible to test other cables of the same fiber to investigate possible ways to improve its FRD or to replace the cable if, for unexpected circumstances, it broke. Because of this, I explored the option of changing the original fiber for one with a better FRD to improve and optimize the instrument efficiency. After contacting several optical fiber manufacturers, Ceramoptec made an offer for two 13 m cables of the RCT WF33x132/280/320P, NA=0.2 fiber, an optical fiber with a 33μm $\times$ 132μm

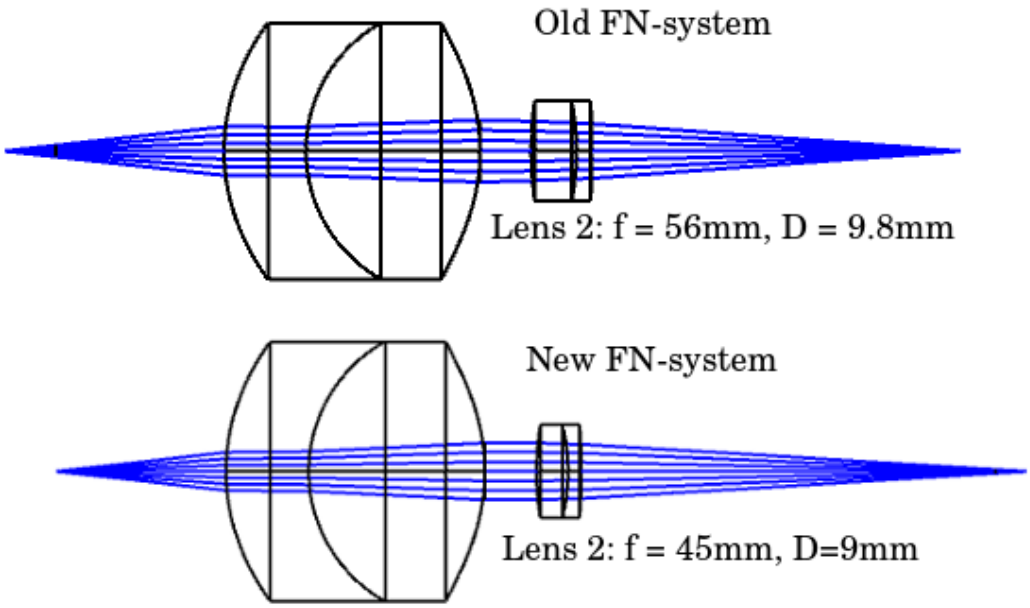

FIGURE 2.3: *Top panel*: Old FN-system. *Bottom panel*: New FN-system.

rectangular core size. Among the companies that offer fiber optics solutions, only Ceramoptec offered a fiber with a similar geometry and core size.

The spectrograph resolving power and spectral sampling are directly related to the fiber core size, so changing the fiber will have a large impact in the instrument performance. The goal is to study the new rectangular fibers, with the aim of improving the instrument efficiency and optimising the resolving power and the spectral sampling.

2.3.1 FN-system

The FN-system is an optical system that converts the F/4.46 focal ratio of the output beam of the fiber into the F/10 focal ratio of the collimator. The original FN-system consisted of two achromat lenses with focal lenghts of 25 mm and 56 mm, respectively. With this design the fiber image size at the focal plane of the collimator is 56μm$\times$224μm, and its projection at the detector plane is of 33μm$\times$132μm, resulting in a spectral resolving power of 65,000 and a mean spectral sampling of 2.4 pix. In addition, the F/10 of the collimator corresponds to a F/4.5 at the output of the fiber, so all the light that emerges from the fiber at a focal ratio lower than 4.5 is lost due to FRD.

With the original FN-system the new fiber image size at the focal plane of the collimator is 74μm $\times$ 296μm, and its projection at the detector plane is 43.5μm$\times$ 174μm, resulting in a spectral resolving power of 48,800 and a spectral sampling of 3.2 pix. The spectral sampling has increased, while the resolving power has decreases considerably. The spectral resolving power is tighly bound to the RV precision of the instrument, as expressed by Equation 1.5. Hence, to change the fiber

and, at the same time, keep the spectral resolution as high as possible, with minimal effort in terms of modifications of the spectrograph optical design, I investigated the replacement of one of the two lenses of the FN-system with the goal of adjusting its magnification factor to boost the resolving power to its highest value keeping the spectral sampling over 2.6 pixel to satisfy the Nyquist criteria. For practical reasons the best option was to replace the second lens of the FN-system, as the first lens is custom-made and optimised for high quality images, and also because its size is not common within off-the-shelf optics companies. Therefore, modifying this part of the FN-system would require substantial modifications in its mechanical mount. The diameter of the second lens is 9 mm, which is much closer to the diameter of the lenses found in stock at optical elements companies, such as Thorlabs or Edmund Optics. The main parameter to modify in the FN-system, in order to boost the resolution of the instrument, is the focal length of the second lens.

After searching through several optics catalogs, I found a lens that fits our strict requirements in the Edmund Optics catalog. This lens is a 12.5 mm diameter double achromat with a focal length of 45 mm. With this lens, the new fiber image size at the focal plane of the collimator is 59.4μm $\times$ 237.6μm, and its projection at the detector plane is 35μm $\times$ 140μm, resulting in a spectral resolving power of 60,700 and a mean spectral sampling of 2.6 pix. This is the highest possible resolution that can be achieved with minimal changes in the optical design of the instrument without undersampling the spectral lines. One could increase even further the resolution, but at the high cost of not have enough pixels to sample each spectral feature. Based in this new configuration, the beam emerging from the fiber at F/5.5 is transformed to a F/10 after the FN-system.

FRD is the change in light's angular distribution in optical fibers (Angel et al., 1977; Ramsey, 1988). FRD is one of the main cause of flux loses when linking telescopes to spectrographs with optical fibers. If a light beam with a given focal ratio is injected into a fiber, the focal ratio of the beam leaving the fiber will be lower than the one of the input beam. Hence, fibers never preserve their original aperture. This degradation highly depends on the physical conditions in which the fiber is used. As an example, Figure 2.4 shows the transmission of a ray parallel to the optical axis of the fiber (F/∞). As soon as the fiber is bent, this ray is deviated from its original direction, exiting the fiber at an angle that depends on the curvature radius of the bending. Similarly, also shown in Figure 2.4, a ray enters the fiber at a F/3, and after successive internal reflections leaves the fiber at a lower focal ratio.

FRD can be caused by diffraction and surface irregularities on fiber walls, bends in the fiber, variations on the refractive index of the core or cladding, and modal diffusion or impurities in the core and/or cladding (Haynes et al., 2011). In case the optics after the fiber does not account for FRD, the light that emerges at an angle larger than the input angle will be lost. In the case of the Waltz, the original design considers that the output focal ratio of the spectrograph fiber should be 4.46, which after passing by the FN-system, is transformed to the focal ratio of the collimator.

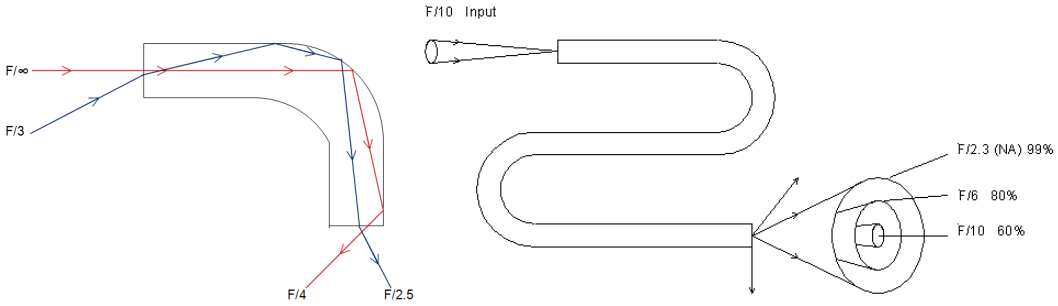

FIGURE 2.4: FRD basic principle.

Beams emerging at a lower focal ratio will get lost if one does not increase the size of the optics.

2.3.2 Focal Ratio Degradation

Experimental setup

The experimental setup to measure FRD was built by Dr. Julian Stürmer to test the optical fibers used in CARMENES. A detailed description of the setup can be found in Stürmer, 2015. Here I will briefly describe the experimental setup.

The main purpose of the experiment of to image a well defined polychromatic source onto an optical fiber and investigate the light distribution of its output far-field (FF). A white LED with the peak around 450 nm was used as a light source. Figure 2.5 shows the optical layout of the setup. The pinhole is imaged onto the fiber under test, which is mounted on a XYZ stage and a mount that provides tip/tilt adjustments. A beamsplitter in the collimated beam allows us to look at the fiber input directly with a camera. By doing so, one can precisely estimate the position of the pinhole image on the tip of the fiber.

Measurement procedure

For measuring the FRD I have to measure the FF of the output beam of the fibers under test as a function of the input angle to each of the fibers. As the distance between the lens that focus the pinhole image and the fiber under test is fixed, I can change the angle at which the light is injected to the fiber by changing the aperture. The aperture is changed by placing apertures with different sizes in the collimated beam. The FF is the image of the cone of light emerging from the fiber.

Observations were made with the CCD detector Starlight LodestarX2, a 752(H) $\times$ 580(V) pixel array with 8.6$\times$8.3μm. The fibers to test are mounted in FC connectors, which are attached to the CCD detector mount with the use of a mechanical adapter. With this setup the mechanical distance between the fiber and the detector is 13.6 mm. By measuring the diameter of the FF image, I can estimate the focal ratio of the beam by using

$$F/\# = \frac{d_{CCD}}{D_{FF}} \tag{2.1}$$

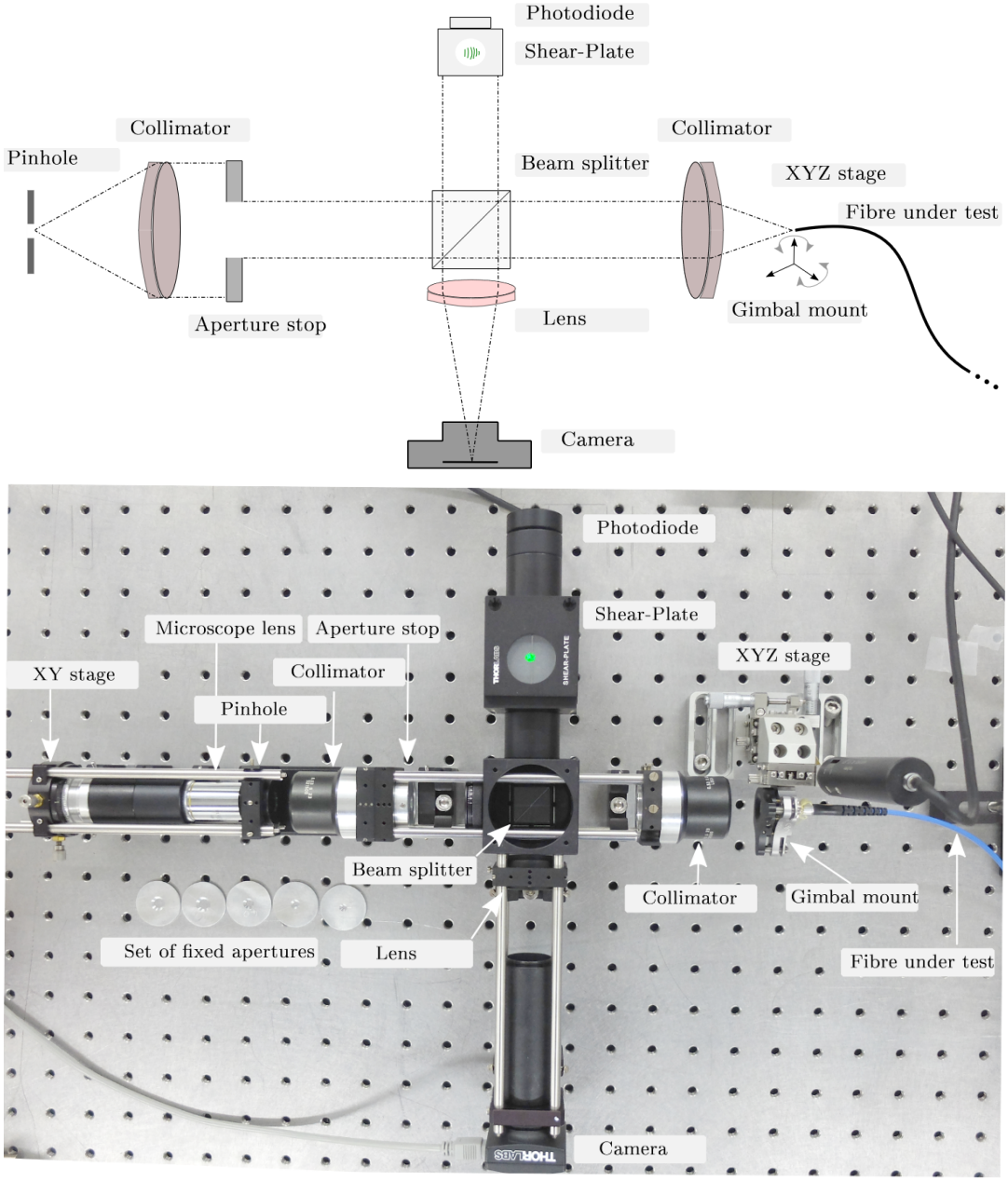

FIGURE 2.5: *Top panel*: Optical setup for re-imaging the pinhole onto the fiber under test. An aperture stop after the first collimation allows setting the F-ratio of the light feeding the fiber. A camera monitors the fiber entrance via a beam splitter and allows the determination of the exact position where the light enters the fiber. A shear plate interferometer is used to ensure that the light is properly collimated. *Bottom panel*: Photo of the optical setup for illuminating the fibers under test. The optics are assembled within a rigid and stable cage system to ensure good mechanical stability. Credit: Stürmer, 2015

where d_{CCD} is the distance from the fiber to the CCD in mm and D_{FF} is the diameter of the FF image in mm. As the FF image is recorded in the pixel space, by knowing the pixel size and the diameter of the FF image in pixels I can transform to the physical space in mm.

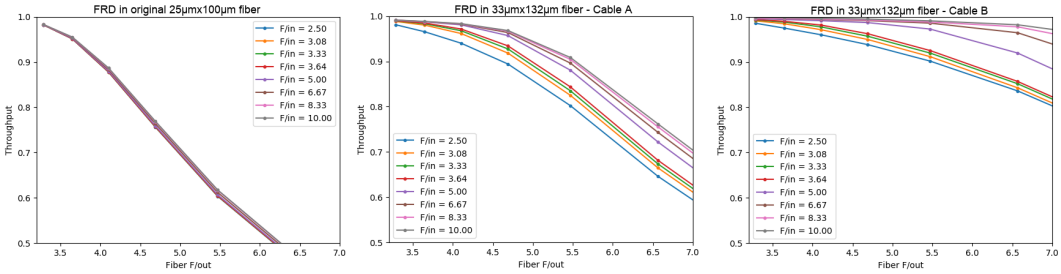

FIGURE 2.6: *Left panel*: FRD in the original fiber. Center: FRD in the new fiber, cable A. *Right panel*: FRD in the new fiber, cable B.

A single FRD measurement consist of a series of FF images for every input F-number. By measuring the diameter of the illumination pattern in these images I can measure the FRD in a particular fiber.

I developed a custom software package to reduce the fiber FF images and to obtain the throughput curves. This package finds the centroid of the FF image, and performs aperture photometry at different radii from the center. In some cases the light cone does not fit completely in the detector. Because of this, the largest aperture is given by the largest circle, with its center at the FF image centroid, that fits in the detector. In consequence, the photometric measurements are relative to this aperture.

Bias and background images are substracted from the test exposures, to correct for the read-out noise and to remove background radiation.

Results

Figure 2.6 shows the results of the FRD measurements in the three fibers under study. These results show that the new fibers perform much better than the original fiber in terms of FRD. In this case the fiber loses are below 5% when using the cable B, instead of the 20% FRD loses of the original fiber. Between the two new fibers acquired, labeled as A and B, respectively, fiber B shows a better performance in FRD. Therefore this is the fiber that will be used to link the front-end with the Waltz spectrograph.

2.3.3 Final spectrograph optical design

From the results of §2.3.1 and §2.3.2, the optimal solution for the spectrograph fiber and FN-system upgrade is the use of a 33μm$\times$132μm fiber at input and output focal ratios of F/5.38 and F/5.5, respectively, to optimize the FRD, together with the replacement of the second lens of the FN system with an achromat double with a focal length of 45 mm. This new design provides a spectral resolving of power of about 60,000 and a mean spectral sampling of 2.6 pix, and also improves the efficiency of the instrument by about 15% with respect to the original design. The main parameters of the spectrograph are summarized in Table 2.1.

R($\lambda/\Delta\lambda$)	60,000
Spectral coverage	450 - 800 nm
Fiber size	Rectangular core 33μm $\times$ 132μm
Fiber aperture on sky	3.5 arsec
Collimator	Parabolic mirror, F = 900 mm
Echelle grating	31.6 lines/mm, 63.5° blaze angle
Cross-dispersion	LF5 prism, apex angle 60°
Camera	Petzval quadruplet apochromat, F = 530 mm, F/5
Detector	Andor iKon-L 936, 2k×2k, 15μm per pixel.
Average spectral sampling	2.6 pix

TABLE 2.1: Main features of the Waltz spectrograph

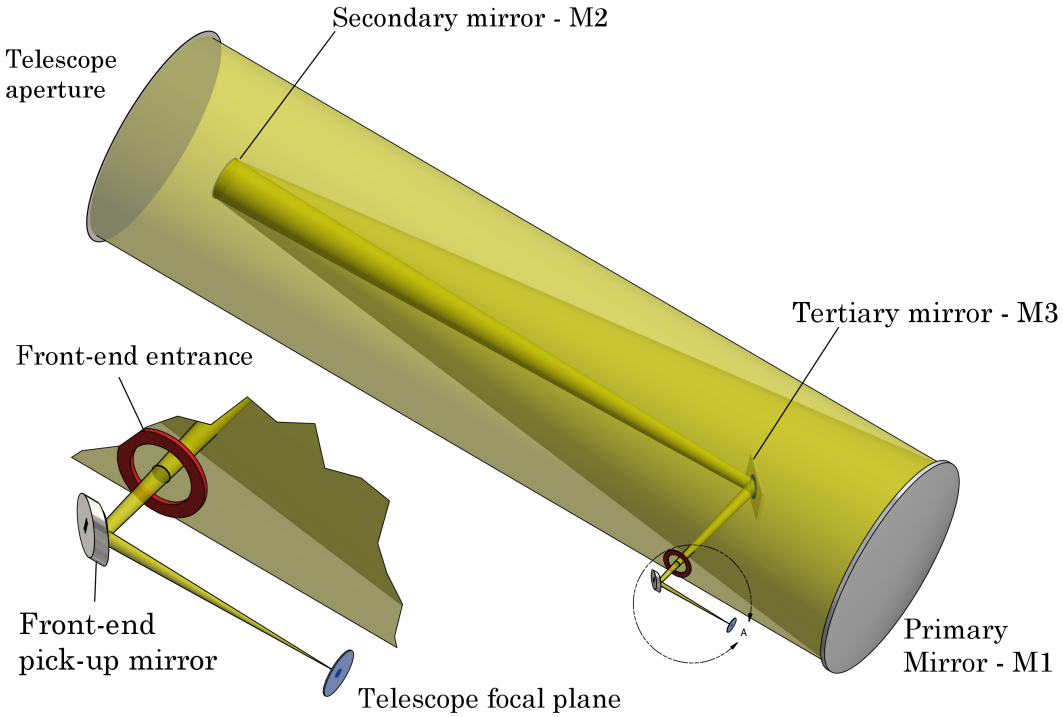

FIGURE 2.7: Optical design of the Waltz telescope. The path of a beam through the telescope is shown in yellow.

2.4 Waltz Front-end

The Front-end is the module that links the telescope with the spectrograph. The Waltz Telescope is located on the Königstuhl (568m) in Heidelberg and is one of the largest telescopes of the LSW. The 72 cm Waltz Telscope saw first light in 1906, and was the first big reflecting telescope whose optics was built by Carl Zeiss Jena. It was one of the biggest telescopes in the world at that time. Originally, the telescope was used in a Newton focus, but today it is used in Nasmyth focus. Its main application has always been spectroscopy. The telescope focal ratio is F/20.4, providing a plate scale of 14.04 arcsec/mm. Figure 2.7 shows the optical design of the telescope. The light from the star enters through the telescope aperture towards the primary mirror (M1), where is reflected to the secondary mirror (M2), and then to the tertiary mirror

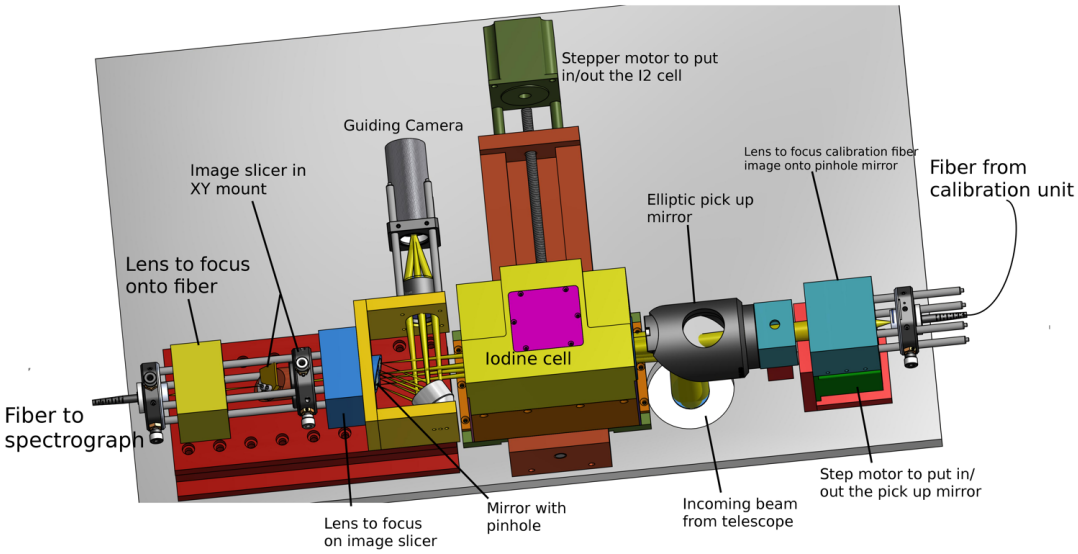

FIGURE 2.8: Preliminary front-end opto-mechanical design

(M3), where the beam is redirected to the Nasmyth focus. In Figure 2.7, I have shown in red the entrance aperture to the front-end module. After M3 the beam is reflected by the front-end pick-up mirror towards the focal plane of the telescope, as shown in Figure 2.7.

This interface must provide the following functions:

- Injection of star light in the optical fiber that feeds the spectrograph at a suitable F/# to optimize FRD.
- Guiding and acquisition, for precise aligment of the star image with the optical fiber
- Injection of calibration light in the spectrograph fiber
- Placing the I2 cell in and/or out of the telescope beam

To optimize the efficiency of the light injection into the spectrograph fiber, I had to do a series of measurements and calculations regarding the performance of the telescope and the optical fiber used to feed the spectrograph. In the following sections I will describe a preliminary opto-mechanical design for the front-end, together with the improvements that had to be done during the construction phase to improve and optimize the fiber coupling efficiency.

2.4.1 Preliminary design

A preliminary opto-mechanical design of the Front-end was presented in Tala et al., 2016. This design considered the theoretical focal ratio F/18.6 and a focal plane scale of 15.4 arcsec/mm. I assume an average seeing better than 3 arcsec. Thus I aim for a fiber projection 2.5 arcsec on-sky. As the telescope is used in a Nasmyth focus, the front-end is mechanically attached to the side of the telescope, where the beam

emerges after being reflected by the M3, by a base plate with size 400 mm $\times$ 700 mm that holds the mechanical mounts of the elements that compose the front-end. The beam is caught by the pick-up mirror to be redirected perpendicularly, leaving the beam axis parallel to the telescope optical axis, towards the focal plane of the telescope. At the focal plane of the telescope there is a mirror-pinhole that plays two important roles. The pinhole works as a spatial filter, filtering the light of the star that one would like to observe, while the mirror reflects the rest of the field of view (FOV) towards the guiding camera to perform field acquisition and guiding. The light that goes through the pinhole passes through an image slicer, that transform the image of the pinhole into a pseudo-slit image, to be efficiently injected into the rectangular fiber that feeds the spectrograph. The slicer is based on the Bowen-Walraven mirror image slicer presented in Tala et al., 2017, however in the case of the Waltz spectrograph, the slicer is mounted in the front-end, instead of the spectrograph.

In order to inject calibration light into the spectrograph, a fiber coming from the calibration unit is mounted behind the pick-up mirror mount. The pick up mirror is mounted in a translation stage that is controlled using a stepper motor, in order to put it in or out of the optical path of the calibration fiber beam. The image of the calibration fiber is focused in the pinhole, so the fiber image plane is the same position of the telescope focal plane. Then it passes through the image slicer to be refocused again into the spectrograph fiber. The image of the calibration fiber is about two times the size of the pinhole, to relax the alignment and centering constraints.

Figure 2.8 shows the preliminary opto-mechanical design of the Waltz front-end. I will refer to the Fiber Feeding Unit (FFU) as the optical system mounted behind the pinhole that focuses the beam from the telescope into the spectrograph fiber. The FFU of this design consists of two lenses, a mirror image slicer and a 5-axis mount that holds the fiber connector, and provides translation and rotation adjustments. After the pinhole, the beam is magnified and refocused in the image slicer by the first lens, to be then refocused by the second lens in the spectrograph fiber.

From this original design some components were upgraded. I presented a conceptual design for the pick-up mirror mount, based in the functionality requirements, and Lutz Geuer from the LSW Mechanics Workshop developed the final design that was manufactured. The final mount of the pick-up mirror is shown in Figure 2.9, and its mechanical design is shown in the final opto-mechanical design of the front-end in Figure 2.15. One of the main features of this mount is that it allows fine-tuning of the orientation of the pick mirror for aligning the optical axis of the telescope with the fiber axis. It is mounted in a translation stage to place it in/out of the calibration fiber beam.

The calibration fiber was originally mounted right behind the pick-up mirror mount, however this configuration led to a fiber image that was roughly four times bigger than the pinhole size, so an upgrade of the opto-mechanics of the calibration fiber was also required.

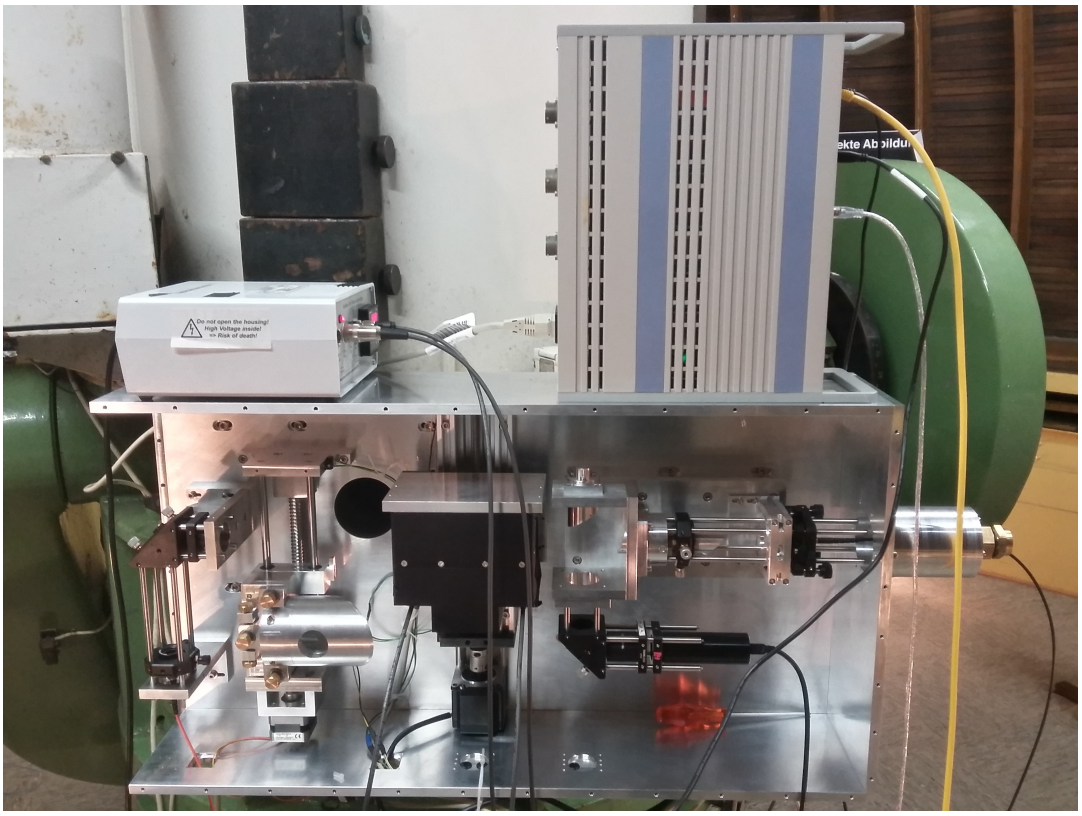

FIGURE 2.9: Picture of the front-end mounted in the Waltz telescope.

Early results

Figure 2.10 shows raw Arcturus and ThAr frames obtained with the Waltz Spectrograph. These frames were obtained before the spectrograph fiber and FN-system upgrades, hence the theoretical resolving power of the Waltz spectrograph is about 65,000 in the optical wavelength range. I used the ThAr lines both to determine the instrumental dispersion and to measure the resolving power of the spectrograph. A set of ThAr lines in the range between 609.88 nm and 610.56 nm was used for this purpose. The dispersion was determined by measuring the full width at half maximum (FWHM) of each line in nm of the wavelength calibrated spectra, and dividing it by the FHWM of each line in pixels on the reduced spectra. I obtained an average value of 0.0025 ± 0.0002 nm/pix for the spectral dispersion in spectral order 97. For the same lines I measure the resolving power by dividing the central wavelength of each line by its FWHM. For this order I obtained an average value of $61{,}656 \pm 1962$, which is in broad agreement with expectations. The scatter on the resolving power is explained by the properties of the spectrum itself. There is a small defocus factor at the edges of the echelle order, due to the non-compensated field curvature of the white pupil relay. Spectral lines close to the center of the detector, where the focus is optimal, demonstrate a resolving power up to 66,000.

Early results show that the spectrograph performance in terms of resolving power and spectral sampling are consistent with theoretical expectations, however the efficiency of the instrument is much less than expected. First of all, I considered a fiber

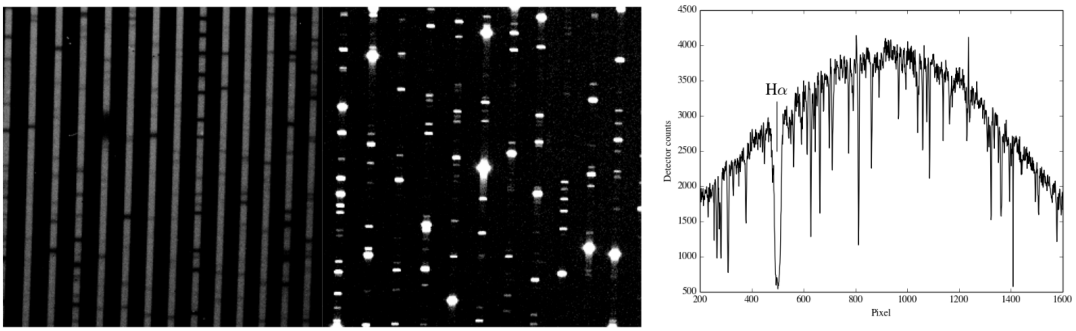

FIGURE 2.10: *Left panel*: Raw spectrum of Arcturus. *Center panel*: Raw spectrum of ThAr. *Right panel*: Extracted spectral order of Arcturus spectrum showing Hα.

aperture on-sky of 2.6 arcsec, but current estimations show that the seeing can vary between 2.5 arcsec to 3.5 arcsec. By assuming that the star is well described by a gaussian profile, I have estimated loses of about 25% if the seeing perfectly matches the fiber aperture.

In addition, the efficiency of the image slicer highly relies on the sharpness of the edges of the mirror used to slice the pinhole image. In the case of the slicer prototype I built, I used off-the-shelf mirrors from Edmund Optics, and carefully polished one side of the mirror, to have a sharp reflective surface for the slicer. To prevent damage in the mirror coating, I left some space between the border of the mirror and the start of the coated surface. However, as the edge of the mirror is not perfectly reflective, part of the light that strikes the slicer will hit the space between the reflective coating and the border of the mirror, leading to light losses.

On top of that, after some nights of observations I noticed that the fiber mount (KC1-S/M, Thorlabs) was mechanically unstable in the short-term. This meant that from night-to-night, most likely due to the mechanical flexures and temperature variations, the position of the fiber changed, losing alignment with the telescope and, as a consequence, losing efficiency. One of the main requirements for the FFU is the stability of the fiber positioning system over the long term, as high precision RV measurements require a stable fiber illumination pattern in the spectrograph fiber that is directly related to the input illumination of the fiber. To solve this problem I exchanged the mount for a more stable one (CP1XY, Thorlabs), but the issue was not that the stroke of the mount was too short (only 0.5 mm in X and Y axes). This becomes a problem in the sense that, as the distance between the pinhole and the fiber becomes greater than 100 mm, small misalignments in the telescope optical axis can shift the image of the pinhole in the fiber plane by more than a few milimeters. Therefore, not only the stability of the fiber mount presents a big constraint for an efficient fiber coupling, but also the distance between the pinhole and the fiber.

For this reason, it was necessary to implement a number of upgrades to the front-end to optimize the fiber coupling efficiency.

2.4.2 Waltz Telescope F/#

According to its optical design, the Waltz telescope focal ratio is 18.6. As the telescope aperture is given by the size of the primary mirror, the focal length of the telescope can be computed from the definition of focal ratio

$$F/\# = \frac{f}{D} \tag{2.2}$$

where f is the distance a beam has travelled and D its corresponding diameter. In the case of the Waltz I know F/# and D, therefore using Equation 2.2 I can calculate the focal length of the telescope. The focal length of the telescope is of great importance as it determines the plate scale of the telescope, which is defined as the angular separation of an object on sky with the linear separation of its image at the focal plane is

$$s = \frac{206265}{f_T} \left[\frac{arcsec}{mm}\right] \tag{2.3}$$

where f_T is the focal length of the telescope. For the Waltz telescope, the focal length is given by

$$f_T = 18.6 \cdot 720 \; mm$$

$$f_T = 13392 \; mm$$

which gives us a telescope plate scale of

$$s = \frac{206265}{13392} \left[\frac{arcsec}{mm}\right] = 15.4 \left[\frac{arcsec}{mm}\right]$$

However this is a theoretical value, as is obtained from the theoretical value of the focal ratio of the telescope. In reality the focal ratio has a different value, therefore the estimated projection of the fiber on-sky is different than expected. In order to obtain a more accurate value of the telescope plate scale I decided to make a direct measurement of the telescope focal ratio.

Experimental procedure and results

To measure the focal ratio of the telescope I removed the FFU, which in any case had to be upgraded, and mounted a CCD camera behind the pinhole. I removed all the optics behind the pinhole, so the beam that is projected onto the CCD camera comes directly from the telescope. To do the measurements I used the Moon, as it is a bright and extended source of light, providing a good and relatively uniform source of light. Therefore, I focus the Moon in the pinhole and observe the telescope pupil with the CCD camera mounted behind the pinhole.

Given the definition of the focal ratio, I need a measure of distance along the optical axis and a measure of the diameter of the beam at that distance. The experimental procedure consist of obtaining images of the telescope pupil at different

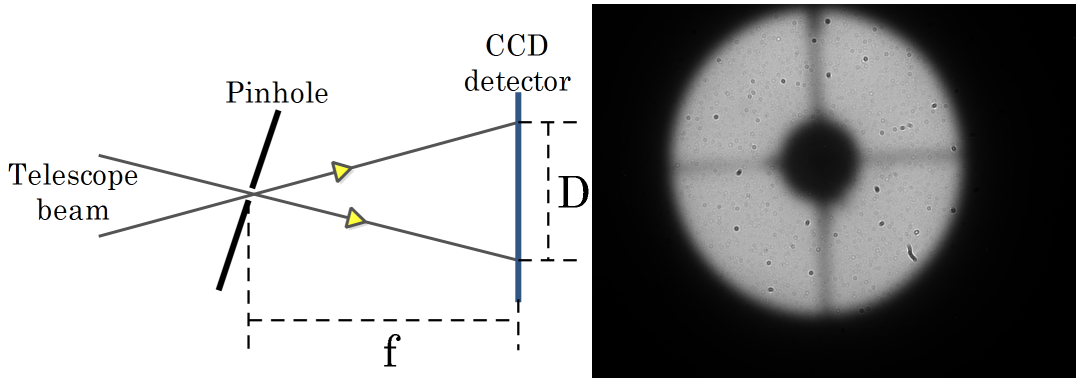

FIGURE 2.11: *Left panel*: Schematic of the experimental setup to measure the telescope focal ratio. *Right panel*: Image of the telescope pupil obtained with a CCD camera.

positions along the optical axis and measuring its diameter in the CCD camera. Figure 2.11 shows a schematic of the setup used to measure the telescope focal ratio.

The reference position is given by the closest mechanical distance between the pinhole and the CCD camera, so the distances along the optical axis are referred to this reference position. The positions of the camera along the optical axis are fixed by a set of spacers with a width of 10 mm that are placed between the pinhole and the CCD camera mounts. This way I know the distance that the CCD camera has been displaced, within the mechanical precision of the spacers, with respect to the reference position. The pupil diameter is measured by detecting on the image the pixels in the detector that are illuminated by the telescope pupil, and finding the pixel positions of the extreme edges of the pupil. The diameter is then the subtraction of the position of the extreme borders of the pupil, in pixels. As I know the pixel size of the detector used, I can transform the pupil diameter from the pixel to the mm space.

By obtaining images of the pupil at different positions along the optical axis with different pupil sizes, I can calculate the focal ratio for each pair of positions and obtain a statistical error for the measurement. With this method, the Waltz Telescope focal ratio is 20.4$\pm$1.4. This value is larger than the theoretical value, even considering the error of the measurements.

With the measured value of the focal ratio I re-calculate the telescope focal length

$$f_T = 20.4 \cdot 720\ mm = 14688\ mm$$

and the telescope plate scale

$$s = \frac{206265}{14688}\left[\frac{arcsec}{mm}\right] = 14.04\left[\frac{arcsec}{mm}\right]$$

and use these values to re-calculate the projection of the fiber on-sky.

2.4.3 Final Waltz Front-end Opto-mechanical Design

Based on the flaws detected in the preliminary opto-mechanical design of the Waltz Front-end, I implemented some modifications to improve the function, efficiency and stability of the system.

Calibration Fiber

The calibration fiber is a 300μm circular core diameter fiber from Thorlabs (M69L05) and it is 15 meters long. In the preliminary design the calibration fiber was mounted right behind the pick-up mirror, as shown in Figure 2.8. This configuration provided a calibration fiber image that was about four times the size of the pinhole. Ideally, to maximize the amount of light that goes from the calibration unit to the spectrograph, one would like to match roughly the size of the fiber image with the pinhole size. To improve the coupling efficiency of calibration light into the spectrograph fiber, and at the same time relax the constraints of the aligment between the calibration fiber and the pinhole, I have estimated that the calibration fiber image size has to be about 1.5 times the size of the pinhole.

Originally, the distance between the fiber and the lens that focuses the fiber image in the pinhole was rather short, as the output focal ratio of the fiber must be transformed to the focal ratio of the telescope. Therefore the lens must considerably magnify the fiber image. While one of the advantages of this configuration is the compactness of the system, its main disadvantage is the light loses due the large fiber image in the pinhole.

To reduce the magnification factor, the distance from the fiber to the lens must be increased. As there is no space left behind the pick-up mirror, because of the limited size of the base plate of the Front-end, I use a right-angle kinematic mirror mount (KCB1C/M, Thorlabs) to install a fold mirror just behind the pick-up mirror mount. This right-angle mount is attached on one end to a mechanical mount that is attached directly to the base plate through a cage system. On the perpendicular side of the right-angle mount, a cage system is used to align the fiber mounted in a XYZ translation stage (CXYZ05/M, Thorlabs) with the lens that transforms the focal ratio of the fiber to the telescope focal ratio (AC254-125-A, Thorlabs) and the fold-mirror. Another mechanical mount attached to the base plate serves as support for this cage system, and also for the fiber and the lens. The final setup of the calibration fiber magnification system is shown in Figure 2.9 and in Figure 2.15.

Fiber Aperture on-sky and Mirror Pinhole

As discussed in §2.4.1, about 25% of the light is lost because the fiber projection on sky is smaller than the actual seeing at the telescope site. Early estimations suggested that the seeing was on the order of 2.5 arcsec, however later seeing estimates obtained from the 70 cm telescope at the LSW suggested that the seeing could easily vary between 2.5 - 3.5 arcsec throughout the year. Therefore, the projection of the

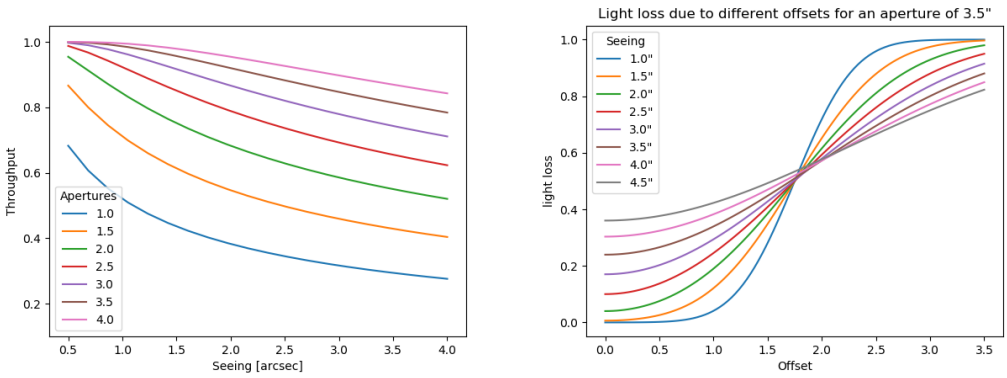

FIGURE 2.12: *Left panel*: Relative efficiency for several circular sky apertures under varying atmospheric seeing conditions. *Right panel*: Light losses in a circular aperture that projects 3.5ön-sky for several atmospheric seeing conditions as a function of the offset in arcsec of the a gaussian PSF in the circular aperture.

fiber on-sky, and hence the mirror pinhole, must be suited to these varying seeing conditions.

To constraint the value of the fiber projection on-sky and of the size of the pinhole, I assume a seeing of 3.5 arcsec with a gaussian profile. Figure 2.12 shows on the left panel the throughput of different apertures on-sky as a function of seeing, considering a gaussian PSF perfectly centered on the aperture. In this case, I am interested in the seeing regime between 2.5 and 3.5 arcseconds. As the goal is to optimize the efficiency of the fiber aperture on-sky, I discard all the apertures with a throughput of less than 0.8 (80%), in the seeing regime of interest. This leave us with only apertures between 3.5 arcsec and 4 arcsec, which already provides strong constraints for the value of the fiber aperture on-sky. However, I must consider that the fiber has a fixed geometry and size, and increasing the aperture means that also the de-magnification factor increases.

Guiding errors decenter the star image in the aperture, producing light loses. This is shown in the right panel of Figure 2.12, where I have plotted the light loss for an aperture of 3.5 arcsec, under different seeing conditions as a function of the offset of the PSF with respect to the aperture in arcseconds. From this plot, it is clear that for a fixed aperture, the light loses are more important if the seeing gets worse. However, the light loses due to offsets increase due to guiding errors and are more important when the seeing conditions are better. For an aperture of 3.5 arcsec and assuming a minimum offset of 0.5 arcsec, the light loses are about 25%, in the case where the seeing is of 3.5 arcsec. I assume that typically the seeing will be better than 3.5 arcsec, so the light losses due to offsets produced by guiding errors should be, in most cases, better than 20%. Hence, I have concluded that the optimal value for the aperture of the fiber on-sky is 3.5 arcsec. To optimize the guiding accuracy and minimize the light losses due to guiding errors, I fixed the size of the projection

of the pinhole on-sky to 3.7 arcsec, a value slightly larger than the fiber aperture on-sky. By considering the measure plate scale of the telescope, 3.7 arcsec corresponds to about 265 μm diameter pinhole, which is the value I have adopted.

Fiber Feeding Unit

As discussed in §2.4.1, one of the main issues with the preliminary design of the instrument was the instability of the fiber mount used and the distance between the pinhole and the spectrograph fiber. To overcome these limitations I have decided to modify the original design, to improve the fiber coupling stability and efficiency.

To solve the problem of the fiber positioning stability, I have exchanged the original fiber mount (KCB1C/M, Thorlabs) for a more stable one (CP1XY, Thorlabs). The CP1XY offers $\pm$0.25 mm of XY travel manipulated by M2.5$\times$0.20 fine pitch adjusters. The stainless steel flexure design provides excellent long-term stability and is ideal for fiber coupling applications or experiments that use spatial filters or pinholes, which require fine positioning. In addition, to overcome the issues related to the misalignment of the telescope optical axis with the fiber axis, I removed the image slicer, and just use one lens to feed the fiber. This allows tthe size of the system to shrink considerably, making it much more compact and stable. The main drawback of removing the image slicer is the light loss due to projecting the roughly circular image of the star in the rectangular fiber.

One way to overcome this limitation is to attach an image slicer directly in the fiber tip, this way the image of the star is transformed into a pseudo-slit before being injected into the spectrograph fiber. This technique is still under development and is not yet ready for being implemented in the Waltz Front-end. However, I have designed the fiber coupling system with the fact that the image of the star will be sliced before entry to the fiber. Figure 2.14 shows an image of an octagonal fiber sliced by an image slicer mounted in its tip. The newest devices developed at Karlsruher Institut für Technologie have 80% throughput, which is not bad (compared to the 60% you would get if you 'mask' the fiber to the same width). However, it is not the slightly over 90% one would expect from models and it is not so certain where the loses come from. One reason could be that the contact between the slicer and the fiber is not perfect (in two cases the slicer did not stick to the fiber tip) causing additional fressnel loses (Stürmer, 2019, priv. comm.).

As stated in §2.4.3, the optimal fiber aperture on-sky is 3.5 arcsec. Based on the measured focal ratio of the telescope, this corresponds to 250μm in the telescope focal plane. Therefore, to efficiently couple the light into the fiber, I must demagnify the projection of the fiber in the telescope focal plane to the size of the fiber. The implementation of the image slicer considers that a circular image with 66μm diameter is transformed into a 33μm $\times$ 132 μm pseudo-slit that is injected into the fiber. Therefore, the 250μm image must be transformed to a 66μm diameter image, so the

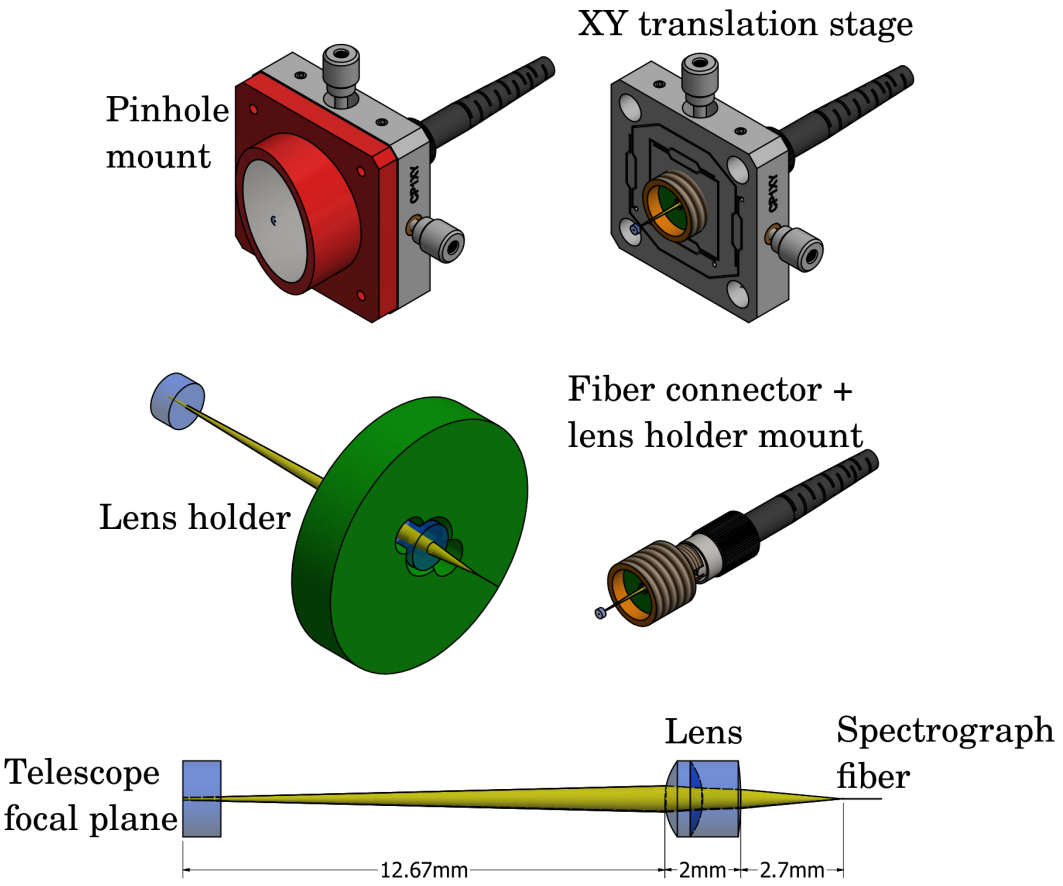

FIGURE 2.13: Fiber feeding unit opto-mechanical design

magnification factor is

$$M = \frac{66\ \mu m}{250\ \mu m} = 0.264$$

and the telescope focal ratio is F/20.4. This means that the input focal ratio to the spectrograph fiber is

$$F/\#_{in} = 20.4 \cdot 0.264 = 5.38$$

Based on these contraints I designed an optical system that consist of a doublet achromat lens (84-127, Edmund Optics), with a focal length of 3 mm and a diameter of 2 mm, which demagnifies the image of the star in the focal plane according to our optical requirements. The main advantange of this optical system is its compactness, as the distance between the pinhole and the fiber is reduced to about 17.4 mm, relaxing considerably the tolerances of the alignment between the telescope and fiber axes. Figure 2.13 shows the opto-mechanical design of the upgraded FFU. In the top images, the red mount corresponds to the pinhole mount, which is attached to the XY precision translation stage that holds the fiber mount. The fiber is mounted to a customized fiber mount, shown in the center-right image in Figure 2.13, that also works as a holder for the lens mount, shown in green in the center-left image in Figure 2.13. This custom fiber mount is screwed into the XY translation stage, so as the

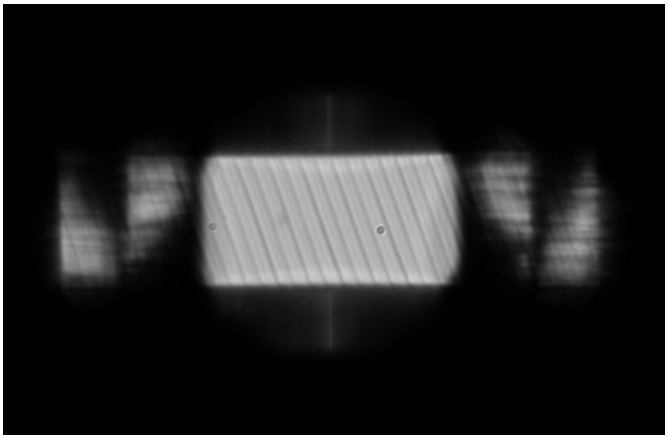

FIGURE 2.14: Octagonal fiber image sliced by an image slicer printed on top of the fiber. Credit: Stürmer, 2019, priv. comm.

lens is mechanically attached to the fiber mount, when adjusting the fiber position along X and Y axes, one also adjusts the position of the lens with respect to the optical axis. The alignment between the lens and the fiber is defined by their positions in the mechanical mount that holds them. The lens mount is a modification of an off-the-shelf 2 mm lens adapter mount (LMRA2, Thorlabs).

Final Design

Figure 2.15 shows the final opto-mechanical design of the Waltz front-end. It incorporates several improvements that will considerably boost the fiber coupling efficiency, with respect to the preliminary design.

The incoming beam from the telescope enters through the front-end window and is captured by the pick-up mirror, that redirects the beam to the focal plane of the telescope where a mirror pinhole is placed. The light that goes throught the pinhole enters the FFU, while the surrounding FOV goes to the acquisition and guiding system. By increasing the pinhole size, the efficiency is boosted by about 20%, and by removing the slicer I was able to reduce the size of the FFU from over 100 mm to only 17 mm, improving the mechanical stability of the fiber positioning system. The FFU was described in §2.4.3. This FFU considers the implementation of a printed slicer in the tip of the fiber, however this technique still has not yet proven its feasibility and is still under development.

For telescope guiding and acquisition I have designed a simple optical system that consists of: a mirror with a small pinhole in its center, a flat mirror, an achromat double, an optical filter and a CCD camera. The reflective pinhole is inclined at an angle 15° with respect to the telescope optical axis. The image of the star to be observed is centered on the pinhole, while the surrounding field is reflected to a flat mirror, which is placed at an angle such that the reflected beam is perpendicular to the telescope optical axis. The beam is reflected towards an achromat double (AC254-040-A, Thorlabs) that focuses the image of the FOV into a CCD camera,

which in this case corresponds to the Starlight Lodestar X2, a 752×580 pixel array with 8.6μm×8.3μm pixel size. Between the achromat lens and the CCD detector is an optical filter (FES0650, Thorlabs) centered at 650 nm, to optimize the guiding of the telescope to the wavelength range of interest, which is the range at which the iodine features are present. Figure 2.16 shows the final opto-mechanical design of the acquistion and guiding system.

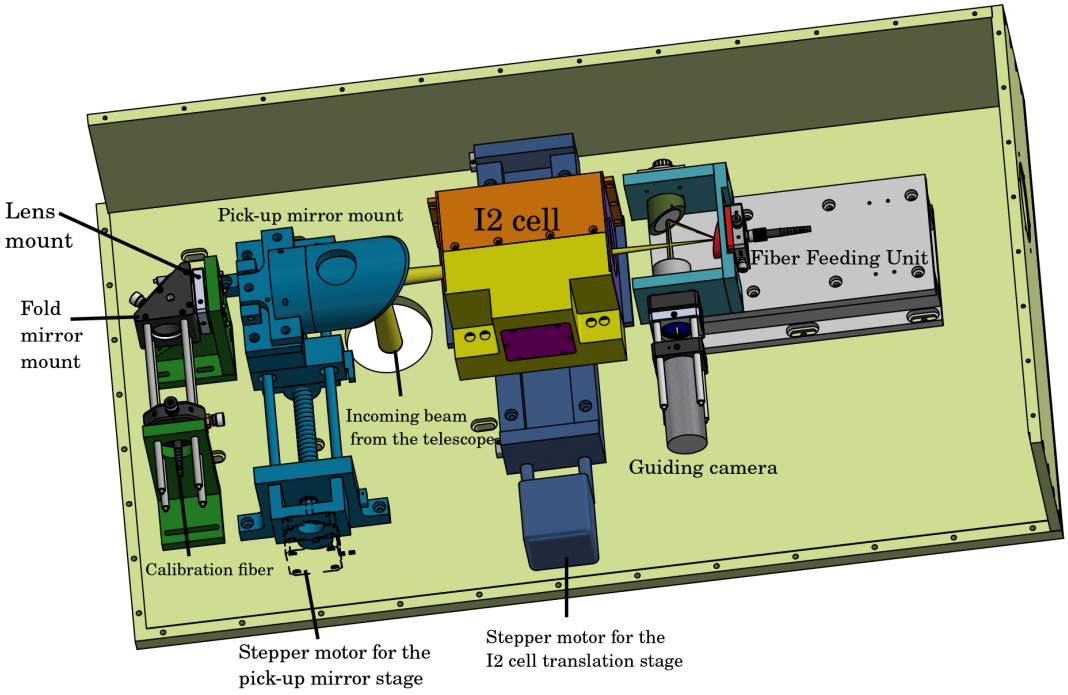

FIGURE 2.15: Final front-end opto-mechanical design

The final design of the Waltz Front-end fulfills all the requirements to optimally couple the starlight to the spectrograph fiber, providing the following functionalities

- Injection of starlight into the spectrograph fiber at a F/5.38 to optimize FRD
- Guiding and acquisition by observing a 4 arcmin FOV sourounding the pinhole
- Injection of calibration light in the spectrograph fiber, by placing the pick up mirror in and out of the calibration fiber beam
- Place the I2 cell in and out of the telescope beam

The opto-mechanical design of the front-end is finished. The new FFU was already sent to the mechanical workshop to be built, but by the time of writing this thesis it is still under construction. Once the new FFU is ready, the next step is to mount it in the front-end, test its performance, and if everything goes as planned, start the instrument commissioning.

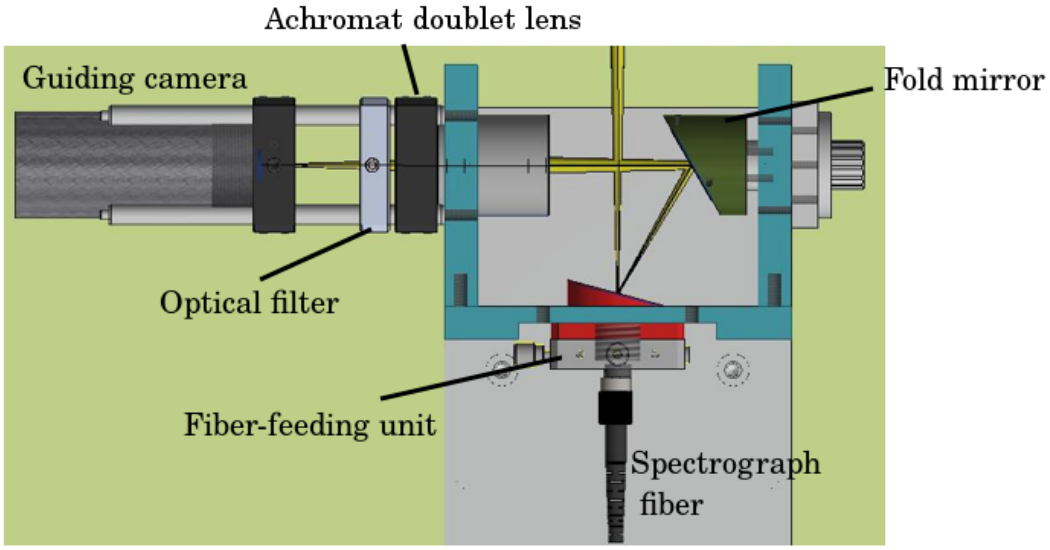

FIGURE 2.16: Opto-mechanical design of the acquisition and guiding system plus the FFU.

2.4.4 Front-end control

There are two movable components in the front-end. One is the translation stage of the pick-up mirror, that places the pick-up mirror in or out of the telescope's beam in order to feed with calibration light the spectrograph fiber, and the second is the translation stage that places the I2 cell in or out of the telescope beam. Both translation stages are moved by stepper motors, which are controlled using Arduino Uno microcontrollers coupled with Motor shields.

Arduino Uno is a microcontroller board that has 14 digital input/output pins (of which 6 can be used as PWM outputs), a USB connection, a power jack and a reset button. It contains everything needed to support the microcontroller; simply connect it to a computer with a USB cable or power it with a AC-to-DC adapter or battery to get started [1]. The Arduino Motor Shield is a driver designed to drive inductive loads such as relays, solenoids, DC and stepping motors. The Motor Shield can be easily coupled to the Arduino Uno microcontroller. Therefore, each stepper motor is connected to the Arduino Motor Shield, which is at the same time attached to the Arduino Uno board. Each Arduino is accessed and controlled by a Raspberry Pi. The Raspberry Pi is a very cheap computer that runs Linux, but it also provides a set of GPIO (general purpose input/output) pins that allow you to control electronic components for physical computing. In the case of the front-end control, the Arduinos are connected to the Raspberry Pi, which is at the same time connected to the LSW network, so that is accessible from the main Waltz instrument computer.

The Raspberry Pi and the two Arduino+Motor Shield are mounted in the so-called Electronic Box, shown in Figure 2.17. This box also includes a driver to control

[1] https://store.arduino.cc/arduino-uno-rev3

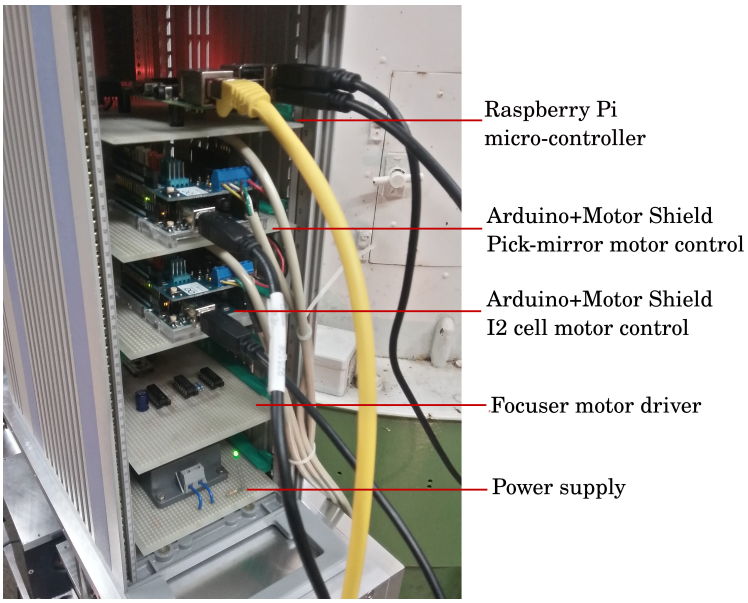

FIGURE 2.17: Picture of the electronic box that contains the components that controls the focuser, and the pick-mirror mount and iodine cell mount stages.

the telescope focuser and a power supply to provide power to the Raspberry Pi and the two Arduinos. The focuser driver is connected directly to the Raspberry Pi.

2.5 Summary

The Waltz Spectrograph is a cross-dispersed fiber-fed echelle spectrograph installed in the 72 cm Waltz Telescope at the LSW whose main scientific goal is continue the Lick survey of giant planets around giant stars, specially to confirm long-term trends that are seen in the data which may hint sub-stellar companions with periods of a decade or more.

The original design of the instrument was presented in Tala et al., 2016. In this original design the spectrograph was fed with starlight using a 25μm $\times$ 100μm rectangular core fiber, providing a spectral resolution of 65,000 and a mean spectral sampling of 2.4 pix. The main drawback of this original design was its poor performance in terms of FRD that provoqued light loses of about 20%, in addition to the fact that this particular fiber is no longer in stock in Ceramoptec, the company that provided the fiber that was used in the original design.

With the goal of improving the instrument performance, I investigated the option of changing the original fiber for another one, with the same geometry, but slightly larger core size. This new fiber is the RCT WF33x132/280/320P, NA=0.2 fiber, an optical fiber with a 33μm $\times$ 132μm rectangular core size. Changing the fiber has a direct impact in the resolving power and the spectral sampling, as well as in the FFU at the Waltz Front-End. So changing the fiber means that it will also change the fiber injection optics and the FN-system optics, to optimize the instrument performance.

The FN-system is a pre-slit optics that transforms the output focal ratio of the spectrograph fiber to the working focal ratio of the spectrograph collimator. In the original design it consists of two double achromat lenses with focal lenghts of 25 mm and 56 mm. The first lens collimates the beam, while the second focus it. With the new fiber and the original FN-system, the spectral resolving power was 48,000. In order to boost the resolution I decided to change the second lens of the FN-system for a double achromat with a focal length of 45 mm, increasing the resolving power to 60,700 with a mean spectral sampling of 2.6 pix. With this configuration, the output beam the F/10 of the collimator corresponds to a F/5.5 at the fiber output, meaning that all rays emerging from the spectrograph fiber at a focal ratio smaller than F/5.5 will be lost.

In addition I developed the opto-mechanical design of the Waltz Front-End. The proposed solution allows to: inject the starlight into the spectrograph fiber with a suitable focal ratio, place the Iodine cell in and/or out of the telescope beam, place the pick-up mirror in and/or out of the telescope beam, inject calibration light into the spectrograph fiber and perform field acquisition and telescope guiding. The Waltz Front-End was built and is working almost as expected. While most of its functionalities are already working fine, the injection of starlight into the spectrograph fiber hasn't been succesfully implemented yet. The original opto-mechanical design wasn't stable at the level required by the tight constraints impossed by the alignment of the fiber with the telescope axis. I designed a new FFU that was optimized for high stability over the long term, which is currently under construction in the LSW Mechanical Workshop. By implementing state-of-the-art 3D printing slicing optics I expect a boost in the fiber coupling by a factor of at least 20 %, with respect to a fiber coupling without a slicer.

The instrument is reaching the end of its construction phase. Once the last modifications of the Front-End are succesfully implemented, the project will continue with the instrument commissioning with the aim of starting science observations as soon as possible.

Chapter 3

RAMSES and the CARMENES wavelength solution

Some of the results presented in this chapter have been published in Tala Pinto et al., 2018. Unless stated otherwise, all figures presented are based on own calculations or measurements.

3.1 Introduction

In order to reach the high precision of todays RV measurements there have been many improvements regarding the design, construction and optimization of high resolution spectrographs. White pupil designs improved instruments efficiencies, optical fibers allowed us to detach instruments from the telescope focal plane and mount them in gravity invariant environments, multi-channel spectrographs increase the wavelength range observed, and thermal and pressure control are critical to achieve few m/s RV precision when using the simultaneous calibration technique. Moreover, new calibration sources, such as etalons or laser frequency combs, are pushing the limit of the RV precision into the cm/s regime. However, in contrast to the advancements in hardware, there has been little work trying to transmit the information of the physical properties of the spectrograph to the instrument data reduction software.

In particular, when performing the wavelength calibration of a given set of spectra, the wavelength solution - the function that maps from pixel to wavelength space - is derived in a purely empirical way, by fitting polynomials to a sparse calibration line spectrum. One way to ensure that the engineering data propagates from instrument building to operations is to use all design and engineering information in a physical model-based description of the instrument and use this to compute the wavelength solution.

The ESO group developed a model-based calibration tool (Ballester and Rosa, 1997) which has been successfully applied to FOS (Rosa et al., 2003) and STIS (Kerber, Bristow, and Rosa, 2006) on HST, as well as CRIRES (Bristow et al., 2006) and X-SHOOTER (Bristow et al., 2010) on the VLT. This model-based approach is limited to on-axis configuration of the optics with all aberration corrections applied together

as a polynomial at the detector plane (Bristow et al., 2006). Following the same philosophy, Chanumolu, Jones, and Thirupathi, 2015 developed a physical model for the Hanle echelle spectrograph that provides the exact position of chief rays leaving only the centroid corrections, which are of the order of sub-pixel, at the detector plane. This particular modeling approach is based on paraxial ray-tracing including exact corrections for some surface types and Buchdahl aberration coefficients for complex modules such as camera systems. In addition, it is able to track the difference in the centroids between two fiber images across the spectrum, as well as instrumental shifts between two fibers, providing an efficient 1D order extraction tool for varying slit positions and orientations (Chanumolu et al., 2017).

Currently, there are several ray tracing softwares commercially available (Optics Studio - Zemax, Code V, OSLO) that perform ray tracing through optical systems with high accuracy, however they are not optimized to perform large amount of calculations to fit their models to real echelle spectroscopic data, as their functionalities are mostly oriented towards optical design. In Optics Studio - Zemax the typical computation time for ray tracing of a thousand wavelengths through an echelle spectrograph is about 2 to 3 minutes in a regular computer. To succesfully fit a Zemax ray tracing model to real spectroscopic data I would have to evaluate the model in the parameter space, at least, several thousands times, a task that with current commercial ray tracing softwares is computationally unfeasible. Also, commercial ray tracing softwares are black boxes, in the sense that they provide a number of functionalities to trace rays in optical systems, but they don't specify what are the exact operations behind these calculations. With the aim of succesfully fitting an echelle spectrograph model to real spectroscopic data to understand the instrument behavior, I have developed a ray tracing software that models the path of photons through a high resolution cross-disperser echelle spectrograph.

In this chapter I present a modeling scheme based on direct ray tracing of the chief ray from the slit to the detector plane of a high resolution spectrograph, applying exact corrections when tracing through curved surfaces. The direct ray tracing provides an accurate theoretical description of the instrument, as opposed to paraxial ray tracing, as it calculates the exact the position of each ray along the optical path of the spectrograph. In most cases HCL spectra are used to derive the model parameters that match the observations. The optimized model can be used to understand instrument behavior, quality checks and trending. The model once matched with the observations can predict the centroid position of any HCL spectral line. I have named the code RAMSES as an achronym for **RA**y tracing **M**odeling **S**oftware of **E**chelle **S**pectrographs.

I present the application of RAMSES to CARMENES as a case study. Based in the optical design of the instrument, RAMSES describes the path of a photon at a given wavelength through the CARMENES VIS and NIR spectrographs. The modeling of CARMENES is done in parallel with science observations, including daily calibrations. At the time of writing of this thesis, the CARMENES survey has been

observing for more than three years, providing a wide baseline of observations and daily calibrations. Using the daily wavelength calibration data I fitted my model to the line positions of the hollow cathode lamps and compute a wavelength solution based in the instrument parameters.

3.2 Fundamentals of Ray Tracing

In geometrical optics, light is described by rays that propagate according to mainly three laws: rectilinear propagation, refraction and reflection. The fourth law is the law of diffraction, that describes the behaviour of light when passing through an infinitesimal slit and its dependance with wavelength. A ray is an idealized model of light, which is defined as a line that is perpendicular to the wavefront of the actual lightbeam, and that points in the direction of the energy flow. While rays are not physical entities, in the sense that one cannot isolate a single ray, they provide a convenient framework to describe the process of imaging by an optical system.

For homogeneous, isotropic media, such as common optical glass, rays are straight lines. In most cases, rays have a position, direction, amplitude, phase and polarization information related to them. At surfaces between different media, rays can refract, reflect or diffract and the interface between the media will, in general, alter the direction and other properties of the ray. In this context, Ray Tracing is a method for calculating the path of waves or particles through an optical system with regions of varying propagation velocity, absorption characteristics, and reflecting surfaces. The optical path length of a ray in a certain medium is equal to the geometrical path length times the refractive index of the medium. A surface passing through the end points of rays that have traveled equal optical path lengths from a point object is called an *optical wavefront*. In this work I will focus mainly in the tracing of chief rays of different wavelengths, in order the optimize the number of computations. For further details on the physics of optical wavefronts, I would recommend Hecht, Zając, and Guardino, 1998, Kidger and Tuchin, 2002 and/or Mahajan, 2014.

3.2.1 Fermat's Principle

Fermat's principle is one of the most important theorems of geometrical optics. While, in practice, it is not used directly in optics design it is useful to derive results that would be impossible to derive in other ways. It states that the time that a ray takes to go from one point to another along its actual path is the same with respect to small changes of that path. By definition, the refractive index of a medium n is the ratio between the speed of light c in vacuum and the speed of light in the medium v. If the *optical path* is defined as the geometrical path that a ray has traveled multiplied by the refractive index of the medium, the Fermat's Principle states that the optical path length of a ray traveling from point to another aloing its actual path is stationary. This statement is very well expressed by the following equation

$$\delta \int_{P_1}^{P_2} n \, dx = 0 \tag{3.1}$$

where δ indicates *differential variation* and dx is an differential element of path length.

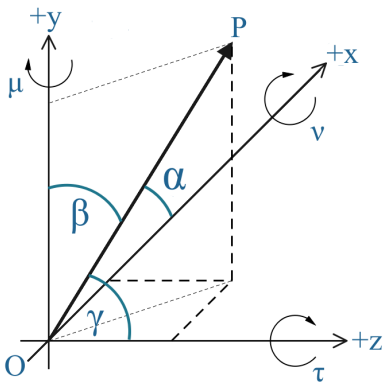

FIGURE 3.1: *Left panel*: Coordinate system orientation. Direction angles (α, β, γ) are positive from axis to ray OP. Rotation angles around xyz-axis are given by μ, ν and τ, respectively. Optical axis is along the z-axis, echelle dispersion direction along x-axis and cross-dispersion direction along y-axis. *Right panel*: 2D projection of the collimator.

3.2.2 Coordinate system and sign convention

Ray are described by the position vector $\vec{x} = [x, y, z]$ and the direction cosines $\vec{d} = [d_x, d_y, d_z]$ in a three dimension Euclidean space, so

$$cos^2\alpha + cos^2\beta + cos^2\gamma = d_x^2 + d_y^2 + d_z^2 = 1 \tag{3.2}$$

where α, β and γ are the direction angles as shown in Figure 3.1. The direction angles are acute, i.e., $0 < \alpha < \pi$, $0 < \beta < \pi$ and $0 < \gamma < \pi$, and they denote the angles between $\vec{x}$ and the unit basis vectors.

Each ray is defined by its wavelength λ, position $\vec{x}$ and direction $\vec{d}$. The optical axis is along the z-axis, the x axis is along the echelle-dispersion direction and y is along cross-dispersion direction. Angles are measured positive from axis to ray, as shown in Figure 3.1.

In the case of centered lenses, the refractive or reflective surfaces have a common optical axis. The curvature radii of a curved surface is defined as concave if $R > 0$, and convex if $R < 0$. Tilts are applied using rotation matrices of the form

$$R_{\mu/x} = \begin{pmatrix} 1 & 0 & 0 \\ 0 & cos\ \mu & -sin\ \mu \\ 0 & sin\ \mu & cos\ \mu \end{pmatrix} \tag{3.3}$$

$$R_{\nu/y} = \begin{pmatrix} cos\ \nu & 0 & -sin\ \nu \\ 0 & 1 & 0 \\ sin\ \nu & 0 & cos\ \nu \end{pmatrix} \tag{3.4}$$

$$R_{\tau/z} = \begin{pmatrix} cos\ \tau & -sin\ \tau & 0 \\ sin\ \tau & cos\ \tau & 0 \\ 0 & 0 & 1 \end{pmatrix} \tag{3.5}$$

where rotations around the x, y and z axis are given by $R_{\mu/x}$, $R_{\nu/y}$ and $R_{\tau/z}$, respectively. The overall rotation matrix is given by the multiplication of each rotation matrix in the following order $R = R_{\mu/x} \cdot R_{\nu/y} \cdot R_{\tau/z}$.

3.2.3 Gaussian Optics

For rays almost normal to the refracting and reflecting surfaces Gauss's small angle approximation can be used. In this approximation, the sines and tangents of the angles of the rays with the optical axis are replaced by the angles, and any diagonal distances are approximated by the corresponding axial distances. Gaussian optics or imaging relates the object distance and size to the image distance and size through the parameters of the imaging system such as the radii of curvature of the surfaces and refractive indices of the media between them. The assumption or approximation of small angles is referred to as the Gaussian or the paraxial (meaning near the optical axis) approximation. A distinction is sometimes made between Gaussian and paraxial optics in that paraxial optics is a limiting case of Gaussian optics in which the angles are infinitesimal quantities. The rays traced in this approximation are called paraxial rays and the corresponding method of ray tracing is referred to as paraxial ray tracing. Because of rotational symmetry, only rays lying in the plane containing the optical axis and the point object under consideration need to be considered to determine the Gaussian image. Such a plane is called the tangential (or meridional) plane, and rays lying in this plane are called tangential (or meridional) rays. Those rays that intersect this plane are called skew rays. Figure 3.2 shows the refraction of a ray in a surface with curvature R in the paraxial approximation.

Gaussian optics only consider the properties of an optical system close to the optical axis. This approach assumes that lenses (and mirrors) form perfect images, with no aberrations. In reality, this assumption is not valid. Real optics have aberrations, which must be reduced in most cases. However, even if the paraxial approximation only covers a small area enclosing the optical axis, many concepts defined for the paraxial region are applicable also outside it (Kidger and Tuchin, 2002). In that sense, the paraxial approximation provides a good insight on the performance of an optical system with a modest effort. For further details on the features of paraxial ray tracing, I recommend Mahajan, 2014.

Refraction and reflection in 2D

In this section I will briefly discuss refraction and reflection laws in 2D.
Let's consider refraction as shown in the left image of Figure 3.3. The optical path from point A to B is

$$[APB] = n\sqrt{x^2 + s^2} + n'\sqrt{(l-x)^2 + s'^2} \tag{3.6}$$

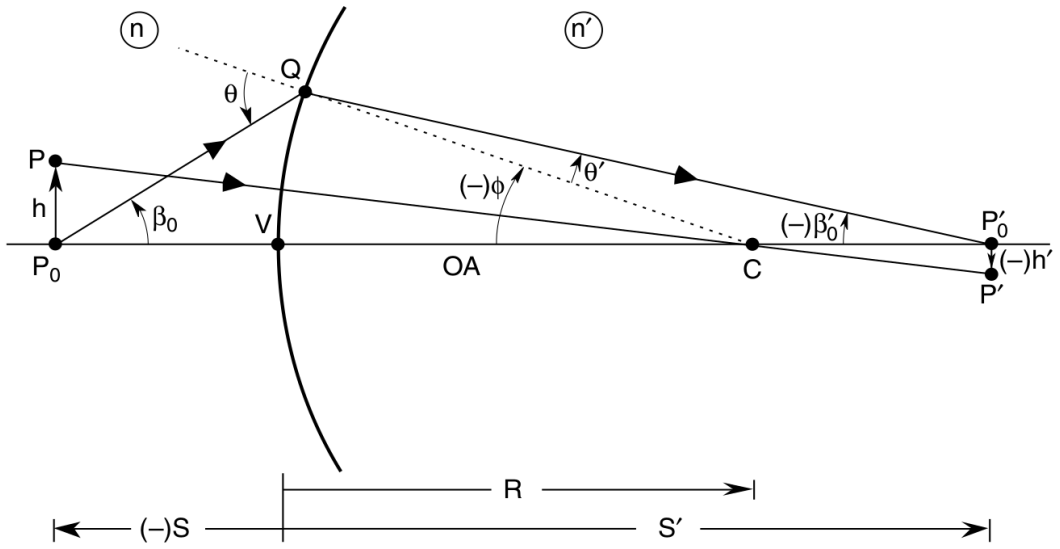

FIGURE 3.2: Gaussian image by a convex spherical refracting surface of radius of curvature R separating media of refractive indices n and n', where $n' > n$. VC is the optical axis of the surface, where V is the vertex of the surface and C is its center of curvature. The axial point object P_0 lies at a distance S, and its image P'_0 lies at a distance S' from V. The angles θ and θ' are the incident and refracted rays P_0Q and P'_0Q, respectively, from the surface normal QC at the point of incidence Q. The slope angles of these rays from the optical axis are β_0 0 and β'_0. The off-axis point object P lies at a height h from the optical axis. Its image P_0 lies at a height h'. Numerically negative quantities are indicated by a negative parenthetical sign (–). Credit: Mahajan, 2014

By the Fermat's principle the derivative of the optical path with respect to x is zero, so

$$\frac{d\,[APB]}{dx} = n\,\frac{x}{\sqrt{x^2+s^2}} - n'\,\frac{(l-x)}{\sqrt{(l-x)^2+s'^2}} = n\,sin\theta - n'\,sin\theta' = 0 \tag{3.7}$$

and

$$n\,sin\theta = n'\,sin\theta' \tag{3.8}$$

where θ and θ' are the incidence and refraction angles of the incident and refracted rays, respectively, and n and n' are the refractive indices before and after refraction.

The incident ray, the refracted ray and the surface normal all lie in the same plane. Eq. 3.8 is the *Law of Refraction*, usually known as the *Snell's Law*. Some consequences of Snell's law are:

- If a ray-surface angle of incidence is equal to zero, then the refraction angle is also zero
- The angle of refraction increases (or decreases) with the angle of incidence
- If the angle of refraction is maximum (90°), then its incidence angle is given by $sin^{-1}[(n'/n)]$, and it is called the *critical angle*. For a typical glass-air interface

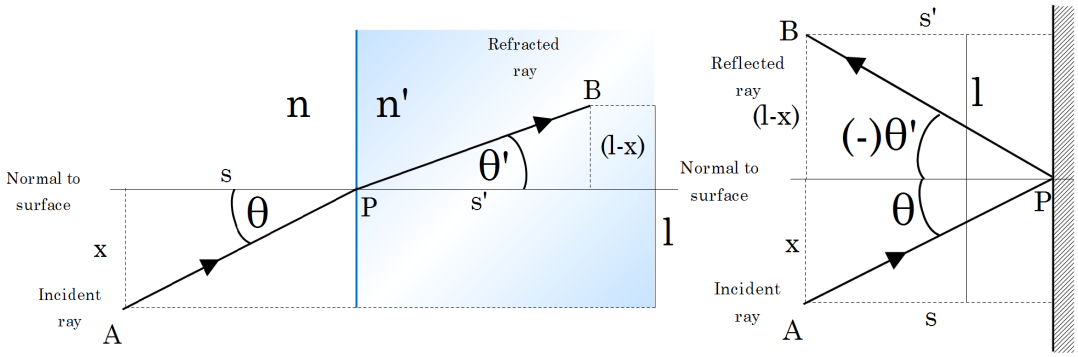

FIGURE 3.3: *Left panel*: Refraction of a ray. AP is a ray incident on a planar surface separation media with refractive indices n and n' at an angle θ with the surface normal. PB is the refracted ray at an angle θ' with respect to the surface normal. *Right panel*: Reflection of a ray. AP is an incident ray on a planar reflective surface at an angle θ with respect to the normal surface, and PB is the corresponding reflected ray at an angle θ' with the surface normal.

where $n = 1.5$ and $n' = 1$, the critical angle is 41.8°. If the incidence angle is larger than the critical angle, then the ray will be reflected according to the law of reflection. This phenomenon is called *Total Internal Reflection (TIR)*.

Similarly, I will consider reflection as shown in the right image of Figure 3.3. The optical path from point A to B is given in this case by

$$[APB] = n\,(\sqrt{x^2 + s^2} - \sqrt{(l-x)^2 + s'2}) \tag{3.9}$$

where the sign minus appears in the second term of Eq. 3.9 because the reflected ray is traveling in the opposite direction with respect to the incident ray. By Fermat's Principle the derivative of Eq. 3.9 with respect to x must be equal to zero, hence

$$\frac{d\,[APB]}{dx} = \frac{x}{\sqrt{x^2 + s^2}} + \frac{(l-x)}{\sqrt{(l-x)^2 + s'^2}} = sin\theta + sin\theta' = 0 \tag{3.10}$$

So

$$\theta = -\theta' \tag{3.11}$$

where θ and θ' are the angles of incidence and reflection with respect to the surface normal at the point of incidence. The incident and reflected rays are co-planar with the surface normal. Equation 3.11 is known as the *Law of Reflection*.

3.2.4 Direct ray tracing

To model an optical system with high accuracy, it is necessary to provide an exact description of the path of rays through it. This is possible by performing direct ray tracing along the system from the object to the image plane. Astronomical spectrographs are composed typically by a set of optical elements placed along the path of the photons, that refract, reflect and/or disperses them. Typically, these optical

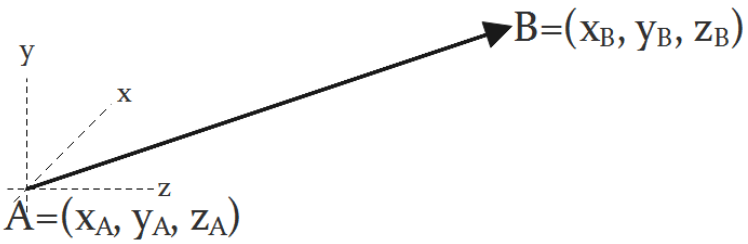

FIGURE 3.4: Rectilinear propagation of a ray from point A to point B.

elements are lenses, mirrors or dispersive elements (prisms, gratings, etc.). In this section I will present the equations that describe the optical path of rays through an echelle spectrograph. In addition to the three main laws of geometrical optics, I include also a brief description of the law of diffraction and its application to ray tracing in diffraction gratings and grisms, the latter as a combination of the law of refraction and diffraction.

Ray propagation in space

In Euclidean space and in a homogeneous medium, i.e. one with a uniform refractive index n, rays propagate in straight lines. Figure 3.4 shows a ray traveling from point A to point B. The position and direction of the ray at A are given by $\vec{x}_A = [x_A, y_A, z_A]$ and $\vec{d}_A = [d_x, d_y, d_z]_A$, respectively. If the ray travels a distance ds along the optical axis, the vector position of the ray at B is given by

$$\vec{x}_B = [\, x_A + \frac{d_{x,A}}{d_{z,A}}\, ds,\; y_A + \frac{d_{y,A}}{d_{z,A}}\, ds,\; z_A + ds\,] \tag{3.12}$$

where $ds = z_B - z_A$. As the ray is traveling through an homogeneus medium the direction is not affected, so $\vec{d}_A = \vec{d}_B$.

Law of Refraction

Let's now consider refraction in a three dimensional space, as shown in Figure 3.5. As illustrated in Figure 3.5, a ray originating at a point A strikes a refracting surface that separates two media with refractive indices n and n' at point P_0. Then it is refracted and passes through the point B. Given the ray AP_0, one would like to know the direction of the ray P_0B. First of all, let's consider another ray from from A to B, but passing through a point P in the vicinity of P_0. I consider that the vector $\vec{OA}$ (the origin of coordinates is now shown in Figure 3.5) can move along the curve through P_0 and satisfies the equation $\vec{OA} = \vec{f}(u)$, where u is the length of this curve from P_0. The optical path length of the ray from A to B through point P is given by

$$\begin{aligned} &= n\; AP + n'\; PB \\ &= n\; |\vec{f}(u) - \vec{r}| + n'\; |\vec{r}' - \vec{f}(u)| \end{aligned} \tag{3.13}$$

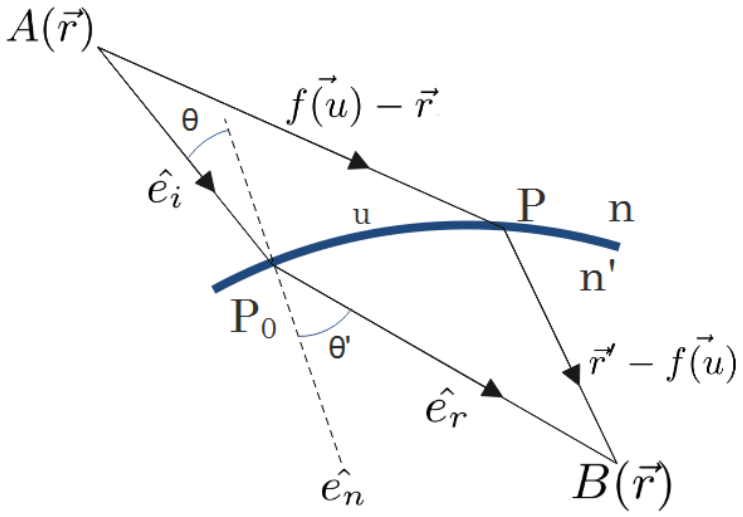

FIGURE 3.5: Refraction of a ray by a surface separating media of refractive indices n and n'. AP_0 and P_0B are the incident and refracted rays, and AP and PB are the corresponding nearby virtual rays. $\hat{e}_n$ is the unit vector along the normal to the surface at point P_0. θ and θ' are the angles the rays make with the surface normal, called the angles of incidence and refraction, respetively. Based on Figure 1-9 from Mahajan, 2014.

As the point P moves, and u varies, a family of paths is generated. By applying Fermat's Principle, one can obtain the true path of a refracted ray

$$\left\{ \frac{d}{du} \left(|\vec{f}(u) - \vec{r}| + n' \, |\vec{r}' - \vec{f}(u)| \right) \right\}_{u=0} = 0 \tag{3.14}$$

with

$$|\vec{f} - \vec{r}| = \sqrt{\vec{f} \cdot \vec{f} + \vec{r} \cdot \vec{r} - 2\vec{f} \cdot \vec{r}} \tag{3.15}$$

By taking the derivative in the absolute value I obtain

$$\frac{d}{du} |\vec{f} - \vec{r}| = \frac{(\vec{f} - \vec{r}) \cdot \frac{d\vec{f}}{du}}{|\vec{f} - \vec{r}|} = \hat{e} \cdot \frac{d\vec{f}}{du} \tag{3.16}$$

where

$$\hat{e} = \frac{\vec{f} - \vec{r}}{|\vec{f} - \vec{r}|} \tag{3.17}$$

is a unit vector pointing in the direction of AP. Similarly,

$$\frac{d}{du} |\vec{r}' - \vec{f}| = -\frac{(\vec{r}' - \vec{f}) \cdot \frac{d\vec{f}}{du}}{|\vec{r}' - \vec{f}|} = -\hat{e}' \cdot \frac{d\vec{f}}{du} \tag{3.18}$$

where

$$\hat{e}' = \frac{\vec{r}' - \vec{f}}{|\vec{r}' - \vec{f}|} \tag{3.19}$$

is a vector unit pointing in the direction along the ray PB. By replacing equations 3.16 and 3.18 in equation 3.14 I obtain

$$\left((n\hat{e} - n'\hat{e}' \cdot \frac{d\vec{f}}{du})\right)_{u=0} = 0 \tag{3.20}$$

The vector $(d\vec{f}/du)_{u=0}$ is tangent to the curve at P_0. But also, ($n\hat{e}$ - $n'\hat{e}'$) must be parallel to the surface normal $\hat{e}_n$ at P_0. Therefore

$$n\hat{e}_i - n'\hat{e}_r = c\hat{e}_n \tag{3.21}$$

where c is a constant. From equation 3.21, $\hat{e}'$, $\hat{e}$ and $\hat{e}_n$ lie in the plane of incidence, as $\hat{e}'$ can be written as a linear combination of $\hat{e}$ and $\hat{e}_n$. Therefore the incident and refracted rays, as well as the surface normal at the point of incidence, are co-planar. By taking a dot product on both sides of equation 3.21 with $\vec{e}_n$ I obtain

$$n\hat{e}_i \cdot \hat{e}_n - n'\hat{e}_r \cdot \hat{e}_n = c \tag{3.22}$$

Which can be written as

$$c = n\ cos\theta - n'\ cos\theta' \tag{3.23}$$

Where θ and θ' are the angles of incidence and refraction that the rays make with the surface normal. By replacing equation 3.23 into equation 3.21 I obtain

$$\hat{e}_r = \frac{n}{n'}\hat{e}_i - (\frac{n}{n'}\ cos\theta - cos\theta')\hat{e}_n \tag{3.24}$$

By taking the cross product with $\hat{e}_n$

$$\hat{e}_r \times \hat{e}_n - \frac{n}{n'}\hat{e}_i \times \hat{e}_n = 0 \tag{3.25}$$

that is equivalent to

$$n\ sin\theta = n'\ sin\theta' \tag{3.26}$$

which is the Snell's Law in 3D with incidence and refracted rays co-planar with the surface normal at the point of incidence. Finally, the direction of the refracted ray can be written as

$$\hat{e}_r = k\ \hat{e}_i + \left[(1 - k^2\ sin^2\theta)^{1/2} - k\ cos\theta\right]^{1/2}\ \hat{e}_n \tag{3.27}$$

where $k = n/n'$.

Law of Reflection

Similarly as for the law of refraction I will derive the law of reflection in three dimensions. Let's consider a ray, whose origin is at point A, that incides a reflective surface at point P_0 and is reflected in a direction that passes through point B, as shown in

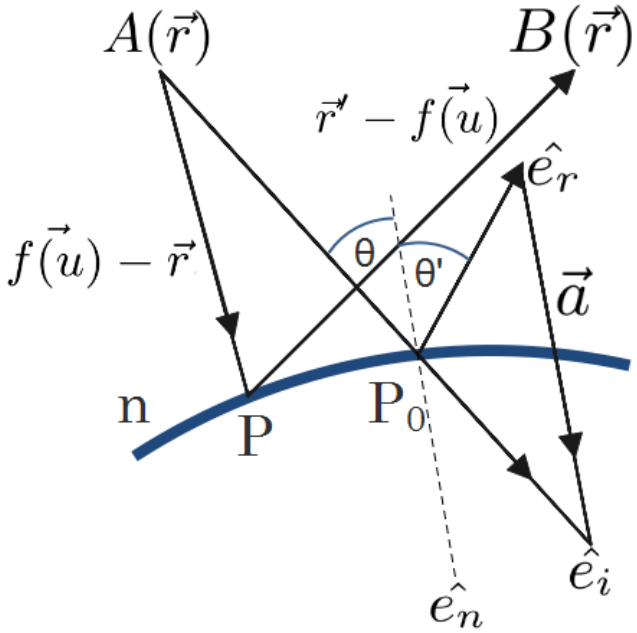

FIGURE 3.6: Reflection of a ray by a reflecting surface in a medium with refractive index n, respectively. AP_0 and P_0B are the incident and reflected rays, and AP and PB are nearby virtual rays. $\vec{e}_n$ is the normal vector to the surface at the point of incidence, and θ and θ' are the angles that the incident and reflected rays make with the surface normal, respectively. Based in Figure 1-10 from Mahajan, 2014

Figure 3.6. Figure 3.6 is not on a plane. Given the direction of the incidence ray AP_0, I would like to determine the direction of the ray P_0B after reflection. If P is a point in the vicinity of P_0, and $\vec{OP} = \vec{f}(u)$, where u is the length of this curve from P_0, the optical path length of the ray from A to B through point P is given by

$$[APB] = n(AP - PB) = n\left(|\vec{f}(u) - \vec{r}| - |\vec{r}' - \vec{f}(u)|\right) \tag{3.28}$$

Where the optical path PB is negative because it travels in the direction opposite to the incident ray. As the point P moves through the curve u, a family of rays is generated, but by Fermat's Principle only one path is the true one. Hence

$$\frac{d}{du}\left(|\vec{f}(u) - \vec{r}| - |\vec{r}' - \vec{f}(u)|\right)_{u=0} = 0 \tag{3.29}$$

By replacing equations 3.17 and 3.19 in equation 3.29 I obtain

$$\left((\hat{e} + \hat{e}') \cdot \frac{d\vec{f}}{du}\right)_{u=0} = 0 \tag{3.30}$$

where $\hat{e}$ and $\hat{e}'$ are the unit vectors along the incident and reflected rays, respectively. The curve is arbitrary as long as it passes by point P_0 and stays in the surface. The vector $(d\vec{f}/du)_{u=0}$ lies along the tangent to the curve at point P_0. Hence, $\hat{e} + \hat{e}'$ must be perpendicular to all tangents to the surface A_0, or $\hat{e} + \hat{e}'$ must be along the normal

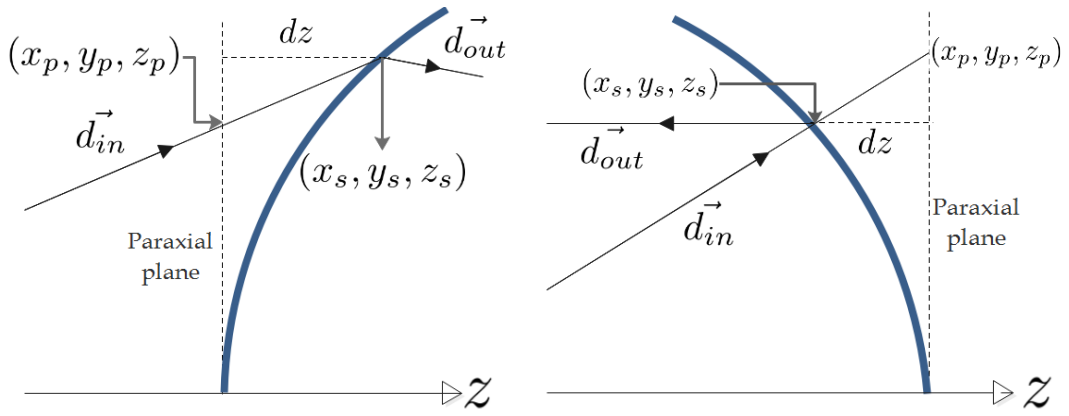

FIGURE 3.7: *Left panel*: a ray incides onto a refracting surface at a point defined by coordinates (x_s, y_s, z_s) with a direction $\vec{d}_{in}$, and is refracted in the direction $\vec{d}_{out}$. *Right panel*: a ray incides onto a reflecting surface at a point defined by coordinates (x_s, y_s, z_s) with a direction $\vec{d}_{in}$, and is reflected in a direction $\vec{d}_{out}$.

$\hat{e}_n$ to the tangent plane at P_0. Therefore, if I evaluate at $u = 0$ I can write

$$\hat{e}_i + \hat{e}_r = a\,\hat{e}_n \tag{3.31}$$

with $a = 2\,cos\theta$, where θ is the angle of incidence of the ray. Hence, the incident and the reflected ray are co-planar with the surface normal. Finally, the direction of the reflected ray is

$$\hat{e}_r = -\hat{e}_i + 2\,\hat{e}_n\,cos\theta \tag{3.32}$$

which is the Law of Reflection in three dimensions.

3.2.5 Ray tracing through curved surfaces

In CARMENES, the collimator and the camera consist of reflective and refractive curved surfaces. The collimator is a parabolic mirror, while the camera is composed of 5 spherical lenses plus a field flattener with a toroidal output surface. For simplicity, toroidal surfaces are modeled as cylindrical surfaces, so in total I consider three types of curved surface types: parabolic, spherical and cylindrical.

In order to trace the path of a ray along a spectrograph I must calculate the position where the ray hits the surface, in order to calculate the normal vector in this position and calculate the true optical path of the ray. Given the position of the ray at the surface, the normal vector and the properties of the surface, I can calculate the output direction of the ray after a curved surface using Eqs. 3.27 or 3.32.

Let's consider the ray entering the curved surface shown in the right panel of Figure 3.1. The ray with incoming direction $\vec{d}_{in}$ is reflected by the collimator mirror to an output direction $\vec{d}_{out}$. If (x_p, y_p, z_p) are the coordinates at the paraxial plane of the surface, and (x_s, y_s, z_s) are the coordinates at the surface, then the direction tangents of the ray are given by where dz is the distance along the optical axis from

the paraxial plane to the surface. In addition, a curved surface with curvature radius r is described by its sag equation, which is given by

$$\frac{d_x}{d_z} = \frac{x_p - x_s}{dz} \tag{3.33}$$

$$\frac{d_y}{d_z} = \frac{y_p - y_s}{dz} \tag{3.34}$$

Where dz is the distance along the optical axis from the paraxial plane to the surface. In optics, *Sag* (or *Saggita*) aplies to either convex or concave surface curvature and represents the physical distance between the vertex point along the curve and the center point of a line drawn perpendicular to the curve from one edge of the optics to the other. The *sag* equations of the surfaces that I consider in this work are given by

$$x^2 + y^2 + (z + r)^2 = r^2, \quad spherical \tag{3.35}$$

$$x^2 + y^2 = 2rz, \quad parabolic \tag{3.36}$$

$$x^2 + (z + r)^2 = r^2, \quad cylindric \tag{3.37}$$

$$x^2 + y^2 = rz\left(1 + \sqrt{1 - (1 + \kappa)\frac{(x^2 + y^2)}{r^2}}\right), \quad aspheric \tag{3.38}$$

Where r is the curvature radius of the surface and x, y and z are the coordinates of a point on the optical surface, and κ is the conic constant. For equations 3.35 to 3.38, I have considered that the origin of coordinates is in the point where the paraxial plane and the optical axis z intersect. By replacing equations 3.33 and 3.34 into the equations 3.35 to 3.38 I can obtain an analytical expresion for dz. If I know dz the I can calculate the exact position of a ray in a given surface.

Spheric surface

In this subsection I will derive a mathematical expression for the quantity dz, shown in Figure 3.7, for the case of an spherical surface. Equations 3.33 and 3.34 can be re-written as

$$x_s = \frac{d_x}{d_z}\, dz - x_p \tag{3.39}$$

$$y_s = \frac{d_y}{d_z}\, dz - y_p \tag{3.40}$$

Where x_s and y_s are the coordinates of the ray on the surface, y_p and y_p are the coordinates of the ray in the paraxial plane, and d_x, d_y and d_z are the components of the direction vector of the ray . If I replace equations 3.39 and 3.40 in equation 3.35 I obtain

$$(\frac{d_y}{d_z}\, dz - y_p)^2 + (\frac{d_x}{d_z}\, dz - x_p)^2 + (dz + r)^2 = r^2 \tag{3.41}$$

Where I have replaced z from equation 3.35 with dz, as they are equivalent if the origin of coordinates is in the intersection between the paraxial plane and the optical

axis. I also define $T_x := d_x/d_z$ and $T_y := d_y/d_z$, so Eq. 3.41 can be written as

$$(T_y\, dz - y_p)^2 + (T_x\, dz - x_p)^2 + (dz + r)^2 - r^2 = 0 \tag{3.42}$$

that is equivalent to

$$(T_x^2 + T_y^2 + 1)\, dz^2 - 2\, dz\, (T_y\, y_p + T_x\, x_p - r) + (y_p^2 + x_p^2) = 0 \tag{3.43}$$

which is a quadratic equation with dz as the unknown variable. By solving equation 3.43 for dz, I obtain

$$dz = \frac{-(x_p\, T_x + y_p\, T_y - r) - r/|r|\, \sqrt{r^2 - (x_p\, T_y - y_p\, T_x)^2 - 2r\, (x_p\, T_x + y_p\, T_y) - (x_p^2 + y_p^2)}}{(T_x^2 + T_y^2 + 1)} \tag{3.44}$$

which gives us the distance dz from the paraxial plane to the position of the ray in the surface, as a function of the position of the ray in the paraxial plane, the direction of the incidence angle and the curvature radius. By replacing the value of dz obtained from equation 3.44 into equations 3.39 and 3.40 I can obtain the x_s and y_s coordinates of a ray position on a spherical surface.

Parabolic surface

The *sag* of a parabolic surface is given by Eq. 3.36. By replacing Eqs. 3.39 and 3.40 in Eq. 3.36, and using the definitions from §3.2.5, I obtain

$$(T_y\, dz - y_p)^2 + (T_x\, dz - x_p)^2 - 2\, r\, dz = 0 \tag{3.45}$$

Following the same procedure that the one for spherical surfaces, the quadratic equation for dz in a parabolic surface is

$$(T_x^2 + T_y^2)\, dz^2 - 2\, (T_y\, y_p\ + T_x\, x_p + r)\, dz + x_p^2 + y_p^2 = 0 \tag{3.46}$$

and its solution is given by

$$dz = \frac{-(x_p\, T_x + y_p\, T_y + r) - r/|r|\sqrt{r^2 - 2r\, (x_p\, T_x + y_p\, T_y) - (y_p\, T_x - x_p\, T_y)^2}}{(T_x^2 + T_y^2)} \tag{3.47}$$

By replacing the value of dz obtained from Eq. 3.47 into Eq. 3.39 and 3.40 one can obtain the x_s and y_s coordinates of a ray position on a parabolic surface.

Cylindric surface

The *sag* of a cylindric surface is given by equation 3.37. By replacing equations 3.39 and 3.40 in Eq. 3.37, and using the definitions from §3.2.5, I obtain

$$(T_y\ dz - y_p)^2 + (dz + r)^2 = r^2 \tag{3.48}$$

Therefore, the quadratic equation for dz in a cylindric surface is

$$(T_y^2 + 1)\ dz^2 - 2\ (T_y\ y_p - r)\ dz + y_p^2 = 0 \tag{3.49}$$

and its solution is given by

$$dz = \frac{(r - y_p\ T_y) - r/|r|\sqrt{r^2 - 2\ r\ y_p\ T_y - y_p^2)}}{(1 + T_y^2)} \tag{3.50}$$

By replacing the value of dz obtained from equation 3.50 into equations 3.39 and 3.40 I can obtain the x_s and y_s coordinates of a ray position on a cylindric surface. I must stress that equation 3.50 applies when the symmetry axis of the cylindric surface is the x-axis. If the symmetry axis is the y-axis, then I must replace T_y by T_x and y_p by x_p in Eqs. 3.48 to 3.50.

Aspheric surface

The *sag* of an aspheric surface is given by Eq. 3.38. By replacing 3.39 and 3.40 in 3.38, I obtain

$$(T_x\ dz - x_p)^2 + (T_y\ dz - y_p)^2 = r\ z\ \sqrt{1 - (1 + \kappa)\frac{(T_x\ dz - x_p)^2 + (T_y\ dz - y_p)^2}{r^2}} \tag{3.51}$$

By choosing

$$c = \frac{1}{r} \tag{3.52}$$

$$Q_1 = 1 - c\ (T_x\ x_p + T_y\ y_p) \tag{3.53}$$

$$Q_2 = 1 + 2\ c\ (c\ x_p\ T_x\ y_p\ T_y - x_p\ T_x\ y_p\ T_y) - c^2\ (1 + \kappa)\ (x_p^2 + y_p^2) \tag{3.54}$$

$$Q_3 = c\ (1 + \kappa + T_x^2 + T_y^2) \tag{3.55}$$

the solution to the quadratic equation 3.51 can be written as

$$dz = \frac{Q_1 - r/|r|\sqrt{Q_2}}{Q_3} \tag{3.56}$$

3.2.6 Diffraction

Diffraction is defined as the phenomena that occurs when a wave encounters an obstacle or a slit with its size of the order of magnitude of the wavelength of the

wave. While diffraction is a phenomenon that applies to all kinds of waves, here I will just refer to electromagnetic waves.

In classical optics, diffraction is closely related with the way in which waves propagate. This is described by *Huygens-Fresnel Principle* and the principle of superposition of waves. The propagation of a wave can be visualized by considering every particle of the transmitted medium on a wavefront as a point source for a secondary spherical wave. The wave displacement at any subsequent point is the sum of these secondary waves. When waves are added together, their sum is determined by the relative phases as well as the amplitudes of the individual waves so that the summed amplitude of the waves can have any value between zero and the sum of the individual amplitudes. Hence, diffraction patterns usually have a series of maxima and minima.

Single slit diffraction

When an electromagnetic wave incides a single slit with width a, the lightbeam from a source located at the top edge of the slit interferes destructively with a source located in the middle of the slit, when the path difference between them is $\lambda/2$. Similarly, the source just below the top of the slit will interfere destructively with the source located just below the middle of the slit at the same angle. By applying this reasoning along the entire length of the slit, the condition for destructive interference for the entire slit is the same as the condition for destructive interference between two narrow slits separated by a distance that is half the width of the slit. This path difference is approximately $a\ \sin\theta/2$, so the minimum intensities occur at the angle θ_{min} given by

$$d\ sin\theta_{\text{min}} = \lambda \tag{3.57}$$

Where a is the slit width, θ_{min} is the angle of incidence at which minimum intensity occurs and λ is the wavelength of the lightbeam. Using a similar argument, the minima obtained at angles θ_m are given by

$$d\ sin\theta_m = m\ \lambda \tag{3.58}$$

where m is an integer other than zero. The principle of single slit diffraction is illustrated in Figure 3.8.

Diffraction gratings

If now I consider n-slits instead of a single slit, the resulting surface is a *diffraction grating*. A diffraction grating is an optical component that consist of a collection of reflecting (or transmitting) elements separated by a distance comparable to the wavelength of the light. These elements can be thought as a collection of diffracting elements, such as a pattern of slits (or apertures) in an opaque surface, or a collection of reflecting grooves engraved on a substrate. The fundamental physical principle of

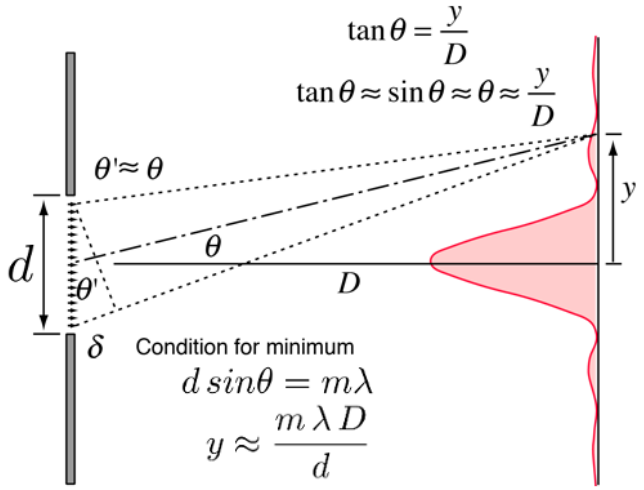

FIGURE 3.8: Diffraction in a single slit. The far-field of the diffraction pattern, also called *Fraunhofer diffraction*, is shown in red.

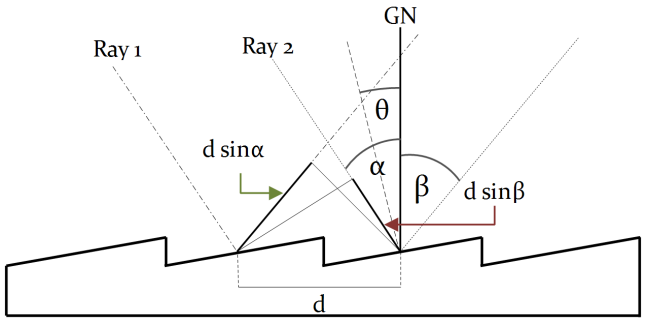

FIGURE 3.9: Two parallel rays are striking a grating at an angle α and are diffracted in a direction given by β. The angle of the grooves is θ. Angles are measured with respect to the grating normal (GN).

the diffraction grating is the spatial modulation of the refractive index, therefore, an electromagnetic wavefront striking a grating surface will have their main properties - electric field amplitude and phase - modified accordingly due to the periodical modulation of the refractive index in the region near the grating surface. Because of this, light passing by a grating is diffracted into several beams travelling in different directions. The directions of these beams depend on the spacing of the grating and the wavelength of the light, such that the grating acts as a dispersive element. A *reflection* grating consist of a grating superimposed on a reflective surface, whereas a *transmission* grating consist of a grating superimposed on a transparent surface.

When monochromatic light is incident on a grating surface, it is diffracted into discrete directions, and there is a unique set discrete direction angles along which, for a given spacing d between grooves, the diffracted light from each groove is in phase with the diffracted light from any other groove, leading to constructive interference. The working principle of a diffraction grating is shown in Figure 3.9 which shows two light rays of a given wavelength λ striking at an angle α and diffract at an angle β by a diffraction grating with groove spacing d. α and β are measured with

respect to the grating normal GN, so angles to the left of the grating normal are positive and angles to the right are negative. The geometrical path difference between light of adjacent grooves is $d(\sin\alpha + \sin\beta)$. The principle of constructive interference states that only when the optical path difference equals the wavelength of the light, or some integral multiple of it, the light of adjacent groove is in phase, leading to constructive interference. This is principle is well expressed by the *grating equation*

$$m\,\lambda = d\,(sin\,\alpha + sin\,\beta) \tag{3.59}$$

Where m is the diffraction order (or spectral order) and is an integer. If the incident light beam is not perpendicular to the grooves, the grating equation is written as

$$m\,\lambda = d\,cos\,\gamma\,(sin\,\alpha + sin\,\beta) \tag{3.60}$$

Where γ is the angle between the incident light ray and the plane perpendicular to the grooves at the center of the grating. The angular dispersion can be calculated by differentiating the Eq. 3.59, so

$$AD_G = \frac{\Delta\theta}{\Delta\lambda} = \frac{m}{d\,cos\theta} \tag{3.61}$$

Where AD_G is the grating angular dispersion. By replacing Eq. 3.59 in Eq. 3.61 I obtain

$$AD_G = \frac{sin\alpha + sin\beta}{\lambda\,cos\beta} \tag{3.62}$$

which is a more general expresion for the angular dispersion of a diffraction grating.

Another interesting feature of diffraction gratings is the *Free Spectral Range (FSR)*, which corresponds to the wavelength range in a given spectral order for which superposition of the adjacent orders does not occur. For a given order m the wavelength of the light that gets diffracted along the direction of λ in order $(m+1)$ is $\lambda + \Delta\lambda$, so

$$\lambda + \Delta\lambda = \frac{m+1}{m}\lambda \tag{3.63}$$

so the FSR is

$$FSR \;=\; \Delta\lambda = \frac{\lambda}{m} \tag{3.64}$$

If m is small, the FSR is large. In contrary, for larger m the FSR is shorter.

In the special case where the diffraction angle is equal to the incidence angle, light is diffracted back towards the direction from which it came, so $\alpha = \beta = \theta$. Hence,

$$m\,\lambda = 2\,d\,sin\,\theta \tag{3.65}$$

This condition is called *Littrow configuration*, and it's widely used among PRV instruments as it minimizes the optical aberrations.

Echelle gratings

An echelle grating is a special type of grating which is characterized by a relatively low groove density, with a groove shape optimized to be used at high incidence angles and high spectral orders. Because of this, their FSR is very small. As a consequence, echelle spectra consist of many short spectral orders overlapped with each other. Because of this, a secondary dispersion element must be used to separate the overlapping orders. This secondary dispersion element is called *Cross-disperser*. The resulting spectrum comes in a 2D format, dispersed in one direction by the echelle and in the perpendicular direction by the cross-disperser. This spectral format allows to cover a wide number of orders, covering a broad spectral range at high spectral resolution. Echelle gratings are commonly used in high resolution spectrographs for the detection of exoplanets, as they provide high resolution over a wide spectral range. An example of a typical echelle spectrum is shown in Figure 1.4.

Diffraction in 3D

Eqs. 3.59 and 3.61 provide a description of the dispersion by a grating in a two-dimensional space. However to describe the path of rays in a spectrograph it is necessary to provide a description of diffraction in a three-dimensional space. Following the generalized ray-tracing approach from Mitchell, 1981, the directions of the diffracted rays are given by

$$\begin{aligned} d_{x,out} &= d_{x,in} \\ d_{y,out} &= \frac{m \cdot \lambda}{d} - d_{y,in} \\ d_{z,out} &= \sqrt{1 - d_{x,out}^2 - d_{y,out}^2} \end{aligned} \tag{3.66}$$

where m is the diffraction order, λ the wavelength and d the groove spacing of the grating, which is related to the grating constant according to $d = 1/G$. The refractive indices before and after the grating are the same. Eq. 3.66 describes diffraction on a reflection grating in a three-dimension space. In this case the grating is positioned in such a way that the echelle dispersion is along the y-axis, so only the y-component of the direction vector is affected. The x-direction is not affected by dispersion, along this axis the ray is reflected. As no simple optical equation allows us to derive the z-component of the direction vector, I derive it using Eq. 3.2.

3.3 RAMSES and its application to CARMENES

I present **RA**y tracing and **M**odeling **S**oftware for **E**chelle **S**pectrographs (RAMSES), a ray tracing software that computes the centroid position on the detector of any spectral feature defined by its wavelength. I employ an object-oriented philosophy in which optical elements are represented by an independent module that describes their optical surfaces and how rays are traced through it. Rays are traced from the slit to the detector in sequential tracing, based on the path that rays follow inside the spectrograph.

A high resolution echelle spectrograph's optical layout typically consists of a slit, a collimator, a high dispersion element, a cross-dispersion element, a camera and a detector. In the case of CARMENES, the slit is composed by two octagonal fibers, the collimator is a parabolic mirror, the main dispersing element an echelle grating, the cross-dispersion element is a grism, the camera is an array of 5 lenses plus a field flattener, and the detector is a CCD. In addition, the CARMENES optical design includes a pre-slit FN-system, which transforms the output beam of the fibers to the working focal ratio of the collimator, and a fold mirror, which redirects the intermediate focus image plane beam to the collimator for a third pass, as shown in Figure 3.10.

The model receives an input array of vectors with the form $[\vec{s}]_i = [m, \lambda]_i$ with $i = 1$ to j, where j is the number of spectral features one would like to trace, m is the spectral order and the wavelength of the spectral line. It is necessary to specify the order and the wavelength, as a spectral line with a given wavelength could fall in two, and in some cases even in three, spectral orders. For each spectral feature, RAMSES computes its position along the spectrograph in a three dimensional space, until it reaches the detector, where the three dimensional coordinates are projected into the two dimesional CCD array. By considering the size of the detector, the number of pixels in the detector and the pixel size, I transform the ray positions from the physical space in mm to the detector space in pixels.

Each optical element is defined by a module that contains the equations that describe the ray tracing through it. Each optical element module receives the position and direction of the ray in the optical element first surface, and output the position and direction of the ray at the last surface. In the case the first and last surface are the same, the position of the input and output ray are equivalent. The modules that describe the optical elements of the spectrograph are: slit, F/N system, collimator, echelle grating, transfer mirror, grism, camera lens and detector. They are defined by a set of attributes related to the physical properties of each element. In addition, I include additional modules that describe the propagation of rays between surfaces, as well as the setting of the orientation of the optical elements. While the directions are defined by the direction cosines, the positions of the rays are defined by their actual physical positions along the spectrograph in mm and are described in cartesian coordinates with the origin centered in the spectrograph's slit.

The environmental conditions of the spectrograph are considered by including a model for the refractive index as a function of temperature and pressure. I also include changes induced by thermal expansion, or contraction, of the optics and mechanics at the working temperature of the instrument.

The parameters of the model corresponds to the positions, orientation and features of the optical elements that compose the spectrograph, as well as the enviromental conditions (temperature and pressure) of it.

In this chapter I present the application of RAMSES to CARMENES VIS and NIR spectrographs as a case of study.

3.3.1 CARMENES optical design

The CARMENES instrument (Quirrenbach et al., 2014), as briefly described in §1.4, is a pair of high-resolution spectrographs covering the wavelength range between 0.52 to 1.71 μm, optimized for precision radial velocity measurements. The visible channel covers the wavelength range between 0.52 - 0.96μm at a measured spectral resolving power of R = 93,400, while the near-infrared channel covers the wavelength range between 0.91 -1.7 μm at a measured spectral resolving power of R = 81,400. The entrance aperture on sky is 1.5 arcsec.

The optical design of both channels consists of a grism cross-dispersed, white-pupil echelle spectrograph working in quasi-Littrow configuration with a two-beam, two-slice image slicer. The VIS channel is housed in a thermally stabilized vacuum vessel at a pressure of $\sim 10^{-5}$ mbar and at a temperature of $\sim$12°C. The NIR channel is also housed in a vacuum vessel stabilized at a temperature of 140 K.

Both channels are fed with two 100 μm diameter octagonal fibers, mounted next to each other, with a 0.346 mm separation center-to-center, to provide a simultaneous reference for instrumental drift corrections. The separation between the fibers results in a minimum separation of 7 pixels between science and calibration pseudo slit projected on the detector. The optical path of the output beam of the optical fibers that feed the spectrograph is described in the next few lines. The F/N lens system converts the F/3.5 output beam of the fibers into the F/10.2 focal ratio of the collimator. The image slicer is placed at the focal plane of the F/N system, where the image of the octagonal fibers are sliced and re-arranged into a pseudo slit. The output beam from the slicer is then projected onto the collimator. The collimator is a parabolic mirror. After the collimator, the beam is reflected to the echelle grating, and reflected back to the collimator. After the second pass on the collimator, the beam is focused into a flat folding mirror that reflects the beam back to the collimator for a third pass. The collimator reflects the beam to the cross-dispersing grism and then to the camera lens that images the spectrum in the detector plane. Figure 3.10 shows the opto-mechanical layout of the VIS channel. The optical design of both channels is similar. Their main differences are the coatings applied to the reflective surfaces -collimator, echelle grating and folding mirror-, the materials and properties of the refractive optical elements - F/N system, cross-dispersion grism

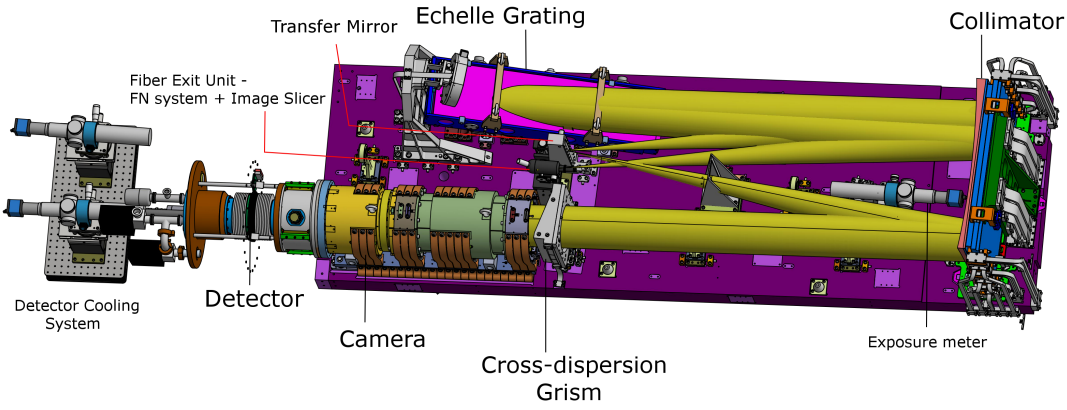

FIGURE 3.10: Opto-mechanical design of the CARMENES VIS channel.

and camera lens system - and the detector characteristics. The collimator, echelle grating and folding mirror are made of Zerodur, for low thermal expansion. Table 3.1 summarizes the main features of the VIS and NIR spectrograph.

Channel	VIS	NIR
Wavelength range	0.55 - 1.05 μm	0.9 μm - 1.7 μm
R ($\lambda/\Delta\lambda$)	93,400	81,400
Fiber input	2×100 μm	2×100 μm
Collimator	f = 1590 mm	f = 1565 mm
Echelle grating	R4, 31.6 l/mm	R4, 31.6 l/mm
Cross-disperser grism	Apex = 17.8°, 223 l/mm	Apex = 17.6°, 80 l/mm
Camera	F/2.94, f = 455 mm	F/3.53, f = 548 mm
Detector	4k × 4k, 15μm/pix	2 2k × 2k, 18μm
Operating temperature	285 K	140 K

TABLE 3.1: Main features of CARMENES VIS and NIR spectrograph.

Top and bottom panel in Figure 3.11 show the tracing of rays from the fiber input to the detector in CARMENES VIS and NIR spectrographs. Both plots were obtained with ZEMAX. Both spectrographs optical designs are similar. They differ mainly in the materials used in the lenses, the coatings applied to the mirrors and the orientation of some optical elements.

3.3.2 Ray tracing modules

Free space tracing

The rays are traced according to equation 3.12. The module that performs ray tracing between two points in a homogeneous medium receives as an input the position and direction of rays and the displacement of the ray along the optical axis. It returns

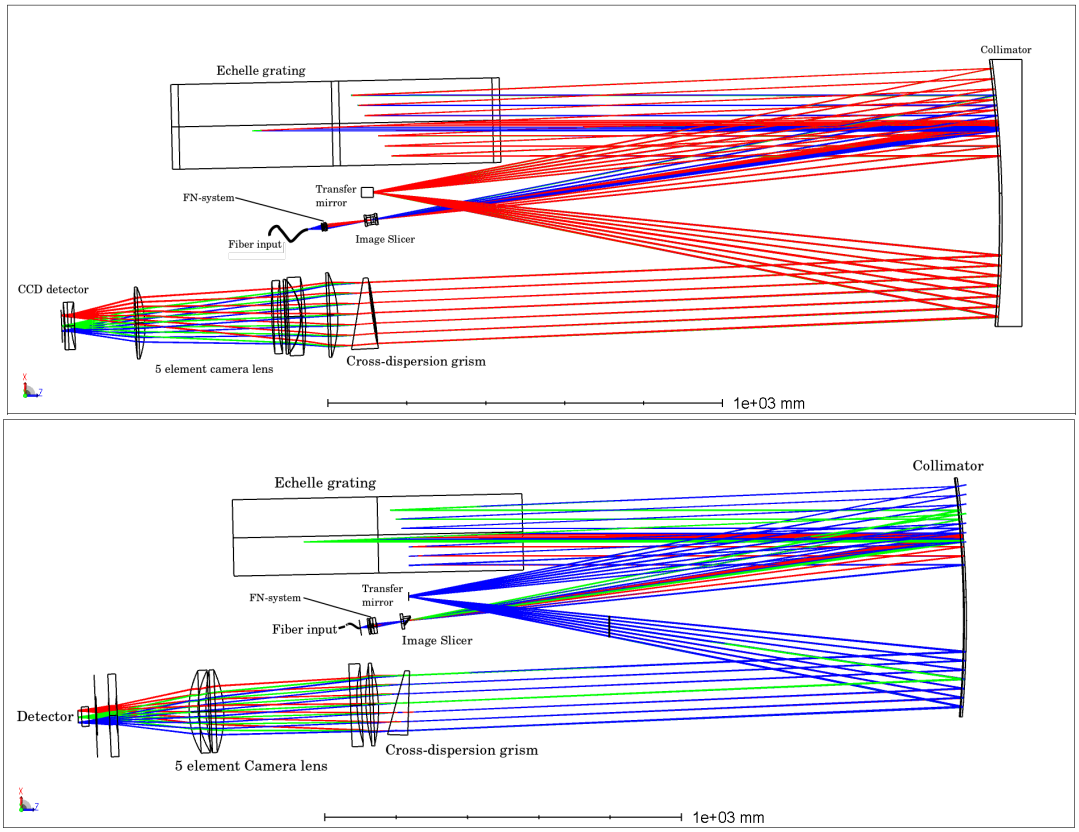

FIGURE 3.11: *Top panel*: Ray tracing through CARMENES VIS channel. *Bottom panel*: Ray tracing through CARMENES NIR channel. Both diagrams were obtained from CARMENES optical designs in ZEMAX.

the position and direction after propagation. The python code of this module is described in the Appendix A §A.1.3.

Refraction

To trace rays in refractive surfaces I apply the following procedure:

- The first step is to calculate the position of a ray on the refractive surface. Depending on the shape of the surface, the distance between the paraxial plane and the position in the optical axis at which the ray falls on the surface can be calculated using equations 3.44, 3.47, 3.50 or 3.56. Once the rays are in the paraxial plane of the surface, I project the ray on the surface using equations 3.39 and 3.40.

- Once on the surface, and by assuming that the incidence and refractive rays are co-planar with the surface normal at the point of incidence, I calculate the incidence angle as

$$cos\, i \;=\; \vec{d} \cdot \vec{n} \tag{3.67}$$

where $\vec{d}$ is the direction cosines vector and $\vec{n}$ is the surface normal at the point if incidence. To calculate the normal vector at the point of incidence I consider

the center of curvature of the surface at a position $\vec{cen} = (0, 0, r)$, so if the vector position of the ray is $\vec{x}$, the normal vector is given by

$$\vec{n} = \frac{\vec{cen} - \vec{x}}{|\vec{cen} - \vec{x}|} \tag{3.68}$$

In every refraction, the origin of coordinates is set to be on the vertex of the refractive surface.

- By knowing the incidence angle, I can calculate the refraction angle by doing

$$sin\ i = \sqrt{1 - cos^2 i} \tag{3.69}$$

$$sin\ r = \frac{sin\ i}{k} \tag{3.70}$$

where $k = n_1/n_0$ and n_0 and n_1 are the refractive indices before and after refraction. So,

$$cos\ r = \sqrt{1 - sin^2 r} \tag{3.71}$$

Finally, the direction of the ray after being diffracted can be calculated using equation 3.27.

An example of a piece of code where I calculate the refraction of rays in the first spherical surface of the VIS channel FN-system is shown in Appendix A §A.1.1.

Reflection

To trace rays through reflective surfaces I apply a similar procedure than for refractive surfaces:

- Same as the first step of §3.3.2.
- Same as the second step of §3.3.2.
- As a consequence of the law of reflection, the incidence and reflected angles are equivalent. Once I know the surface normal vector at the point of incidence and the incidence angle, I can calculate the direction of the reflected rays using equation 3.32.

An example of a piece of code where I calculate the reflection of rays in the collimator surface of the VIS channel is shown in Appendix A §A.1.2.

Slit

The entrance slit is defined by its position $\vec{x} = (x, y, z)$ and angles of orientation μ_{slit}, ν_{slit} and τ_{slit}. In the case of CARMENES the slit consist of two octagonal fibers, so I consider x and y positions for the two of them. I will name fiber A as the fiber that carries the information of the stellar spectra, and fiber B for the calibration fiber.

	VIS			NIR		
Sf. no	R [mm]	Thick [mm]	Mat.	R [mm]	Thick [mm]	Mat.
1	108.104	4.0	S-FPL51	32.3	9.1	CaF2
2	-27.736	0.5	Air	-24.3	2.0	Air
3	52.280	2.5	S-TIM2	39.1	6.0	S-FTM16
4	14.453	7.0	S-FPL51	9.8	1.0	Air
5	-48.529	97.4	Air	10.9	9.1	CaF2
6	—	—	—	-18.1	66.0	Air

TABLE 3.2: Curvature radii, thicknesses and materials for the lenses used in CARMENES VIS and NIR FN-system. Data extracted from ZEMAX CARMENES optical design as-built.

The parameters associated to this module are: slit position in x-axis for fiber A, slit position in y-axis for fiber A, slit position in x-axis for fiber B, slit position in y-axis for fiber B, defocus along z-axis of both fibers and tilts in x,y and z axes for both fibers. Both fibers are mechanically mounted in the same mount, so the defocus and orientation of both fibers are the same.

The fibers are separated by a distance of 0.346 mm center-to-center and the line that joins the center of both fibers is aligned perpendicular to the echelle dispersion. The initial position of the rays for both fibers are

$$x_A = -0.175, \quad y_A = 0. x_B = 0.175, \quad y_B = 0.$$

The code that initialises the slit coordinates is described in Appendix A §A.1.4.

F/N system

The F/N system is defined by the curvature radii of the surfaces, and the glass materials and thicknesses of the lenses used. After defining the initial position and direction of the slit, the rays are traced from the slit to the paraxial plane of the first surface of the FN-system. The inputs to this module are the position and direction of the beam at the paraxial plane of the first surface, the orientation of the FN-system and the properties of the lenses or mirrors used. The outputs are the positions and directions of the rays in the last surface of the system.

In CARMENES VIS and NIR the FN-system consist of lenses and all surfaces are spherical. The VIS FN-system consist of a singlet made out of *S-FPL51* glass, and a double that consist of two lenses in optical contact. The glass used for the first lens of the doublet is *S-TIM2*, while the glass of the second lens is *S-FPL51*. The properties of the lenses used in the VIS and NIR FN-systems are listed in Table 3.2, respectively. Figure 3.12 shows the optical layout of the VIS and NIR FN-system.

As the FN-system consist of refractive surfaces I apply the law of refraction to describe the ray tracing through it. The procedure followed to perform refraction in a curved surface is described in §3.3.2.

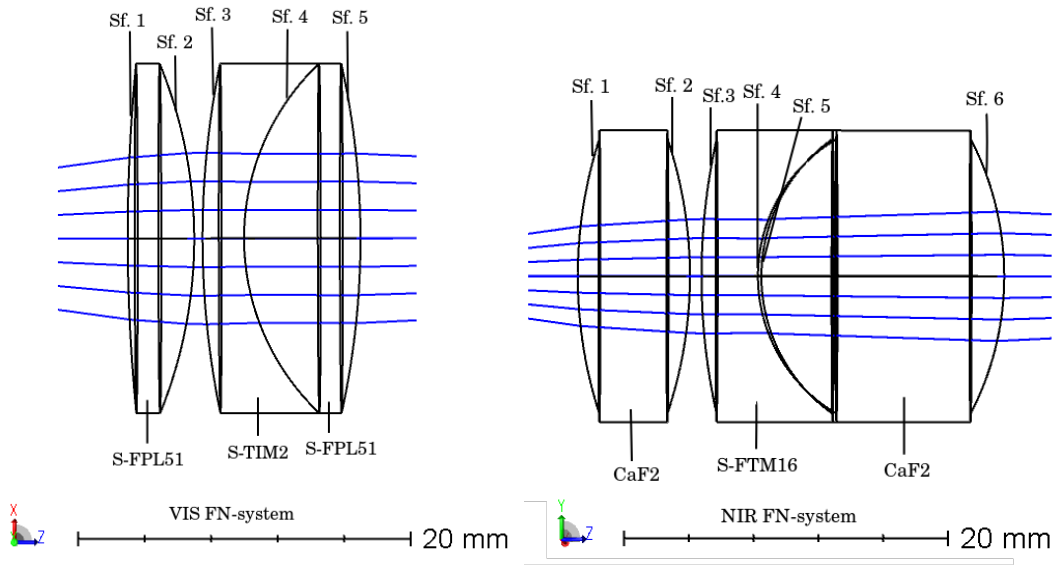

FIGURE 3.12: *Left panel*: Optical layout of the VIS channel FN-system. *Right panel*: Optical layout of the NIR channel FN-system. Rays going through both systems are represented as blue lines. The surface number and the material of the lenses are also shown.

The parameters related to this module are the angles of orientation of this optical system. The code that performs the ray tracing operations through the FN-system is described in detail in Appendix A in §A.1.5.

Collimator

The collimator is an optical element whose main purpose is to leave all the rays parallel to each other before striking the grating. The input to this module are the coordinates at the paraxial plane of the collimator and the incidence direction of the ray. The output are the position of the ray at the surface of the mirror and the direction of the ray after the reflection on the mirror's surface. The procedure followed to trace the rays that hit the collimator is described in §3.3.2, and an example of a code that computes reflection on a collimator is shown in Appendix A in §A.1.2. The focal lenghts of VIS and NIR collimators are 1590 mm and 1565 mm, respectively.

The parameters related to this module are: the position along the optical axis of the collimator with respect to the spectrograph's slit and the physical properties of the optical element itself (i.e. surface type, curvature radii, conic constant).

Echelle grating

The echelle grating is defined by the grating constant G and the orientation of the grating. The inputs to this module are the position of the rays in the grating surface, the direction at which the rays incide the grating, a vector T that defines the orientation of the grating, the spectral order m, the wavelength λ and the grating constant G. I assume that the refractive indices before and after the grating are the same.

Once the ray hits the grating, their coordinates and directions are transformed to a coordinate system centered and oriented with respect to the grating plane. Once the rays are diffracted, they are transformed back to the spectrographs coordinate system. Equations 3.66 describe diffraction on a reflection grating. The output of this module is the position and direction of the rays after diffraction. The parameters of this module are: the grating constant $G = 1/d$, the orientation of the grating and its position along the optical axis.

The code that describes the propagation of rays through a diffraction grating is shown in Appendix A §A.1.6.

Folding mirror

The folding mirror is a flat mirror and is described by its position along the optical axis with respect to the collimator and its orientation. The input to this module are the positions and directions of the rays in the mirror surface. The output is the direction of the traced rays as determined by the law of reflection, given by equations 3.32. The parameters of this module are: the position of the mirror along the optical axis with respect to the collimator, the tilt around x-axis and the tilt around y-axis. The code that performs the ray tracing in a flat mirror is described in Appendix A §A.1.7.

Grism

The cross-dispersion element is a grism. A grism is a prism with a transmission grating in the output surface. It is defined by the prism apex angle, the grating constant of the output surface, the base thickness, and the position and orientation angles. Both input and output surfaces are tilted around the y-axis with respect to the optical axis. Once the rays are in the paraxial plane of the grism first surface, I project them in the tilted input grism surface. The grism module evaluates the Snell's law at the input surface following the procedure described in §3.3.2. Once refracted in the entrance surface, rays are traced from the input to the output surface using equations 3.12. Rays are then projected in the tilted output surface of the grism. Once at the output surface I apply the Snell's law to refract the rays due to the glass to air interface, and I calculate diffraction angles at the grating surface where the input angles to the grating surface are the ones that I obtain after refracting the rays from the glass to air interface. The output surface of the grism acts as a transmission grating and it disperses rays in a direction perpendicular to the echelle dispersion, thus diffraction in the grism is given by

$$\begin{aligned} d_{x,out} &= \frac{m \cdot \lambda}{d_G} + d_{x,out} \\ d_{y,out} &= d_{y,in} \\ d_{z,out} &= \sqrt{1 - d_{x,out}^2 - d_{y,out}^2} \end{aligned} \tag{3.72}$$

	VIS	NIR
Input angle	2.4°	2.4°
Apex	17.8°	17.6°
Base thick [mm]	40	35
Material	LF5	Infrasil
Grating	223 lines/mm	80 lines/mm

TABLE 3.3: Main properties of VIS and NIR grisms.

	VIS			NIR		
Sf. no	R [mm]	Thick [mm]	Mat.	R [mm]	Thick [mm]	Mat.
1	-299.99	-26.079	S-FPL51	-425.387	-34.854	CaF2
2	Infinity	-55.821	Air	530.758	-25.28	Air
3	-558.957	-11.65	S-BAM4	453.907	-18.041	S-FTM16
4	-147.498	-0.995	Air	Infinity	-355.710	Air
5	-147.491	-38.06	S-FPL53	-290.228	-49.678	CaF2
6	-2146.267	-19.695	Air	517.481	-22.535	Air
7	495.252	-15.060	S-BSL7	233.415	-24.924	S-FTM16
8	999.741	-322.220	Air	243.563	-205.810	Air
9	-262.531	-25.980	S-BAM4	374.898	-20.037	ZnSe
10	1097.820	-160.486	Air	667.256	-58.539	Air
11	218.190	-8.07	S-LAL10	Infinity	-20	Infrasil
12	Infinity	-10	Silica	Infinity	-10	Air
13	531.430	-6.090	Air	—	—	—

TABLE 3.4: Curvature radii, thicknesses and materials for the lenses used in CARMENES VIS and NIR FN-system. Data extracted from ZEMAX CARMENES optical design as-built.

where d_G is the groove spacing of the grism output surface, m is the grism diffraction order, which in our case is $m = 1$, and λ is the wavelength.

The main properties of VIS and NIR grisms are shown in Table 3.3. The parameters associated to the grism are: the position of the grism along the optical axis with respect to the collimator, the decentering along x and y axes, the tilts around x and y axes, the grism grating constant d_G and the $Apex$ angle. The code that performs the ray tracing through the grism is described in Appendix A §A.1.8.

Camera

The camera module performs the ray tracing through a multi-element optical system that focuses the spectrum on the detector. The CARMENES VIS camera consist of five lenses plus a field flattener. The field lens acts as entrance window to the detector head dewar in the case of the VIS channel. The CARMENES NIR camera consist of four lenses plus a field flattener and an additional plano-parallel plate that corresponds to the entrance window of the detector dewar. All lenses are "air-spaced" due to the fact that the instrument is working in vacuum. The optical layout of the cameras of both channels is shown in Figure 3.13.

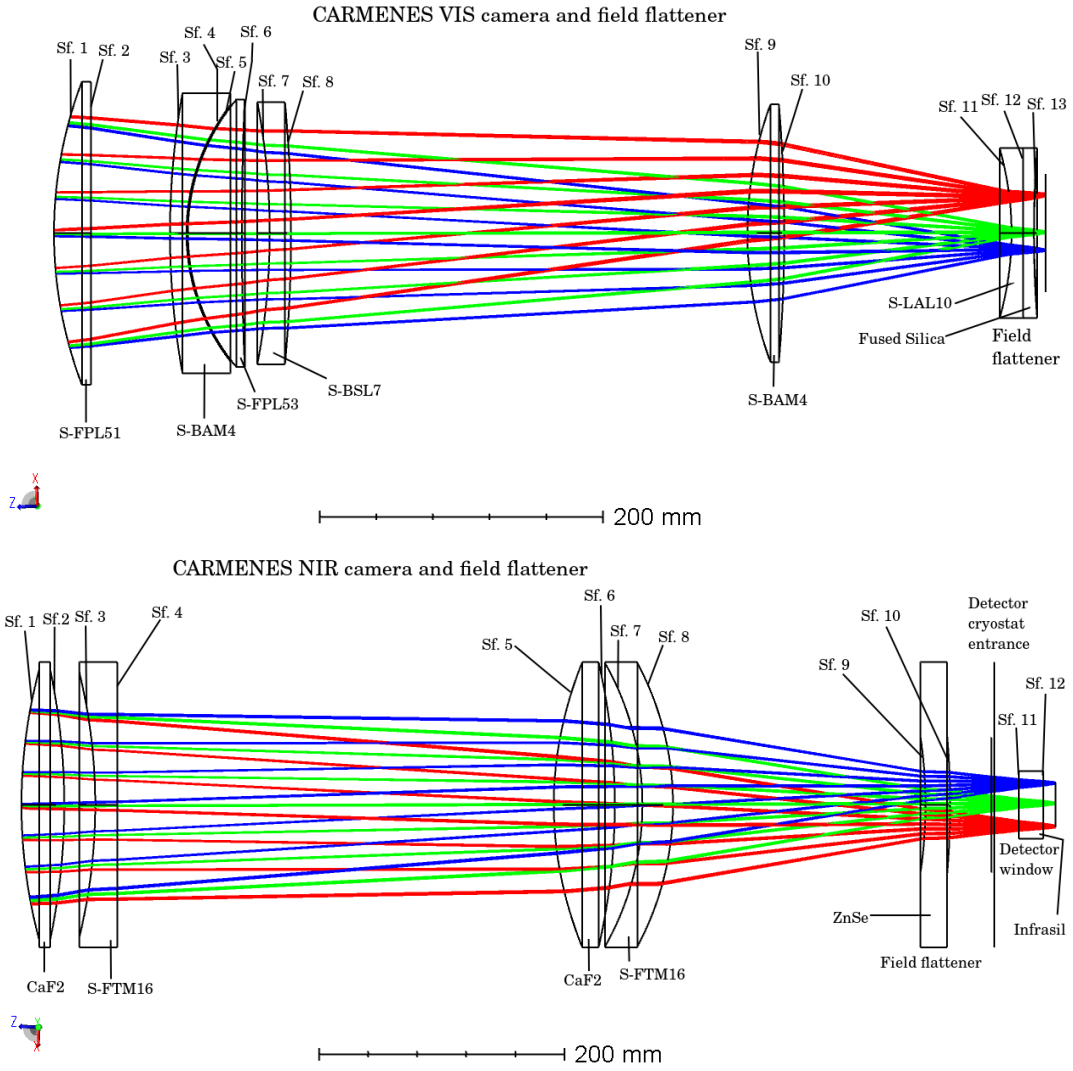

FIGURE 3.13: *Top panel*: optical layout of the CARMENES VIS camera and field flattener. *Bottom panel*: optical layout of the CARMENES NIR camera and field flattener. Both figures were obtained from the ZEMAX CARMENES optical design.

After the grism output surface I trace each ray to the paraxial plane of the first surface of the first lens of the camera. These are the input coordinates to this module. For each surface of the camera I calculate the exact position of the ray on the surface, and rays are traced following the procedure described in §3.3.2.

The field flattener is mechanically separated from the rest of the camera and is mechanically connected to the detector. Because of this, we treat the first five optical elements of the camera as one element (CAM), and the field flattener (FF) as another. The output from CAM is then traced through the FF to the detector plane. Because of this, decentering and tilts are independent in CAM and FF. All surfaces are spherical, except for the last surface of the VIS FF which is toroidal. For simplicity we approximate the toroidal surface with a cylindrical surface, described by equation 3.48.

The parameters related to this module are the camera decenterings and tilts in

VIS detector	
Type	e2v CCD231-84, deep-depletion, back-illuminated
Format	4112×4096, 4 outputs
Pixel size	15 μm
Read-out noise	4.5 e^- at 450 kpix/s
Read-out time	10 sec at 450 kpix/s (4 ports)
Quantum efficiency	>90% 460nm - 780nm, >60% 900 nm, >40% 930 nm
Dark current	< 10^{-3} e^-/pix/sec @ 163 K
Charge storage	350,000 e^-
Flatness	< 20 μm peak-to-valley
Operating temperature	163 K

TABLE 3.5: Main properties of VIS detector.

NIR detector	
Type	HAWAII-2RG
Format	Two 2048×2048 arrays
Pixel size	18 μm
Read-out noise	< 18 e^- at 100 kHz/s
Quantum efficiency	>70%
Dark current	< 0.05 e^-/pix/sec @ 77 K
Charge storage	> 100,000 e^-
Flatness	< 20 μm peak-to-valley
Gap between arrays	2.2 mm (approx. 123 pixels)
Operating temperature	> 77 K

TABLE 3.6: Main properties of NIR detector.

the x and y axis. In adittion, as the field flattener lens is detached from the first elements of the camera, I include also the following parameters: the distance between the main camera and the field flattener, the orientation and decenterings of the field flattener, and the distance between the last surface of the field flattener and the detector.

Detector

The detector is described by the number of pixels in the x and y directions, the pixel size, position and orientation.
In the case of the VIS channel, the detector is a e2v CCD231-84 with 4112×4096 pixel array with 15μm pixel size. The CCD is a deep-depletion back-illuminated device. The CCD properties are summarized in Table 3.5.

The NIR channel detector is a HAWAII-2RG detector provided by the company Teledyne Scientific & Imaging. The CARMENES NIR spectrograph uses a mosaic of two 2k×2k HAWAII-2RG arrays with a 18 μm pixel size and a cut-off wavelength at 2.5 μm. A model of the NIR detector array is shown in Figure 3.14. The two detector arrays are separated by a physical distance of about 2.2 mm. The main properties of the NIR detector are listed in Table 3.6.

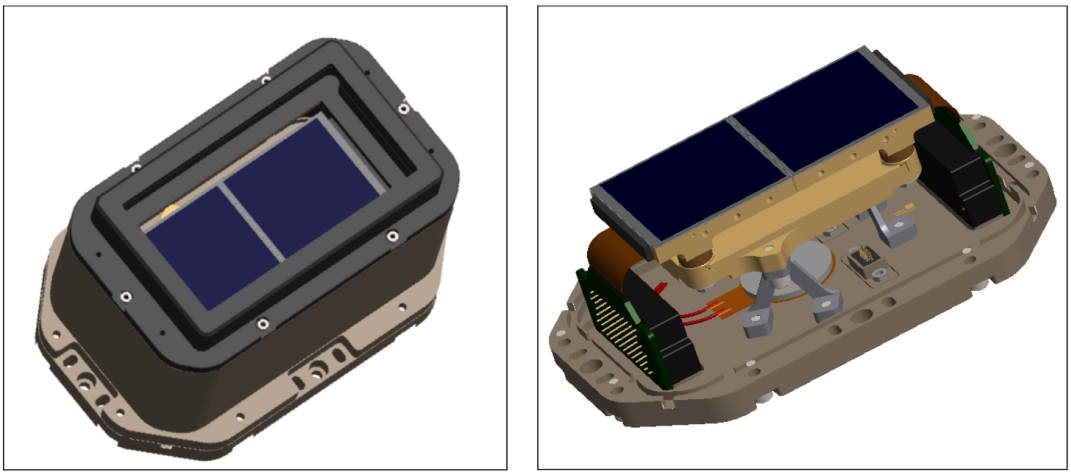

FIGURE 3.14: CARMENES NIR detector mosaic with filter support (left) housing the two detector arrays (right). Credit: CARMENES Consortium.

After the camera and field flattener, the rays are traced to the image plane where the detector is located. The position of the rays traced are in mm, so by considering the detector geometry I transform the rays from the physical space in mm to the detector space in $pixel$. If the position of a ray in the image plane is given by the coordinate pair (x_{ip}, y_{ip}), then the coordinates in the detector space (x_{det}, y_{det}) are given by

$$\begin{aligned} x_{det} &= x_{ip}/pix\_size + npix_x/2 \\ y_{det} &= y_{ip}/pix\_size + npix_y/2 \end{aligned} \tag{3.73}$$

where pix_size is the pixel size, $npix_x$ is the number of pixels along x-axis and $npix_y$ is the number of pixels in the y-direction.

The parameters related to this module are: the detector spatial orientation, the decentering along x and y axes and the defocusing along the optical axis. For the NIR detector, I also include the physical gap between the two detector arrays of the NIR detector as an extra parameter.

The code that performs the discretization of the rays positions into the detector space is shown in Appendix A §A.1.9.

3.3.3 Environment modeling

The path that a photon will follow inside an optical glass depends on the properties and the chemical composition of the glass material. In CARMENES, the grisms and the lenses of the objective camera are made of a variety of materials from different glass catalogs. While glass manufacturer catalogs provide refractive indices for the different materials with an accuracy of $\pm\ 3{\cdot}10^{-5}$, they are referenced to a reference temperature, which is typically 20° or 25°, depending on the glass and on the catalog. As CARMENES does not work at those temperature, it is necessary to develop a model that allows us to compute refractive indices at any temperature and pressure.

Furthermore, mechanical and optical components will expand or contract when exposed to changes in temperature, so it necessary to take into account these changes to model the instrument with high accuracy.

In this section I will describe a way to model the enviromental conditions inside the a spectrograph, by focussing in the calculation of the refractive index of a given material at any temperature and/or pressure and including a model to describe the expansion and contraction of materials as a function of temperature changes. The refractive index modeling scheme is based in the prescription that ZEMAX/Optics Studio optical design software uses[1].

Refractive index

There are two ways of referencing refractive indices: absolute and relative. While the absolute measurements are made using vacuum as the reference medium, relative measurements use air as reference, normally at Standard Temperature and Pressure (STP), which is 20°C and 1 Atm. Values for the refractive index at arbitrary temperatures and pressures can be related to the values of the index at the reference temperature and pressure through the absolute (vaccum referenced) refractive index of air (n_{air}). In RAMSES, the refractive index of air is always equal to 1.0 at the system temperature (T_s) and pressure (P_s).

Based in the ZEMAX/Optics studio prescription to calculate refractive indices at arbitrary temperatures, the basic steps for calculating the index for each type of glass at each wavelength are:

- Scale the wavelength to air at the reference temperature of the glass and a pressure of 1 Atm.
- Compute the relative index of glass at the reference temperature from the dispersion formula
- Compute the index of air at the reference temperature of the glass
- Compute the absolute index of the glass (relative to vacuum) at the reference temperature
- Compute the change in absolute index of refraction of the glass at the surface temperature
- Compute the index of air at the system temperature and pressure

The result of this process, which is the index of the glass at the surface temperature and pressure relative to air at the system temperature and pressure, is what RAMSES uses for ray tracing. This procedure also applies to air, meaning that the index of air will also vary accordingly with temperature and pressure.

[1] https://customers.zemax.com/os/resources/learn/knowledgebase/how-zemax-calculates-refractive-index-at-arbitrary

Wavelength in air at arbitrary pressure and temperature

The value of wavelength in air at the reference temperature and pressure of the glass is given by

$$\lambda_{air} = \frac{\lambda_{vac}}{n} \tag{3.74}$$

where λ_{air} refers to the value of wavelength in air, λ_{vac} is the wavelength in vacuum and n is the refractive index of air. For calculating the refractive index of air at any temperature and pressure I use the Ciddor equation, following the prescription from *NIST*[2]. To do so, I must first define the following constants

$$\begin{aligned}
&w_0 = 295.235 \quad k_0 = 238.0185 \quad a_0 = 1.58123 \times 10^{-6} \\
&w_1 = 2.6422 \quad k_1 = 5792105 \quad a_1 = -2.9331 \times 10^{-8} \\
&w_2 = -0.03238 \quad k_2 = 57.362 \quad a_2 = 1.1043 \times 10^{-10} \\
&w_3 = 0.004028 \quad k_3 = 167917 \\
&b_0 = 5.707 \times 10^{-6} \quad c_0 = 1.9898 \times 10^{-4} \quad d = 1.83 \times 10^{-11} \\
&b_1 = -2.051 \times 10^{-8} \quad c_1 = -2.376 \times 10^{-6} \quad e = -0.765 \times 10^{-8} \\
&p_{R1} = 101325 \quad T_{R1} = 288.15 \quad Z_a = 0.9995922115 \\
&\rho_{vs} = 0.00985938 \quad R = 8.314472 \quad M_v = 0.018015
\end{aligned}$$

If $S = 1/\lambda^2$, where λ is the wavelength in vacuum

$$\begin{aligned}
r_{as} &= 10^{-8}\Big(\big[k_1/(k_0 - S)\big] + \big[k_3/(k_2 - S)\big]\Big) \\
r_{vs} &= 1.022 \times 10^{-8}\big[w_0 + w_1\, S + w_2\, S^2 + w_3\, S^3\big]
\end{aligned}$$

If x_{CO2} is the CO_2 concentration in μmol/mol

$$\begin{aligned}
M_a &= 0.0289635 + 1.2011 \times 10^{-8}(x_{CO2} - 450) \\
r_{axs} &= r_{as}\big[1 + 5.34 \times 10^{-7}(x_{CO2} - 450)\big] \\
T &= t + 273.15 \\
Z_m &= 1 - \frac{p}{T}\big[a_0 + a_1\, t + a_2\, t^2 + (b_0 + b_1\, t)\, \chi_v^2\big] + \big(\frac{p}{T}\big)^2\,(d + e\, \chi_v^2)
\end{aligned}$$

where $\chi_v = (RH/100) \cdot f(p,t) \cdot p_{sv}(t)/p$ is the mole fraction, RH is the relative humidity in percent and $p_{sv} = 10^6(2C/X)^4$ is the vapour pressure saturation. If I now define

$$\begin{aligned}
&K_1 = 1.16705214528 \times 10^3 \quad K_2 = -7.24213167032 \times 10^5 \quad K_3 = -1.70738469401 \times 10^1 \\
&K_4 = 1.20208247025 \times 10^4 \quad K_5 = -3.23255503223 \times 10^6 \quad K_6 = 1.49151086135 \times 10^1 \\
&K_7 = -4.82326573616 \times 10^3 \quad K_8 = -4.82326573616 \times 10^5 \quad K_9 = -2.38555575678 \times 10^{-1} \\
&K_10 = 6.50175348448 \times 10^2
\end{aligned}$$

[2]https://www.nist.gov/publications/index-refraction-air

$$\Omega = T + K_9/(T - K_10)$$
$$A = \Omega^2 + K_1\,\Omega + K_2$$
$$B = K_3\,\Omega^2 + K_4\,\Omega + K_5$$
$$C = K_6\,\Omega^2 + K_7\,\Omega + K_8$$
$$X = -B + \sqrt{B^2 - 4AC}$$

and

$$\rho_{axs} = p_{R1}\,M_a/(Z_a\,R\,T_{R1})$$
$$\rho_v = \chi_v\,p\,M_v/(Z_m\,R\,T) \qquad \rho_a = (1-\chi_v)\,p\,M_a/(Z_m\,R\,T)$$

the refractive index at given environmental conditions is

$$n = 1 + \frac{\rho_a}{\rho_{axs}}\,r_{axs} + \frac{\rho_v}{\rho_{vs}}\,r_{vs} \tag{3.75}$$

By replacing equation 3.75 in equation 3.74 I can calculate the wavelength in air at a given temperature and pressure for a given vacuum wavelength.

Relative index of glass at the reference temperature

The relative refractive index of a glass at the reference temperature is calculated using the dispersion formula, or more commonly known, the Sellmeier equation. The Sellmeier equation is an empirical relation between the refractive index and wavelength for a particular transparent medium and is used to calculate the dispersion of light in a medium. The equation is

$$n_{rel}^2 = 1 + \frac{K_1\,\lambda^2}{\lambda^2 - L_1} + \frac{K_2\,\lambda^2}{\lambda^2 - L_2} + \frac{K_3\,\lambda^2}{\lambda^2 - L_3} \tag{3.76}$$

where n is the refractive index, λ is the wavelength in μm, K_{123} and L_{123} are the *Sellmeier coefficients* which are determined experimentally. Equation 3.76 provides the value of the refractive index at the reference temperature, which is typically 20°C or 25°C.

Refractive index of air at the reference temperature of the glass

The absolute refractive index of air at a temperature T and P is given by

$$n_{air} = 1 + \frac{(n_{ref} - 1)\,P}{1 + (T - 15)\cdot 3.4785 \times 10^{-3}} \tag{3.77}$$

where

$$n_{ref} = 1 + \left[6432.8 + \frac{2949810\,\lambda^2}{146\,\lambda^2 - 1} + \frac{25540\,\lambda^2}{41\,\lambda^2 - 1}\right]\cdot 1 \times 10^{-8} \tag{3.78}$$

where λ is the wavelength at the system temperature and pressure, P is the pressure in atmospheres, and T is the temperature in Celsius degrees (Riekert, 1961). Using equation 3.77 I can calculate the refractive index of air at any temperature, in particular at the reference temperature of glass and at the working temperature of the instrument.

Absolute refractive index of glass at the reference temperature

The relative refractive index of glass is converted to an absolute value using the formula

$$n_{abs}(T_{ref}, P_{ref}) = n_{air}(T_{ref}, P_{ref})\, n_{rel}(T_{ref}, P_{ref}) \tag{3.79}$$

where $n_{air}(T_{ref}, P_{ref})$ can be obtained using equation 3.77 and n_{rel} is calculated using equation 3.76.

Change in absolute index of refraction of glass at arbitrary temperature

Since the relative index was calculated at the reference temperature and pressure, the absolute index is calculated using the absolute index of air at this same temperature and pressure. The absolute index of the glass at the glass temperature and pressure is determined from

$$n_{abs}(T, P) = n_{abs}(T_{ref}, P_{ref}) + \Delta n_{abs} \tag{3.80}$$

where Δn_abs is calculated using the formula

$$\Delta n_{abs} = \frac{n^2 - 1}{n}\left[D_0\, \Delta T + D_1\, \Delta T^2 + D_2\, \Delta T^3 + \frac{E_0\, \Delta T + E_1\, \Delta T^2}{\lambda^2 - \lambda_{TK}^2}\right] \tag{3.81}$$

In the above formula n is the relative refractive index at the reference temperature and pressure, ΔT is the difference between the glass temperature and the reference temperature, λ is the wavelength at the temperature of the glass, and D_0, D_1, D_3, E_0, E_1 and λ_{TK} are the thermal dispersion coefficients of the glass. Finally, the relative index at the glass temperature and pressure is

$$n(T, P) = n_{abs}(T, P)/n_{air}(T, P) \tag{3.82}$$

Thermal expansion

Thermal expansion refers to the tendency of matter to change its shape, area and volume in response to a change in temperature. When temperature is increased in a material, the heat added increases the average amplitude of the vibrations of the atoms that compose the material. This increases the mean separation between the atoms causing the expansion of the material.
In the case of CARMENES, the temperature variations inside the vacuum tank will

produce changes in the mechanical mounts where the optics are mounted and in the optics themselves. To keep the thermal expansion algorithm rather simple, I implement a linear expansion model to account for this effect, so

$$\Delta L = \alpha_L \, L \, \Delta T \tag{3.83}$$

where α_L is the coefficient of thermal expansion (CTE), L is the length of the material, and ΔL is the difference in temperature. This estimation works well as long as the linear expansion coefficient does not change much over the change in temperature ΔT, and the fractional change in length is small $\Delta L/L \ll 1$. In RAMSES the quantities that are affected by linear expansion are: lenses curvature radii and thicknesses, optical elements orientation angles, and distances between the optical elements by considering the thermal expansion of the optical bench.

CARMENES materials

In this section I will list all the material used in CARMENES VIS and NIR spectrographs. For each material I will present the Sellmeier coefficients and the thermal dispersion coefficients.
Regarding the thermal dispersion coefficients, they were already included in the glass catalog of the CARMENES VIS Zemax model. For the NIR channel I used the Index Fitting Tool available in Zemax/Optics Studio to obtain the Sellmeier and thermal dispersion coefficients[3]. In this case, I had to input a table with measurements of the refractive index as a function of wavelength at different temperatures available in the literature. With this information Zemax performs a fit to the set of equations presented in §3.3.3 was done, where the parameters to fit are the Sellmeier coefficients and the thermal dispersion coefficients. The measurements of the refractive index at different temperatures as a function of wavelength are obtained from Leviton, 2007 for CaF2 and Infrasil, from Leviton, Frey, and Kvamme, 2008 for ZnSe and from Leviton, Frey, and Henry, 2013 for S-FTM16.

The top table from Table 3.8 shows the Sellmeier coefficients while the bottom table in Table 3.8 shows the thermal dispersion coefficients. Using these coefficients I can compute the refractive index at any temperature and pressure for all the glasses used in CARMENES VIS and NIR spectrographs, using equation 3.82.

The VIS CTE are collected from the CARMENES Zemax optical design glass catalog. The NIR CTE are collected from experimental measurements available in the literature. For the materials used in the NIR channel, the CTE for CaF2 and ZnSe are obtained from Feldman, 1978, for Infrasil is obtained from Okaji et al., 1995 and for S-FTM16 is obtained from Brown, Epps, and Fabricant, 2004. Table 3.7 shows the CTE for the glass materials used in the CARMENES VIS and NIR spectrographs.

For the mechanical expansions, i.e. optical bench expansion, due to temperature variations I only consider two materials: Aluminum and Zerodur. While most of the

[3] https://customers.zemax.com/os/resources/learn/knowledgebase/fitting-index-data-in-zemax

mounts are made out of aluminum, the collimator and the echelle grating are made of Zerodur. The CTE of the aluminum alloy (UNS A96061) used in the mechanical mounts is 20.31×10^{-6} and the CTE of Zerodur is 0.0101×10^{-6}.

VIS							
Material	LF5	S-FPL51	S-FPL53	S-LAL10	S-BAM4	S-BSL7	Silica
CTE [10^{-6} K^{-1}]	9.1	13.1	14.5	6.1	8.4	7.2	0.51

NIR				
Material	CaF2	Infrasil	ZnSe	S-FTM16
CTE [10^{-6} K^{-1}]	11.1	-0.23	4.6	6.8

TABLE 3.7: *Top panel*: VIS CTE. *Bottom panel*: NIR CTE.

Material	K_1	K_2	K_3	L_1	L_2	L_3
LF5	1.28035628	0.163505973	0.893930112	0.00929854416	0.0449135769	110.493685
S-FPL51-FN	0.244797528	0.973298851	0.693296827	0.0168483698	0.00439052381	129.704009
S-FPL51-CAM	0.00660312688	1.21161297	42274.8591	0.0508009151	0.00674508202	7779533.65
S-FPL53	0.376860986	0.6764123017	1.606634714	0.000395413025	0.008906810508	377.2424694
S-LAL10	1.53919083	0.356803936	1.12329285	0.00787335112	0.0274402737	89.2761349
S-BAM4	0.8858675772	0.6369145887	3.452981815	0.000594015863	0.028265065680	378.6528412
S-BSL7	1.25657676	0.0141512027	75433.5842	0.008176191	0.0480349086	7769032.35
Silica	0.6961663	0.4079426	0.8974794	0.004679148	0.01351206	97.934
S-TIM2	0.131440035	1.42457669	1.46124993	0.0574943358	0.0107880488	146.365803
CaF2	0.0670929954	0.974672825	4.09021222	0.0178869595	0.0050730898	1266.00652
S-FTM16	1.39698378	0.0745059039	1.10856264	0.0117596094	0.0712940688	116.411095
Infrasil	0.389688462	0.710709254	0.884054889	0.0033506362	0.010472622	97.0187451
ZnSe	2.28598369	2.59803398	725465.684	0.00149727627	0.0893997326	518793583.

Material	D_0	D_1	D_2	E_0	E_1	λ_{TK}
LF5	-2.27e-6	9.71e-9	-2.83e-11	8.36e-7	9.95e-10	2.28e-1
S-FPL51	-1.91e-5	-4.44e-9	-4.62e-11	3.74e-7	4.39e-10	1.63e-1
S-FPL53	-2.22e-5	-1.06e-8	-4.91e-11	2.77e-7	3.92e-10	2.06e-1
S-LAL10	4.83e-6	1.07e-8	-3.51e-11	5.85e-7	6.98e-10	1.96e-1
S-BAM4	-1.96e-6	1.25e-8	-3.24e-11	5e-7	6.02e-10	2.88e-1
S-BSL7	1.7e-6	1.43e-8	-4.27e-11	4.08e-7	6.74e-10	2.01e-1
S-TIM2	1.62e-7	1.19e-8	-3.5e-11	6.49e-7	8.6e-10	2.91e-1
Silica	2.237e-5	0.0	0.0	0.0	0.0	0.0
CaF2	-2.05e-5	-6.73e-8	1.53e-10	9.40e-8	1.15e-10	2.93e-1
S-FTM16	-8.32e-6	1.97e-9	6.80e-11	2.64e-7	5.96e-10	3.72e-1
ZnSe	5.57e-5	6.46e-8	-3.60e-10	5.97e-6	1.22e-8	4.05e-1
Infrasil	1.4e-5	3.81e-8	-3.33e-11	1.01e-8	3.69e-11	3.83e-1

TABLE 3.8: *Top panel*: Sellmeier coefficients for the materials used in CARMENES VIS and NIR spectrographs. *Bottom panel*: thermal dispersion coefficients for the materials used in CARMENES VIS and NIR spectrographs

Parameter space

In total the VIS channel model has 44 parameters, and the NIR channel 45 parameters. While the majority of the parameters are the same for both channels, as their designs are very similar, I include the physical gap between the two detectors in the NIR channel as an additional parameter. They are listed in Table 3.9.

3.3.4 RAMSES comparison with Zemax

I compare RAMSES with the commercial ray tracing software ZEMAX. For a list of wavelengths, I performed ray tracing through the spectrograph using RAMSES and ZEMAX. I evaluate the performance of our model by calculating the rms of the difference between the x and y positions at the detector focal plane with respect to Zemax, resulting in a rms of $1/10^3$ of a pixel . Figure 3.15 shows the echellogram traced with our model in yellow triangles and traced by Zemax in blue squares. Both models coincide up to a precision of a thousand of a pixel.

RAMSES offers more flexibility when modifying the source code to implement additional functionalities, and it runs three orders magnitude faster than Zemax, making it ideal for performing optimization routines that require a large number of calculations.

3.4 Fitting CARMENES calibration spectra with RAMSES

Once the model is built, the next step is to adjust its parameters to match the built instrument. The parameters cover various aspects of the spectrograph physics, e.g. spatial position and orientation of the manufactured optics, glass properties, and enviroment conditions. The optimization procedure adjusts the parameters in the model to match the calibration data obtained with the instrument. However, the different parameters affect the resulting position of the spectral lines in the detector plane in different ways and orders of magnitude. To decide which are the most relevant parameters to optimize, I made an error budget of RAMSES parameter space to study the effects of each parameter in the line positions at the detector plane.

3.4.1 Parameters selection

I considered two different approaches for the computation of the error budget: one based in how each parameter is affected by small temperature changes and another where parameters of the same kind, e.g. tilt angles, distances, decenterings and grating constants, vary equally according to some fixed value.

Error budget based in temperature variations

The temperature variations can be of the order of 0.3 K over a few days in the VIS channel, and of the order of 0.3 K over half a day in the NIR channel. Therefore I

Parameter	VIS	NIR	Description
slit_dec_x_a [mm]	-0.175	-0.175	Fiber A decenter in x-axis
slit_dec_y_a [mm]	0.0	0.0	Fiber A decenter in y-axis
slit_dec_x_b [mm]	0.175	0.175	Fiber B decenter in x-axis
slit_dec_y_b [mm]	0.0	0.0	Fiber B decenter in y-axis
slit_defocus [mm]	0.0	0.0	Fiber A and B defocus
slit_tilt$_x$ [°]	0.0	0.0	Fiber A and B tilt around x-axis
slit_tilt$_y$ [°]	-8.5	-8.5	Fiber A and B tilt around y-axis
slit_tilt$_z$ [°]	-9.01	-8.5	Fiber A and B tilt around z-axis
d_slit_col [mm]	1594.31	1563.95	Distance between slit focal plane and collimator
coll_tilt$_x$ [°]	0.	0.	Collimator tilt around x-axis
coll_tilt$_y$ [°]	0.	0.	Collimator tilt around y-axis
ech$_G$ [lines/mm]	31.6	31.6	Echelle grating constant
ech_blaze [°]	-75.76	-75.2	Echelle grating tilt around x-axis
ech_gamma [°]	1.2	1.2	Echelle grating tilt around y-axis
ech_tilt$_z$ [°]	0.0	0.0	Echelle grating tilt around z-axis
d_col_trf [mm]	-1594.31	-1563.95	Distance between collimator and transfer mirror
trf_mirror_tilt$_x$ [°]	0.0	0.0	Transfer mirror tilt around x-axis
trf_mirror_tilt$_y$ [°]	0.0	0.0	Transfer mirror tilt around y-axis
d_col_grm [mm]	0.0	0.0	Distance between collimator and grism
grism_dec$_x$ [mm]	236.36	231.36	Grism decentering along x-axis
grism_dec$_y$ [mm]	0.0	0.0	Grism decentering along y-axis
grm_tilt$_x$ [°]	0.0	0.0	Grism tilt around x-axis
grm_tilt$_y$ [°]	2.4	2.4	Grism tilt around y-axis
grm$_G$ [lines/mm]	223.	80.	Grism grating constant
grm_apex [°]	17.8	17.8	Grism Apex
d_grm_cam [mm]	-50.0	-50.0	Distance between the grism and the camera
cam_dec$_x$ [mm]	0.0	0.0	Camera decentering along x-axis
cam_dec$_y$ [mm]	0.0	0.0	Camera decentering along y-axis
cam_tilt$_x$ [°]	0.0	0.0	Camera tilt around x-axis
cam_tilt$_y$ [°]	0.0	0.0	Camera tilt around y-axis
d_cam_ff [mm]	-157.8	-205.8	Distance between camera and field flattener
ff_dec$_x$ [mm]	0.0	0.0	Field flattener decentering along x-axis
ff_dec$_y$ [mm]	0.0	0.0	Field flattener decentering along y-axis
ff_tilt$_x$ [°]	0.0	0.0	Field flattener tilt around x-axis
ff_tilt$_y$ [°]	0.0	0.0	Field flattener tilt around y-axis
ff_tilt$_z$ [°]	0.0	0.0	Field flattener tilt around z-axis
d_ff_ccd [mm]	-5.0	-10.	Distance between the field flattener and the detector
ccd_dec$_x$ [mm]	0.0	0.0	Detector decentering along x-axis
ccd_dec$_y$ [mm]	4.2	4.2	Detector decentering along y-axis
ccd_defocus [mm]	0.0	0.0	Detector defocus
ccd_tilt$_x$ [°]	0.0	0.0	Detector tilt around x-axis
ccd_tilt$_y$ [°]	0.0	0.0	Detector tilt around y-axis
ccd_tilt$_z$ [°]	0.0	0.0	Detector tilt around z-axis
detectors gap [mm]	—	2.2	Gap between detectors (only NIR)
t [°C]	12	-133.	Temperature
p [Pa]	0.0001	0.0001	Pressure

TABLE 3.9: RAMSES VIS and NIR parameters. They are initialised based on the CARMENES ZEMAX model as built. The VIS channel simulation has 44 parameters in total, and the NIR channel simulation has 45 parameters in total.

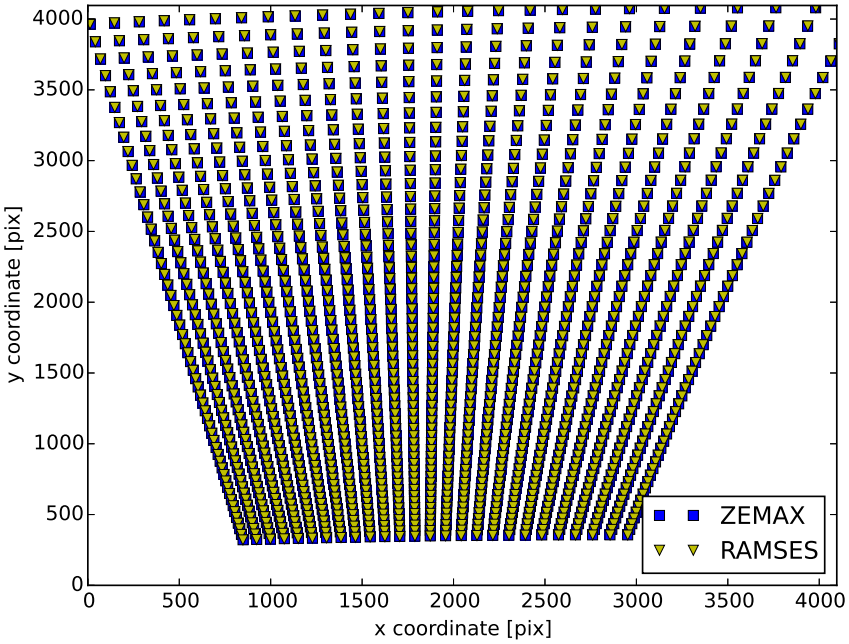

FIGURE 3.15: Echellogram traced by Zemax (blue squares) and RAMSES (yellow triangles). Echelle dispersion is across x-axis and cross-dispersion is across y-axis.

considered 0.3 K as the amplitude of the temperature variations, when studying how these variations affect the different parameters. While these variations can be smaller over the short term, I use 0.3 K just as a reference for the temperature amplitude, to compare the effect on the different parameters.

Based in the parameter list from Table 3.9, I identify four different types of parameters: distances between optical elements, decenterings and defocus, tilts of the optical elements, and the groove spacing of the echelle grating and grism output surface. For each kind of parameter I've estimated the amplitude of their variations due to temperature fluctuations using equation 3.83. As stated before, I assume ΔT = 0.3 K. For the distances between the optical elements I considered that they change because of the thermal expansion/contraction of the optical bench where they are mounted, so the CTE in this case is the one of aluminum 5083, which is the material used in the optical bench. For the decentering and tilts I also considered the CTE of aluminum 5083, as the mounts of the different optical elements are also made of this material. Equation 3.83 describe linear expansion/contractions, however I've assumed, just as an approximation, that the same formula applies for the changes in the tilt angles. Even if it might not completely correct, it is a valid approximation to get an idea of how tilt angles could be affected by temperature variations. For the grating constants of the echelle grating and of the grism, I assume that the temperature fluctuations have an effect in their groove spacing. The echelle grating is made of Zerodur, so the CTE of this component is the one of Zerodur. Similarly, the

grism material is *LF5* in the VIS channel and *Infrasil* in the NIR channel, so the CTE of these materials are considered when calculating the expansion or contraction of the groove spacing in these optical elements.

A table summarizing the results of the error budget based in temperature fluctuations is shown in Appendix B, in Tables B.1 and B.2 for the VIS and NIR channels, respectively.

Error budget based in uniform variations

In this case I have considered that the variations in the parameters are not due to temperature fluctuations, but instead they vary according to some fix value. I did this to compare the changes in the spectral lines positions for the different parameters in a consistent way. For example, I can vary all the parameters related to tilt angles by the same amount, and then study which tilt parameters are more important in terms of variation of the spectral line positions in the detector plane. For the fiber A and B position and orientation I have considered special parameters variations, as they are mounted in such a way that they motion is limited by the mechanical mount where the fibers are mounted. Based on this, the amplitude of the decentering of the fiber positions is 0.005μm, while the tilts around the rotation axes is 0.001°. For the distances and decentering parameters I consider that the amplitude of their variations is of 0.1 mm, while for the tilts in the optical elements the amplitude of the variations is $0.1\ ^\circ$. For the grating constants, the amplitude of the variation in the groove spacing is of 0.2 mm.

A table summarizing the results of the error budget based in uniform parameters variations is shown in Appendix B, in Tables B.3 and B.4 for the VIS and NIR channels, respectively.

Final Parameters

Based in the results from §3.4.1, I have selected 20 parameters to optimize when fitting RAMSES to the CARMENES calibration data. At the spectral resolution of CARMENES spectrographs, one pixel is equivalent to 1 km/s, roughly. Hence, 1 m/s correspond to 1/1000 pix in the detector plane. To decide which parameters are more relevant at the moment of optimizing the model against the data, I made a list of the parameters in which Δx is larger than 10^{-5} in Tables B.1 and B.2, for the VIS and NIR channels, respectively. In parallel, I made another list of the 30 parameters with the largest value of Δx in Tables B.3 and B.4, for the VIS and NIR channel respectively. Finally, I've cross-matched these two lists, obtaining a set of 20 parameters, which are optimized when fitting the model to the data. Table 3.10 shows the final list of optimization parameters for the VIS and NIR channel, respectively. The initial value for this parameters is obtained from the CARMENES optical design as built, that already consider the tolerances and dimensions of the built instrument. Once the instrument is built, these values may vary slightly from

VIS	NIR
ccd_tilt_z	ccd_tilt_z
$coll\_tilt_x$	$trf\_mirror\_tilt_x$
ech_blaze	ech_blaze
$ccd\_ff\_tilt_z$	$trf\_mirror\_tilt_y$
$trf\_mirror\_tilt_y$	grm_tilt_x
d_cam_ff	cam_tilt_x
cam_tilt_x	ech_z
grm_tilt_x	cam_tilt_y
ccd_defocus	$grism\_dec_y$
cam_tilt_y	cam_dec_y
$trf\_mirror\_tilt_x$	$ccd\_ff\_dec_y$
$ccd\_ff\_tilt_x$	d_cam_ff
d_col_trf	ccd_ff_decx
ech_z	cam_dec_x
$ccd\_ff\_tilt_y$	ech_G
ech_G	ech_gamma
$ccd\_ff\_dec_y$	$grism\_dec_x$
ech_gamma	d_ff_ccd
$ccd\_ff\_dec_x$	d_grm_cam
grm_G	gap

TABLE 3.10: List of parameters to optimize when fitting RAMSES to the CARMENES calibration data.

the instrument design parameters, so it is necesary to establish true values. This may also be the case after interventions, resulting in a physical change in the instrument. The effect at the detector of the most relevant parameters for different wavelengths is investigated using patterns in vector maps, showing the difference between the design and perturbed mapping of the spectral positions.
Figure 3.16 shows some examples of vector maps showing the differences in position of a set of spectral lines when the parameters are perturbed by a small ammount. While the final shifts are a combined effect of all the parameters, by selecting subsets of parameters and studying the residuals of the vector maps I can have a better understanding of the parameter space.

3.4.2 Spectral features selection

I tested RAMSES against HCL exposures obtained with the CARMENES VIS and NIR spectrographs. The wavelength calibration strategy for CARMENES is based on the use of HCL spectra to create a wavelength solution to calibrate the Fabry-Perot spectrum that is observed simultaneously with science observations to track for instrumental drifts. The VIS channel uses three different HCLs: Th-Ne, U-Ar and U-Ne, while the NIR channel uses a U-Ne lamp. We use the Redman, Nave, and Sansonetti, 2014 catalog for the Th lines, Sarmiento et al., 2014 for the U lines, and the NIST Atomic Spectra Database(Kramida et al., 2016) for the Ne and Ar lines.

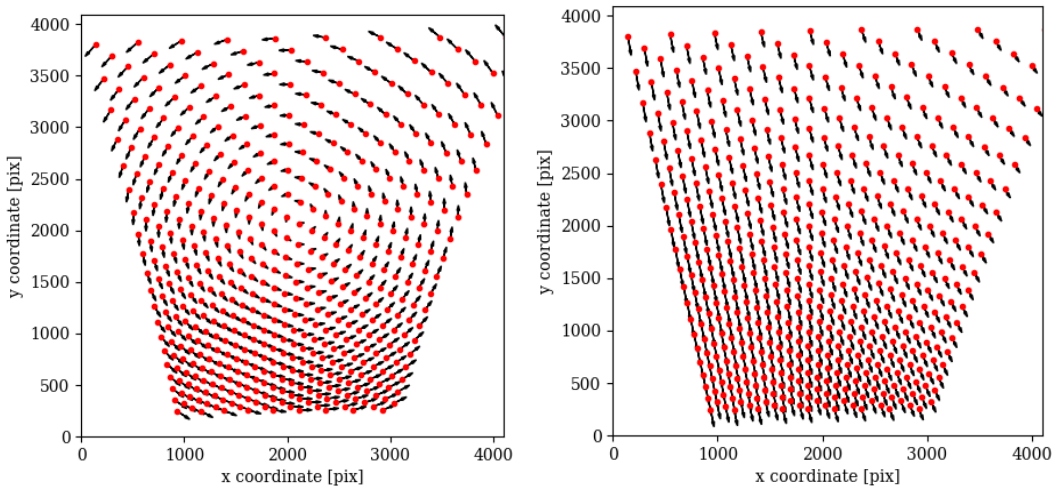

FIGURE 3.16: Vector plots that show the direction in which the lines move when varying the different model parameters.

The data of the position of the spectral lines is extracted directly from one of the data products of the CARMENES reduction pipeline CARACAL. CARACAL is the extraction software that performs the CCD reduction (bias, dark and flats), spectral order location and extraction, flat normalisation and wavelength calibration. The most important variable of the pipeline is *cs_lines* ("calibration set lines") which is a structure containing information about the line positions and wavelengths of selected calibration lines (see Table 3.11). First, the positions x_k of the calibration lines λ_k are re-measured in the order o_k of the extracted spectrum. Then a wavelength solution $x(\lambda, o)$ is fitted to the measured position x_k with direct regression (Bauer, Zechmeister, and Reiners, 2015). In the VIS channel close to 15,400 spectral lines are

field	type	unit	comment
WLC	double	Å	"computed" wavelength $\lambda(x_i, o_i)$
WLL	double	Å	laboratory wavelength λ_i
POSC	double	pix	computed line position $x(\lambda_i, o_i)$
POSM	double	pix	measured line position x_i
POSME	double	pix	error estimate of POSM $\sigma(x_i)$
POSMY	double	pix	vertical position y_i of the line
XFIRST	int	pix	start of line window
XLAST	int	pix	end of line window
APPROX	string	—	fit type ('G: gaussian')
WIDTH	double	—	fit parameter width
HEIGHT	double	—	fit parameter amplitude
ORDER	int	—	relative echelle order m
ABSO	int	—	absolute echelle order o_m
FLAG	int	—	line flag (0: ok, 1: saturated, 2: offccd, 4:clipped)

TABLE 3.11: The structure of the variable *cs_lines*. Source: CARMENES consortium.

identified in the HCL spectra. From this initial set of lines, I have chosen all the lines

that with flag = 0, POSME < 1 pix and with |POSM - POSC| < 1 pix. This filters out roughly 5,400 lines, leaving a set of about 10,000 spectral lines. However, fitting the model to the data using 10,000 spectral lines is a computationally expensive task, so it is necesary to reduce the number of lines to optimize the computation time. From the set of 10,000 lines, I have removed all the lines with POSME = 0 and |POSM-POSC| > 0.02 pix, resulting in a list of about 3,700 lines. From this set I choose 360 spectral lines distributed all over the detector.

3.4.3 Optimization algorithms

To fit RAMSES to the CARMENES calibration data I used two different optimization algorithms: Simulated Annealing (SA) and Nested Sampling (NS). In this section I will briefly describe them.

Simulated annealing

SA is a probabilistic method for finding the global minima of a function that may possess several local minima. It mimics the annealing process in which a material is slowly cooled so that, while its structure freezes, it reaches a minimum energy state (Kirkpatrick, Gelatt, and Vecchi, 1983). Starting with a current point i in a state j, a neighborhood point i' of the point i is generated. The algorithm moves from point i to i' using a probabilistic criteria that is dependent on the 'temperature in state j. This temperature is analogous to that in physical annealing, and serves here as a control parameter. If the solution at i' is better than the existing solution, then this new point is accepted. If the new solution is worse than the existing solution, then the probability of accepting the point is defined as $exp(-(f(i') - f(i))/T(j))$, where the function f corresponds to the value of the objective function at a given point, and $T(j)$ is the temperature at the state j. After a given number of neighbourhood points are evaluated, the temperature is decreased and a new state $(j + 1)$ is created. Due to its exponential form, the probability of the acceptance of a neighborhood point is higher at high temperature, and is lower as temperature reduces. In this way, the algorithm searches for a large number of neighborhood points in the beginning, but a lower number of points as temperature is reduced (Amaran et al., 2016).

To fit a physical model to the instrument, I employ an optimization routine. Figure 3.17 shows the flowchart of the procedure. The main advantages of using SA are its ability to deal with highly non-linear models and its ability to approach the global minimum without getting stuck in a local one. It is also quite versatile since it does not rely on any restrictive properties of the model. Two of its weaknesses are that one has to take into account the different types of constraints of the model, and that there is a clear trade-off between the quality of the solutions and the time required to compute them.

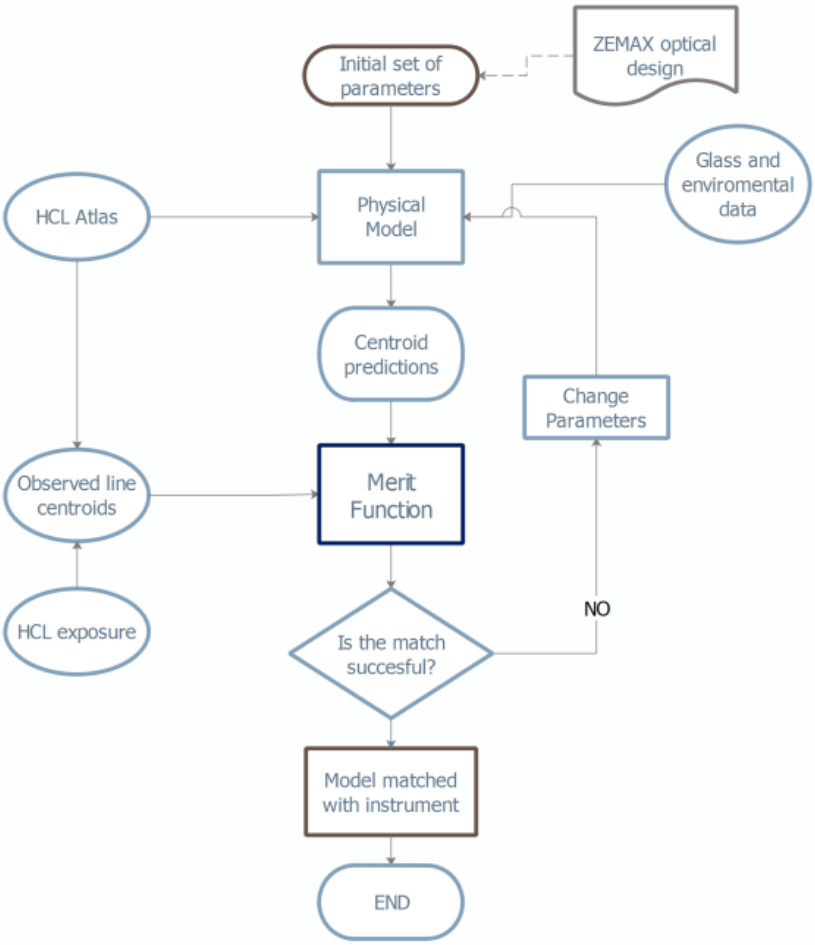

FIGURE 3.17: Flowchart of model optimization algorithm to match with instrument observations. Based on the flowchart from Bristow, Kerber, and Rosa, 2008.

Implementation of simulated annealing procedures require choosing parameters such as the initial and final temperatures, the rate of cooling, and number of function evaluations at each temperature. For this work I've implemented a SA routine written in Python[4] that allows to adjust the initial and final temperatures, as well as the numbers of steps in each iteration.

A typical SA algorithm can described by the following steps

- Set initial parameters, initial guess i, starting temperature T_0, number of iterations per temperature k, stopping criteria, and temperature scale s.
- Repeat until stopping condition is reached
  - Iterate from $j = 1$ to k
  - Generate a new point, i'
  - Calculate $\Delta = f(i') - f(i)$
    - If $\Delta < 0$, $i = i'$

[4] https://github.com/perrygeo/simanneal

    * If $\Delta > 0$, generate a random number r between 0 and 1.
      If $p = exp(-(f(i') - f(i))/T_k) > r, i = i'$
  - Next iteration j
  - $T_{k+1} = s\ T_k$
  - Check stopping condition

I have set the initial temperature at T_i=25000 K and the final temperature at $T_f = 10^{-4}$, evaluating the function 5000 times in this case. Each SA cycle last about 2.5 min in an average computer.

The function in this case is defined as the difference between the measured position of the HCL emission lines and the predicted position in the detector of the HCL emission lines with a given wavelength. The probability function is defined by

$$p = \exp\left(-\Delta/T\right) \tag{3.84}$$

with

$$\Delta = \sqrt{\Delta_x^2 + \Delta_y^2} \tag{3.85}$$

where Δ_x and Δ_y are the difference between the measured and predicted spectral lines positions along the x and y axis, respectively. They are expresed as follows

$$\Delta_x = x_m - x(m,\lambda)_{\mathrm{R}} \tag{3.86}$$

$$\Delta_y = y_m - y(m,\lambda)_{\mathrm{R}} \tag{3.87}$$

where x_m and y_m are the coordinates of the spectral lines measured in the detector in pixels, and $x(m,\lambda)_R$ and $y(m,\lambda)_R$ are the coordinates of a spectral line predicted by RAMSES, which receives as an input a list of spectral lines defined by their wavelength λ and their spectral order m. The values of x_m, y_m, λ and m are extracted directly from the *cs_lines* file described in §3.4.2. In this case x_m=POSM, y_m=POSMY, λ=WLL and m=ORDER, from the labels in the fields in Table 3.11. I ran the SA routine until the value of rms of the Δ was half a pixel.

Nested Sampling

Bayesian Inference is a method of statistical inference in which Bayes' theorem is used to estimate the probability for a hypothesis as more evidence or information becomes available, and its use can be divided into two categories: parameter estimation and model selection. In that sense Bayesian inference methods provide a consistent approach to the estimation of a set of parameters Θ in a model (or hypothesis) H for the data D. The following presentations of Bayesian inference and Nested Sampling are based in the sections 2 and 3 from Feroz, Hobson, and Bridges, 2009.

Bayes theorem states that

$$P(\Theta|D,H) = \frac{P(D|\Theta,H)\ P(\Theta|H)}{P(D|H)} \tag{3.88}$$

where $P(\Theta|D,H) \equiv P(\Theta)$ is the posterior probability distribution of the parameters, $P(D|\Theta,H) \equiv \mathcal{L}(\Theta)$ is the likelihood, $P(\Theta,H) \equiv \pi(\Theta)$ is the prior, and $P(D|H) \equiv Z$ is the Bayesian evidence, which can be computed by

$$Z = \int \mathcal{L}(\Theta)\ \pi(\Theta)\ d^D\Theta \tag{3.89}$$

where D is the dimensionality of the parameter space.

In parameter estimation, the normalising factor is usually ignored, since it is independent of the parameters Θ, and inferences are obtained by taking samples from the unnormalised posterior using standard MCMC methods, where at equilibrium the chain contains a set of samples from the parameter space distributed according to the posterior. This posterior constitutes the complete Bayesian inference of the parameter values, and can be marginalised over each parameter to obtain individual parameters constraints.

Nested Sampling (NS) (Skilling, 2006) is a Monte Carlo technique aimed at efficient evaluation of the Bayesian evidence, but produces posterior inferences as by-product. It exploits the relation between the likelihood and the prior volume to transform the multidimensional evidence integral from Eq. 3.89 into a one-dimensional integral. The 'prior volume' X is defined by $dX = \pi(\Theta)d^D\Theta$, so that

$$X(\lambda) = \int_{\mathcal{L}(\Theta)>\lambda} \pi(\Theta)d^D\Theta \tag{3.90}$$

where the integral extends over the region(s) of parameter space contained within the iso-likelihood contour $\mathcal{L}(\Theta) = \lambda$. The evidence integral (Eq. 3.89) can be written as

$$Z = \int_0^1 \mathcal{L}(X))dX \tag{3.91}$$

where $\mathcal{L}(X)$, the inverse of Eq. 3.90, is a monotonically decreasing function of X. Thus, if one can evaluate the likelihoods $\mathcal{L}_i = \mathcal{L}(X_i)$, where X_i is a sequence of decreasing values,

$$0 < X_M < \cdots < X_2 < X_1 < X_0 = 1 \tag{3.92}$$

and the evidence can be approximated as a weighted sum

$$Z = \sum_{i=1}^{M} \mathcal{L}_i\ w_i \tag{3.93}$$

where the weights are given by $w_i = 0.5(X_{i-1} - X_{i+1})$.

Once the evidence Z is found, posterior inferences can be easily generated using

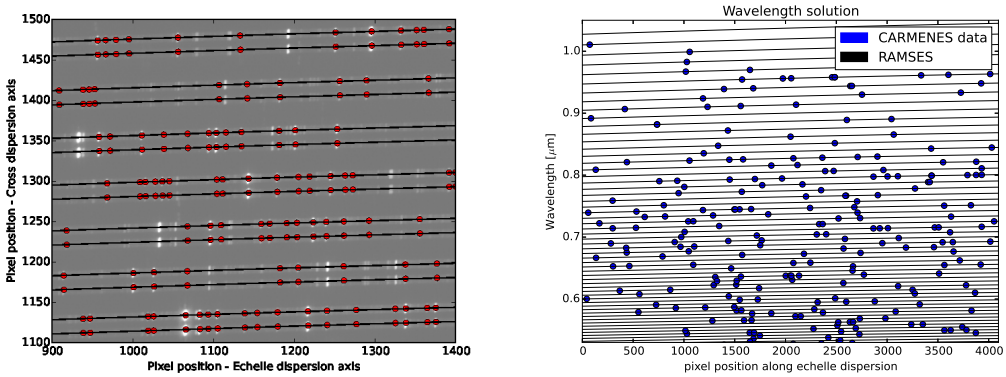

FIGURE 3.18: *Left panel*: The red points corresponds to the measured positions of the selected spectral features on the CCD across different orders of a U-Ar lamp spectra. The black line is the RAMSES prediction for the position of the wavelengths along the echelle dispersion direction. *Right panel*: Wavelength solution $x = x(\lambda)$ computed with RAMSES. The x-axis corresponds to the spectral line position along the echelle dispersion direction and the y-axis is the wavelength of that particular feature.

the full sequence of points generated in the NS process (Feroz, Hobson, and Bridges, 2009).

In this work I use PyMultinest (Buchner et al., 2014; Buchner, 2016) to perform the parameter estimation when fitting RAMSES to the CARMENES calibration data. The two main parameters of the PyMultinest algorithm are the **priors**, or also called prior probability distribution, and the **Likelihood function**. The prior is the probability distribution that would express one's beliefs about this quantity before some evidence is taken into account. The Likelihood function is the joint probability distribution of observed data expressed as a function of statistical parameters. It describes the relative probability or odds of obtaining the observed data for all permissible values of the parameters, and is used to identify the particular parameter values that are most plausible given the observed data.

3.4.4 Results and Analysis - VIS channel

Simulated Annealing

I performed the simulations while the instrument was already in operation. I obtained the data for the positions of the spectral lines on the detectors from the CARMENES data archive. I start with an initial guess based on the design parameters of the spectrograph from ZEMAX. Figure 3.18 shows the match between our model and an observation, for the set of wavelengths used for optimization. The left panel in Figure 3.18, shows a section of a UAr spectrum. On top of it we plot the line positions derived by the CARMENES reduction pipeline, together with the wavelength solution calculated by RAMSES, for the two fibers that feed the spectrograph. As the line list we are using contains spectral lines from ThNe, UAr and UNe HCLs, some

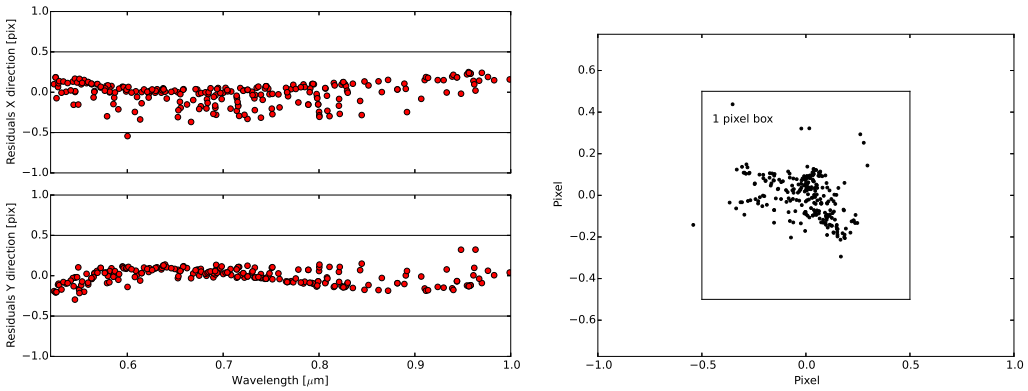

FIGURE 3.19: *Left panel*: Residuals in echelle and cross dispersion direction for a sample of spectral lines. *Right panel*: Scatter of residuals. The box represents one pixel.

of the positions from the catalog don't match the image in Figure 3.18, as the spectra we show in this figure corresponds to a UAr spectrum. However, the positions for the U and Ar lines are in agreement with expectations.

The right panel in Figure 3.18 shows the wavelength solution. The blue points correspond to the x-position in pixels of the selection of spectral lines used to fit our data, while the black lines correspond to the wavelength solution calculated by RAMSES.

I achieve sub-pixel accuracy by optimizing the different parameters. The residuals are shown in the left panel in Figure 3.19. The scatter of the residuals seems to concentrate around the center, but we observe a gradient in the residuals of the y axis. This might be related to a parameter that could require special weighting when optimizing. However, due to the strong degeneracies in the parameter space it is not simple to disentangle the particular effect of one parameter on the residuals, as they are strongly correlated. The right panel of Figure 3.19 shows the residuals between the measured positions of spectral lines and the prediction from our model. The square indicates one pixel of the detector. We observe an asymmetry in the distribution, however without a detailed analysis of the line centering method it is not possible to relate the asymmetry to systematics in either the model or the measurements. Our model currently fits all the lines with a rms better than half a pixel. The plots shown in Figure 3.18 and Figure 3.19 correspond to some preliminary results presented in Tala Pinto et al., 2018, and they correspond to the fit done to the line positions at MJD = 58099 d.

This fit was performed with an incomplete version of RAMSES. After completion of the code I re-fitted RAMSES to CARMENES, but now starting from the first date of the survey, to use the results from this date as a reference to understand how the parameters of the instrument have changed with time since the start of the survey.

Figure 3.20 show the post-fit residuals obtained with the SA routine. In this case the rms of Δ, which is a quantity that represents mean difference between the model and the calibration data in x and y axes, is about 0.5 pix, however there are many

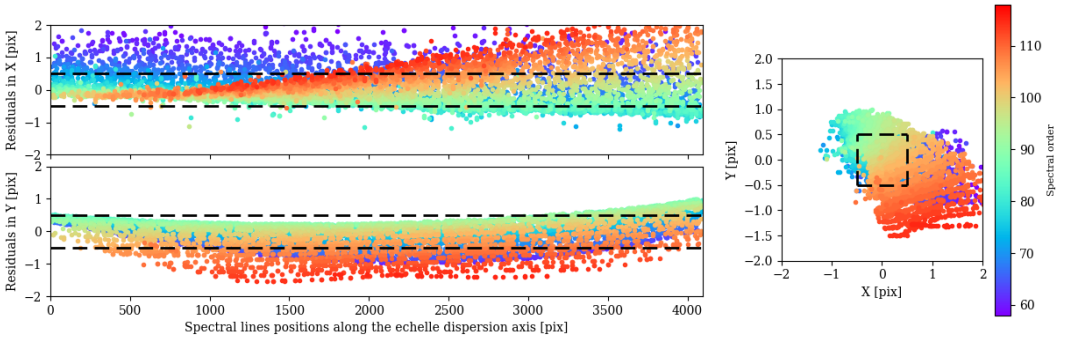

FIGURE 3.20: Simulated annealing post-fit residuals in the VIS channel. *Top-left* panel: post-fit residuals of the line positions in the echelle dispersion direction (x axis) color-coded by spectral order. *Bottom-left panel*: post-fit residuals of the line positions along the cross-dispersion direction (y-axis) color coded by spectral order. *Right panel*: Scatter of the residuals of each spectral line with respect to their measured position color coded by spectral order. The dashed box corresponds to one pixel.

spectral lines who are much scattered, some of them with differences between the measured and predicted position of about 1.5 pix. The post-fit residual points are color coded as a function of spectral order. The top panel in Figure 3.20 show the post-fit residuals in the echelle and cross dispersion axess (x and y-axis), respectively. The rms of the residuals along these axes is XX pix. By visual inspection, the scatter in the residuals is larger on the left side of the detector for the lower orders (redder wavelengths) and larger on the right side of the detector for the higher orders (bluer wavelengths). In addition, along the x axis most the residuals are concentrated above the -0.5 pix dashed line shown in left panels in Figure 3.20. A similar behaviour is observed in the y-residuals shown in the bottom-left panel of Figure 3.20, where the y-residuals are concentrated below the 0.5 pix dashed line. The residuals along the cross dispersion axis show that the higher orders (bluer wavelenghts) are considerably much more scattered than the others. The right panel in Figure 3.20 shows the residuals between the measured positions of spectral lines and the prediction from our model color coded by spectral order. The dashed square indicates one pixel of the detector. There is a clear asymmetry in the distribution, however, as pointed out for the preliminary results, without a detailed analysis of the line centering method it is not possible to relate the asymmetry to systematics in either the model or the measurements.

Based on these results, the fit is good for the spectral lines in orders that are close to the center of the detector, and becomes slightly worse for the extreme orders. It is not clear if these systematics are due to a purely geometrical effect that could be corrected by fine-tuning the detector, or some other optical element, or if it is related to the echelle and/or grism dispersion. At the moment of writing this thesis, the SA routine is still running trying to improve the results with the aim of reducing the residuals even more.

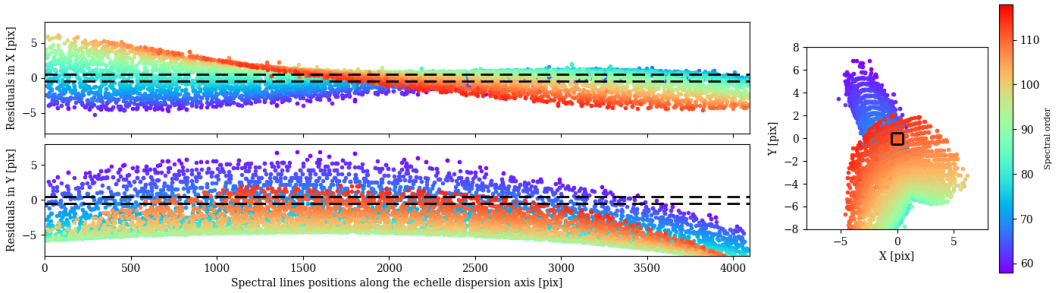

FIGURE 3.21: NS post-fit residuals in the VIS channel. *Top-left panel*: post-fit residuals of the line positions in the echelle dispersion direction (x axis) color-coded by spectral order. *Bottom-left panel*: post-fit residuals of the line positions along the cross-dispersion direction (y-axis) color coded by spectral order. *Right panel*: Scatter of the residuals of each spectral line with respect to their measured position color coded by spectral order. The dashed box corresponds to one pixel.

Nested Sampling

For fitting the CARMENES calibration data using NS I define a set of priors for the parameter space and Likelihood function. For the priors, I have defined different priors to different parameters, depending on the type of parameter. I have identified four type of parameters: tilt angles of optical elements, decenterings of optical elements, distances between the optical elements, and grating constant values. For all of them I use uniform priors, so that the prior probability function is constant function. This can be interpreted as meaning that all possible values are equally likely a priori. I assume this as I have no information about the current state of the parameters that produced a given dataset, therefore I assume a constant prior with minimum and maximum values centered at the parameter value, with the aim of limiting the range of the parameter space, and optimize the time it takes to explore it. In the case of the tilt angles parameters I have chose uniform priors with a parameter range of 0.5° centered at the initial parameter value. For the decentering values I have considered a decentering range of 0.5 mm in each direction (x and y axes) centered at the initial parameters value. For the distances between the optical elements I have considered displacements between the optical elements of 5 mm, which seems a bit unrealistic, as the change in the position of the optical elements due to the expansion and/or contraction of the optical bench where they are mounted is much smaller than the adopted value. However, having a wider prior should not impose any contraints in the final result, apart from extending the calculation time, as a wider prior means that the size of the parameter space in which NS looks for optimal solutions becomes larger as well. For the grating constants of the echelle grating and grism I have considered that a parameter range of 0.18 lines/mm in the case of the echelle grating, and 0.25 lines/mm. In the case of the echelle grating, the decision of the prior was done based in the ranges in which the grating equation is valid for the wavelength range of the spectrograph. If the echelle grating constant is larger or smaller than 31.6 ± 0.18, then the angles at which the rays are diffracted become

too large and the term under the square root in the z-component of the direction cosines from Eq. 3.66 becomes negative, leading to an undefinition of the direction. Therefore the prior on the grating constants is motivated by the physically possible angles for the diffracted rays.

The likelihood is, for mathematical convenience, a loglikelihood that is defined as

$$\mathcal{L} = \sum_{i=1}^{p}(\sigma_{x,i} + \sigma_{y,i}) + \sum_{i=1}^{p}\frac{\Delta_{x,i}}{\sigma_{x,i}} + \sum_{i=1}^{p}\frac{\Delta_{y,i}}{\sigma_{y,i}} \tag{3.94}$$

where p is the number of spectral lines used in the fit, σ_x and σ_y are the uncertainties in the measured coordinates of the spectral lines in detector and Δ_x and Δ_y are defined by Eq. 3.86 and Eq. 3.87, respectively. In this case the CARMENES data reduction pipeline only provides uncertainties for the measured position of the spectral lines along the x axis, and not for the y positions, as shown in Table 3.11. So I assume that the errors in the measured position of the lines along the y axis are the same as for the x axis.

Figure 3.21 show the post-fit residuals obtained after performing parameter estimation with NS. These results are obtained by averaging the spectral lines positions obtained by evaluating RAMSES in each parameter set of the post-weighted distribution of the parameter space. The rms of the post-fit residuals along the X and Y axes - corresponding to the echelle and cross-dispersion direction - are of 5.3 pix and 4.7 pix, respectilvely. While there is a large number of spectral lines that are fitted with an accuracy better than one pixel, there are many in which the residuals are larger than one pixel, reaching values larger than 5 pixels in many cases.

The post-fit residuals along the X-axis are shown the top-left panel in Figure 3.21. I observe a clear trend as a function of spectral order. The residuals of the higher orders are scattered towards positive values in the left part of the detector and towards negative values in the right part of the detector. At the same time, the residuals of the lower orders are scattered towards negative values in the left part of the detector and towards positive values in the right part of the detector. When observing the residuals along the Y axis, shown in the bottom- left panel in Figure 3.21, they don't seem to be centered around the central part of the detector - which corresponds to the orders coded with green color tones - and they seem to have an offset of about 5 pixels towards negative values.

One interesting feature of Bayesian inference analysis is that it provides information about the uncertainties in the parameters and about how the parameters are related to each other. This is very useful to disentangle possible degeneracies in the parameters space and bi-modalities in the model. Fig 3.22 show the post-weighted distribution of the parameters, and the relation between them. The different parameters are labeled in the x and y axes. At a first glance, I do not observe any important correlation between the different parameters, except for the following pair of parameters: ech_G versus ech_blaze and cam_tilt_y versus grm_apex. A possible explanation for the observed correlation between ech_G and ech_blaze is the fact that,

as expressed by Eq. 3.66, there is a direct dependancy between the grating constant and the dispersion of the echelle grating, which is a function of the orientation of the angle of the grating, defined in RAMSES by the parameter ech_blaze. A possible explanation for the observed correlation between cam_tilt_y and grm_apex is that the rays go to the camera after being traced through the grism, therefore any change in the grism dispersion will have an impact in the orientation of the camera when trying to find the optimal solution for the parameter estimation. Due to the orientation of the grism, it makes total sense that the dispersion in the grism, characterized among other parameters by its grating constant, is correlated with the orientation of the camera in the y-axis. I do not observe any additional clear correlations in Figure 3.22.

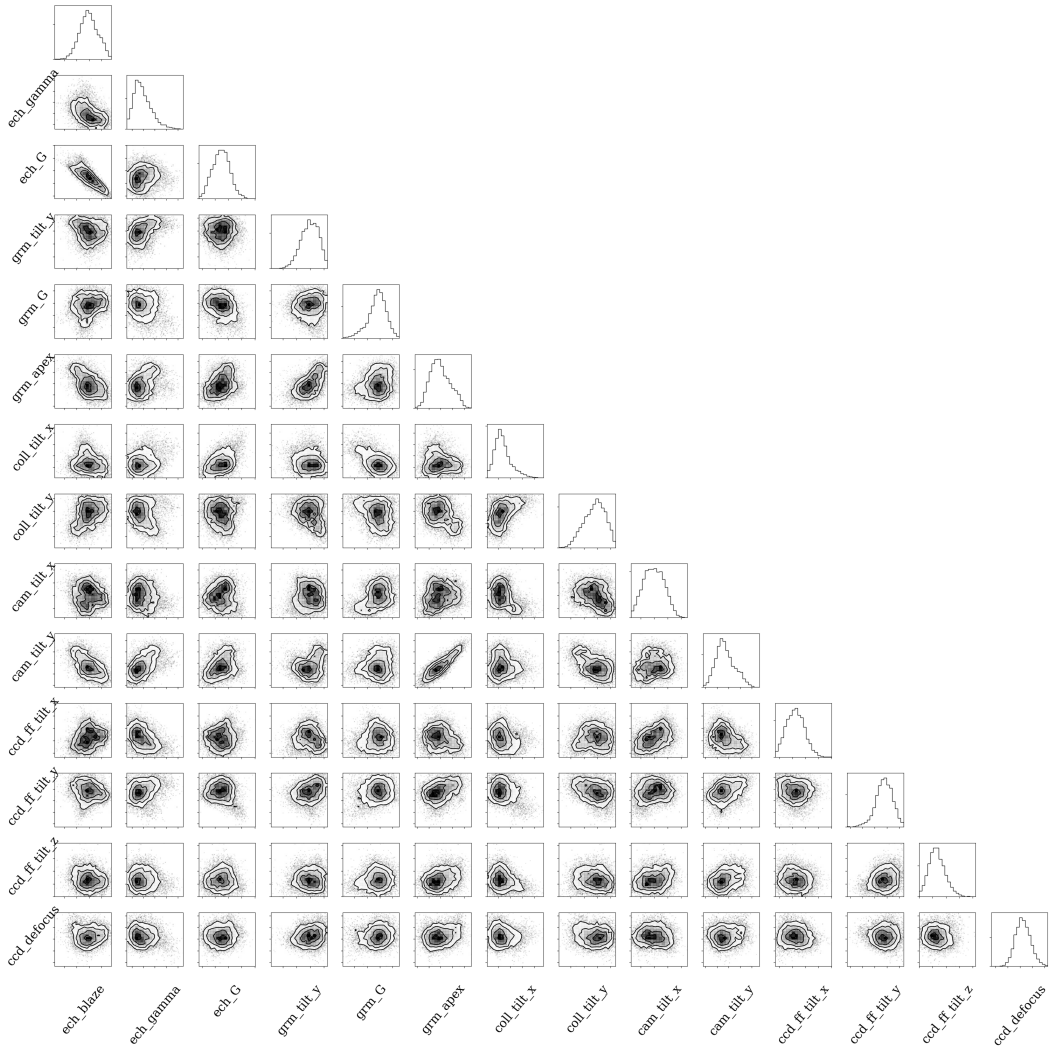

FIGURE 3.22: Corner plot showing the correlation between the most relevant parameters estimated by NS when fitting RAMSES to the CARMENES calibration data. I have removed the numbers in the ticks of the correlation plots for an optimal visualization.

Parameter	Original value	Sim. Ann.	Multinest
ech_blaze	75.2	75.3091	75.4130±0.0019
ech_gamma	1.2	1.1281	1.5252±0.0019
ech_G	31.6	31.5722	31.5763±0.0002
grism_tilt_y	2.4	2.3836	2.3264±0.0121
grism_G	223	222.8031	223.1791±0.0207
grism_apex	17.8	17.6687	16.9178±0.0117
coll_tilt_x	0	-0.3452	-0.3495±0.0006
coll_tilt_y	0	-0.1262	0.3435±0.1516
cam_tilt_x	0	0.5219	0.3810±0.0075
cam_tilt_y	0	-0.3479	0.1199±0.9674

TABLE 3.12: Comparison between the calculated parameters from simulated annealing and multinest.

Simulated Annealing versus Nested Sampling

It is clear by comparing Figure 3.20 and Figure 3.21 that SA provides better results in the parameter estimation. The rms of the residuals is at least one order of magnitude larger in NS. Just by observing the shape of the residuals (not the value of the rms) it seems they are inverted for each optimization method. In the case of SA the scatter of the residuals of the higher orders is larger in the right part of the detector, behaviour that is exactly the opposite as what I observe in residuals of NS, where the scatter of the residuals of the higher orders is larger to the left part of the detector. In addition, by comparing the post-fit residuals in the Y-axis, while the shape looks similar with both techniques, they seem to be inverted, as in SA the 'cut' in the distribution of residuals is close to the 0.5 pix dashed line, while in NS the position in this feature has a negative value. Also, in the case of SA the scatter of the residuals is larger for the higher spectral orders, while in NS it is larger for the lower orders. This might be an indication that there is one parameter that is not perfectly fitted and that it could be introducing systematics in the post-fit residuals.

Table 3.12 show the value of ten parameters as estimated by SA and NS, compared to their original design value. The echelle grating parameters *ech_blaze* and *ech_G* seem are the only ones who seem to be consistent in both methods. In the case of *ech_blaze*, its value is larger than the original value in both methods, but it is larger in the estimations from NS. In the case of the echelle grating constant, described by the parameter *ech_G*, the SA and NS estimations are consistent. This seem to be the case also for the parameter *coll_tilt_x*, where the predicitons from both method are also consistent. In the rest of the parameters listed in Table 3.12 the predictions from SA broadly disagree with the NS estimations.

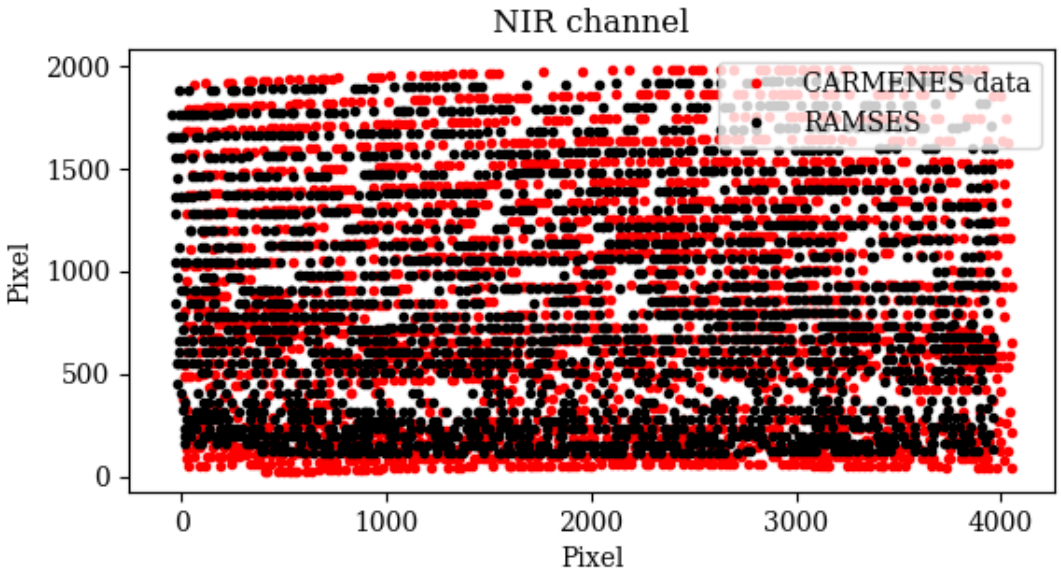

FIGURE 3.23: The red points show the positions in the detector the spectral lines from the HCL used in the wavelength calibration of CARMENES NIR spectra. The black points show the prediction for the position of these lines by RAMSES.

3.4.5 Early Results - NIR channel

The red points in Figure 3.23 correspond to the positions in the detector of the spectral lines from the HCL used in the wavelength calibration of CARMENES NIR spectra. The black points show the prediction for the position of these lines by RAMSES. In this case I have only optimised the decentering of the detector. At the moment of writing this thesis, none of the optimization routines studied here have provided a solution with a post-fit rms in the residuals of less than 50 pixels. However this is just a preliminary result, and further improvements in the parameters of the optimization routines should improve the post-fit rms of the residuals.

3.5 Times series of the CARMENES calibration lines positions

In order to keep the instrument enviroment stable, CARMENES VIS and NIR spectrographs are placed inside a vacuum vessel provides the required thermal and pressure environmentto operate the spectrographs at stable conditions. An air aconditioning system keeps the rooms where the spectrographs are installed at a stable ambient temperature. In the VIS channel, the vaccum vessel keeps the spectrograph at an almost constant temperature and pressure. In the NIR channel, the spectrograph is enclosed with a radiation shield actively cooled with thermalized nitrogen gas that flows through strategically positioned heat exchangers to remove its radiative load. The cooling system has an external preparation unit (N2GPU), which provides the nitrogen gas through actively vaporizing liquid nitrogen with heating

resistances and a three stage circuit flow, each one controlled by an independent PID (Mirabet et al., 2014).

To study how the instrument has evolved with time, I make a characterization of the position of the spectral lines of the calibration data. There are two main motivations to do this. The first one is to study how the spectral lines positions have changed since the start of the survey, and use this information to investigate the nature of the Nightly-Zero-Points (NZPs), a daily RV correction that one must do in order to achieve the precision required to detect low amplitude RV signals. The second motivation is to identify the nature of the evolution of the lines positions, as use this information to fit RAMSES to these dates and study how the parameters of RAMSES -parameters that resemble the physical state of the instrument- change as a function of time.

The data to characterize the WS is extracted directly from the *cs_lines* file described in §3.4.2. I will use the expresion 'fiber drift' to describe the difference between the position of the spectral lines of the calibration frames of the spectra of a given fiber (A or B) with respect to its position the first night of observation of the survey, so it is not an actual motion of the fiber in its mount. I will use the expression 'differential drift' to describe the difference in position along the echelle dispersion axis between the spectral lines from fiber A with respect to the ones from fiber B, so it is not the actual change in the relative positions in the fibers mount. Both terms are used because that is the usual nomenclature we employ within the CARMENES consortium.

3.5.1 Hollow Cathode Lamps lines

The quality of the wavelength solution relies in the ability to identify spectral features in the calibration spectra, therefore, the number of spectral lines in the HCL spectra plays an important role, and it can be a limiting factor, when aiming at very high precision RV measurements Lovis and Pepe, 2007.

As the lamps are used, the cathodes are gradually worn away and deformed by sputtering. The following phenomena may be observed when a lamp is reaching the end of its life

- The lamp does not emit light, and the lamp current does not vary even if the current control knob is changed,
- Extreme variations occur in the line intensity and the lamp current may also vary in some cases
- The line intensity weakens significantly and the signal-to-noise ratio deteriorates

Therefore, HCLs aging have a strong effect in the quality of the wavelength calibration, and hence, the could have an effect in the measured radial velocities.

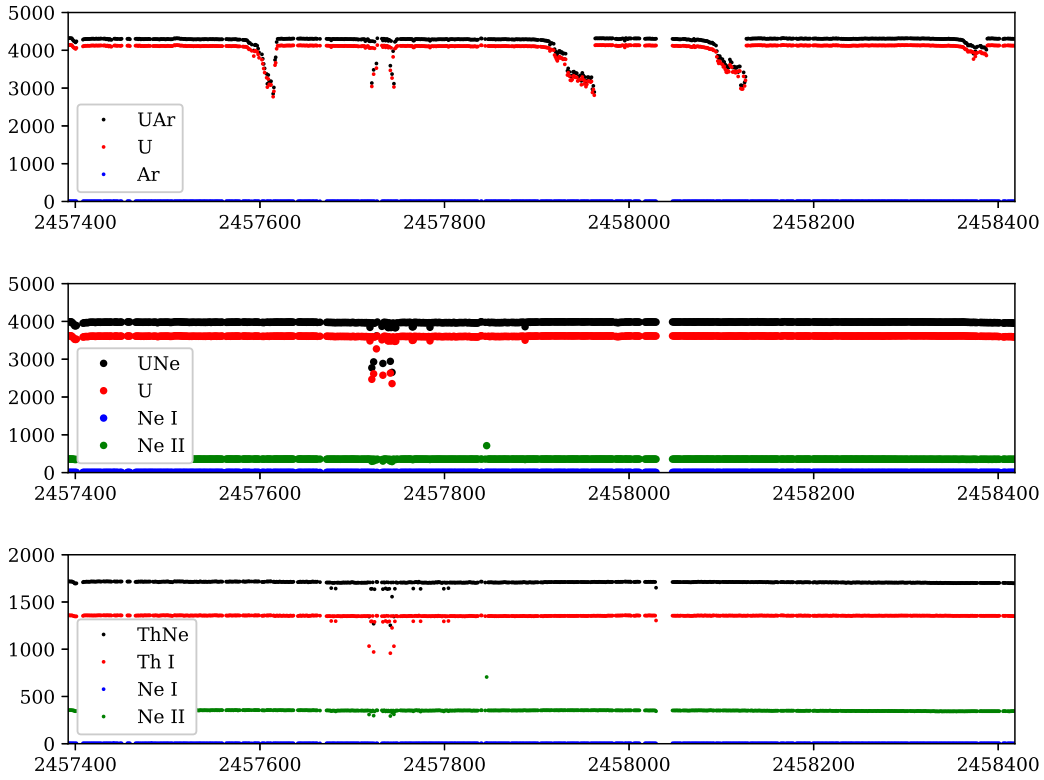

FIGURE 3.24: *Top panel*: Number of lines in the UAr lamp. *Middle panel*: Number of lines in the UNe lamp. *Bottom panel*: number of lines in the ThNe lamp.

Figure 3.24 show the time series of the HCL for CARMENES VIS and NIR channels. While in the case of the VIS channel the wavelength solution is built based in the position of the spectral lines of the Uranium Argon (UAr), Uranium Neon (UNe) and Thorium Neon (ThNe) lamps, the NIR only uses the UNe lamp spectra. The mean number of lines in the UAr lamp is 4292, where 4116 are U lines and 176 are Ar lines. The mean number of lines in the UNe lamp is 3891, where 3611 are U lines, 270 are NeII lines and only 10 are NeI. The mean number of lines in the ThNe lamp is 1636, where 1355 are ThI lines, 280 are NeII lines and only 1 is a NeI line. To count the number of lines I only considered the lines with the flag = 0.

While in the case of the UNe and ThNe lamps the total number of lines remains almost constant, this is not the case for the UAr lamp, where I can clearly identify the moment at which the lamp is reaching its lifetime when the number of U lines start to decrease. After changing the lamp for a new one, the number of U lines increase again to a number close to the mean value.

3.5.2 Temperature evolution

Temperature stability is essential for achieving precise RVs, and as studied before, changes in a few mK can result in shifts of a small fraction of a pixel in the detector

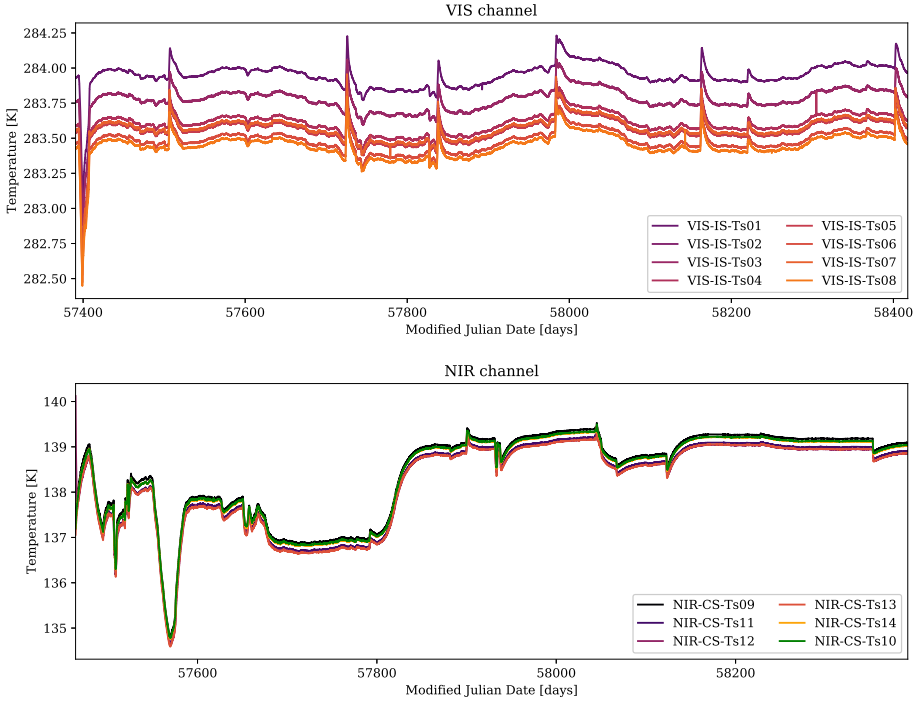

FIGURE 3.25: Time series of the temperature measured inside the spectrographs vacuum tanks by various temperature sensors.

plane, which are translated into instrumental RV shifts. As part of the characterization of the CARMENES WS, I study the time series of the temperature fluctuations since the start of the survey. Each spectrograph contains a set of temperature sensors used to measure the temperature inside the vacuum, in different places all over the optical bench and in some of the optics mounts.

I have extracted the measurements of the enviroment temperature inside the spectrographs for a number of temperature sensors, and plotted the time series of these measurements in Figure 3.25.

In the VIS channel the amplitude of the temperature measured by the different sensors is about 1 K, while within one single sensor the temperature varies about 0.3 K over a few days and only about 0.002 K over the short term (few hours). Excluding the observed peaks in the temperature time series of the VIS channel, the temperature itselfs varies smoothly with time.

In the NIR channel the temperature changes measured by the sensors seems to be more dramatic, as the temperature changes in the instrument can be of several degrees over the long term, as shown in Figure 3.25.

3.5.3 Instrument Interventions

Since the start of the survey the instrument has been subject of several interventions, as part of the quality control routines, with the objective of keeping the instrument performance as optimal as possible. These interventions are closely connected with the evolution of the instrument, and in many cases they can lead to significant shifts

in the positions of the spectral lines in the detector. A technical log database registers the nature of interventions done to the instrument hardware. Here I have listed the ones seem to that play an important role in the position of the lines in the detector. As the control systems of both channels are different, I consider different interventions for each channel. The Modified Julian Date (MJD) at which the interventions occured is indicated with a vertical colored dashed line in the plots fo the following sections, that show the time series of the evolution of the spectral lines positions. They are labeled according to their nature.

For the VIS channel I have selected the following interventions

- CR SP: refers to the regeneration of the sorption pumps in the detector cryostat
- VT SP: refers to the regeneration of the sorption pumps in the vacuum tank cryostat
- FE interv.: corresponds to an adjustment of the screws in the fiber mount at the front-end that were loose and was affecting the fiber illumination.
- New lamp: corresponds to the change of the HCLs in the calibration unit
- 2K offset: refers to an adjustment of 2 K in the temperature of the room where the calibration units are installed

and for the NIR channel the following

- CS instabilities: refers to the reported instabilites detected in the detector cryostat
- LN2 pump: refers to the pumping of LN2 through the pipes of the radiation shield
- Valve on/off: refers to the interventions related with the manipulation of the valve that controls the flowing of nitrogen gas in and out of the radiation shield (see Figure 1 from Mirabet et al., 2014)
- Drill: refers to a technical report where the intervention involved the drilling of a hole to support the manifold valve.
- FE interv.: is the same of the VIS channel
- No tech. notes: correspond to large offsets observed that don't have a technical report associated with the MJD of the observed drift.

I include two additional interventions that are related to the FP. The first one is *FP diffusers*, that refers to the installation of diffusers to homogeneize the illumination of the fiber that carries the FP spectrum. The second is *FP on/off/on*, that refers to a period in which an alternative strategy for the lamps that illuminate the FP was tested. The test consisted in comparing the instrument performance when the FP lamp was permanently on with respect to a period in which the FP lamp was on just during the observing times. After this intervention the FP lamp is on permanently.

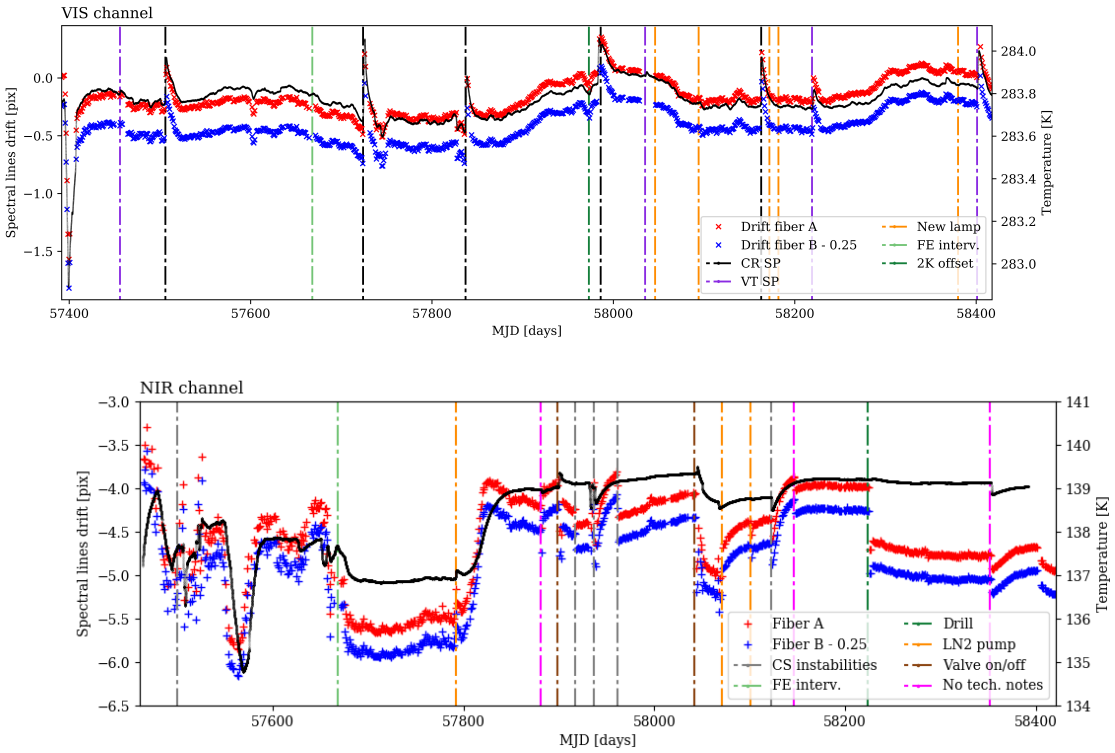

FIGURE 3.26: Time series of the fiber drifts. Drift of fiber A is plotted in blue while the drift of fiber B is plotted in red. The black corresponds to the time series of one of the temperature sensors. *Top pannel*: VIS channel. *Bottom panel*: NIR channel.

3.5.4 Fibers drifts - Hollow Cathode Lamps

One key parameter in the construction of the wavelength solution is the position of the spectral lines in the detector. With the goal of understanding how the position of the lines change with time, I characterized the drift of the spectrum of fiber A and B, by calculating the average of the difference of the position of the spectral lines of the calibration data a function of time. To do this, I've extracted the data of the detected position of the spectral lines in the detector from the *cs_lines* structure, and choose all the lines with *flag=0*. Then I've measured the change in the line position with respect to the first day of science observations, which for the VIS is the 2016-01-03, while for the NIR is the 2016-02-20. In the case of the NIR channel, even if the science observations started earlier, I consider the 2016-02-20, which is the day after the last NIR channel hardware intervention, as registered in the technical reports.

In this context, I define a drift as the change in the position of the spectral lines in the detector with respect to their position when the survey started. As the spectrographs are fed with two optical fibers, I will refer as 'drift in Fiber A' and 'drift in fiber B', to the drifts observed in the lines of the spectra generated due to the illumination of each fiber. I do not refer to a physical drift of the optical fibers in their mechanical mounts, even though that could be the case.

Figure 3.26 show the time series drifts in both fibers since the start of the survey. The top panel show the drifts in the VIS channel, while the bottom panel show the

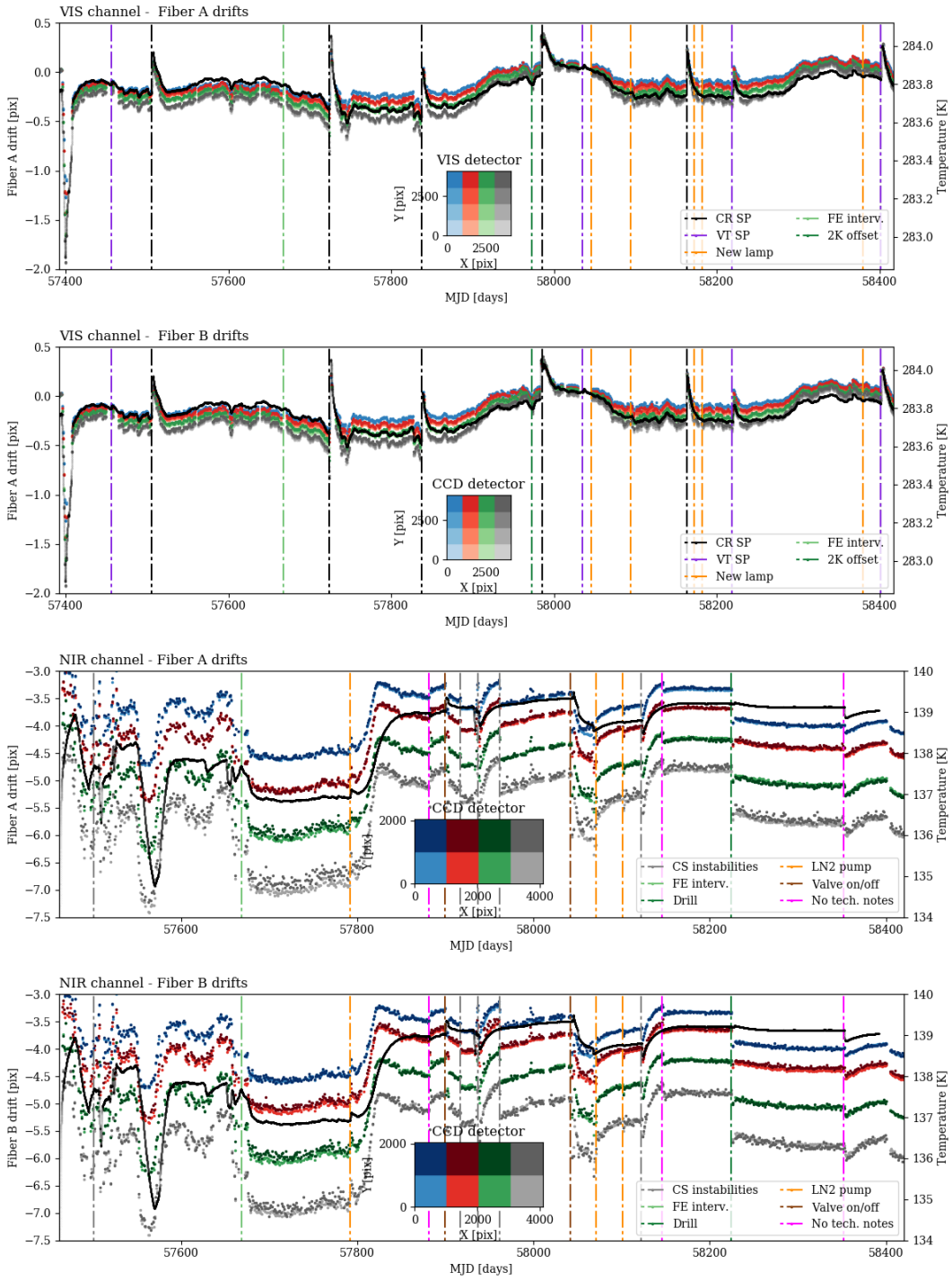

FIGURE 3.27: Time series of the fiber drifts in the HCL spectral lines from the calibration data as a function of the position in the detector. *Top panel*: drift in fiber A in the VIS channel. *Top-center panel*: drift in fiber B in the VIS channel. *Bottom-center*: drift in fiber A in the NIR channel. *Bottom*: drift in fiber B in the NIR channel.

drifts in the NIR channel. I have applied an offset of 0.25 pix to the drift of fiber B to distinguish it from the drifts of fiber A. The left axis show the drift in the spectral lines with respect to the start of the survey and the right axis show the instrument temperature in K. In both channels it is very clear how the fiber drifts follow the

temperature variations over time. In the VIS channel I observe a huge drift at the beginning of the survey, which most likely is explained by a temperature variation of about 1°K in the same period. After this initial jump of the lines, the amplitude of the temperature fluctuations over time is about $\Delta T = 0.4$°K, which is translated into an amplitude of the drifts of about 0.7 pix. Similarly, in the NIR channel the drifts of the spectral lines seems to be correlated with the temperature variations over time. The amplitude of the temperature variations is $\Delta T \sim 4$ K leading to an amplitude of the drifts of about 2 pixels.

In the VIS channel I observe a set of peaks in the fiber drifts. These peaks are associated with the regeneration of the sorption pumps in the detector cryostat or in the vacuum tank, which are marked with a black and purple dashed line in Figure 3.26, respectively. The sorption pumps accumulate the water inside the detector cryostat, and once is saturated the temperature is increased to evaporate the water and empty the sorption pump. This increment in the temperature of the detector cryostat is transferred to the spectrograph, which is observed as a temperature variation and, as a consequence, as a drift in the spectral lines. Once the sorption pump is empty, the temperature slowly decreases taking some time - about 7 days - to estabilize. However, it seems that this is not the case for all the sorption pump events, as the first VT SP event does not seem to have a strong effect in the instrument temperature or in the spectral lines positions.

Surprisingly, I do not observe any special change in the fiber drifts for the interventions labeled as *new lamp*. This means that the number of lines is large enough so that the change of the HCLs don't affect the computation of the average drifts of the lines in the detector.

I identify a small valley in the temperature and drift curves at MJD = 57973 d, which is related to a 2K error in the settings in the air aconditioning system that controls the temperature in the NIR channel room, VIS channel room, calibration unit and Technical Area room, so all later temperatures are 2K higher now. This is translated to a temperature fluctuation of a hundred of a degree, which translates into a drift of about 0.1 pix.

There seem to be not strong effect of the *FE interv.* in the average drift of fiber A and B.

In the NIR channel, the temperature fluctuations are more drastic, leading to larger drifts in the spectral lines with respect to the VIS channel. In the bottom panel of Figure 3.26, I have marked with a gray dashed lined the interventions related to what in the Technical Log has been reported as *CS instabilities*. The *CS instabilities* intervention at MDJ = 57500 refers to a valve that stopped working in the detector cryostat, and its effect does not seem to introduce a large offset in the fibers drifts, contrary to what is observed in the other interventions of the same nature.

I observe small offsets in the fiber drifts every time liquid nitrogen is pumped into the system, and some of them seem to have an effect in the instrument temperature while others do not. One big offset is observed at the intervention *Valve*

on/off, where after replacing the manifold valve the lines show a drift of about half a pixel, in both fibers. There is another important drift in the fibers at MJD = 58224 which is related to the drilling of a hole in the wall of the NIR spectrograph room, as reported in the Technical log. This drift is related to an intervention related to external factors and it does not correlate with the instrument temperature, as observed. There are additional relevant fibers drifts, which are marked with a magenta vertical dashed line in the bottom panel in Figure 3.26, but there is no technical report about interventions occurring at the MJD of these drifts.

Figure 3.27 show the time series of the spectral lines drifts since the start of the survey in the VIS and NIR channel as a function of the lines position in the detector. I have divided the detector in 16 quadrants where each quadrant is represented by a color. The blue points correspond to the spectral lines in the left side of the detector, the red points to the lines in the left-center part of the detector, the green to the lines in the right-center part of the detector and the grey points to the right part of the detector. So each color represents a different quadrant along the echelle dispersion axis, while the different tones for each color represent a different quadrant along the cross-dispersion axis, as shown in Figure 3.27.

For each quadrant I have calculated the difference of the lines positions with respect to their position when the survey started. The average drift corresponds to the black points. In both channels there is an offset as a function of color. The drift of the spectral lines is larger in the left side of the detector than in the right side of it. This behavior is observed for both channels, however thee offset is larger in the NIR channel, most likely due to the larger temperature variations.

In the both channels I notice that the effect of the interventions in the drifts of the fibers as a function of detector quadrant is similar to the effect observed in the average drifts. This means that the interventions affect the positions of all the spectral lines in the same way. Also in both channels there is an offset between the fibers drifts for different quadrants along the echelle dispersion axis, as the position along . This can be clearly observed in Figure 3.27, where the points with different colors have an offset between them along the y-axis. In the VIS channel the offset between the right and left quadrants in the detector has a maximum of 0.25 pix, but in some regions can of only 0.1 pix. In the NIR channel this effect is more significant, as the offset between the drift of the lines in the right part of the detector is about 2.5 pix. I also note that even if the regions cover the same physical area in the detector (the area of each quadrant is 1024 pix$\times$1024 pix), the offset between the adjacent quadrants is smaller for the quadrants to the left side of the detector. The offset between the blue and red points is about 0.5 pix, while the offset between the green and gray points is about 1 pix. This effect is also observed in the VIS channel.

3.5.5 Differential drift - Hollow Cathode Lamps

The key to achieve high precision RVs with the simultaneous calibration method is the observation of a secondary calibration spectrum simultaneously with the science

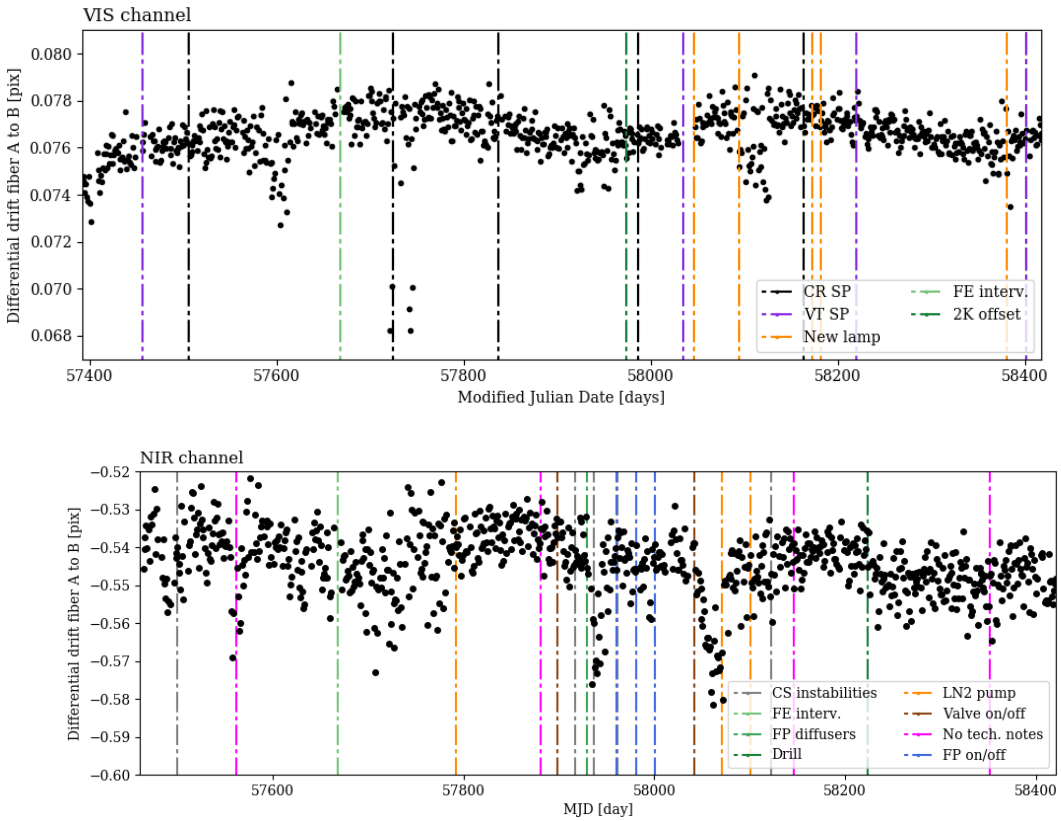

FIGURE 3.28: Differential drift of the spectral lines in fiber A with respect to fiber B. *Top panel*: VIS channel. *Bottom panel*: NIR channel.

observation. That is why the instrument is fed by two fibers, the science fiber (fiber A) and a calibration fiber (fiber B). The idea behind this method is that additional instrumental drifts can be corrected by observing the drifts in the calibration spectrum, which is at rest with respect to Earth. Therefore the relative drift between the spectrum of fiber A with respect to the spectrum of fiber B is crucial to keep track of these instrumental drifts.

Figure 3.28 show the average differential drift of the spectral lines in fiber A with respect to fiber B for the VIS and NIR channel. While in the VIS channel the amplitude of the average differential drift is about 0.006 pix - without considering outliers -, the same value in the NIR channel is about 0.06 pix, one order of magnitude larger. It seems that there no strong effect of the interventions in the time series of the differential drifts. This makes sense, as the interventions affect the whole instrument, therefore the spectrum of both fibers. As observed in the time series of the drifts of the individual fibers, the change of the HCLs doensn't seem to affect the value of the differential drifts.

In the VIS channel, there is one CR SP intervention at MJD = 57724 d, where the black dashed line crosses some differential drift outliers, so it could be that these outliers are produced by the regeneration of the sorption pump in the cryostat, however this behavior is not observed in the other CR SP interventions. In addition, there is large scatter in the differential drifts right after the *New lamp* intervention at

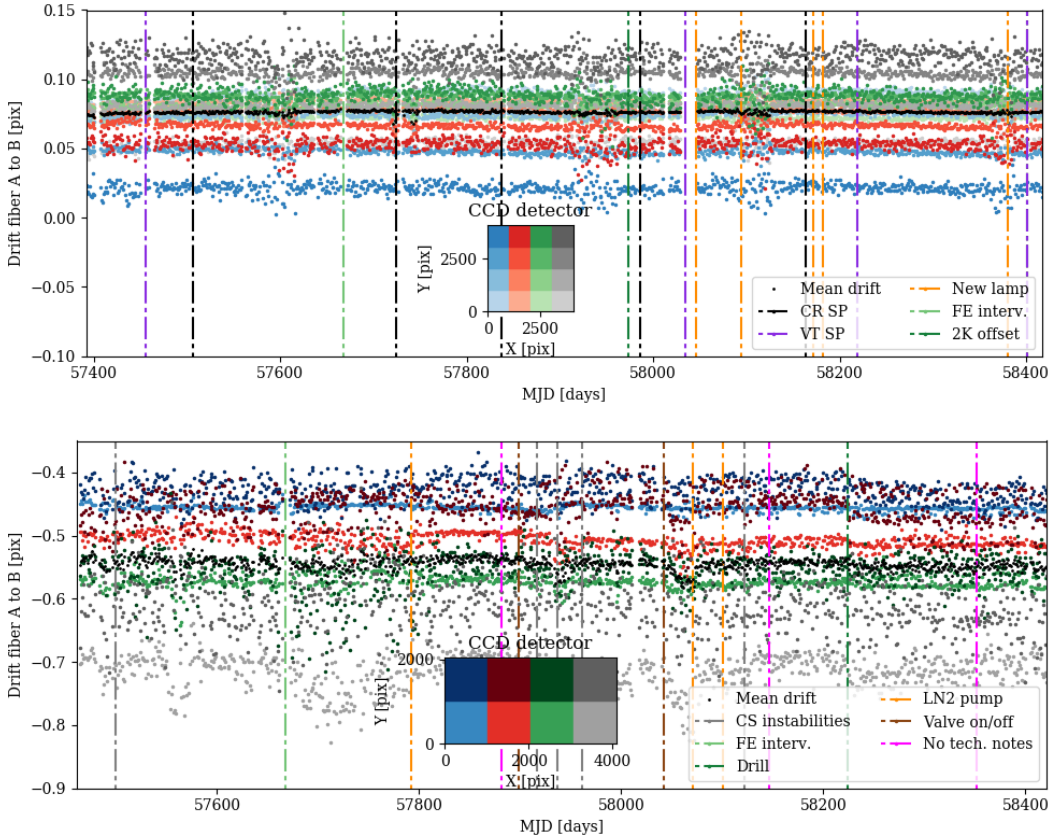

FIGURE 3.29: Differential drift between fiber A and B as a function of the quadrant in the detector. *Top panel*: VIS channel. *Bottom panel*: NIR channel.

MJD = 58094 d, but a similar behaviour is not observer in the other interventions of the same nature, therefore most likely this scatter is not cause by the change of the lamps. I also observe a large scatter in the differential drifts close to MJD = 57600 d, but there is no technical report around these dates.

In the NIR channel, I observe large variations in the differential drifts around MJD = 57937 d and MJD = 58071 d. While the first one seems to be related to the instabilities in the detector cryostat, the second seems to be related to the intervention in the on/off valve. In adittion, before the first LN2 pump intervention the differential drifts are more scattered than after it, so apparently the first LN2 pump intervention seemed to stabilize slightly the value of the differential drift. Also, I observe a clear offset in the differential drifts after the intervention related to the hole drilling in the room of the NIR channel. I see no strong effect of the rest of the interventions in the value of the differential drifts.

Figure 3.29 show the differential drift between fiber A and B as a function of quadrant in the detector. Just as I observe in Figure 3.27, there is an offset in the differential drifts as a function of the line positions along the echelle dispersion axis. The effect of the interventions in the differential drifts per quadrant seems to have

the same effect than for the average differential drift. In the VIS channel the differential drifts as a function of detector quadrant are less scattered than in the NIR channel. Also, in the NIR channel the scatter in the differential drifts of the extreme left and right (blue and gray) quadrants is larger than in the central quadrants (red and green). In addition, I observe an offset in the differential drift as a function of quadrant along the cross-dispersion axis. The differential drifts are larger for the spectral lines located in the upper part of the NIR detector.

3.5.6 Fibers drifts - Fabry-Perot

The scientific observations consist of a simultaneous observation of stellar spectra in fiber A and a FP spectra in fiber B. The FP spectra are used to measure and correct for any residual instrumental drifts present in the observations. Therefore, the drift of the FP lines will have an important role in the precision of the RV measurements.

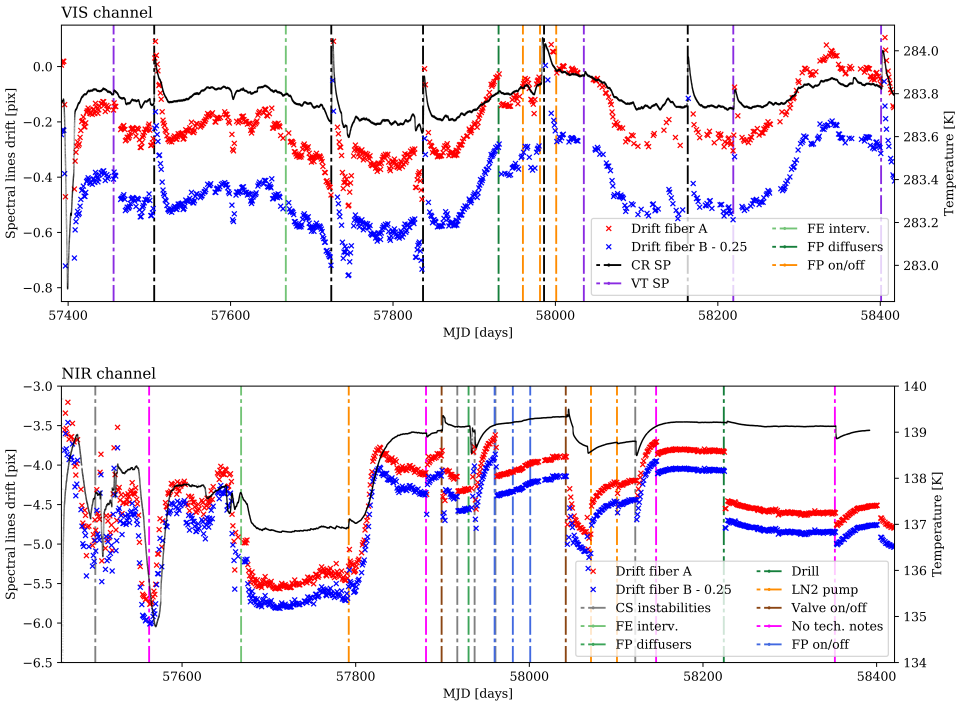

FIGURE 3.30: Drift of FP lines in fiber A and B. *Top panel*: VIS channel. *Bottom panel*: NIR channel.

In order to characterize the time series of the FP line positions, I have measured the drift of the FP spectral lines with respect to the first science observation, just as I did for the HCL in §3.5.4. In this case, the FP lines are characterized by the spectral order and the peak number of each individual lines. I have used only the FP calibration data. No science observation is included for this analyisis.

Figure 3.30 show the time series of the average drift of the FP lines in fiber A and B. Just as in §3.5.4, I have applied an offset of 0.25 pix to the drifts in fiber B for visualization. These FP drifts seem to be of the same order of the drifts observed in the HCLs, and just as observed in the HCLs drifts, the FP drifts also seem to

follow the temperature fluctuations over time, even though the HCL lines seem to be more affected by temperature. However there are a couple of events in the time series of the fiber drifts that does not seem to correlate with temperature, but with interventions related to the FP functioning.

As mentioned in §3.5.3, for the characterization of the FP drifts I have considered two additional interventions, 'FP diffusers' and 'FP on/off'. In the case of the first, there is a clear offset of about 0.1 pix in the VIS channel after the 'FP diffusers' intervention, meaning that the input illumination to the fiber that carries the FP information has a huge impact in the performance of the FP. However this offset is not observed in the NIR channel.

I observe some offsets in the period of time in which the 'FP on/off/on' test was carried out, however just before the FP lamp was left permanently on there was a regeneration of the detector cryostat sorption pump, making it difficult to disentangle the effect of each intervention on the fiber drifts. Regarding the rest of the interventions, they affect the fiber drifts in the FP in the same manner as they affect the drifts in the HCLs.

I performed the same analysis than in §3.5.4 for the fiber drifts as a function of the position of the spectral lines in the detector. Figure 3.31 show the drifts in fiber A and B for the VIS and NIR channel for the different quadrants in the detector. Just as I observed in the drifts of the HCLs, there is an offset between the fiber drifts for the different quadrants along the echelle dispersion axis. However in the NIR channel, the fiber drifts are less scattered than in the HCLs drifts.

Regarding the interventions, they seem to affect the fiber drifts per quadrant in the same manner than the average fiber drift.

3.5.7 Differential drifts - Fabry-Perot

Figure 3.32 show the differential drift of the FP spectral lines between fiber A and fiber B. In the VIS channel the amplitude differential drifts is abou 0.01 pix, while in the NIR channel is about 0.03 pix. However, just by visual inspection, the NIR show more variations.

Contrary to what I observe in the differential drifts of the HCLs, the differential drifts in the FP have large offsets, that I can easily relate to some of the interventions listed in §3.5.3. In the VIS channel, there is an offset of about 0.007 pix in the differential drift of the FP lines after the front-end intervention. However, this is an effect that is observed only in the VIS channel, as the NIR does not seem to be affected by this intervention. I observe another jump at MJD = 57930 d, which is most likely related to the 'FP diffusers' intervention. This intervention affects both channels in a similar way, as in both channels the offset in the differential drifts after this intervention is about 0.0075 pix. This is interesting, as this intervention is one of the few that affect both channels in the same way, in the sense that it generates the same offset for both channels. In the VIS channel, the 'CR SP' and 'VT SP' interventions does

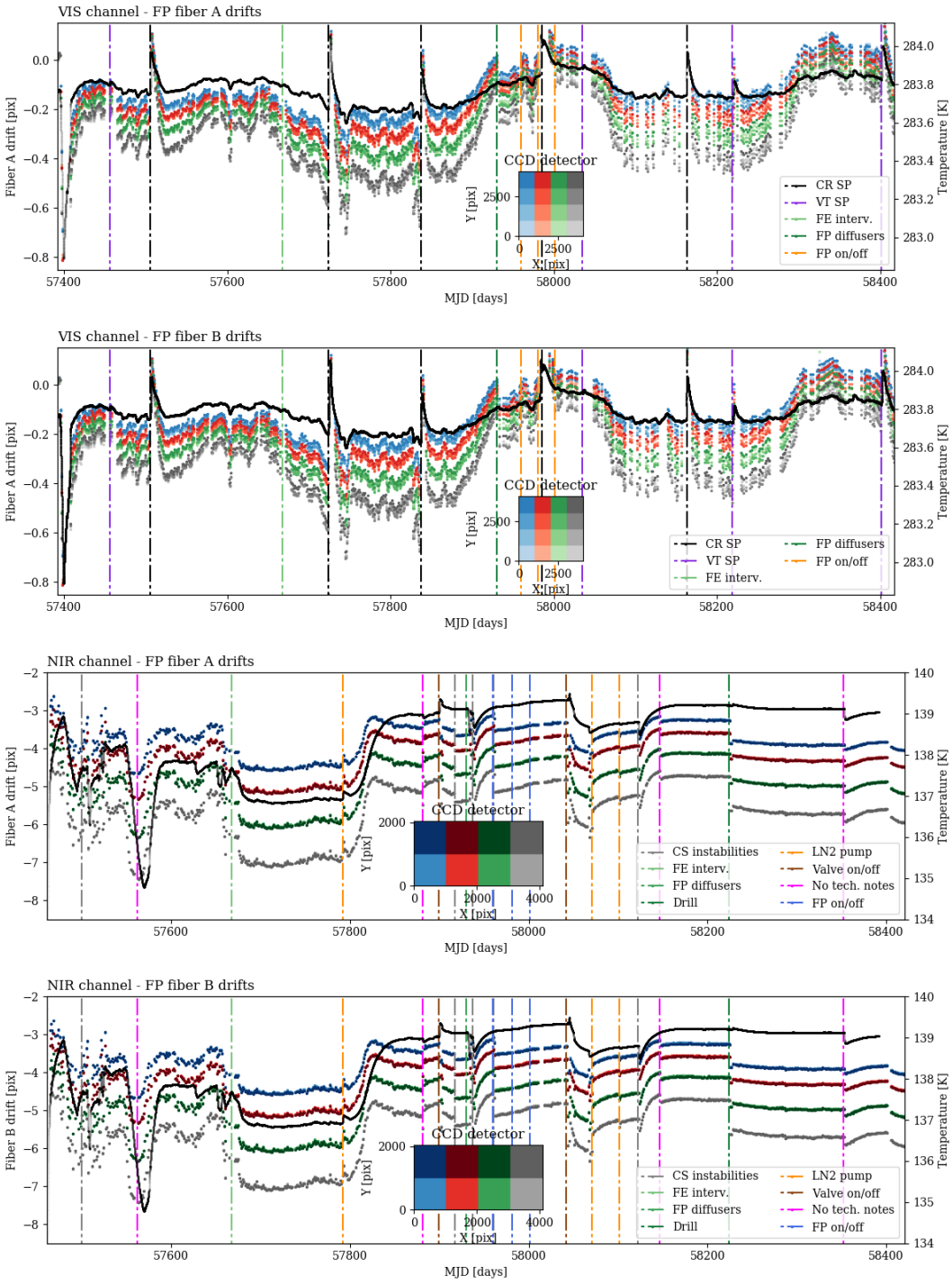

FIGURE 3.31: Time series of the fiber drifts in the FP spectral lines from the calibration data as a function of the position in the detector. *Top panel*: drift in fiber A in the VIS channel. *Top-center*: drift in fiber B in the VIS channel. *Bottom-center*: drift in fiber A in the NIR channel. *Bottom panel*: drift in fiber B in the NIR channel.

not seem to play an important role, while in the NIR channel the 'LN2 pump' seem to generate an offset in the differential drifts for the event at MJD = 57792 d.

There is a huge jump in the value of the differential drifts at MJD = 57881 d, unfortunately there is no Technical report that could give a hint about what happened

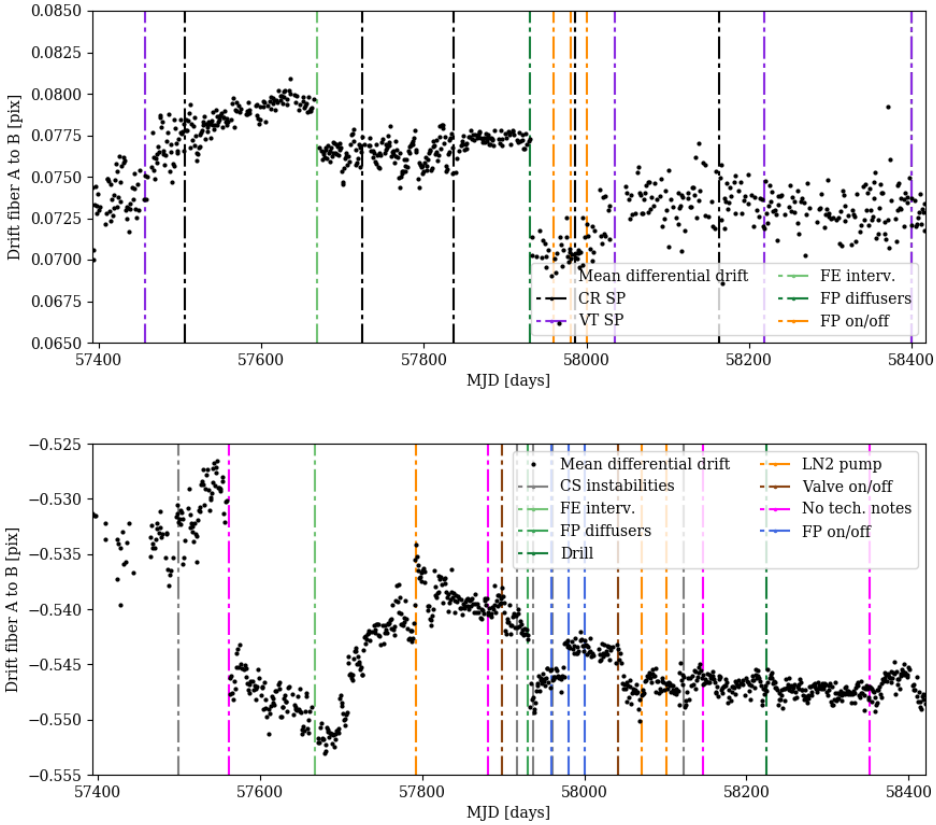

FIGURE 3.32: Differential drift of the FP spectral lines between fiber A and B. *Top panel*: VIS channel. *Bottom panel*: NIR channel.

here. The rest of the 'No tech. notes' interventions don't seem to affect the value of the FP differential drift.

Just as observed in the drifts of the individual fibers, the interventions in the on/off valve also generates an offset, as seen in Figure 3.32, and I also observe a small offset after the 'FP on/off/on' intervention at MJD = 57981 d, when the lamp of the FP is turned on just when its used.

Figure 3.33 show the differential drift of the FP lines of fiber A with respect to fiber B as a function of the quadrant in the detector. Just as observed in Figure 3.29, there is an offset between the differential drift measured in different quadrants in the detector along the direction of the echelle dispersion, however in the FP the scatter is much smaller compared to the scatter observed in the differential drift per quadrant in the HCLs. There is an offset also for the differential drift measured in different quadrants along the cross-dispersion direction. In both channels the value of the differential drift is larger in the upper part of the detector, and it decreases as I move to the lower quadrants.

The interventions don't seem to have an additional effect on the differential drift per quadrant. They affect the differential drift per quadrant in the same way they affect the average differential drift.

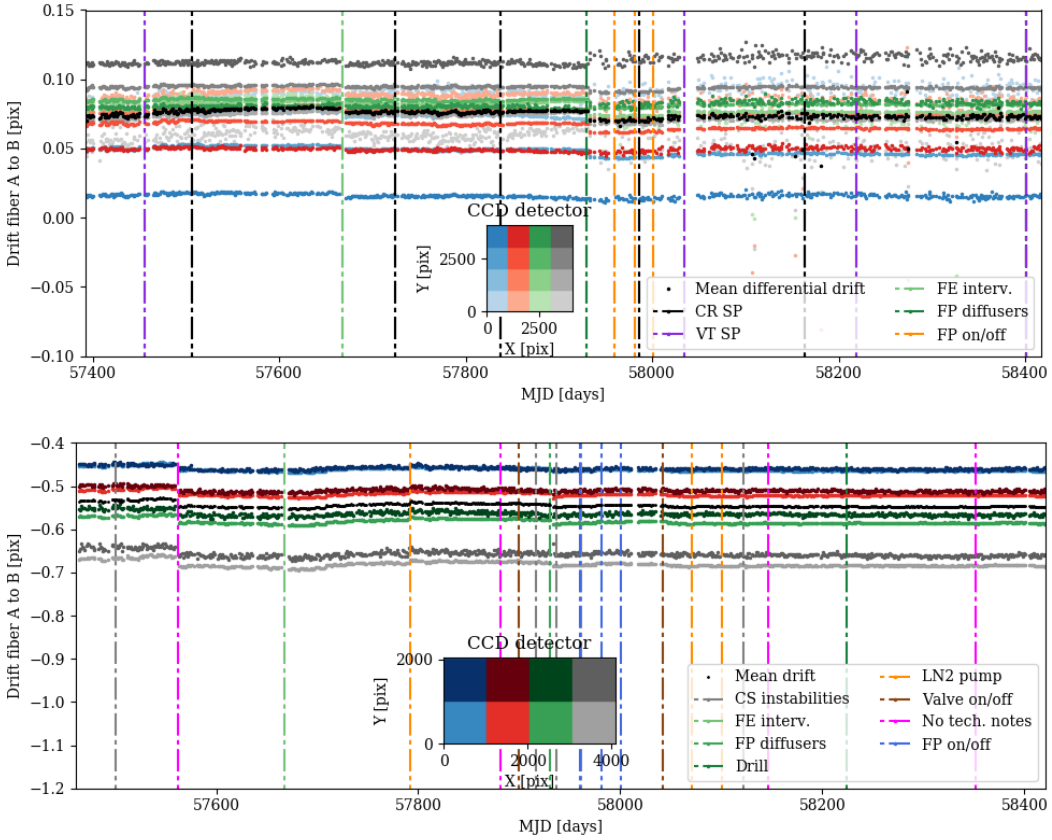

FIGURE 3.33: Differential drift between fiber A and B of the FP as a function of quadrant in the detector. *Top panel*: VIS channel. *Bottom panel*: NIR channel.

3.5.8 Predictions from RAMSES - Fiber drifts and differential drifts

One feature of RAMSES is that it incorporates the dependancy with temperature and pressure of the optical path of the wavelength features from slit to detector. While the effect on the spectral lines positions due to pressure variations is several order of mangnitudes smaller than the typical observed drift, this is not the case for the temperature variations. With the aim of trying to disentangle events in the time series of the fibers and differential drifts observed in the calibration data that could not be directly related to temperature variations, I simulate the drift in the spectral lines positions due to the measured temperature variations with RAMSES and I compare it with the observed drifts.

The time series of the fiber drifts simulated by RAMSES are calculated in the following way. In the case of the VIS channel, first I fitted RAMSES to the calibration data to the lines positions measured at MJD = 57408 d, which is immediately after the large temperature variations, and subsequent fibers drift, measured in the firsts nights of observation. As described in §3.3.3, the temperature acts through the changes in the curvatures, thicknesses and refractive indices of the optical elements, as well as through the mechanical flexures of the optical bench, simulated through the change in the separation between the optical elements due to thermal expansion.

Once I obtain a solution where the rms of the fit is about 0.5 pix, I fix the parameters of the model and set the temperature in the model to the temperature that is measured by one of the sensors inside the vacuum vessel. Using the time series data of the temperature variations in the spectrographs, I can model the time series of the fiber drifts as a function of temperature using RAMSES. While a more accurate approach would be to perform a fit on every observing night, on top of the temperature setting, it is an computationally expensive task to perform, as for each night RAMSES can take several hours to optimize the fit. If I consider that the survey has been running for more than three years now, the computation time imposes strong constraints for this calculation. Therefore, to simplify the problem I decided to fix the parameters, and only vary the temperature. Figure 3.34 and Figure 3.35 shows, in the top and central panels, the time series of the average fiber A and B drifts, shown in blue, plotted together with the predictions of the fiber A and B drifts from RAMSES, shown in red, for the VIS and NIR channel, respectively. The temperature variations are shown in black. The bottom panel shows the residuals between the drifts measured in the data and the drifts predicted by RAMSES.

I have refered the drifts and differential drifts with respect to the first date considered for this calculation, so that the drift and differential drifts are zero at the beginning of the time series shown in Figure 3.34 and Figure 3.35. This way, the measured and the model values start both at zero, making it easier to compare how the model deviates from the data as a function of time.

VIS channel

In the VIS channel, the model predictions for the fiber drifts in both fibers follow the temperature variations. However when I look the residuals, the model predictions are not fully consistent with the drifts measured in the calibration data. At the beginning of the time series the model match the data with an accuracy of about 0.05 pix until MDJ = 57552 d, where the model start to deviate from the data. Between MDJ = 57552 d and MJD = 57726 d the drifts predicted by the model are larger than the observed drifts, however after MJD = 57726 d this trend change and the model predictions become smaller than the observed drift for the rest of the survey. There is an intervention occurring at MJD = 57724 d that corresponds to a regeneration of the cryostat sorption pump. It could be that for this intervention, and most likely for all the other interventions involving the regeneration of the cryostat sorption pumps, my model underestimates the impact of the temperature variations over the spectral lines positions. However the temperature setting in my model consider the data of one temperature sensor, to keep the model rather simple. As shown in Figure 3.25, the different temperature sensors located in the spectrographs measure slightly different temperatures. So the different parts of the instrument are at different temperatures, and this is not considered in my model. On the other hand, my modeling scheme only considers temperature variations, and other type of interventions are not taken into account. This could lead to underestimations in the

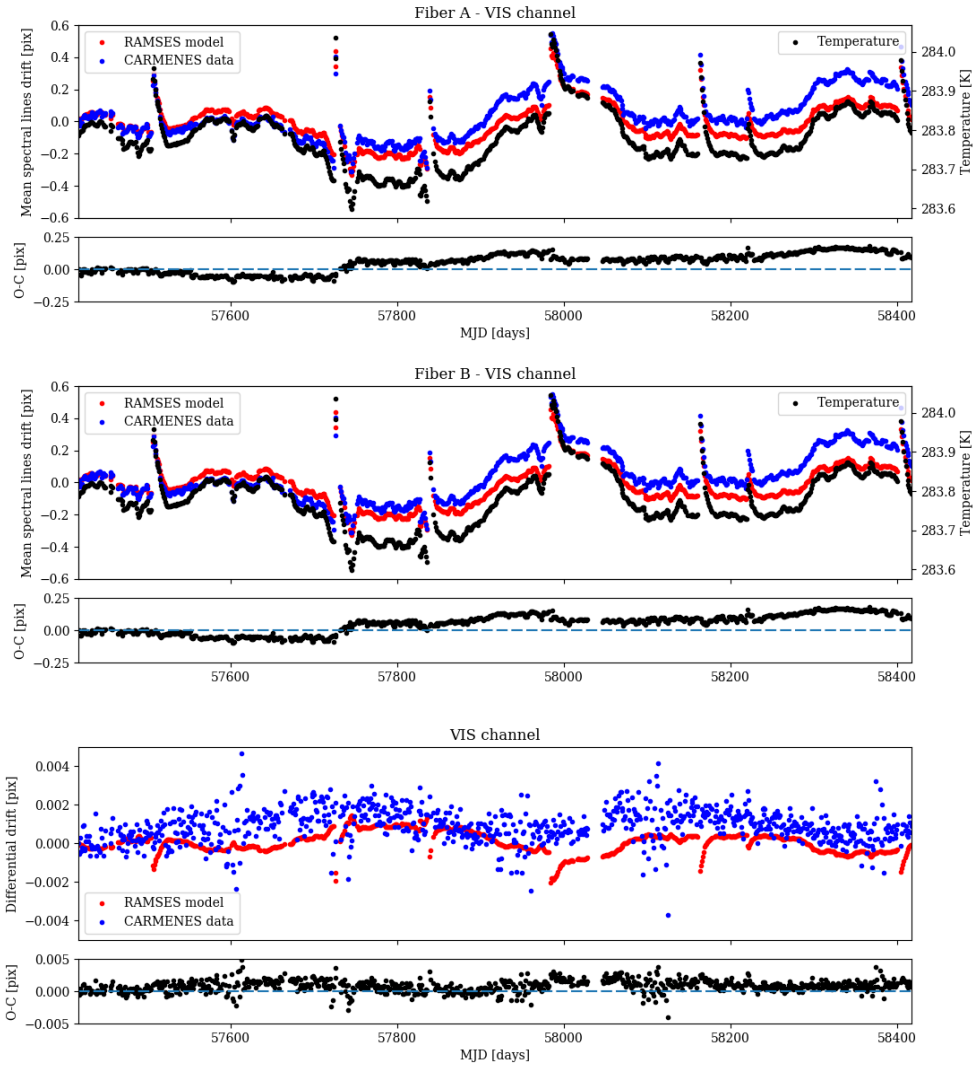

FIGURE 3.34: *Top and Middle panels*: VIS channel time series of the drifts in fibers A and B measured in the calibration data (blue) and predicted by RAMSES (red). *Bottom panel*: VIS channel time series of the differential drifts between fibers A and B measured in the calibration data (blue) and predicted by RAMSES (red).

fibers drifts that could explain the differences between the data and the model. In any case, the model reproduce the observations with an accuracy better than half a pixel, however the differences in the fiber drifts between the data and the model become larger as a function of time. When I compare the observed and modeled differential drifts in the VIS channel, the model predictions seem to follow the same trend as the data, even though they are slighly underestimated, as seen in the bottom panel in Figure 3.34.

The effect of the large temperature variations due to the regeneration of the sorption pumps is also present in the estimations for the differential drifts by RAMSES, as I several depths are observed in the time series of the differential drifts predicted by RAMSES, that coincide with the time at which these CR SP interventions occur. This mean that the temperature variations have a different impact on each fiber,

drifting the lines of the spectra of one fiber more than the other, behaviour that is not observed in the data.

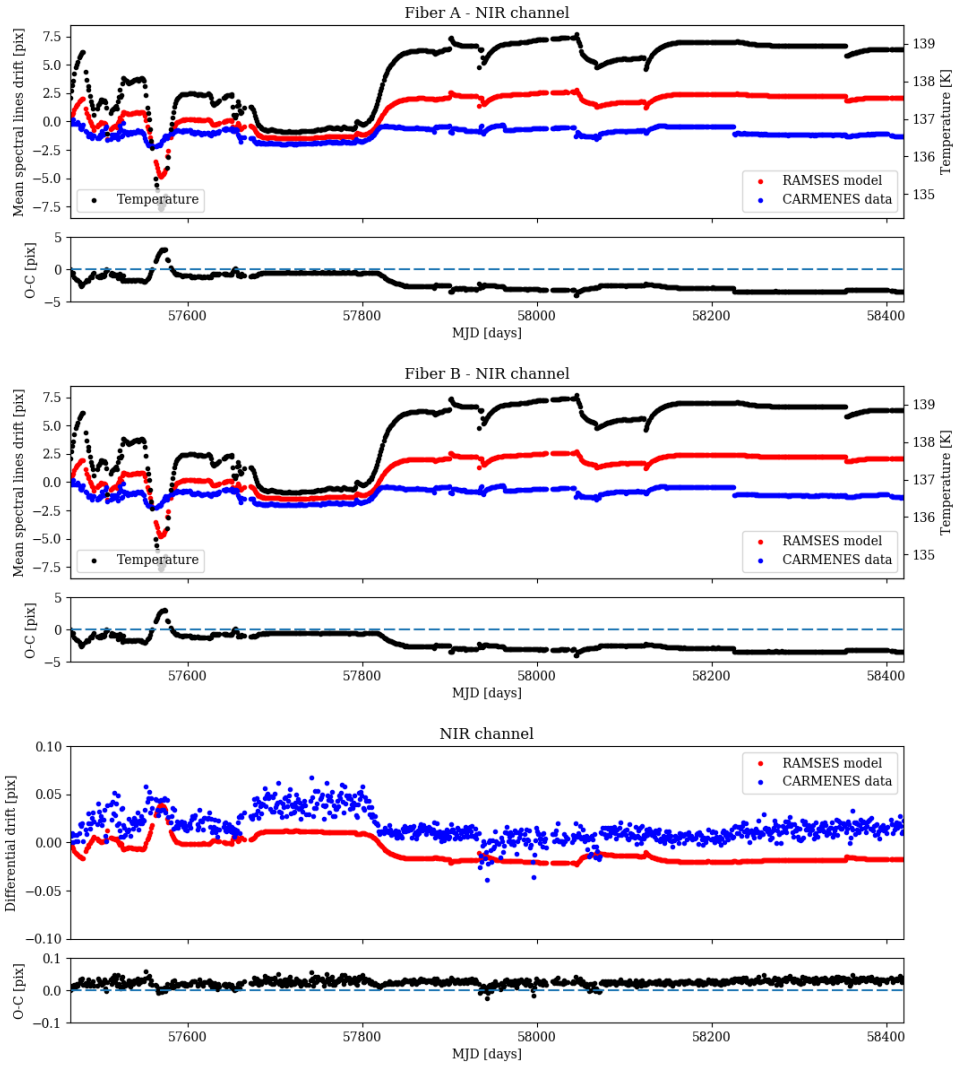

FIGURE 3.35: *Top and Middle panels*: NIR channel time series of the drifts in fibers A and B measured in the calibration data (blue) and predicted by RAMSES (red). *Bottom panel*: NIR channel time series of the differential drifts between fibers A and B measured in the calibration data (blue) and predicted by RAMSES (red).

In general, the predictions from the model are slightly smaller than what is observed. The rms of the residuals is 0.001 pix.

NIR channel

In the NIR channel, the model predictions for the fiber drifts in both fibers follow the temperature variations, as expected. However the predictions from the model differ considerably from what is observed in the data. While at the begining of the time series the residuals of the fiber drifts are in average of about 2.5 pixels, it decreases to about half a pixel between MJD = 57680 d and MJD = 57816 d, and then it start

to increase systematically with time. This behaviour is observed in the drifts of both fibers, as shown in Figure 3.35.

When I compare the observed and modeled differential drifts in the NIR channel, the model predictions seem to follow the same trend as the data, and similarly to what I observe in the VIS channel, they are slighly underestimated, as seen in the bottom panel in Figure 3.35. In general, the differential drifts predictions from the model are smaller than what is observed. The rms of the residuals is 0.027 pix.

I must stress that my model only characterize the drifts of the instruments due to temperature fluctuations spectrographs, and not the effect of external interventions in the overall instrument performance.

3.5.9 Nightly Zero Points versus the differential drifts

As discussed in §3.5.3, a number of instrumental effects and calibration issues were identified, which affect the data from the spectrographs on the m s^{-1} level. Therefore, for each night dedicated to the CARMENES Survey an instrumental nightly zero point (NZP) of the RVs is calculated as the weighted mean RV of the RV-quiet stars that were observed in that night (Tal-Or et al., 2019). Each RV measurement is corrected for its NZP and the NZP error is propagated into the measurement uncertainty. The median NZP uncertainty was found to be about 1 m s^{-1}, while their scatter is about 2.5 m s^{-1}. For the seven planetary systems investigated by Trifonov et al., 2018, it has been found that the NZP-corrected RVs improve the rms velocity dispersion around the best-fit models by about 25% on average (Quirrenbach et al., 2018).

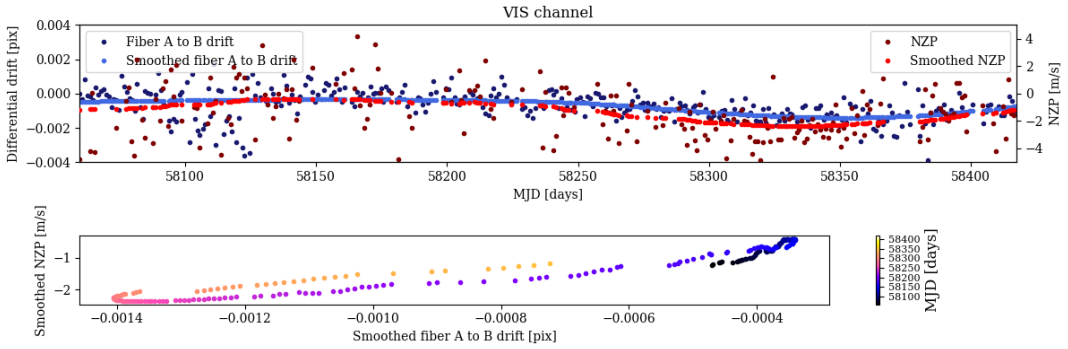

FIGURE 3.36: *Top panel*: Time series of the differential drifts in the VIS channel plotted together with the time series of the VIS NZPs. *Bottom panel*: smoothed differential drift versus the smoothed NZPs, color coded according to the MJD of each (diff. drift, NZP) pair.

The NZPs allows to identify and correct for systematic errors well below the noise level of the instrument (Tal-Or et al., 2019), however the nature of this correction is still not clear. In this section I propose a possible explanation for the nature of the NZPs, which is related to the variations of the differential drifts over time. This is motivated by the basic principle of the simultaneous calibration technique, that

consist of observing the spectra of a secondary calibration source obtained simultaeously with the stellar spectra to correct for instrumental drifts. If the nature of the NZPs is instrumental, then they could be related to the differential drift between the spectra of the two fibers, as the difference in the line positions between the two fibers sets the magnitude of the instrumental drifts.

Figure 3.36 show the time series of the average differential drifts in the VIS channel (dark blue points) plotted together with the time series of the VIS NZPs (dark red points). For this analysis I considered only the differential drifts and NZPs after the intervention in which the FP lamp was left on, as before this date there were other interventions that affected the spectra in various different ways. Just by visual inspection it looks as if the differential drifts between fiber A and B follow the same trend as the NZP, however due to the scatter of the measurements it is not so clear that the differential drift correlates with the NZPs. In order to identify possible trends in the differential drift and NZP datasets, I have applied a Savitzky–Golay filter (Savitzky and Golay, 1964). The Savitzky–Golay filter is a filter that can be applied to a set of data points for the purpose of smoothing the data to increase the precision of the data without distorting the signal tendency. This is achieved by fitting successive sub-sets of adjacent data points with a low-degree polynomial by the method of linear least squares. The smoothed differential drifts and NZPs are shown as light blue points and light red blue points in Figure 3.36, respectively. In the bottom panel in Figure 3.36 I show the smoothed differential drift versus the smoothed NZPs, color coded according to the MJD of each (diff. drift, NZP) pair. In this plot I can clearly identify a correlation between the differential drift between fibers A and B and the NZPs.

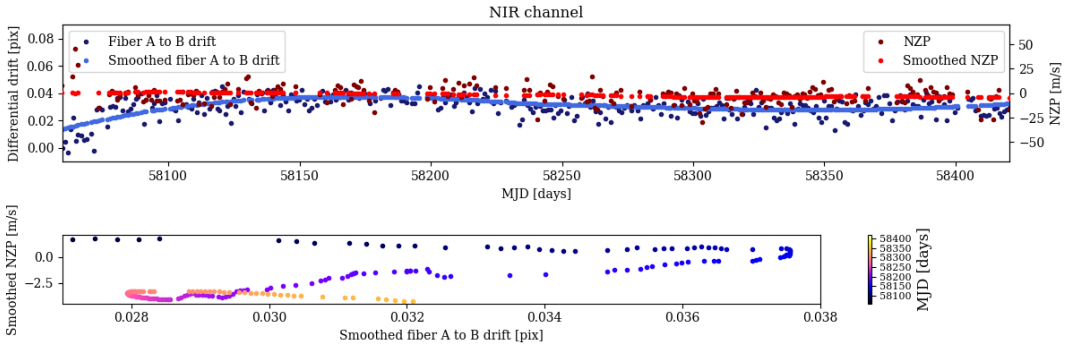

FIGURE 3.37: *Top panel*: Time series of the differential drifts in the NIR channel plotted together with the time series of the NIR NZPs. *Bottom panel*: smoothed differential drift versus the smoothed NZPs, color coded according to the MJD of each (diff. drift, NZP) pair.

Figure 3.37 show the time series of the average differential drifts in the NIR channel (dark blue points) plotted together with the time series of the NIR NZPs (dark red points). By quickly comparing the values of the NZPs and the differential drifts with respect to the VIS channel, I notice that they are, in general, one order of magnitude larger. To identify possible trends in the datasets, I applied a Savitzky–Golay

filter. The smoothed data for the differential drifts and the NZPs are shown in light blue and light red in Figure 3.37, respectively. In the bottom panel in Figure 3.37 I have plotted the smoothed differential drifts versus the smoothed NZPs, color coded according to the MJD of each (diff. drift, NZP) pair. Based on this plot, it is not so clear that the differential drifts are correlated with the NZPs, as for the black and dark blue points in the bottom panel in Figure 3.37 there seems to be no correlation. However, I do observe a correlation described by the blue-to-pink points in the correlation plot from Figure 3.37, which then seems to dissapear again (pink-to-yellow points). Therefore, in the NIR channel, it is not clear that the differential drifts are correlated with the value of the NZPs.

3.6 Discussion and Outlook

In this chapter I have presented RAMSES, a ray tracing software written in Python, that simulates the optical path of rays in a cross-dispersed fiber-fed echelle spectrograph. This modeling scheme is based on direct ray tracing of the chief ray from the spectrograph slit to the detector plane, applying exact corrections when tracing through curved surfaces. The equations that describe the path of rays through the spectrograph are derived from fundamental principles. They describe the propagation of rays through refractive and reflective surfaces, and the law of diffraction, in a 3-dimensional euclidean space. By including a model to simulate the dependance of the optical path of rays through the spectrograph optics with temperature and pressure, RAMSES can provide a detailed description of any high resolution spectrograph.

I presented the application of RAMSES to CARMENES as a case study. I modeled the VIS and NIR channel, and use these models to fit the calibration data used to build the WS. The CARMENES model has a total of 45 parameters, including the temperature and the pressure. The temperature is set to the instrument temperature at the date in which the calibration data, that is used to fit the models, was taken. To investigate the impact of the different parameters in the position of the spectral lines in the detector, I performed an error budget of RAMSES parameter space. From the results provided by the error budget, I selected the 20 parameters that have the largest impact on the spectral lines positions when fitting the models to the data.

To fit the models to the data I have explored two different approaches: Simulated Annealing and Nested Sampling. Simulated annealing is a probabilistic technique for finding the global optimum of a given function, and it is inspired in the annealing process in metals, a technique involving heating and controlled cooling of a material to increase the size of its crystals and reduce their defects. This notion of slow cooling implemented in the SA algorithm is interpreted as a slow decrease in the probability of accepting worse solutions as the solution space is explored. Accepting worse solutions is a fundamental property because it allows for a more extensive search for the global optimal solution. On the other hand, NS is a Monte Carlo technique based in Bayesian inference that aims at efficient evaluation of the Bayesian evidence, but produces posterior inferences as by-product. Both approaches provide parameters estimations, but following completely different optimization philosophies.

From the results presented in §3.4.4, SA seems to perform better than NS in terms of precision of the fit, as seen in Figure 3.20, and it can be several orders of magnitude faster than NS. However, NS seems to be more robust, as it explores the whole parameter space, evaluates the Bayesian evidence - allowing to compare different models - and provide a post-weighted distribution of the value of the parameters optimized, information that can be used to disentangle possible correlations between the different parameters. In addition, it provides uncertainties in the parameters values estimations, which is something that SA cannot supply. The main drawback is

that, in average, to fit RAMSES to the CARMENES calibration data, NS takes about 400 hours for a fit with 20 parameters, which is much longer than SA, and it does not even ensure an optimal fit. At least not under the current configuration. The main advantage is that, even if currently the SA fits are better, the post-weighted distribution of the parameter space allows to use this information to decide whether two parameters are correlated, and if so, remove one of them from the optimization routine. Decreasing the parameter space will also decrease the time of the calculations.

In order to use RAMSES to succesfully track the motion of the spectral lines of the HCL, and obtain a more detailed description of the current state of the spectrographs, it is necessary to reduce the post-fit residuals down to the 10^{-3} pix level. The best fit so far has a post-fit rms of the residuals of about half a pixel with the SA method, and about 4 pix with NS. At the moment of writing this document the SA routine is still pushing to reduce the post-fit residuals, however the improvement are very small for the computation time consumed. A deeper knowledge of the different parameters of the optimization routines should help in improving the quality of the fits, especially in NS, where a higher precision in the fits and in the parameter estimation could provide relevant information to detect bi-modalities in the parameter space.

One improvement that can be implemented in RAMSES is the inclusion of an optical aberrations correction. A real optical system does not perform ideal imaging. All rays emerging from a single object point do not converge to a single image point. The difference between the ideal image position and the real ray's intersection point on the Gaussian image plane, called the transverse aberrations, need to be established for the camera system to know the ray's output coordinates to a high accuracy. Transverse aberrations are typically modeled with the use of a series of aberration polynomia. Buchdahl, 1956 has shown that the coefficients of any order can be calculated by paraxial ray trace of two rays, a marginal ray of an on-axis object point and a chief ray from the maximum radial field point. This methodology is used to calculate the coefficients given the camera optics description and the rotationally symmetric camera optics. This is just an example of aberration coefficients that could be used to improve RAMSES and the quality of the fits.

To study how the instrument has evolved with time, I performed a characterization of the position of the spectral lines of the calibration data. By studying the Technical Reports of the CARMENES observing log, I have been able to identify some interventions to the instrument that are directly correlated with the observed drifts of the spectral lines. In the case of the VIS channel, the regeneration of the sorption pumps in the vacuum tank and in the detector cryostat generate temperature variations that are transferred to the instrument, which is observed as a drift in the spectral lines. In the case of the NIR channel, the pumping of LN2 through the pipes of the radiation shield produce drastic temperature variations that are translated into drastic fiber drifts. Other interventions have been identified, and its effect

over the fibers drifts has been, in most cases, identified. There are a couple of large offsets in the fibers drifts and differential drifts that don't have an entry in the technical report, hence, the reason for these large drifts remains unknown. In any case, it is clear that the instrument has changed its original configuration since the start of the survey, as not all the interventions are related to temperature fluctuations. Identifying the interventions, and the time in which they occurred, is of great importance, as I can use this information to fit RAMSES to the data and investigate how these interventions could have affected the instrument optical configuration.

In addition, I have studied the fibers drifts and differential drifts as a function of the position of the lines in the detector plane. In most cases there was a clear offset for the average fiber drifts measured in different quadrants in the detector, especially along the direction of the echelle dispersion. While one could tend to think that this is an effect produced by the dispersion, as lines towards one extreme of the detector seem to be more shifted than in the other extreme, this behaviour is also observed in the differential drifts. As the dispersion in both fibers comes from the same grating, I discarded the echelle dispersion as the source of this offset. A possible explanation for the observed offset is the detector orientation. If the detector is tilted, the projection of the relative positions of the fibers will be different in different zones of the detector. As I observe a small offset also for lines in different quadrants along the cross-dispersion direction, which is also observed in the differential drifts, I could combine these observations to constraint the detector position. To test if this is feasible, the next step would be to use RAMSES to study how the predicted fiber drifts and differential drifts are affected by the detector position and orientation.

With the aim of trying to disentangle events in the time series of the fibers and differential drifts observed in the calibration data, that could not be directly related to temperature variations, I have simulated the drift in the spectral lines positions due to the measured temperature variations with RAMSES and compare it with the observed drifts. In the VIS channel, the model predictions for the fiber drifts in both fibers follow the temperature variations. When I look at the differential drifts the predictions from the model are slightly smaller than what is observed with a rms of the residuals of about 0.001 pix. There is an apparent periodic trend in the time series of the differential drifts which seems to be broadly consistent with the predictions of the time series of the differential drifts from RAMSES. As in this case the only parameter of RAMSES that has changed is the temperature, a possible explanation for the apparent periodic trend in the time series is related to the temperature variations in the instrument. In the NIR channel the story is quite different. While the predictions from RAMSES follow the temperature variations, as well as the measured drifts and differential drifts, their effect is much larger than what is observed.

Finally, I investigated the possible relation between the measured differential drifts between the spectrographs fibers and the NZPs, motivated mainly by the basic principle of the simultaneous calibration technique, that consist of observing the spectra of a secondary calibration source obtained simultaeously with the stellar

spectra to correct for instrumental drifts. Whilst the data is quite noisy during the early and mid phases of the survey, the differential drifts of the VIS channel seem to show a correlation with the VIS NZPs. However, the calculation presented in this thesis is only preliminary, and further and deeper analysis is required to conclude that such correlation exists. In the NIR channel it is not possible to establish such correlation. While more data will always help to improve the quality of the calculations, I need to investigate which tools are the most adequate to perform such analysis.

The development of RAMSES is finished in its first phase, which considers the direct tracing of rays from slit to detector. The next step involve the inclusion of aberration corrections to push the post-fit rms down to the thousand of a pixel level and the improvement of the optimization routines. With the current model it is possible to study the influence of the temperature variations in the position of the spectral lines of the calibration data. This is of extreme relevance as the quality of the wavelength solution, and consequently the precision in the RVs, highly relies in the accuracy of the determination of the spectral line positions of the HCLs. The final goal for an application like RAMSES is to provide a purely physical wavelength solution that allows to calibrate echelle spectra to a sub m/s level.

Chapter 4

Giant Planets around Giants Stars

The results presented in this chapter will be published in Tala Pinto et al. (in prep). All figures presented are based on own calculations or measurements.

4.1 Introduction

Since the detection of the first exoplanet orbiting a K giant star (Frink et al., 2002), about 120 planets around G and K giant stars have been discovered. The discovery of planets orbiting giant stars allow us to probe the effects of stellar evolution on planetary systems and to test planetary formation theories in the intermediate mass regime (1–3 $M_{\odot}$). This is mainly because massive main-sequence stars have fewer spectral lines and higher rotation velocities, making it harder to measure precision radial velocities (RVs). In contrast, intermediate mass stars on the giant branch are cool and have many spectral lines and small rotation rates. Hence, evolved giant stars are ideal targets for exoplanet searches using the RV method, and many surveys have been looking for planets around these stars in the last decades (Setiawan et al., 2003; Döllinger et al., 2007; Johnson et al., 2007; Sato et al., 2008a; Niedzielski and Wolszczan, 2008; Wittenmyer et al., 2011; Jones et al., 2011; Lee et al., 2012).

However, the interpretation of precise radial velocities of G and K giant stars can be a bit ambiguous at times, as the recent examples of γ Draconis (Hatzes et al., 2018) and Aldebaran (Hatzes et al., 2015; Farr et al., 2018; Reichert et al., 2019) have shown. For both K giants the periodic radial velocity signal remained stable over many years, but later disappeared and apparently came back with a phase shift, inconsistent with the signal being due to an orbiting planet. Similarly, Delgado Mena et al., 2018 present evidence for a correlation of radial velocities with the full width at half maximum or the inverse slope of the bisector of the cross correlation function for three K giant stars in open clusters, two of which had been considered planet hosts previously (Lovis and Mayor, 2007b). These studies show that one must be extremely cautious when claiming exoplanet detections around these stars, especially for the more evolved stars with relatively large luminosities and radii, or late K spectral types.

In our Lick sample, I have identified secure planets around ten stars (Frink et al., 2002; Reffert et al., 2006; Liu et al., 2008; Sato et al., 2008a; Mitchell et al., 2013;

Trifonov et al., 2014; Wittenmyer et al., 2016; Ortiz et al., 2016; Quirrenbach et al., 2019). I found planet candidates around a number of stars, some of which display a linear trend in the RVs on top of the planet candidate periodicity, which could be indicative of sub-stellar objects in very long orbits.

TABLE 4.1: Stellar parameters.

Parameter	HD 25723	3 Cnc	44 UMa	17 Sco
Spectral Type[1]	K1 III	K3 III	K3 III	K3 III
Evol. Stage[4]	HB (77%)	HB (86%)	HB (94%)	RGB (56%)
m_V [mag][1]	5.611±0.010	5.588±0.010	5.111±0.009	5.239±0.009
$B-V$ [mag][1]	1.062±0.018	1.317±0.015	1.355±0.005	1.394±0.005
Parallax (HIP2) [mas][2]	8.48±0.37	4.11±0.51	4.99±0.33	8.62±0.35
Distance [pc][2]	$117.9^{+5.38}_{-4.9}$	$243.3^{+34.5}_{-26.9}$	$200.4^{+14.2}_{-12.4}$	$116.0^{+4.9}_{-4.5}$
m_G [mag][5]	5.2903±0.0013	5.1730±0.0022	4.6222±0.0022	4.7009±0.0037
Parallax (Gaia) [mas][3]	8.68±0.10	4.00±0.15	5.76±0.12	7.98±0.16
Luminosity [$L_\odot$][4]	$87.99^{+6.10}_{-5.57}$	$478.82^{+97.95}_{-76.70}$	$569.56^{+56.27}_{-53.70}$	$179.62^{+11.10}_{-9.55}$
Mass [$M_\odot$][4]	$2.12^{+0.41}_{-0.55}$	$2.94^{+0.36}_{-0.33}$	$2.19^{+0.10}_{-0.43}$	$1.22^{+0.13}_{-0.14}$
Radius [$R_\odot$][4]	$13.76^{+0.56}_{-0.56}$	$39.38^{+3.68}_{-3.31}$	$45.12^{+1.97}_{-2.32}$	$25.92^{+0.78}_{-0.74}$
$T_{\rm eff}$ [K][4]	4766^{+49}_{-38}	4319^{+24}_{-22}	4215^{+12}_{-13}	4157^{+11}_{-10}
Age [Gyr][2]	$0.95^{+0.59}_{-0.25}$	$0.43^{+0.22}_{-0.12}$	$1.05^{+0.50}_{-0.18}$	$5.13^{+2.12}_{-1.33}$
log g[cm/s^2][4]	$2.50^{+0.10}_{-0.07}$	$1.71^{+0.06}_{-0.06}$	$1.46^{+0.04}_{-0.06}$	$1.70^{+0.04}_{-0.06}$
[Fe/H] [dex][5]	−0.03±0.10	0.06±0.10	−0.21±0.10	−0.01±0.10
$v \sin i$ [km s^{-1}][5]	3.66±1.40	5.73±0.94	3.61±1.20	3.98±1.11
Max. Rot. Period [days]	308.2	520.2	948.4	457.1

1. HIP, Perryman et al., 1997, 2. HIP2, van Leeuwen, 2007, 3. Gaia DR2, Gaia Collaboration, 2018, 4. Stock, Reffert, and Quirrenbach, 2018, 5. Hekker and Meléndez, 2007

In this paper I present two new exoplanets and two planet candidates from the Lick sample, together with the study of the properties of the Lick sample planet population as a function of the evolutionary stage of the planet host stars.

The paper is organized as follows. In Sect. 2 I discuss our observations. In Sect. 3 I present stellar parameters of the stars under study, including the latest results from Stock, Reffert, and Quirrenbach, 2018, and in Sect. 4 I present the orbital parameters for the planetary systems. I provide a discussion of our results in Sect. 5, and compare the planet occurrence rates in the Lick and Express (Jones et al., 2011) samples as a function of stellar evolutionary stage. In Sect. 6 I summarize the results.

4.2 Observations and Stellar Parameters

The RV measurements were obtained using the Hamilton Echelle Spectrograph (Vogt, 1987) fed by the 0.6 m CAT at Lick Observatory, equipped with an I2 cell to measure precise radial velocities (Butler et al., 1996). There are 12 years of data for our full sample of K and G giant stars, of which the four stars presented here are members. The resulting RV measurements have a median precision of 6.5 m s^{-1} for HD 25723 (= HIP19011), 6.2 m s^{-1} for 3 Cnc (= HIP39177), 5.7 m s^{-1} for 44 UMa (= HIP53261)

and 5.4 m s^{-1} for 17 Sco (= HIP79540). Giant stars have larger RV jitter than main-sequence stars, on the order of 10–20 m s^{-1} or larger, depending on the individual star (Hekker et al., 2006), so better RV precision would not significantly increase the detection threshold of a planetary signal.

The main stellar parameters of the four stars discussed in this paper are listed in Table 4.1. Magnitudes and trigonometric parallax measurements are available from both Hipparcos and Gaia DR2. The Gaia values are more precise for the four stars listed here, but this is not generally true for all stars in the Lick survey (star brighter than 4.5 mag have typically more precise astrometry in Hipparcos); for consistency, the stellar parameters for the Lick sample in Stock, Reffert, and Quirrenbach, 2018 were based on the Hippparcos values.

Spectroscopic metallicities and rotational velocities were determined by Hekker and Meléndez, 2007. Stock, Reffert, and Quirrenbach, 2018 have derived masses, radii, ages, surface gravities, effective temperatures, luminosities and evolutionary stages for 372 stars of the Lick sample, by comparing spectroscopic, photometric and astrometric observables to grids of stellar evolutionary models using Bayesian inference. This methodology includes the initial mass function and evolutionary timescales of the stars as a prior. From the 372 stars in the Lick sample, 70 (19%) are more likely on the red giant brach (RGB), while the remaining 302 (81%) are probably on the horizontal branch (HB). Three of the stars presented here are on the HB - HD 25723, 3 Cnc, 44 UMa -, all with probabilities larger than 75%, while only 17 Sco is more likely (56%) on the RGB. Thus, the evolutionary stage of HD 17 Sco is relatively uncertain. For the HB stars the masses are 2.12 $M_\odot$, 2.94 $M_\odot$ and 2.19 $M_\odot$ for HD 25723, 3 Cnc and 44 UMa, respectively. If they were on the RGB instead, the masses of HD 25723 and 3 Cnc would not change considerably, while the mass of 44 UMa would be only 1.74 $M_\odot$. The mass of 17 Sco is 1.22 $M_\odot$ if on the RGB and only 0.88 $M_\odot$ if on the HB. As can be seen, 3 Cnc and 44 UMa are a bit more evolved than the other two stars, with radii of about 40 $R_\odot$ and luminosities around 500 $L_\odot$. Those are the two stars whose potential companions I label as planet candidates, partly because of the more evolved stage of their host stars as well as the increased RV jitter level that goes along with that, as explained in the next section.

4.3 Keplerian orbits and instrinsic stellar effects

I fitted Keplerian orbits to the RV data via χ^2 minimization. For each orbital solution six parameters were fitted: the orbital period P, the periastron time T_0, the longitude of the periastron ω, the orbital eccentricity e, and the semi-major axis of the stellar orbit $a_1 \; sin \; i$, plus a RV offset to which the orbits are referred to, which is not constrained by our measurements. All of the fitted parameters, with the exception of the RV offset, are included in Table 4.2. Uncertainties in the orbital parameters are based on the χ^2 fitting.

Parameter	HD 25723	3 Cnc	44 UMa	17 Sco
P [days]	456.6±1.4	853.6±4.9	785.7±4.3	578.4±1.9
T_0 [JD-2 450 000]	3122.6±37.5	3806.7±157.0	3560.3±56.9	3294.4±63.8
e	0.12±0.05	0.04±0.04	0.11±0.04	0.06±0.04
ω [deg]	116.8±0.5	275.2±1.2	135.6±0.5	57.0±0.7
K [m s^{-1}]	37.79	216.07	158.74	92.40
m sin i [M_{Jup}]	2.3	20.8	12.1	4.3
a [AU]	1.49	2.51	2.16	1.45
f(m) [$M_\odot$]	$2.495 \cdot 10^{-9}$	$8.897 \cdot 10^{-7}$	$3.193 \cdot 10^{-7}$	$4.702 \cdot 10^{-8}$
Stellar jitter [m s^{-1}]	15.70	61.81	45.08	31.29
Reduced χ^2	6.76	98.35	62.10	34.86

TABLE 4.2: Orbital parameters.

The amplitude of the expected astrometric motion due to these companions is 0.026 mas, 0.138 mas, 0.133 mas and 0.083 mas for HD 25723, 3 Cnc, 44 UMa and 17 Sco, respectively. The precision of the astrometric measurements from Hipparcos is larger than 1 mas. Hence, no meaningful constraints could be placed on either the companion mass or the orbital inclination for either planet.

4.3.1 Stellar jitter

Although giant stars show only a very small level of photometric variability during the RGB and HB evolutionary stages, I investigate here whether intrinsic stellar phenomena in combination with stellar rotation could possibly be responsible for the periodic RV variations that I observe. Hatzes, 2002 made predictions of the spot filling factors as a function of the projected rotational velocity and the amplitude of the observed RV signal. Given a spot filling factor I can predict the photometric variations due to spots, and use this information to derive constraints on the observed RV variability. To test if the observed RV signals are due to rotational modulation of surface features, I compare the observed period in the RV time series with the rotational period of the star. In addition, I looked for periodicities in Hipparcos photometric time series data and compare it with the observed RV period.

Furthermore, giants stars are known to be pulsate, displaying several radial and non-radial pulsation modes at different frequencies and with different amplitudes (Hatzes and Cochran, 1993; Bedding et al., 2011; Wood, 2015). When a star pulsates non-radially, parts of the stellar surface move towards the observer, while others move away, affecting the shape of the spectral lines and introducing a shift in the RV measurements. Hence, a pulsation frequency can produce RV variations with the same frequency. Radial pulsation periods in giant stars are usually of the order of a few hours to a few days (e.g. Hatzes and Cochran, 1995, De Ridder et al., 2006). Using the scaling relations from Kjeldsen and Bedding, 2011, I estimate the amplitude of these RV variations due to solar-like, radial pulsations. As the RV amplitudes and periods expected from solar-like oscillations are inconsistent with what I observe in the RVs, I reject radial pulsations as the source of the RV variability. In addition, I

compare the RV amplitude for stellar oscillations with the observed RV jitter in the residuals of the Keplerian fits.

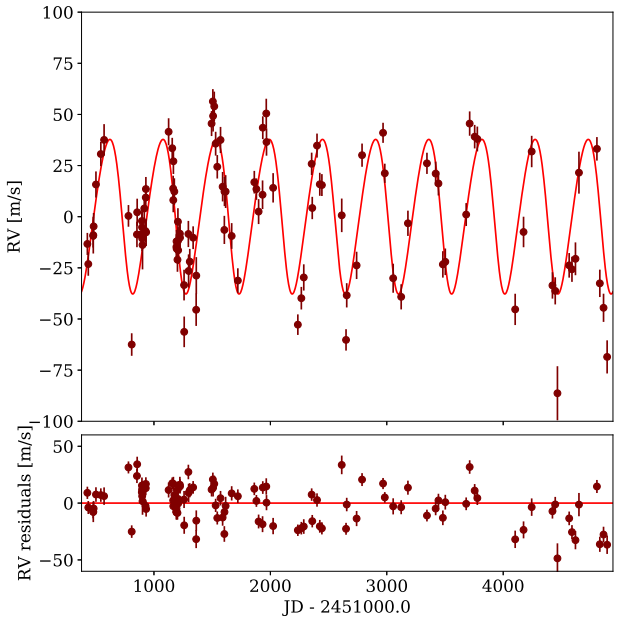

FIGURE 4.1: Radial velocity curve for HD 25723. *Top Panel*: RV data with best Keplerian fit. *Bottom Panel*: residual RV data after subtraction of best fit.

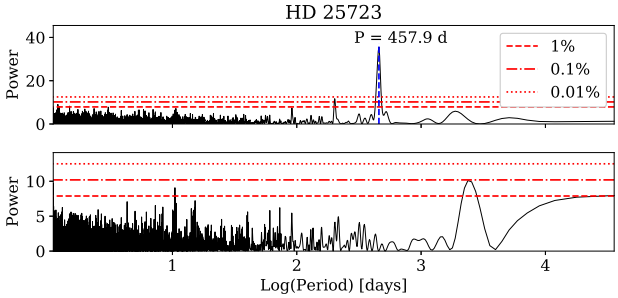

FIGURE 4.2: *Top Panel*: periodogram of the RV data for HD 25723. The second peak above the line indiacting a FAP of 0.1% is a yearly alias of the main peak. *Bottom Panel*: periodogram for the residual data after subtraction of the best fit.

4.3.2 RV analysis

HD 25723 b

The time series of the 107 RV measurements of HD 25723 is shown in Figure 4.1, along with the best Keplerian fit to the data. The RVs are listed in §C.1. The lower panel shows the residual RV data, after subtraction of the best Keplerian fit. The RV variations are clearly periodic, with a very significant peak in the periodogram

(Figure 4.2), for which the Keplerian orbit solution yields a period of about 457 days. The best-fit orbital parameters are listed in Table 4.2.

I observe a second significant peak in the periodogram of the original data, shown in Figure 4.2, at a period of about 202 days, which corresponds to the yearly alias of the 457 day peak and vanishes in the periodogram of the residuals in Figure 4.2 after the Keplerian fit has been subtracted. I observe two further peaks at 10.5 days and at 2381.2 days (6.5 years), but they are not significant at the 0.01 % false alarm probability (FAP) level, although especially the long period stands out. It could potentially become significant in an extended RV time series; the current RV data cover less than two times the period.

If one assumes that star spots are the cause for the observed RV variations, then the rotation period of the star must coincide with the period of the RV data within the errors. Based on the value of the projected rotational velocity and the stellar radius listed in Table 4.1, the rotation period can be calculated as $P = 2\pi R_*/(v \sin i)$. The maximum rotation period of the star is 308 days, and is calculated for the maximum radius that the star can have and its minimum projected rotational velocity, according to the uncertainties of both quantities. This period is not consistent with the observed 457 day period in the RV data. Furthermore, I do not observe any periodicity in the Hipparcos photometry at the orbital period predicted by the Keplerian orbit. Hence, I conclude that rotational modulation cannot be the primary source of RV variability observed in HD 25723.

The mean precision of the RV measurements is 6.5 m s^{-1}, smaller than the actual 16.7 m s^{-1} rms of the residuals. To compute the stellar jitter I have quadratically substracted the mean of the observational error to the rms of the residuals. The additional RV jitter value is 15.3 m s^{-1}, which is consistent with the 15.1 m s^{-1} amplitude of solar-like oscillations predicted with the scaling relations from Kjeldsen and Bedding, 2011.

3 Cnc b

I have measured 67 precision RVs for 3 Cnc, shown in Figure 4.3 and listed in §C.2. , along with the best Keplerian fit to the data. The lower panel shows the residual RV data, after subtraction of the best Keplerian fit.

The periodogram, shown in Figure 4.4, reveals a strong peak at 857 days. There is a secondary significant peak at 663 days, which again corresponds to a yearly alias and, as expected, is absent in the periodogram of the residuals . I observe a third peak, with less significance but still above the 0.1% false alarm probability, at a period of 4.3 days. It might be related to solar-like radial pulsations; the main pulsation period for a star with the parameters of HIP 39177 would be 1.7 days according to the scaling relations by Kjeldsen and Bedding, 2011, so a bit shorter, but in general of the same order. The Keplerian fit provides a period of ∼853 days. The best-fit orbital parameters are listed in Table 4.2. The bottom panel of Figure 4.4 shows the periodogram of the residuals, after the best-Keplerian fit subtraction. I observe

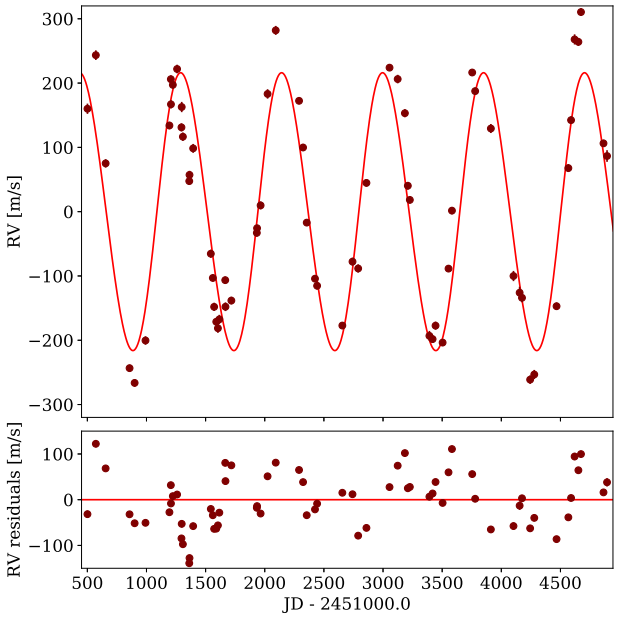

FIGURE 4.3: Radial velocity curve for 3 Cnc. *Top Panel*: RV data with best Keplerian fit. *Bottom Panel*: residual RV data after subtraction of best fit.

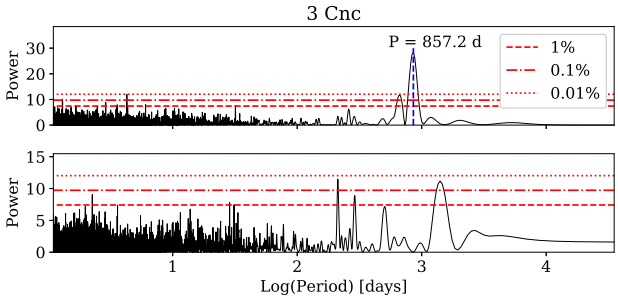

FIGURE 4.4: *Top Panel*: periodogram of the RV data for 3 Cnc. *Bottom Panel*: periodogram for the residual data after subtraction of best fit. I observe two peaks over the 0.1% FAP at periods 211 days and 1405 days.

two significant peaks above the 0.1 % FAP in the residuals periodogram, at 211 and 1405 days. The smaller period could in principle be the rotation period. Both signals in the periodogram are too weak to make any additional claims; the confirmation of a possible second companion would require a lot more RV data. In order to discard rotational modulation as the source of the primary RV variation, I compare the period of the best Keplerian fit with the rotational period of the star. Based on the projected rotational velocity and stellar radius, listed in Table 4.1, the maximum of the rotation period is 520.2 days, which is smaller than the orbital period of the planetary companion.

I examined Hipparcos photometrical data to investigate stellar photometric variability, and the amplitude of the photometrical variations is about 1.5%, which is of the same order of magnitude as the expectations from SOAP2.0. However, I do not

observe any significant photometric variations at the orbital period. Hence, I discard rotational modulation as a cause for the observed RV variability.

The mean precision of the RV measurements is 6.3 m s^{-1}, smaller than the actual 58.4 m s^{-1} rms of the post-fit residuals. The additional RV jitter is 58.1 m/s, which is broadly consistent with the 76.5 m s^{-1} amplitude of solar-like oscillations predicted from Kjeldsen and Bedding, 2011.

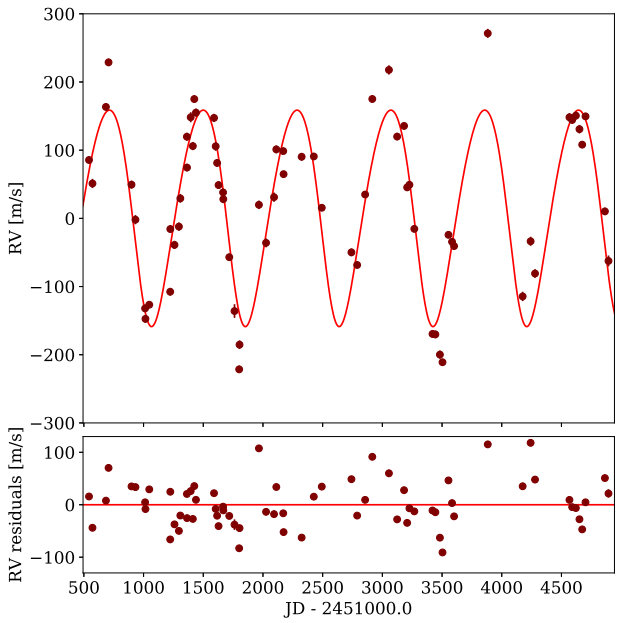

FIGURE 4.5: Radial velocity curve for 44 UMa. *Top Panel*: RV data with best Keplerian fit. *Bottom Panel*: residual RV data after subtraction of best fit.

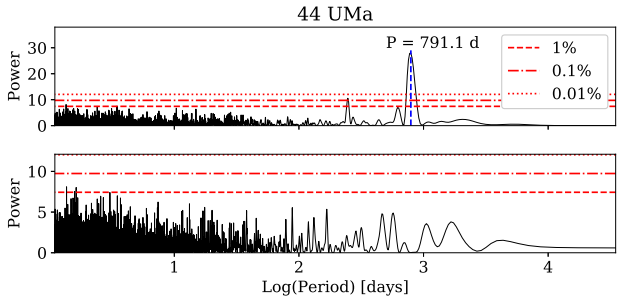

FIGURE 4.6: *Top Panel*: periodogram of the RV data for 44 UMa. *Bottom Panel*: periodogram for the residual data after subtraction of best fit.

44 UMa b

There are 68 precision RV measurements for 44 UMa. They are shown in Figure 4.5, along with the best Keplerian fit to the data. The lower panel shows the residual of the RV data, after the best-fit subtraction. There is a clear large amplitude RV signal

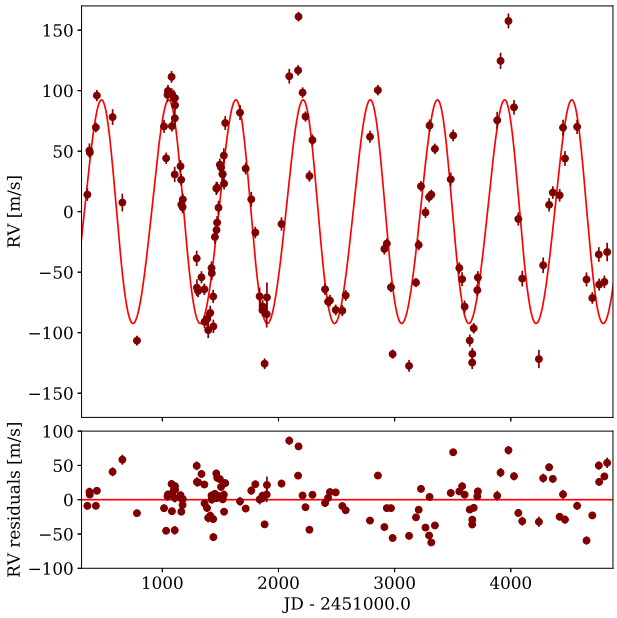

FIGURE 4.7: Radial velocity curve for 17 Sco. *Top Panel*: RV data with best Keplerian fit. *Bottom Panel*: residual RV data after subtraction of best fit.

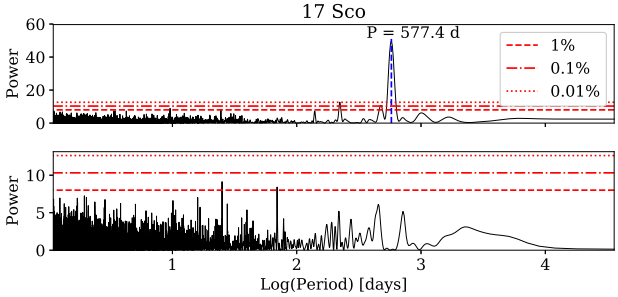

FIGURE 4.8: *Top Panel*: periodogram of the RV data for 17 Sco. *Bottom Panel*: periodogram for the residual data after subtraction of best fit.

in the data. The periodogram from Figure 4.6 reveals a strong peak at 791 days. There is a smaller, but still significant peak at around 246 days that corresponds to a yearly alias. After removing the best Keplerian fit to the data, I do not observe significant peaks in the residuals periodogram.

To test if the RV variability could arise from rotational modulation I compare the rotation period of the star with the observed RV periodicity. From the projected rotational velocity and the stellar radius, both listed in Table 4.1, I have estimated the maximum rotation period at 948.4 days. This value is larger than the orbital period of the planetary companion, but within the uncertainties the stellar rotation period it is consistent with the observed RV periodicity. In addition, I have estimated the spot filling factor and the resulting photometric variations due to the presence of spots. Based on Hatzes, 2002, given the RV amplitude and the projected rotational velocity, the spot filling factor is 6.5%. SOAP2.0 predicts photometrical variations of

5.0%, 3.1% and 2.1% for two, three and four spots, respectively, for the calculated spot filling factor. The amplitude of the Hipparcos photometric variation is about 1.7%, which is broadly consistent with the SOAP2.0 expectations. In this case, it is possible that a group of spots could explain the observed photometry, however I do not see any periodicity in the photometry at the rotation period of the star. Hence, rotational modulation cannot be the source of the observed RV variations.

The value of the stellar jitter is 43.1 m/s. This additional jitter is inconsistent with the 157.0 m s^{-1} amplitude of solar-like oscillations expected from Kjeldsen and Bedding, 2011. Currently there is no scaling relation that can satisfactorily predict the large diversity of oscillation amplitudes of the giant stars in the Lick survey and a more detailed understanding of their interiors must first be reached (Günther, 2019).

17 Sco b

I have measured 121 precision RVs for this star, shown in Figure 4.7, together with the best Keplerian fit to the data. The lower panel shows the residual of the RV data, after the best-fit subtraction. I observe a large amplitude periodic RV variability in our data. I computed a Lomb-Scargle periodogram to look for periodic signals, shown in Figure 4.8. I observe a very clear and strong peak at ∼577 days, and a second peak at ∼222 days, which corresponds to a yearly alias. After the removal of the best Keplerian fit, no prominent peaks are observed in the residuals periodogram. The full set of orbital parameters is listed in Table 4.2.

I calculated the rotational period of the star, to compare it with the observed RV periodical variability and study if the source of these variations is due to stellar rotation. Given the stellar radius and projected rotational velocity, both listed in Table 4.1, the maximum rotation period is about 457.1 days. This period is not consistent with the orbital period of the companion. The spot filling factor (Hatzes, 2002) is 3.2 %, which can produce photometric variations of 5.2%, 2.5% and 1.5% if I consider one, two and three spots, respectively (Dumusque, Boisse, and Santos, 2014). The amplitude of the photometric data is only of 1.2%, much smaller than the expected variations due to spots. Also, I could not find any period in the photometry related to the observed period in the RV time series. Hence, rotational modulation cannot be the source of the observed RV variations. The rms of the Keplerian fit is 31.3 m s^{-1}, which leads to a RV jitter of 28.95 m/s. This additional jitter is inconsistent with the 126.3 m s^{-1} amplitude of solar-like oscillations expected from Kjeldsen and Bedding, 2011. As in the case of 44 UMa, this scaling relation cannot explain the variety of oscillation periods present in our sample of giant stars, and further understanding of stellar interiors must be first reached (Günther, 2019).

4.4 Discussion

4.4.1 Sub-stellar companions

Our analysis indicates that the most probable explanation for the observed periodicity in the RV time series of the stars presented here is the presence of planetary companions. The Keplerian fits indicate that these objects have the typical characteristics of giant planets around K giant stars - massive planets with orbital periods of several hundreds of days. I examined Hipparcos photometric data and I have not found any periodicities at the RV period. I must stress, though, that the Hipparcos data were not taken simultaneously with the RV data and that the precision and cadence is not ideal to reveral low-amplitude photometric periodicity. Nevertheless, the rotational period of the stars are not consistent with the RV periodicities. Hence, it is most likely that the detected periods of several hundred days in our stars are due to planetary companions, instead of instrinsic stellar effects. All four planetary orbits are relatively circular with semi-major axes ranging from 1.5 AU to 2.5 AU, as is common in giant planets orbiting giant stars (Jones et al., 2014).

From our results, three of the substellar companions are in the giant planet regime, with minimum masses of 2.3 m_J, 12.1 m_J and 4.3 m_J for HD 25723, 44 UMa and 17 Sco, respectively. The minimum mass of the companion orbiting 3 Cnc is 20.8 m_J, so that it should be considered a brown-dwarf according to the criteria of the minimum mass required to ignite deuterium in the core. However, as the distinction between brown dwarfs and giant planets is still a matter of debate, mainly because of the contrasting theories of planet and brown dwarf formation (Chabrier et al., 2014), I will consider all of the substellar companions found in the Lick survey as giant planets, motivated by the ν Oph system where the two orbiting brown dwarfs are more likely to have formed in like planets (Quirrenbach et al., 2019).

Including the sub-stellar companion orbiting 3 Cnc, there are four planets with masses larger than 13 m_J from a total of 16 planets discovered in the Lick sample. Two of them orbit the giant stars ν Oph in an almost 6:1 resonance (Quirrenbach et al., 2019), and another one orbit the giant star τ Gem (Mitchell et al., 2013). When I look at the population of planets around giant stars, the planets with masses above 13 m_J represent 9.8 % of the overall sample. This is in strong contrast with what is observed for main-sequence stars, where the massive planets ($m_P > 13\ m_J$) frequency within 2–3 au around A-F stars is below 4% at the 1σ level (Borgniet et al., 2019). Giant planetary companions appear to be much more abundant around giants stars in the mass regime of our sample, than around Solar-type main-sequence stars, as established by Johnson et al., 2010, and other surveys have shown that giant planets are more frequent around intermediate giant stars(Döllinger et al., 2009).

The result from Quirrenbach et al., 2019 is of great importance, as it provides strong constraints on the formation process of high-mass planets around giant stars, in favor of a "planet-like" formation process in a circumstellar disk, either through

core accretion or through a disk instability, with respect to a "stellar-like" formation process through gas cloud fragmentation. These observations are supported by the theoretical predictions from Kennedy and Kenyon, 2008, so a planet formation mechanism around intermediate-mass stars is the most probable for explaining the origin of the planets presented here.

I observe a large scatter in the residuals of the RVs of 3 Cnc plus two significant peaks in the residuals periodogram over the 0.1 % FAP, which suggest that there might be additional intrinsic stellar RV variability in our measurements or a possible candidate for a secondary planetary companion in a long period orbit. Saio et al., 2015 discuss oscillatory convective modes in red giants as a possible explanation of the long secondary periods. These oscillatory convective modes are non-adiabatic g-modes present in very luminous stars, such as red giants with $\log L/L_{\odot} \gtrsim 3$. Figure 4.9 shows the period-luminosity (PL) relation of these oscillatory convective modes for two mixing length parameters (α= 1.2, 1.9). Is it worth to remark that if I extend this PL relation towards higher periods in the low luminosity regime of the oscillatory convective modes with mixing length parameter α = 1.2, the relation would pass very close to the points where many planets are located in the PL plane. In particular, this would be the case for two of the targets presented here, 3 Cnc and 44 UMa. In the case of 44 UMa the most likely explanation for the observed RV periodicity is the hypothesis of the planetary companion, and since the residuals do not show additional features at the orbital period, I discard intrinsic stellar phenomena as the source of the observed RVs.

4.4.2 Evolutionary stages

Several studies have investigated the fate of planets after they evolve off the main-sequence up the giant branch. Many of them predict that planetary systems will be subject of profound changes during the post-main sequence evolution of their host stars, due to planet engulfment as the radius of the star increases (Sato et al., 2008b) or by changes in the orbital distance due to stellar mass loss or stellar tides (Villaver et al., 2014; Kunitomo et al., 2011). In addition, by knowing the evolutionary stage, I can derive the position of the planet around the host star at the time the star was on the main sequence (Villaver et al., 2014; Currie, 2009).

Stock, Reffert, and Quirrenbach, 2018 derived probabilities for the current post-main sequence evolutionary stages for the stars in the Lick planet search sample. Based in their results, 81% of the stars in our sample are more probably on the HB, while 19% are on the RGB. From a total of 15 planetary systems detected, 13 of the host stars are on the HB, while only two host stars are more likely to be ascending the RGB. From these 15 planets, two were detected by other groups (Liu et al., 2008; Sato et al., 2007). If I define the planet occurrence rate as the number of planets divided by the number of stars of that sample, the planet occurrence rates are $5.3^{+1.6}_{-1.3}$% and $4.3^{+4.0}_{-2.3}$%, for HB and RGB stellar populations, respectively. The uncertainties in the

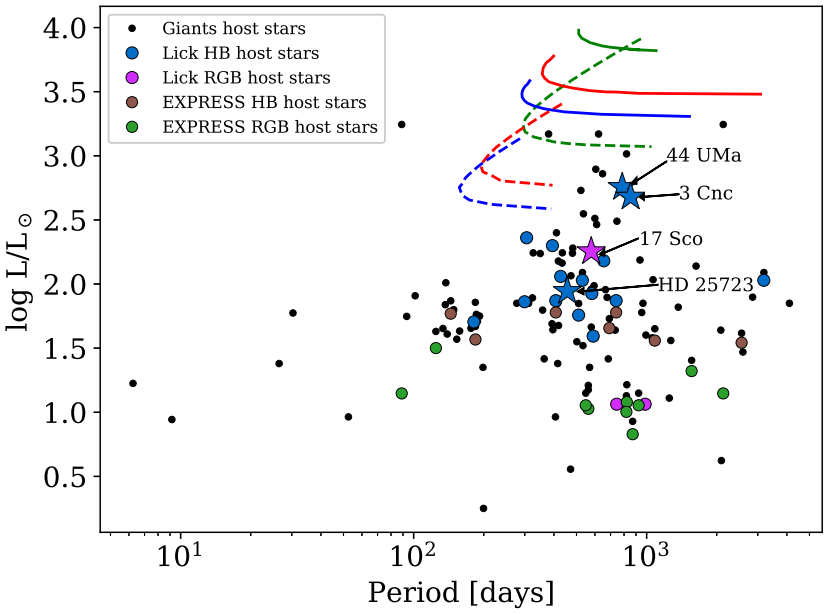

FIGURE 4.9: Period-Luminosity relations of oscillatory convective modes with mixing length parameters of 1.9 (dashed line) and 1.2 (solid line), for stars with 1 $M_{\odot}$ (blue), 1.3 $M_{\odot}$ (red) and 2.0 $M_{\odot}$ (green). The black small circles are planets around giants stars, the blue circles and pink circles are the planets found in the Lick survey, the orange and the orange stars are the targets presented in this paper.

planet occurrence rates correspond to the lower and upper confidence interval limits for a binomial distribution (Agresti and Coull, 1998).

Besides the evolutionary stage determinations by Stock, Reffert, and Quirrenbach, 2018 for the Lick survey, a survey for planets around giant stars that has published evolutionary stages for their stars is EXPRESS (Jones et al., 2011). Their estimations are based on the comparison of the position of the star in the HR diagram with evolutionary tracks using the interpolation method. From the 164 stars of the EXPRESS sample, 122 are on the RGB and 42 on the HB, representing 76% and 24% of the overall population, respectively. To compare both samples (EXPRESS and Lick) in a consistent way, I have estimated the evolutionary stages of the EXPRESS sample using the method described in Stock, Reffert, and Quirrenbach, 2018. The new estimation of the evolutionary stages of the EXPRESS sample reveals that from a total of 164 stars, 101 (62%) are ascending the RGB, while 63 (38%) are on the HB. Just as I observed in the Lick sample, some stars that were originally in the RGB changed their evolutionary stage to the HB when applying the Bayesian inference method. This behaviour, as suggested by Stock, Reffert, and Quirrenbach, 2018, might be explained by the bias towards the RGB present in the interpolation method.

In addition, I determined of the number of planets orbiting host stars from EXPRESS by cross-matching their published target list and the NASA Exoplanet Archive. I stress that it is possible that not all the planets in the Lick and EXPRESS sample have been detected already, so for the estimation of the number of planets in this

sample I only count the ones that are already published. From the total population of 14 planets, 8 host stars (57%) are on the RGB and 6 (43%) are on the HB. As a function of the evolutionary stage, the HB and RGB planet occurrence rates are $11.1^{+5.5}_{-4.0}$ % and $9.9^{+3.9}_{-3.0}$ %, respectively.

In each survey the evolutionary stages planet ocurrence rates are consistent with each other within the error bars. These results are of great relevance as they prove that there is no strong effect of stellar evolution in the planet ocurrence rates, as expected from theoretical models (Villaver et al., 2014; Kunitomo et al., 2011). As there is no influence of stellar evolution in the planet ocurrence rates, I can compute them for the complete sample. The planet occurrence rate of the Lick survey is $5.1^{+1.4o}_{-1.1}$%, while the planet ocurrence rate of the EXPRESS sample is $10.4^{+2.9}_{-2.4}$ %. I must emphasize, however, that the criteria for publishing could be different for each survey. In the case of the Lick survey I know that there are at least two secure planets plus several planet candidates within our sample of planet candidates, but I require more data and analysis to confirm them. The confirmation of the latter could increase the value of the evolutionary stages planet ocurrence rates, at the level in which they are consistent with the EXPRESS sample. In that sense, the evolutionary stages planet ocurrence rates of the Lick survey corresponds to a lower limit.

4.5 Summary/Conclusion

I report the detection of four substellar companions orbiting the K giant stars HD 25723, 3 Cnc, 44 UMa and 17 Sco, using the Hamilton Echelle Spectrograph at Lick Observatory. The companion around 3 Cnc has a minimum mass of about 21 m_J, which falls in the brown dwarf regime. The companions around HD 25723, 44 UMa and 17 Sco have minimum masses of 2.3 m_J, 12.1 m_J and 4.3 m_J, respectively, falling in the planetary regime. All four planets have almost circular orbits, and their orbital features have been stable for over 12 years. By comparing with available photometry, I consider the presence of planetary companions as the most likely explanation for the observed RV variations. In addition, I studied the planet occurrence rates as a function of the stellar evolutionary stages for two different giant planets surveys, Lick and EXPRESS. As in each survey the planet occurrence rates for HB and RGB host stars are consistent with each other, I conclude that there is no evidence of a strong effect of stellar evolution in the planet occurrence rates for stellar populations at different evolutionary stages.

Chapter 5

Conclusions

The Radial Velocity method is one of the leading techniques for the discovery and characterization of extrasolar planet. With this technique the first planet around a MS star was found, the first planet around an evolved K giant was found, and more recently Earth-like planets have been discovered orbiting M-dwarfs stars.

Cross-disperser echelle spectrographs housed in a gravity invariant and thermally and pressurized controlled enviroment provides nowadays the suitable resolving power and environment stability to push the limits ot the planetary detections down to Earth-like planets, achieving RV precisions better than 1 m s^{-1}. The development of new calibration techniques, such as Fabry-Perot etalons and Laser Frequency Combs, provide a regular and stable wavelength reference to calibrate the stellar spectra over a wide spectral range, pushing the limit of the instrumental precision to only a few cm/s.

However, the success of a PRV instrument not only relies in the characteristics of the spectrograph, as in this thesis it has been shown that the stability in the coupling of stellar light into the optical fibers that feed the spectrograph is crucial. In the case of the Waltz Spectrograph, the preliminary Front-end design I developed for the Waltz Telescope was unstable at the level that I had to adjust the position of the fiber every night, so I had to re-design the fiber feeding system to optimize its mechanical stability. In the case of CARMENES, by analyzing the time series of the line positions of the calibration data, I detected drifts in the line positions caused by changes in the illumination of the fiber that links the telescope with the spectrographs.

However, even if one provides high resolving power and controls the environment with an accuracy of only a few mK, there could be still systematics in the RVs. As an example I show that the correction of the measured RVs by the NZPs in CARMENES is crucial to detect low-amplitude signals in the time series of the RVs. While the nature of the NZPs is still unclear, I developed a physical model of the instrument that I used to fit the CARMENES HCL spectral lines positions in the detector. This model has shown that the trend observed in the time series of the differential drifts could be related to residual effects cause by the temperature variations in the instrument, providing additional information that could help to understand the nature of the NZPs.

Finally, I presented the detection of four substellar companions orbiting the K

giant stars HD 25723, 3 Cnc, 44 UMa and 17 Sco. After analyzing twelve years of RV data, the most probable explanation for the observed RV variations is the presence of planetary companions. However, one must be careful when claiming planetary companions as the interpretation of precise radial velocities of G and K giant stars can be a bit ambiguous at times. In addition, I studied the dependancy of the planet occurrence rates for two different samples of exoplanets around giant stars as a function of their evolutionary stages, concluding that there is no strong effect of stellar evolution in the planet occurrence rates. At least not when the stars evolve off the RGB to the HB. These observational are important to understand the stellar evolution influences planetary orbits and help putting constraints to the theory of planet formation and evolution.

To master the RV technique is it extremely important to understand how the hardware, the software and the actual stellar RV measurements can be intepreted to succesfully discover exoplanets orbiting other stars, an understanding that I succesfully acquired during my PhD.

Exoplanetary science with the RV method opened a new field in Modern Astronomy and with current technology it is possible to detect planets like the Earth. The next generation of echelle spectrographs will push the detection limit even further, allowing to characterize the planet atmospheres with high resolution spectra.

Appendix A

RAMSES code

The code is completely written in the programming language Python, version 3.7. One of the advantages of using Python is that there is a wide variety of libraries and tools that I use in this code to ease the computation of complex calculations. I use also some standard Python packages for the traditional mathematical operations. I hereby list the packages that are used in the code overall, leaving out of this list the packages that are used in specific modules. Those will be listed when presenting the code of the module where they correspond.

In RAMSES the position vector is defined letter H and the direction cosines by DC.

A.1 Main ray tracing modules

A.1.1 Example of refraction

Code:

```
# Position of the rays is H_out. Here I calculate the position of
# rays on a spherical surface.
H_out, n = spheric_surface.dZ(H_out, DC_out, r_sf0)

# air refractive index
n0 = refraction_index.nair_abs(l0, t, p)

# surface refractive index
n1 = refraction_index.n(l0, t, p, material_sf0)
k = n1 / n0

# incidence angle
cosi = DC_out[:, 0] * n[:, 0] + DC_out[:, 1] * n[:, 1]
       + DC_out[:, 2] * n[:, 2]
sini = np.sqrt(1 - cosi ** 2)

# refraction angle
sinr = sini / k
cosr = np.sqrt(1 - sinr ** 2)
# direction cosines after refraction
```

```
DC_out[:, 0] = DC_out[:, 0] / k + (cosr - cosi / k) * n[:, 0]
DC_out[:, 1] = DC_out[:, 1] / k + (cosr - cosi / k) * n[:, 1]
DC_out[:, 2] = DC_out[:, 2] / k + (cosr - cosi / k) * n[:, 2]
```

A.1.2 Example of reflection

Code:

```
x_p = H[:, 0]
y_p = H[:, 1]
T_x = DCs[:, 0]/DCs[:, 2]
T_y = DCs[:, 1]/DCs[:, 2]

r1 = 2*r
dz = (-(x_p*T_x + y_p*T_y - r1/2) - r1/np.abs(r1)*np.sqrt((r1/2)**2 - r1*(x_p*

# Coordinates at collimator surface
H[:, 0] = H[:, 0] + dz*T_x
H[:, 1] = H[:, 1] + dz*T_y
H[:, 2] = old_z_coor + dz

# Normal vector at collimator surface
n[:, 0] = -H[:, 0]/np.sqrt(H[:, 0]**2 + H[:, 1]**2 + r**2)
n[:, 1] = -H[:, 1]/np.sqrt(H[:, 0]**2 + H[:, 1]**2 + r**2)
n[:, 2] = r/np.sqrt(H[:, 0]**2 + H[:, 1]**2 + r**2)

# Incidence angle calculation
cosi = DCs[:, 0] * n[:, 0] + DCs[:, 1] * n[:, 1] + DCs[:, 2] * n[:, 2]

# Output ray direction
DC_out[:, 0] = DCs[:, 0] - 2 * cosi * n[:, 0]
DC_out[:, 1] = DCs[:, 1] - 2 * cosi * n[:, 1]
DC_out[:, 2] = DCs[:, 2] - 2 * cosi * n[:, 2]
```

A.1.3 Free space tracing

The script called *trace.py* contains the function $to\_next\_surface(H, DC, z\_1)$ whose parameters are the position vector H, the direction cosines DC and the position along the optical axis to which I want to trace the ray z_1.

Code:

```
def to_next_surface(H, DC, z_sf1):

    Hout = np.zeros([len(H), 3])
    z0 = copy.copy(H[:, 2])
    z1 = np.full(len(H), z_1)
    d = z1 - z0
    # coordinates in the next surface paraxial plane
```

```
    Hout[:, 0] = (H[:, 0]+((DC[:, 0]/DC[:, 2])*d))
    Hout[:, 1] = (H[:, 1]+((DC[:, 1]/DC[:, 2])*d))
    Hout[:, 2] = H[:, 2] + d
    return Hout
```

A.1.4 Slit

The script called 'slit.py' contains the function slit_params_init(H, DC, dec_x, dec_y, defocus)' that initializes the coordinates and direction of the slit. It receives as additional parameters the decentering in x and y axes and defocus along z-axis. The default initial direction is along the optical axis pointing in the positive direction, so DC=[0, 0, 1].

Code:

```
def slit_params_init(H, DC, dec_x, dec_y, defocus):

    H[:, 0] += dec_x
    H[:, 1] += dec_y
    H[:, 2] += defocus
    DC[:, 0] = 0.
    DC[:, 1] = 0.
    DC[:, 2] = 1.

    return H, DC
```

A.1.5 FN-system

A script called *fn_system.py* contains the function $tracing(H, DC, Tin, l0, t, p, fn\_data)$, that receives as an input the position of the rays in the paraxial plane of the FN-system first surface H, the direction cosines of the incoming rays DC, the orientation of the FN-system given by a vector $Tin = [\nu, \mu, \tau]$ where ν, μ and τ represent rotations around the x, y and z-axes, respectively, the temperature t, the pressure p and the array fn_data that contains the information of the properties of the optical surfaces of the FN-system. In the case of CARMENES this array contains the information listed in Tables from section 3.3.2.

Code:

```
def tracing(H, DC, Tin, l0, t, p, fn_data):

    H[:, 2] = 0

    #Orientation
    DC_out = transform.transform(DC, -Tin)
    H_out = transform.transform(H, -Tin)
    H_out[:, 0] = H_out[:, 0] - (DC_out[:, 0] / DC_out[:, 2]) * (H_out[:, 2])
    H_out[:, 1] = H_out[:, 1] - (DC_out[:, 1] / DC_out[:, 2]) * (H_out[:, 2])
```

```
H_out[:, 2] = 0.

H_plane = copy.copy(H_out)

# Lens 1
#sf0
r_sf0 = fn_data[0][1]
r_sf0 = cte.recalc(r_sf0, 'caf2', t)
material_sf0 = fn_data[0][3]

H_out, n = spheric_surface.dZ(H_out, DC_out, r_sf0)

n0 = refraction_index.nair_abs(l0, t, p)  # coming from air
n1 = refraction_index.n(l0, t, p, material_sf0)
k = n1 / n0
cosi = DC_out[:, 0] * n[:, 0] + DC_out[:, 1] * n[:, 1]
       + DC_out[:, 2] * n[:, 2]
sini = np.sqrt(1 - cosi ** 2)
sinr = sini / k
cosr = np.sqrt(1 - sinr ** 2)
DC_out[:, 0] = DC_out[:, 0] / k + (cosr - cosi / k) * n[:, 0]
DC_out[:, 1] = DC_out[:, 1] / k + (cosr - cosi / k) * n[:, 1]
DC_out[:, 2] = DC_out[:, 2] / k + (cosr - cosi / k) * n[:, 2]

# sf0 - sf1
z_l1_out = fn_data[0][2]
z_l1_out = cte.recalc(z_l1_out, 'caf2', t)

H_out = trace.to_next_surface(H_out, DC_out, z_l1_out)
H_out[:, 2] = 0

# sf 1
r_sf0 = fn_data[1][1]
r_sf0 = cte.recalc(r_sf0, 'caf2', t)
material_sf1 = fn_data[1][3]
H_out, n = spheric_surface.dZ(H_out, DC_out, r_sf0)
n0 = refraction_index.n(l0, t, p, material_sf0)
n1 = refraction_index.nair_abs(l0, t, p)  # coming from air
k = n1 / n0
cosi = DC_out[:, 0] * n[:, 0] + DC_out[:, 1] * n[:, 1] \\
       + DC_out[:, 2] * n[:, 2]
sini = np.sqrt(1 - cosi ** 2)
sinr = sini / k
cosr = np.sqrt(1 - sinr ** 2)
DC_out[:, 0] = DC_out[:, 0] / k + (cosr - cosi / k) * n[:, 0]
DC_out[:, 1] = DC_out[:, 1] / k + (cosr - cosi / k) * n[:, 1]
DC_out[:, 2] = DC_out[:, 2] / k + (cosr - cosi / k) * n[:, 2]
```

```
# End lens 1

# Lens 1 - lens 2
z_l1_l2 = fn_data[1][2]
z_l1_l2 = cte.recalc(z_l1_l2, 'alum5083', t)
H_out = trace.to_next_surface(H_out, DC_out, z_l1_l2)
H_out[:, 2] = 0.

# Lens 2
r_sf0 = fn_data[2][1]
r_sf0 = cte.recalc(r_sf0, 'sftm16', t)
material_sf0 = fn_data[2][3]
H_out, n = spheric_surface.dZ(H_out, DC_out, r_sf0)

# sf0
n0 = refraction_index.nair_abs(l0, t, p)  # coming from air
n1 = refraction_index.n(l0, t, p, material_sf0)
k = n1 / n0
cosi = DC_out[:, 0] * n[:, 0] + DC_out[:, 1] * n[:, 1]
       + DC_out[:, 2] * n[:, 2]
sini = np.sqrt(1 - cosi ** 2)
sinr = sini / k
cosr = np.sqrt(1 - sinr ** 2)
DC_out[:, 0] = DC_out[:, 0] / k + (cosr - cosi / k) * n[:, 0]
DC_out[:, 1] = DC_out[:, 1] / k + (cosr - cosi / k) * n[:, 1]
DC_out[:, 2] = DC_out[:, 2] / k + (cosr - cosi / k) * n[:, 2]

# sf 0 - sf 1
z_l2 = fn_data[2][2]
z_l2 = cte.recalc(z_l2, 'sftm16', t)
H_out = trace.to_next_surface(H_out, DC_out, z_l2)
H_out[:, 2] = 0

# sf1
r_sf1 = fn_data[3][1]
r_sf1 = cte.recalc(r_sf1, 'sftm16', t)
material_sf1 = fn_data[3][3]
H_out, n = spheric_surface.dZ(H_out, DC_out, r_sf1)
n0 = refraction_index.n(l0, t, p, material_sf0)
n1 = refraction_index.nair_abs(l0, t, p)
k = n1 / n0
cosi = DC_out[:, 0] * n[:, 0] + DC_out[:, 1] * n[:, 1]
       + DC_out[:, 2] * n[:, 2]
sini = np.sqrt(1 - cosi ** 2)
sinr = sini / k
cosr = np.sqrt(1 - sinr ** 2)
DC_out[:, 0] = DC_out[:, 0] / k + (cosr - cosi / k) * n[:, 0]
DC_out[:, 1] = DC_out[:, 1] / k + (cosr - cosi / k) * n[:, 1]
```

```
DC_out[:, 2] = DC_out[:, 2] / k + (cosr - cosi / k) * n[:, 2]

# End lens 2

# Lens 2 - Lens 3
z_l2_l3 = fn_data[3][2]
z_l2_l3 = cte.recalc(z_l2_l3, 'alum5083', t)
H_out = trace.to_next_surface(H_out, DC_out, z_l2_l3)
H_out[:, 2] = 0

# Lens 3
# sf0
r_sf0 = fn_data[4][1]
r_sf0 = cte.recalc(r_sf0, 'caf2', t)
material_sf0 = fn_data[4][3]
H_out, n = spheric_surface.dZ(H_out, DC_out, r_sf0)

n0 = refraction_index.nair_abs(l0, t, p)  # coming from air
n1 = refraction_index.n(l0, t, p, material_sf0)

k = n1 / n0
cosi = DC_out[:, 0] * n[:, 0] + DC_out[:, 1] * n[:, 1]
     + DC_out[:, 2] * n[:, 2]
sini = np.sqrt(1 - cosi ** 2)
sinr = sini / k
cosr = np.sqrt(1 - sinr ** 2)
DC_out[:, 0] = DC_out[:, 0] / k + (cosr - cosi / k) * n[:, 0]
DC_out[:, 1] = DC_out[:, 1] / k + (cosr - cosi / k) * n[:, 1]
DC_out[:, 2] = DC_out[:, 2] / k + (cosr - cosi / k) * n[:, 2]

# sf0 - sf1
z_l3_sf0_sf1 = fn_data[4][2]
z_l3_sf0_sf1 = cte.recalc(z_l3_sf0_sf1, 'caf2', t)

H_out = trace.to_next_surface(H_out, DC_out, z_l3_sf0_sf1)
H_out[:, 2] = 0.

# sf1
r_sf1 =fn_data[5][1]
r_sf1 = cte.recalc(r_sf1, 'caf2', t)
material_sf1 = fn_data[5][3]
H_out, n = spheric_surface.dZ(H_out, DC_out, r_sf1)

n0 = refraction_index.n(l0, t, p, material_sf0)
n1 = refraction_index.nair_abs(l0, t, p)  # coming from air
k = n1 / n0
cosi = DC_out[:, 0] * n[:, 0] + DC_out[:, 1] * n[:, 1]
       + DC_out[:, 2] * n[:, 2]
```

```
    sini = np.sqrt(1 - cosi ** 2)
    sinr = sini / k
    cosr = np.sqrt(1 - sinr ** 2)
    DC_out[:, 0] = DC_out[:, 0] / k + (cosr - cosi / k) * n[:, 0]
    DC_out[:, 1] = DC_out[:, 1] / k + (cosr - cosi / k) * n[:, 1]
    DC_out[:, 2] = DC_out[:, 2] / k + (cosr - cosi / k) * n[:, 2]

    # End lens 3

    # we propagate to focal plane
    z_fn_ff = fn_data[5][2] + 26.
    z_fn_ff = cte.recalc(z_fn_ff, 'alum5083', t)
    H_out = trace.to_next_surface(H_out, DC_out, z_fn_ff)
    H_out[:, 2] = 0.
    return H_out, DC_out
```

A.1.6 Echelle dispersion

The script called *echelle.py* contains the function $diffraction(H, DC, T, m, l, G)$ that receives as a parameter the position (H) and direction (DC) of rays, a vector $T = [\alpha, \beta, \gamma]$, that defines the orientation of the grating where α, β and γ correspond to rotations around the x, y and z axes, respectively, the spectral order m, the wavelength l in μm and the grating constant G.

Code:

```
def diffraction(H, DC, T, m, l, G):

    DC_out = np.zeros([len(DC), 3])
    Hout = np.zeros([len(DC), 3])
    DC = transform.transform(DC, -T)
    H = transform.transform(H, -T)
    Hout[:, 0] = H[:, 0] - (DC[:, 0] / DC[:, 2]) * (H[:, 2])
    Hout[:, 1] = H[:, 1] - (DC[:, 1] / DC[:, 2]) * (H[:, 2])
    Hout[:, 2] = 0.

    if DC[0][1] == 0:
        signy = np.full(len(DC), 1)
    else:
        signy = (DC[:, 1]/np.abs(DC[:, 1]))

    signz = (DC[:, 2]/np.abs(DC[:, 2]))
    DC_out[:, 0] = DC[:, 0]
    DC_out[:, 1] = signy*(m*l*G - np.abs(DC[:, 1]))
    DC_out[:, 2] = signz*(np.sqrt(1 - DC_out[:, 0]**2 - DC_out[:, 1]**2))

    DC_out[:, 2] = - DC_out[:, 2] # Reflection at the grating plane
    DC_out_final = transform.transform2(DC_out, T)
```

```
    Hout = transform.transform2(Hout, T)
    Hout[:, 0]=Hout[:, 0]-(DC_out_final[:, 0]/DC_out_final[:, 2])*(Hout[:, 2])
    Hout[:, 1]=Hout[:, 1]-(DC_out_final[:, 1]/DC_out_final[:, 2])*(Hout[:, 2])
    Hout[:, 2]=0.

    return Hout, DC_out_final
```

A.1.7 Flat mirror

The following code performs reflection in a flat mirror. It receives as an input the position H and direction DC of the rays, and a vector T that defines the orientation of the mirror.

Code:

```
def flat_out(H, DC, T):

    DC_out = np.zeros([len(DC), 3])
    H_out = np.zeros([len(DC), 3])

    DC = transform.transform(DC, -T)
    H_out = transform.transform(H, -T)
    H_out[:, 0] = H[:, 0] - (DC[:, 0] / DC[:, 2]) * (H[:, 2])
    H_out[:, 1] = H[:, 1] - (DC[:, 1] / DC[:, 2]) * (H[:, 2])
    H_out[:, 2] = 0.

    # mirror default normal
    n0 = np.zeros([len(DC), 3])
    n0[:, 2] = 1
    n = transform.transform(n0, T)

    cosi = DC[:, 0] * n[:, 0] + DC[:, 1] * n[:, 1] + DC[:, 2] * n[:, 2]

    DC_out[:, 0] = DC[:, 0] - 2 * cosi * n[:, 0]
    DC_out[:, 1] = DC[:, 1] - 2 * cosi * n[:, 1]
    DC_out[:, 2] = DC[:, 2] - 2 * cosi * n[:, 2]

    DC_out = transform.transform2(DC_out, T)
    H_out = transform.transform2(H_out, T)
    H_out[:, 0]=H[:, 0]-(DC_out[:, 0]/DC_out[:, 2])*(H_out[:, 2])
    H_out[:, 2]=0.

    return H_out, DC_out
```

A.1.8 Grism

The following code performs ray tracing through a grism. The script called *grism.py* contains the function *def dispersion(H, DC, Tin, l0, material, apex, GD, t, p, dec_x, dec_y)*

that receives as a parameter the rays positions H, the rays directions DC, a vector Tin that defines the orientation of the grism, the $apex$ angle, the grating constant GD, the temperature t, the pressure p and the decentering along x and y axes dec_x and dec_y, respectively.

Code:

```
def dispersion(H, DC, Tin, l0, material, apex, GD, t, p, dec_x, dec_y):

    DC_out = np.zeros([len(DC), 3])
    H_out = np.zeros([len(H), 3])

    # Coordinate break 0
    # Decenter
    H[:, 0] = H[:, 0] + dec_x
    H[:, 1] = H[:, 1] + dec_y
    #Tilt
    DC = transform.transform(DC, -Tin)
    H = transform.transform(H, -Tin)
    H_out[:, 0] = H[:, 0] - (DC[:, 0] / DC[:, 2]) * (H[:, 2])
    H_out[:, 1] = H[:, 1] - (DC[:, 1] / DC[:, 2]) * (H[:, 2])
    H_out[:, 2] = 0.
    # End coordinate break 0

    # Grism input surface
    tilt_y_sf_in = 6.
    T_sf_in = np.array([0, tilt_y_sf_in*np.pi/180, 0])
    DC = transform.transform(DC, -T_sf_in)

    H_out = transform.transform(H_out, -T_sf_in)
    H_out[:, 0] = H_out[:, 0] - (DC[:, 0] / DC[:, 2]) * (H_out[:, 2])
    H_out[:, 1] = H_out[:, 1] - (DC[:, 1] / DC[:, 2]) * (H_out[:, 2])
    H_out[:, 2] = 0.

    # Refractive indices
    n0 = refraction_index.nair_abs(l0, t, p)
    n1 = refraction_index.n(l0, t, p, material)
    n2 = refraction_index.nair_abs(l0, t, p)  # output in air

    # surface default normal
    n = np.zeros([len(DC), 3])
    n[:, 2] = -1.

    k = n1/n0
    cosi = DC[:, 0]*n[:, 0] + DC[:, 1]*n[:, 1] + DC[:, 2]*n[:, 2]
    sini = np.sqrt(1 - cosi**2)
    sinr = sini/k
    cosr = np.sqrt(1 - sinr**2)
```

```
DC_out[:, 0] = DC[:, 0] / k + (cosr - cosi / k) * n[:, 0]
DC_out[:, 1] = DC[:, 1] / k + (cosr - cosi / k) * n[:, 1]
DC_out[:, 2] = DC[:, 2] / k + (cosr - cosi / k) * n[:, 2]
# End grism first surface, alles gut bei hier

DC_out = transform.transform2(DC_out, T_sf_in)
H_out = transform.transform2(H_out, T_sf_in)
H_out[:, 0] = H_out[:, 0] - (DC_out[:, 0] / DC_out[:, 2]) * (H_out[:, 2])
H_out[:, 1] = H_out[:, 1] - (DC_out[:, 1] / DC_out[:, 2]) * (H_out[:, 2])
H_out[:, 2] = 0.


# Trace to next surface
d_trf_col = np.full(len(H), -40.)
H_out = trace.to_next_surface(H_out, DC_out, d_trf_col)
H_out[:, 2] = 0.

# Coordinate break 1
T_sf_out = np.array([0, -(apex - 6)*np.pi/180, 0])
DC_out = transform.transform(DC_out, -T_sf_out)

H_out = transform.transform(H_out, -T_sf_out)
H_out[:, 0] = H_out[:, 0] - (DC_out[:, 0] / DC_out[:, 2]) * (H_out[:, 2])
H_out[:, 1] = H_out[:, 1] - (DC_out[:, 1] / DC_out[:, 2]) * (H_out[:, 2])
H_out[:, 2] = 0.

# End coordinate break 1

# Grism output surface
# Snell law at aperture surface
k = n2 / n1
cosi = DC_out[:, 0] * n[:, 0] + DC_out[:, 1] * n[:, 1]
       + DC_out[:, 2] * n[:, 2]
sini = np.sqrt(1 - cosi ** 2)
sinr = sini / k
cosr = np.sqrt(1 - sinr ** 2)

DC_out[:, 0] = DC_out[:, 0] / k + (cosr - cosi / k) * n[:, 0]
DC_out[:, 1] = DC_out[:, 1] / k + (cosr - cosi / k) * n[:, 1]
DC_out[:, 2] = DC_out[:, 2] / k + (cosr - cosi / k) * n[:, 2]
# End of Snell law at aperture, alles gut

# Coordinate break 2
T_sf_out_grating = np.array([0, 0, 90*np.pi/180])
DC_out = transform.transform(DC_out, -T_sf_out_grating)
H_out = transform.transform(H_out, -T_sf_out_grating)
# End of coordinate break 2, alles gut
```

```
    # Diffraction grating
    signz = (DC[:, 2] / np.abs(DC[:, 2]))

    m = 1
    DC_out[:, 0] = DC_out[:, 0]
    DC_out[:, 1] = (m * l0 * GD + DC_out[:, 1])
    DC_out[:, 2] = signz * (np.sqrt(1 - DC_out[:, 0] ** 2 - DC_out[:, 1] ** 2))
    # End diffraction

    # Coordinate break 3
    DC_out = transform.transform(DC_out, T_sf_out_grating)
    DC_out = transform.transform(DC_out, T_sf_out)
    DC_out[:, 2]=signz*(np.sqrt(1 - DC_out[:, 0] ** 2 - DC_out[:, 1] ** 2))
    H_out = transform.transform(H_out, T_sf_out_grating)
    H_out = transform.transform(H_out, T_sf_out)
    H_out[:, 0] = H_out[:, 0] - (DC_out[:, 0] / DC_out[:, 2]) * (H_out[:, 2])
    H_out[:, 1] = H_out[:, 1] - (DC_out[:, 1] / DC_out[:, 2]) * (H_out[:, 2])
    H_out[:, 2] = 0.
    # End grism

    return H_out, DC_out
```

A.1.9 CCD detector

The script *CCD_vis.py* contains the function *mm2pix(ws)* that receives as an input an array that contains the information of a set of spectral feature (spectral order, wavelength, position and directions), and transform their positions from the physical space in *mm* to the detector space in *pix*.

Code:

```
def mm2pix(ws):
    pix_size_arr = np.full(len(ws), 15.e-3)
    detector_size_x = 4250.
    detector_size_y = 4200.
    ws[:, 2] = -ws[:, 2]
    ws[:, 3] = ws[:, 3] / pix_size_arr + detector_size_x / 2
    ws[:, 2] = ws[:, 2] / pix_size_arr + detector_size_y / 2
    return ws
```

Appendix B

Error budget of RAMSES parameters

This appendix contains the tables that summarize the results of the RAMSES parameters error budget.

B.1 Error budget based in temperature fluctuations

Tables B.1 and B.2 summarize the results of the error budget due to temperature fluctuations for the VIS and NIR channel, respetively. ΔParameters refers to the amount that each parameter is affected by a change in the temperature of 0.3°K, Δx is the rms of the change in the spectral lines positions along the echelle dispersion axis, and Δy is the rms of the change in the spectral lines positions along the cross-dispersion axis. The parameters are sorted in descending order, based on its effect over the spectral line positions along the echelle dispersion axis. I have highlighted with colors the parameters that affect the position of the spectral lines in the detector plane by more than 10^{-4}.

B.2 Error budget based in uniform variations - VIS

Tables B.3 and B.4 summarize the results of the error budget due to uniform variations in the parameters space for the VIS and NIR channels, respetively. ΔParameters refers to the amount that each parameter is affected, Δx is the rms of the change in the spectral lines positions along the echelle dispersion axis, and Δy is the rms of the change in the spectral lines positions along the cross-dispersion axis. The parameters are sorted in descending order, based on its effect over the spectral line positions along the echelle dispersion axis. I have highlighted with colors the parameters that affect the position of the spectral lines in the detector plane by more than 10^{-1}.

VIS			
Parameter	ΔParameter	Δx [pix]	Δy [pix]
ccd_tilt_z	6.09E-06	5.41E+01	5.66E+01
coll_tilt_x	6.09E-06	1.36E-01	2.38E-02
ech_blaze	-4.62E-04	1.17E-01	1.73E-02
coll_tilt_y	6.09E-06	2.22E-02	1.69E-02
ccd_ff_tilt_z	6.09E-06	1.63E-02	9.37E-03
trf_mirror_tilt_y	6.09E-06	6.06E-03	7.62E-03
d_cam_ff	-9.62E-04	3.39E-03	5.36E-03
cam_tilt_x	6.09E-06	2.76E-03	4.03E-03
grm_tilt_x	6.09E-06	2.60E-03	3.76E-03
ccd_defocus	6.09E-06	1.42E-03	2.09E-03
cam_tilt_y	6.09E-06	9.93E-04	1.94E-03
trf_mirror_tilt_x	6.09E-06	8.15E-04	1.78E-03
d_slit_col	9.72E-03	8.04E-04	1.57E-03
ccd_ff_tilt_x	6.09E-06	7.05E-04	1.44E-03
d_col_trf	-9.72E-03	6.14E-04	1.41E-03
ech_z	6.09E-06	5.44E-04	1.10E-03
ccd_ff_tilt_y	6.09E-06	4.41E-04	1.09E-03
ech_G	9.57E-08	3.61E-04	5.54E-04
ccd_ff_dec_y	6.09E-06	3.33E-04	3.75E-04
ech_gamma	7.31E-06	2.78E-04	3.66E-04
ccd_ff_dec_x	6.09E-06	2.73E-04	3.10E-04
grm_G	6.09E-04	2.06E-04	2.47E-04
d_ff_ccd	-3.05E-05	1.68E-04	1.57E-04
grm_apex	4.86E-05	1.29E-04	1.08E-04
grm_tilt_y	1.46E-05	5.87E-05	1.01E-04
grism_dec_y	6.09E-06	3.03E-05	3.90E-05
cam_dec_y	6.09E-06	2.94E-05	3.16E-05
grism_dec_x	1.44E-03	2.83E-05	2.29E-05
d_grm_cam	-3.05E-04	2.01E-05	6.23E-06
cam_dec_x	6.09E-06	6.45E-06	6.15E-06
slit_tilt_y	-2.58E-08	4.18E-06	4.01E-06
slit_dec_y_a	3.03E-09	2.66E-06	2.88E-06
slit_tilt_x	3.03E-09	1.44E-06	1.84E-06
slit_dec_x_a	-5.30E-10	9.52E-07	1.12E-06
ccd_tilt_x	6.09E-06	1.08E-07	3.87E-08
ccd_tilt_y	6.09E-06	1.75E-09	3.01E-09
slit_tilt_z	-2.73E-08	1.30E-09	2.97E-09
d_col_grm	6.09E-06	2.27E-12	9.09E-13
ccd_dec_y	2.56E-05	1.36E-12	4.55E-13
ccd_dec_x	6.09E-06	9.09E-13	0.00E+00

TABLE B.1: Error budget of RAMSES parameters and its effect on the spectral line positions along the detector. ΔParameters refers to the amount that each parameter is affected by a change in the temperature of 0.3°K, Δx is the rms of the change in the spectral lines positions along the echelle dispersion axis, and Δy is the rms of the change in the spectral lines positions along the cross-dispersion axis.

NIR			
Parameter	ΔParameter	Δx [pix]	Δy [pix]
coll_tilt_x	6.09E-06	4.11E+00	2.58E+00
ccd_tilt_z	6.09E-06	7.97E-01	4.33E-01
coll_tilt_y	6.09E-06	7.87E-01	4.05E-01
trf_mirror_tilt_x	6.09E-06	4.10E-01	3.41E-01
ech_blaze	-4.58E-04	3.43E-01	2.12E-01
trf_mirror_tilt_y	6.09E-06	1.66E-01	1.26E-01
grm_tilt_x	6.09E-06	1.06E-01	6.50E-02
cam_tilt_x	6.09E-06	9.62E-02	4.05E-02
ech_z	6.09E-06	4.57E-02	3.67E-02
d_slit_col	9.53E-03	1.97E-02	1.53E-02
cam_tilt_y	6.09E-06	1.44E-02	3.61E-03
grism_dec_y	6.09E-06	7.99E-03	2.44E-03
cam_dec_y	6.09E-06	7.98E-03	1.63E-03
ccd_ff_dec_y	6.09E-06	7.22E-03	1.54E-03
d_cam_ff	-1.25E-03	2.10E-03	1.42E-03
ccd_ff_dec_x	6.09E-06	1.70E-03	1.20E-03
cam_dec_x	6.09E-06	1.17E-03	1.20E-03
ech_G	9.57E-08	1.05E-03	7.86E-04
ech_gamma	7.31E-06	9.10E-04	2.25E-04
gap	1.34E-05	7.45E-04	1.79E-04
grism_dec_x	1.41E-03	5.98E-04	1.70E-04
d_ff_ccd	-6.09E-05	5.55E-04	1.51E-04
d_grm_cam	-3.05E-04	2.49E-04	1.18E-04
ccd_ff_tilt_z	6.09E-06	2.43E-04	1.06E-04
grm_tilt_y	1.46E-05	7.26E-05	5.93E-05
ccd_ff_tilt_x	6.09E-06	3.39E-05	1.63E-05
ccd_ff_tilt_y	6.09E-06	4.81E-06	1.53E-05
grm_G	5.52E-06	2.25E-06	1.25E-05
grm_apex	-9.38E-07	2.07E-06	5.28E-07
slit_dec_y_a	3.03E-09	6.07E-07	9.16E-08
slit_tilt_y	-2.58E-08	4.21E-07	3.01E-08
slit_tilt_x	3.03E-09	1.60E-07	2.44E-08
slit_dec_x_a	-5.30E-10	2.84E-08	5.18E-09
slit_tilt_z	-2.58E-08	1.57E-08	2.79E-09
ccd_tilt_x	6.09E-06	4.18E-11	1.82E-12
ccd_tilt_y	6.09E-06	2.64E-11	6.82E-13
d_col_grm	6.09E-06	5.46E-12	0.00E+00
ccd_dec_y	2.56E-05	9.09E-13	0.00E+00

TABLE B.2: Error budget of RAMSES parameters and its effect on the spectral line positions along the detector. ΔParameters refers to the amount that each parameter is affected by a change in the temperature of 0.3°K, Δx is the rms of the change in the spectral lines positions along the echelle dispersion axis, and Δy is the rms of the change in the spectral lines positions along the cross-dispersion axis.

VIS			
Parameter	ΔParameter	Δx [pix]	Δy [pix]
ccd_tilt_z	1.00E-01	2.54E+03	2.65E+03
ech_G	2.00E-01	1.09E+03	1.08E+02
ech_blaze	1.00E-01	6.04E+01	8.90E+00
coll_tilt_x	1.00E-01	5.10E+01	8.63E+00
ech_gamma	1.00E-01	7.71E+00	8.46E+00
coll_tilt_y	1.00E-01	7.50E+00	6.07E+00
ccd_ff_tilt_z	1.00E-01	6.33E+00	2.87E+00
trf_mirror_tilt_y	1.00E-01	3.08E+00	2.75E+00
cam_tilt_x	1.00E-01	1.90E+00	2.02E+00
grm_tilt_x	1.00E-01	1.76E+00	1.83E+00
ccd_ff_tilt_x	1.00E-01	9.77E-01	1.58E+00
grm_apex	2.00E-01	7.37E-01	1.36E+00
cam_tilt_y	1.00E-01	7.28E-01	9.41E-01
d_ff_ccd	1.00E-01	7.16E-01	9.25E-01
ccd_defocus	1.00E-01	7.14E-01	8.76E-01
grm_tilt_y	1.00E-01	7.01E-01	8.03E-01
d_cam_ff	1.00E-01	4.96E-01	8.01E-01
trf_mirror_tilt_x	1.00E-01	4.89E-01	7.38E-01
ccd_ff_dec_y	1.00E-01	4.33E-01	4.35E-01
ccd_ff_tilt_y	1.00E-01	4.01E-01	4.35E-01
ccd_ff_dec_x	1.00E-01	2.05E-01	3.81E-01
ech_z	1.00E-01	1.71E-01	2.25E-01
slit_dec_y_a	5.00E-03	7.84E-02	1.73E-01
grm_G	1.00E-01	5.81E-02	8.67E-02
cam_dec_y	1.00E-01	2.74E-02	3.13E-02
grism_dec_y	1.00E-01	2.69E-02	1.54E-02
slit_dec_x_a	5.00E-03	2.10E-02	1.14E-02
d_col_trf	1.00E-01	1.22E-02	6.65E-03
ccd_tilt_y	1.00E-01	1.11E-02	6.49E-03
d_slit_col	1.00E-01	8.38E-03	5.57E-03
slit_tilt_x	1.00E-03	7.68E-03	3.76E-03
ccd_tilt_x	1.00E-01	7.51E-03	3.70E-03
d_grm_cam	1.00E-01	5.40E-03	3.56E-03
grism_dec_x	1.00E-01	3.15E-03	5.94E-04
cam_dec_x	1.00E-01	3.01E-03	3.70E-04
slit_tilt_y	1.00E-03	1.07E-03	1.09E-05
slit_tilt_z	1.00E-03	4.85E-05	3.18E-12
d_col_grm	1.00E-01	4.55E-12	9.09E-13
ccd_dec_y	1.00E-01	2.73E-12	9.09E-13
ccd_dec_x	1.00E-01	1.82E-12	0.00E+00

TABLE B.3: Error budget of RAMSES parameters and its effect on the spectral line positions along the detector. ΔParameters refers to the amount that each parameter, Δx is the rms of the change in the spectral lines positions along the echelle dispersion axis, and Δy is the rms of the change in the spectral lines positions along the cross-dispersion axis.

NIR			
Parameter	ΔParameter	Δx [pix]	Δy [pix]
ccd_tilt_z	1.00E-03	8.28E+03	2.56E+03
ech_G	5.00E-02	7.87E+03	2.48E+03
coll_tilt_x	1.00E-03	2.83E+00	7.40E-01
ech_blaze	1.00E-03	1.12E+00	3.57E-01
slit_dec_y_a	5.00E-03	9.99E-01	3.04E-01
d_ff_ccd	1.00E-01	9.67E-01	3.00E-01
coll_tilt_y	1.00E-03	5.40E-01	2.93E-01
trf_mirror_tilt_x	1.00E-03	4.49E-01	2.25E-01
slit_dec_x_a	5.00E-03	2.68E-01	1.66E-01
d_cam_ff	1.00E-01	2.30E-01	1.53E-01
d_slit_col	1.00E-01	2.06E-01	1.46E-01
ech_gamma	1.00E-03	1.87E-01	1.41E-01
grm_apex	5.00E-02	1.51E-01	9.09E-02
trf_mirror_tilt_y	1.00E-03	1.28E-01	5.38E-02
grm_tilt_x	1.00E-03	1.22E-01	4.39E-02
cam_tilt_x	1.00E-03	1.11E-01	3.17E-02
gap	1.00E-03	5.56E-02	2.91E-02
slit_tilt_x	1.00E-03	5.22E-02	2.73E-02
ech_z	1.00E-03	4.61E-02	2.34E-02
cam_dec_x	1.00E-01	4.45E-02	2.06E-02
ccd_ff_tilt_z	1.00E-03	3.96E-02	1.87E-02
grism_dec_y	1.00E-02	2.67E-02	1.75E-02
cam_dec_y	1.00E-02	2.67E-02	1.64E-02
ccd_ff_dec_y	1.00E-02	2.36E-02	1.16E-02
slit_tilt_y	1.00E-03	1.66E-02	9.83E-03
cam_tilt_y	1.00E-03	1.35E-02	7.61E-03
ccd_ff_tilt_x	1.00E-03	9.37E-03	3.85E-03
grm_tilt_y	1.00E-03	6.74E-03	3.70E-03
grism_dec_x	1.00E-02	5.58E-03	3.23E-03
ccd_ff_dec_x	1.00E-02	4.10E-03	3.21E-03
d_grm_cam	1.00E-03	1.16E-03	3.93E-04
ccd_ff_tilt_y	1.00E-03	1.12E-03	2.33E-04
slit_tilt_z	1.00E-03	5.86E-04	9.31E-05
grm_G	1.00E-03	5.58E-04	3.46E-07
ccd_tilt_x	1.00E-03	1.23E-06	2.96E-12
ccd_tilt_y	1.00E-03	6.91E-07	9.09E-13
d_col_grm	1.00E-01	6.37E-12	0.00E+00
ccd_dec_y	1.00E-02	1.82E-12	0.00E+00

TABLE B.4: Error budget of RAMSES parameters and its effect on the spectral line positions along the detector. ΔParameters refers to the amount that each parameter, Δx is the rms of the change in the spectral lines positions along the echelle dispersion axis, and Δy is the rms of the change in the spectral lines positions along the cross-dispersion axis.

Appendix C

Measured Radial Velocities

C.1 HD 25723

JD [days]	RV [m s^{-1}]	σ_{RV} [m s^{-1}]
2451428.0	-15.4	5.4
2451436.0	-25.2	5.7
2451477.9	-11.5	5.7
2451478.9	-11.1	9.0
2451481.9	-6.8	6.5
2451501.8	13.7	6.4
2451543.7	28.5	5.9
2451571.7	35.5	7.7
2451781.0	-1.7	5.3
2451808.9	-64.6	5.5
2451853.9	-10.8	6.2
2451855.9	0.1	6.6
2451895.8	-10.5	5.5
2451896.8	-4.2	7.0
2451897.8	-7.2	7.5
2451898.8	-12.7	6.1
2451901.8	-15.9	11.9
2451916.7	1.9	6.4
2451927.7	-9.1	5.5
2451929.7	7.3	6.2
2451930.7	11.4	5.9
2451932.7	-9.7	6.7
2452126.0	39.4	6.6
2452157.0	31.4	5.1
2452165.0	11.7	6.3
2452166.0	6.0	5.9
2452167.0	25.0	6.2
2452175.0	10.2	6.5
2452192.9	-16.8	6.3
2452193.9	-14.2	5.6
2452194.9	-17.7	6.6
2452202.0	-23.1	5.9
2452205.9	-4.5	6.6
2452206.9	-13.9	6.7
2452207.9	-18.5	6.6
2452222.8	-10.4	7.0
2452223.8	-12.4	6.3
2452258.7	-35.5	7.5
2452259.8	-58.4	7.5
2452295.7	-10.5	6.4
2452297.7	-28.6	8.1
2452307.7	-24.0	6.2
2452336.6	-12.4	5.6
2452362.6	-47.6	7.9
2452363.6	-30.9	9.0
2452495.0	43.4	6.1
2452506.0	54.3	6.0
2452508.0	47.1	7.6
2452518.0	51.8	7.2
2452530.0	33.6	5.8
2452543.9	22.3	5.7
2452571.9	35.4	6.4
2452589.9	12.6	7.2
2452604.7	-8.6	6.9
2452605.8	10.2	7.1
2452615.8	10.2	8.0
2452667.7	-11.5	6.3
2452720.6	-33.3	6.0
2452862.0	14.8	5.5
2452880.0	11.4	5.2
2452899.0	0.4	6.1
2452932.9	8.6	7.0
2452934.9	41.4	5.6
2452964.8	48.4	7.2
2452966.8	34.4	6.7
2453023.7	12.0	7.2
2453236.0	-54.9	5.0
2453266.0	-41.9	5.5
2453286.9	-31.8	6.4
2453354.7	23.8	5.5
2453359.8	2.2	5.5
2453400.7	32.7	5.9
2453424.6	13.8	5.6
2453442.6	13.4	5.3
2453613.0	-1.4	8.2
2453650.0	-62.3	5.2
2453655.9	-40.5	5.9
2453740.8	-25.9	6.7
2453787.6	28.0	5.7
2453968.0	38.9	4.9
2453982.9	19.1	4.7
2454054.9	-32.2	7.1
2454123.7	-41.3	6.2
2454181.6	-5.3	6.2
2454345.0	24.0	5.2
2454419.8	19.0	5.9
2454443.7	14.1	5.9
2454481.7	-25.4	6.5
2454502.7	-24.1	6.5
2454682.0	-1.0	5.6
2454712.0	43.4	5.9
2454754.9	37.0	5.7
2454777.8	35.9	6.1
2455102.9	-47.4	7.7
2455174.8	-9.6	7.5
2455244.7	29.8	7.7
2455423.0	-35.7	6.4
2455447.0	-38.3	6.6
2455465.9	-88.4	13.2
2455566.8	-25.9	6.0
2455590.7	-27.8	6.1
2455620.7	-22.7	8.0
2455650.7	19.4	10.3
2455805.0	31.1	5.7
2455830.0	-34.7	6.7
2455861.9	-46.6	6.9
2455892.8	-70.6	8.1

FIGURE C.1: Measured RVs for HD 25723

C.2 3 Cnc

JD [days]	RV [m s^{-1}]	σ_{RV} [m s^{-1}]
2451543.0	72.6	5.1
2451571.9	38.1	6.7
2451684.7	150.4	5.2
2451706.7	215.8	5.5
2451899.0	36.4	5.8
2451932.0	-14.9	6.7
2452012.8	-145.1	5.5
2452015.8	-160.4	5.9
2452047.7	-139.7	5.1
2452223.0	-120.7	5.6
2452224.0	-28.7	5.7
2452259.0	-51.9	6.0
2452295.9	-25.1	6.1
2452307.9	16.3	6.3
2452362.8	106.7	5.9
2452363.8	61.5	5.5
2452394.8	135.3	7.4
2452412.7	93.0	6.0
2452424.7	161.9	5.4
2452438.7	142.1	5.9
2452590.1	134.3	6.0
2452604.1	92.6	6.5
2452616.0	68.3	5.8
2452628.0	35.8	5.8
2452665.9	25.0	5.4
2452667.9	15.1	5.9
2452717.8	-70.0	5.1
2452761.7	-148.9	10.0
2452800.7	-234.4	5.4
2452803.7	-198.3	6.3
2452966.1	6.8	6.2
2453025.9	-48.9	6.5
2453092.8	18.1	6.8
2453111.8	88.1	5.7
2453169.7	85.7	4.3
2453172.7	51.8	4.5
2453324.1	77.3	5.7
2453425.8	77.8	4.6
2453492.7	2.5	4.5
2453741.1	-62.9	5.6
2453788.9	-81.4	4.8
2453855.7	21.9	4.6
2453915.7	162.0	5.3
2454055.1	204.7	6.8
2454123.9	106.9	5.4
2454181.8	122.5	5.4
2454207.7	32.4	4.5
2454226.8	36.2	4.9
2454267.7	-28.4	5.1
2454420.0	-182.5	5.5
2454444.1	-183.2	5.6
2454482.1	-212.9	6.1
2454503.8	-224.0	5.0
2454553.8	-37.2	4.8
2454583.8	-47.4	5.5
2454600.8	-53.7	5.2
2454882.9	258.3	6.6
2455175.1	-127.5	6.8
2455241.9	-46.6	6.6
2455278.8	-93.9	6.3
2455567.0	135.2	6.1
2455589.9	131.3	5.3
2455620.9	137.6	5.9
2455650.8	117.8	6.2
2455673.8	95.1	4.9
2455701.7	136.5	5.2
2455864.1	-2.8	5.4
2455894.0	-75.5	8.0

FIGURE C.2: Measured RVs for 3 Cnc

C.3 44 UMa

JD [days]	RV [m s^{-1}]	σ_{RV} [m s^{-1}]
2451354.7	17.1	5.2
2451372.8	53.5	5.9
2451375.7	51.9	4.0
2451427.7	72.7	4.1
2451436.6	99.0	4.6
2451572.1	81.2	6.5
2451656.0	10.5	7.3
2451781.7	-103.6	4.1
2452014.9	73.5	5.4
2452032.9	47.1	4.7
2452044.8	99.6	5.8
2452048.8	102.8	5.0
2452079.8	114.4	4.8
2452081.8	99.7	5.3
2452082.8	73.7	4.5
2452099.7	96.6	6.8
2452106.7	33.8	6.3
2452107.7	80.2	6.7
2452108.7	96.9	4.8
2452109.7	90.9	4.5
2452156.7	40.5	5.1
2452162.6	29.4	4.8
2452163.7	8.9	5.0
2452174.6	6.7	5.0
2452176.6	13.1	4.8
2452296.0	-35.6	6.4
2452298.1	-59.7	6.9
2452308.0	-62.6	5.1
2452337.1	-51.2	5.0
2452362.0	-61.1	4.8
2452363.9	-88.0	5.2
2452384.9	-85.9	5.7
2452395.0	-94.9	6.6
2452412.8	-80.6	5.9
2452423.8	-43.5	5.4
2452425.8	-47.8	5.8
2452437.8	-67.1	5.4
2452439.8	-91.8	5.5
2452452.8	-17.9	5.6
2452464.8	22.2	5.4
2452466.7	-12.1	5.3
2452471.7	-6.0	5.3
2452472.8	22.8	4.8
2452483.8	6.3	5.7
2452495.7	41.8	5.0
2452505.7	39.6	5.4
2452517.7	34.2	6.0
2452519.7	33.9	5.1
2452529.7	49.4	6.1
2452531.6	26.2	4.9
2452541.6	76.3	5.7
2452669.0	84.9	6.3
2452717.9	38.6	4.9
2452765.9	13.3	6.1
2452800.8	-14.2	4.8
2452837.8	-67.0	7.3
2452861.7	-78.4	5.1
2452863.7	-75.3	5.4
2452880.7	-122.6	4.4
2452898.6	-81.7	11.0
2452900.6	-67.8	12.3
2453026.1	-7.2	5.5
2453092.9	114.9	6.1
2453168.9	119.7	4.3
2453172.7	164.1	4.0
2453207.7	101.4	4.4
2453232.7	81.6	4.2
2453266.6	32.5	4.7
2453292.6	62.1	4.7
2453401.1	-61.1	4.7
2453427.0	-71.3	4.2
2453443.0	-70.4	4.8
2453492.9	-78.2	4.5
2453549.8	-78.8	4.6
2453578.8	-66.1	4.5
2453788.0	64.9	5.0
2453855.9	103.4	4.3
2453911.8	-27.8	4.7
2453932.8	-23.4	4.2
2453968.7	-59.4	4.1
2453982.7	-114.7	3.8
2454124.1	-124.4	4.9
2454183.9	-55.6	3.8
2454207.0	-24.5	4.4
2454226.9	24.0	4.3
2454265.8	2.4	4.5
2454296.7	15.1	4.4
2454300.8	74.2	5.0
2454315.7	17.1	4.2
2454346.7	54.9	4.4
2454483.1	29.8	5.6
2454504.0	66.0	4.8
2454556.9	-43.5	4.7
2454580.9	-52.7	5.7
2454602.9	-75.5	5.1
2454646.8	-103.5	5.0
2454667.7	-121.7	5.4
2454668.8	-114.5	4.9
2454680.7	-93.3	4.4
2454711.7	-61.8	4.8
2454716.7	-51.4	5.2
2454883.0	78.5	7.0
2454912.0	127.6	6.7
2454979.9	160.6	6.2
2455027.7	89.2	6.0
2455064.8	-3.0	5.5
2455098.7	-52.3	6.5
2455242.1	-118.8	7.5
2455279.0	-41.3	6.5
2455329.9	8.7	5.6
2455361.8	18.8	5.2
2455420.7	16.6	5.2
2455449.7	72.4	6.6
2455466.6	46.9	6.1
2455571.1	73.1	5.9
2455651.9	-53.0	5.8
2455701.9	-68.3	4.8
2455757.8	-32.3	6.1
2455760.8	-57.2	5.0
2455805.7	-55.0	5.2
2455829.6	-30.3	7.6

FIGURE C.3: Measured RVs for 44 UMa

C.4 17 Sco

JD [days]	RV [m s^{-1}]	σ_{RV} [m s^{-1}]
2451501.0	160.9	8.0
2451571.8	244.3	7.5
2451654.7	75.9	6.5
2451857.0	-242.6	5.4
2451899.9	-265.5	6.0
2451991.7	-199.5	6.6
2452194.0	134.9	5.8
2452206.0	206.9	5.8
2452207.0	167.8	6.4
2452222.9	198.1	5.4
2452258.9	222.7	6.7
2452295.8	131.9	6.3
2452297.9	163.6	8.0
2452307.8	117.4	6.5
2452361.7	48.3	5.6
2452363.8	58.0	6.3
2452394.7	99.3	6.9
2452544.0	-64.6	6.3
2452561.0	-102.3	5.4
2452572.1	-147.2	6.4
2452590.0	-170.4	5.8
2452604.0	-180.5	7.1
2452615.9	-166.6	7.0
2452665.9	-105.7	5.5
2452667.9	-147.0	6.8
2452717.7	-137.4	5.9
2452933.0	-32.1	5.8
2452935.0	-24.9	4.8
2452965.0	10.6	6.2
2453023.9	184.0	7.3
2453092.8	282.8	6.9
2453290.0	173.2	4.4
2453324.0	100.6	5.5
2453354.9	-16.2	5.1
2453424.8	-103.4	5.2
2453442.7	-114.4	5.7
2453656.0	-176.3	5.5
2453741.9	-76.9	6.2
2453789.8	-87.5	6.3
2453859.7	45.6	5.7
2454055.0	224.8	5.2
2454123.9	207.1	6.6
2454184.8	154.0	6.2
2454209.7	41.1	5.9
2454226.7	19.1	5.4
2454392.1	-192.4	7.7
2454419.1	-197.4	6.0
2454444.0	-176.5	6.3
2454503.8	-202.8	5.4
2454553.7	-87.7	5.3
2454582.7	2.4	5.7
2454754.0	217.3	4.8
2454779.0	188.3	5.2
2454911.7	130.2	7.0
2455103.0	-99.3	7.9
2455155.0	-125.2	9.3
2455175.0	-133.1	7.0
2455243.8	-260.4	6.6
2455278.7	-252.4	7.1
2455467.1	-146.2	5.8
2455566.9	68.6	6.1
2455589.8	143.2	5.9
2455619.8	268.7	7.9
2455651.7	264.9	6.2
2455673.7	311.3	6.0
2455864.0	107.1	5.6
2455894.0	87.4	9.0

FIGURE C.4: Measured RVs for 17 Sco

Bibliography

Agresti, Alan and Brent A. Coull (1998). "Approximate Is Better than "Exact" for Interval Estimation of Binomial Proportions". In: *The American Statistician* 52.2, pp. 119–126. ISSN: 00031305. URL: http://www.jstor.org/stable/2685469.

Amaran, Satyajith et al. (2016). "Simulation optimization: a review of algorithms and applications". In: *Annals of Operations Research* 240.1, pp. 351–380. ISSN: 1572-9338. DOI: 10.1007/s10479-015-2019-x. URL: https://doi.org/10.1007/s10479-015-2019-x.

Andreas Kaufer, Luca Pasquini (1998). "FEROS: the new fiber-linked echelle spectrograph for the ESO 1.52-m telescope". In: vol. 3355. DOI: 10.1117/12.316798. URL: https://doi.org/10.1117/12.316798.

Angel, J. R. P. et al. (1977). "A very large optical telescope array linked with fused silica fibers". In: 218, pp. 776–782. DOI: 10.1086/155734.

Ballester, P. and M. R. Rosa (1997). "Modeling echelle spectrographs". In: *Astronomy and Astrophysics Supplement Series* 126, pp. 563–571. DOI: 10.1051/aas:1997283.

Baranne, A., M. Mayor, and J. L. Poncet (1979). "CORAVEL - A new tool for radial velocity measurements". In: *Vistas in Astronomy* 23, pp. 279–316. DOI: 10.1016/0083-6656(79)90016-3.

Baranne, A. et al. (1996). "ELODIE: A spectrograph for accurate radial velocity measurements." In: 119, pp. 373–390.

Bauer, F. F., M. Zechmeister, and A. Reiners (2015). "Calibrating echelle spectrographs with Fabry-Pérot etalons". In: 581, A117, A117. DOI: 10.1051/0004-6361/201526462. arXiv: 1506.07887 [astro-ph.IM].

Bedding, Timothy R. et al. (2011). "Gravity modes as a way to distinguish between hydrogen- and helium-burning red giant stars". In: 471, pp. 608–611. DOI: 10.1038/nature09935. arXiv: 1103.5805 [astro-ph.SR].

Belorizky, D. (1938). "Le Soleil, Etoile Variable". In: *L'Astronomie* 52, pp. 359–361.

Benatti, Serena (2018). "Multi-Wavelength High-Resolution Spectroscopy for Exoplanet Detection: Motivation, Instrumentation and First Results". In: *Geosciences* 8, p. 289. DOI: 10.3390/geosciences8080289. arXiv: 1808.02302 [astro-ph.IM].

Borgniet, S. et al. (2019). "Extrasolar planets and brown dwarfs around AF-type stars. X. The SOPHIE sample: combining the SOPHIE and HARPS surveys to compute the close giant planet mass-period distribution around AF-type stars". In: 621, A87, A87. DOI: 10.1051/0004-6361/201833431. arXiv: 1809.09914 [astro-ph.EP].

Bristow, P., F. Kerber, and M. R. Rosa (2008). "Advanced Calibration Techniques for Astronomical Spectrographs". In: *The Messenger* 131, pp. 2–6.

Bristow, P. et al. (2006). "Model based wavelength calibration for CRIRES". In: *Society of Photo-Optical Instrumentation Engineers (SPIE) Conference Series*. Vol. 6270. 62701T. DOI: 10.1117/12.670785.

Bristow, Paul et al. (2010). "Using the X-shooter physical model to understand instrument flexure". In: *Ground-based and Airborne Instrumentation for Astronomy III*. Vol. 7735. Society of Photo-Optical Instrumentation Engineers (SPIE) Conference Series, p. 77357C. DOI: 10.1117/12.856097.

Brown, Warren R., Harland W. Epps, and Daniel G. Fabricant (2004). "The Cryogenic Refractive Indices of S-FTM16, a Unique Optical Glass for Near-Infrared Instruments". In: *Publications of the Astronomical Society of the Pacific* 116.823, pp. 833–841. DOI: 10.1086/424496. URL: https://doi.org/10.1086.

Buchdahl, H. A. (1956). "Optical aberration coefficients. I. The coefficient of tertiary spherical aberration". In: *Journal of the Optical Society of America (1917-1983)* 46.11, p. 941.

Buchner, J. (2016). *PyMultiNest: Python interface for MultiNest*. Astrophysics Source Code Library. ascl: 1606.005.

Buchner, J. et al. (2014). "X-ray spectral modelling of the AGN obscuring region in the CDFS: Bayesian model selection and catalogue". In: 564, A125, A125. DOI: 10.1051/0004-6361/201322971. arXiv: 1402.0004 [astro-ph.HE].

Burke, Christopher J. et al. (2015). "Terrestrial Planet Ocurrence Rates for the Kepler G-K dwarf sample". In: *The Astrophysical Journal* 809.1, p. 8. DOI: 10.1088/0004-637x/809/1/8.

Butler, R. P. et al. (1996). "Attaining Doppler Precision of 3 M s-1". In: 108, p. 500. DOI: 10.1086/133755.

Butler, R. Paul and Geoffrey W. Marcy (1996). "A Planet Orbiting 47 Ursae Majoris". In: *The Astrophysical Journal* 464.2, pp. L153–L156. DOI: 10.1086/310102. URL: https://doi.org/10.1086%2F310102.

Campbell, B. and G. A. H. Walker (1979). "Precision radial velocities with an absorption cell". In: 91, pp. 540–545. DOI: 10.1086/130535.

Cassan, A. et al. (2012). "One or more bound planets per Milky Way star from microlensing observations". In: 481, pp. 167–169. DOI: 10.1038/nature10684. arXiv: 1202.0903 [astro-ph.EP].

Chabrier, G. et al. (2014). "Giant Planet and Brown Dwarf Formation". In: *Protostars and Planets VI*, pp. 619–642. DOI: 10.2458/azu_uapress_9780816531240-ch027. arXiv: 1401.7559 [astro-ph.SR].

Chanumolu, A. et al. (2017). "Performance results of HESP physical model". In: *Experimental Astronomy* 43, pp. 39–58.

Chanumolu, Anantha, Damien Jones, and Sivarani Thirupathi (2015). "Modelling high resolution Echelle spectrographs for calibrations: Hanle Echelle spectrograph, a case study". In: *Experimental Astronomy* 39, pp. 423–443. DOI: 10.1007/s10686-015-9457-y. arXiv: 1505.00397 [astro-ph.IM].

Cincunegui, C., R. F. Díaz, and P. J. D. Mauas (2007). "Hα and the Ca II H and K lines as activity proxies for late-type stars". In: 469, pp. 309–317. DOI: 10.1051/0004-6361:20066503. arXiv: astro-ph/0703511 [astro-ph].

Currie, Thayne (2009). "On the Semimajor Axis Distribution of Extrasolar Gas Giant Planets: Why Hot Jupiters are Rare Around High-Mass Stars". In: *The Astrophysical Journal Letters* 694.2, p. L171. URL: http://stacks.iop.org/1538-4357/694/i=2/a=L171.

De Ridder, J. et al. (2006). "Discovery of solar-like oscillations in the red giant \varepsilon Ophiuchi". In: 448, pp. 689–695. DOI: 10.1051/0004-6361:20053331.

Delgado Mena, E. et al. (2018). "Planets around evolved intermediate-mass stars. II. Are there really planets around IC 4651 No. 9122, NGC 2423 No. 3, and NGC 4349 No. 127?" In: 619, A2, A2. DOI: 10.1051/0004-6361/201833152. arXiv: 1807.09608 [astro-ph.EP].

Döllinger, M. P. et al. (2007). "Discovery of a planet around the K giant star 4 Ursae Majoris". In: 472, pp. 649–652. DOI: 10.1051/0004-6361:20066987. eprint: astro-ph/0703672.

Döllinger, M. P. et al. (2009). "Planetary companions around the K giant stars 11 Ursae Minoris and HD 32518". In: 505, pp. 1311–1317. DOI: 10.1051/0004-6361/200911702. arXiv: 0908.1753 [astro-ph.EP].

Dumusque, X., I. Boisse, and N. C. Santos (2014). "SOAP 2.0: A Tool to Estimate the Photometric and Radial Velocity Variations Induced by Stellar Spots and Plages". In: 796, 132, p. 132. DOI: 10.1088/0004-637X/796/2/132. arXiv: 1409.3594 [astro-ph.SR].

Eadie, Gwendolyn M. and William E. Harris (2016). "BAYESIAN MASS ESTIMATES OF THE MILKY WAY: THE DARK AND LIGHT SIDES OF PARAMETER ASSUMPTIONS". In: *The Astrophysical Journal* 829.2, p. 108. DOI: 10.3847/0004-637x/829/2/108. URL: https://doi.org/10.3847.

Farr, W. M. et al. (2018). "Aldebaran bs Temperate Past Uncovered in Planet Search Data". In: 865, L20, p. L20. DOI: 10.3847/2041-8213/aadfde. arXiv: 1802.09812 [astro-ph.SR].

Feldman Albert; Horowitz, Deane; Waxler Roy M.; Dodge Marilyn J. (1978). "Optical materials characterization : final technical report". In: *National Bureau of Standards (U.S.)*

Feroz, F., M. P. Hobson, and M. Bridges (2009). "MULTINEST: an efficient and robust Bayesian inference tool for cosmology and particle physics". In: 398.4, pp. 1601–1614. DOI: 10.1111/j.1365-2966.2009.14548.x. arXiv: 0809.3437 [astro-ph].

Fischer, D. A., G. W. Marcy, and J. F. P. Spronck (2014). "The Twenty-five Year Lick Planet Search". In: 210, 5, p. 5. DOI: 10.1088/0067-0049/210/1/5. arXiv: 1310.7315 [astro-ph.EP].

Frink, S. et al. (2001). "A Strategy for Identifying the Grid Stars for the Space Interferometry Mission". In: 113, pp. 173–187. DOI: 10.1086/318610. eprint: astro-ph/0011190.

Frink, S. et al. (2002). "Discovery of a Substellar Companion to the K2 III Giant ι Draconis". In: 576, pp. 478–484. DOI: 10.1086/341629.

Gaia Collaboration (2018). "VizieR Online Data Catalog: Gaia DR2 (Gaia Collaboration, 2018)". In: *VizieR Online Data Catalog* 1345.

Griffin, R. (1973). "On the possibility of determining stellar radial velocities to 0.01 km s^{-1}." In: 162, pp. 243–253. DOI: 10.1093/mnras/162.3.243.

Günther, Robin (2019). "Examining Scaling Relations for Solar-like Oscillations with K and G Giants from the Lick Planet Search". Undergraduate Thesis. Ruprecht-Karls-Universität Heidelberg.

Hatzes, A. P. (2002). "Starspots and exoplanets". In: *Astronomische Nachrichten* 323, pp. 392–394. DOI: 10.1002/1521-3994(200208)323:3/4<392::AID-ASNA392>3.0.CO;2-M.

Hatzes, A. P. and W. D. Cochran (1993). "Long-period radial velocity variations in three K giants". In: 413, pp. 339–348. DOI: 10.1086/173002.

— (1995). "The Radial Velocity Variability of alpha Persei: A Low-Amplitude Cepheid outside the Instability Strip?" In: 452, p. 401. DOI: 10.1086/176311.

Hatzes, A. P. et al. (2015). "Long-lived, long-period radial velocity variations in Aldebaran: A planetary companion and stellar activity". In: 580, A31, A31. DOI: 10.1051/0004-6361/201425519. arXiv: 1505.03454 [astro-ph.SR].

Hatzes, A. P. et al. (2018). "The Radial Velocity Variability of the K-giant γ Draconis: Stellar Variability Masquerading as a Planet". In: 155, 120, p. 120. DOI: 10.3847/1538-3881/aaa8e1. arXiv: 1801.05239 [astro-ph.SR].

Hatzes, Artie P., William D. Cochran, and Michael Endl (2010). "The Detection of Extrasolar Planets Using Precise Stellar Radial Velocities". In: *Planets in Binary Star Systems*. Ed. by Nader Haghighipour. Dordrecht: Springer Netherlands, pp. 51–76. ISBN: 978-90-481-8687-7. DOI: 10.1007/978-90-481-8687-7_3. URL: https://doi.org/10.1007/978-90-481-8687-7_3.

Haynes, D. M. et al. (2011). "Relative contributions of scattering, diffraction and modal diffusion to focal ratio degradation in optical fibres". In: 414, pp. 253–263. DOI: 10.1111/j.1365-2966.2011.18385.x.

Heacox, W. D. (1986). "On the application of optical-fiber image scramblers to astronomical spectroscopy". In: 92, pp. 219–229. DOI: 10.1086/114154.

Hecht, E., A. Zając, and K. Guardino (1998). *Optics*. Addison-Wesley world student series. Addison-Wesley. ISBN: 9780201838879. URL: https://books.google.de/books?id=QJYULgEACAAJ.

Heeren, Paul (2016). "'Constructing an Echelle Spectrograph for Doppler Spectroscopy of G/K Giant Stars'". Master Thesis. Ruprecht-Karls-Universität Heidelberg.

Hekker, S. and J. Meléndez (2007). "Precise radial velocities of giant stars. III. Spectroscopic stellar parameters". In: 475, pp. 1003–1009. DOI: 10.1051/0004-6361:20078233. arXiv: 0709.1145.

Hekker, S. et al. (2006). "Precise radial velocities of giant stars. I. Stable stars". In: 454, pp. 943–949. DOI: 10.1051/0004-6361:20064946. eprint: astro-ph/0604502.

Høg, Erik (2017). "Astrometric accuracy during the past 2000 years". In: *arXiv e-prints*, arXiv:1707.01020, arXiv:1707.01020. arXiv: 1707.01020 [astro-ph.IM].

Johnson, J. A. et al. (2007). "Retired A Stars and Their Companions: Exoplanets Orbiting Three Intermediate-Mass Subgiants". In: 665, pp. 785–793. DOI: 10.1086/519677. arXiv: 0704.2455.

Johnson, John Asher et al. (2010). "Giant Planet Occurrence in the Stellar Mass-Metallicity Plane". In: *Publications of the Astronomical Society of the Pacific* 122.894, pp. 905–915. DOI: 10.1086/655775. URL: https://doi.org/10.1086%2F655775.

Jones, M. I. et al. (2011). "Study of the impact of the post-MS evolution of the host star on the orbits of close-in planets. I. Sample definition and physical properties". In: 536, A71, A71. DOI: 10.1051/0004-6361/201117887. arXiv: 1110.6459 [astro-ph.EP].

Jones, M. I. et al. (2014). "The properties of planets around giant stars". In: 566, A113, A113. DOI: 10.1051/0004-6361/201323345. arXiv: 1406.0884 [astro-ph.EP].

Kennedy, G. M. and S. J. Kenyon (2008). "Planet Formation around Stars of Various Masses: The Snow Line and the Frequency of Giant Planets". In: 673, pp. 502–512. DOI: 10.1086/524130. arXiv: 0710.1065.

Kerber, F., P. Bristow, and M. R. Rosa (2006). "STIS Calibration Enhancement (STIS-CE) : Dispersion Solutions Based on a Physical Instrument Model". In: *The 2005 HST Calibration Workshop: Hubble After the Transition to Two-Gyro Mode*. Ed. by A. M. Koekemoer, P. Goudfrooij, and L. L. Dressel, p. 309.

Kidger, M.J. and V.V. Tuchin (2002). *Fundamental Optical Design*. Press Monographs. Society of Photo Optical. ISBN: 9780819439154. URL: https://books.google.de/books?id=mberzJtkU4MC.

Kirkpatrick, S., C. D. Gelatt, and M. P. Vecchi (1983). "Optimization by Simulated Annealing". In: *Science* 220.4598, pp. 671–680. ISSN: 0036-8075. DOI: 10.1126/science.220.4598.671. eprint: https://science.sciencemag.org/content/220/4598/671.full.pdf. URL: https://science.sciencemag.org/content/220/4598/671.

Kjeldsen, H. and T. R. Bedding (2011). "Amplitudes of solar-like oscillations: a new scaling relation". In: 529, L8, p. L8. DOI: 10.1051/0004-6361/201116789. arXiv: 1104.1659 [astro-ph.SR].

Kramida, A. et al. (2016). "NIST Atomic Spectra Database (ver. 5.3)". In:

Kunitomo, M. et al. (2011). "Planet Engulfment by 1.5-3 M Red Giants". In: *The Astrophysical Journal* 737.2, p. 66. URL: http://stacks.iop.org/0004-637X/737/i=2/a=66.

Lee, B.-C. et al. (2012). "Detection of an exoplanet around the evolved K giant HD 66141". In: 548, A118, A118. DOI: 10.1051/0004-6361/201118014. arXiv: 1211.2054 [astro-ph.SR].

Lee, Chien-Hsiu (2018). "Exoplanets: Past, Present, and Future". In: *Galaxies* 6, p. 51. DOI: 10.3390/galaxies6020051. arXiv: 1804.08907 [astro-ph.EP].

Leviton, Douglas B., Bradley J. Frey, and Ross M. Henry (2013). "Temperature-dependent refractive index measurements of S-FPL51, S-FTM16, and S-TIM28 to cryogenic temperatures". In: vol. 8863. DOI: 10.1117/12.2024821. URL: https://doi.org/10.1117/12.2024821.

Leviton, Douglas B., Bradley J. Frey, and Todd Kvamme (2008). "High accuracy, absolute, cryogenic refractive index measurements of infrared lens materials for JWST NIRCam using CHARMS". In: *arXiv e-prints*, arXiv:0805.0090, arXiv:0805.0090. arXiv: 0805.0090 [physics.optics].

Leviton Douglas B., Frey Bradley J. Madison Timothy J. (2007). "Temperature-dependent refractive index of CaF2 and Infrasil 301". In: vol. 6692. DOI: 10.1117/12.735594. URL: https://doi.org/10.1117/12.735594.

Li, Chih-Hao et al. (2008). "A laser frequency comb that enables radial velocity measurements with a precision of 1cms^{-1}". In: 452.7187, pp. 610–612. DOI: 10.1038/nature06854. arXiv: 0804.0955 [astro-ph].

Liu, Y.-J. et al. (2008). "A Substellar Companion to the Intermediate-Mass Giant 11 Comae". In: 672, pp. 553–557. DOI: 10.1086/523297. arXiv: 0709.0645.

Lovis, C. and M. Mayor (2007a). "Planets around evolved intermediate-mass stars. I. Two substellar companions in the open clusters NGC 2423 and NGC 4349". In: 472, pp. 657–664. DOI: 10.1051/0004-6361:20077375. arXiv: 0706.2174.

— (2007b). "Planets around evolved intermediate-mass stars. I. Two substellar companions in the open clusters NGC 2423 and NGC 4349". In: 472, pp. 657–664. DOI: 10.1051/0004-6361:20077375. arXiv: 0706.2174.

Lovis, C. and F. Pepe (2007). "A new list of thorium and argon spectral lines in the visible". In: 468.3, pp. 1115–1121. DOI: 10.1051/0004-6361:20077249. arXiv: astro-ph/0703412 [astro-ph].

Mahajan, V.N. (2014). *Fundamentals of Geometrical Optics*. Press Monograph Series. SPIE Press. ISBN: 9780819499981. URL: https://books.google.de/books?id=_xP9oAEACAAJ.

Marcy, G. W. and R. P. Butler (1992). "Precision radial velocities with an iodine absorption cell". In: 104, pp. 270–277. DOI: 10.1086/132989.

Mayor, M. and D. Queloz (1995). "A Jupiter-mass companion to a solar-type star". In: 378, pp. 355–359. DOI: 10.1038/378355a0.

Mayor, M. et al. (2003). "Setting New Standards with HARPS". In: *The Messenger* 114, pp. 20–24.

McCracken, Richard A., Jake M. Charsley, and Derryck T. Reid (2017). "A decade of astrocombs: recent advances in frequency combs for astronomy". In: *Opt. Express* 25.13, pp. 15058–15078. DOI: 10.1364/OE.25.015058. URL: http://www.opticsexpress.org/abstract.cfm?URI=oe-25-13-15058.

Mirabet, E. et al. (2014). "CARMENES ultra-stable cooling system: very promising results". In: *Advances in Optical and Mechanical Technologies for Telescopes and Instrumentation*. Vol. 9151. 91513Y. DOI: 10.1117/12.2055570.

Mitchell, C. J. (1981). "Generalized ray-tracing for diffraction gratings of arbitrary form". In: *Journal of Optics* 12, pp. 301–308. DOI: 10.1088/0150-536X/12/5/003.

Mitchell, D. S. et al. (2013). "Precise radial velocities of giant stars. V. A brown dwarf and a planet orbiting the K giant stars τ Geminorum and 91 Aquarii". In: 555, A87, A87. DOI: 10.1051/0004-6361/201321714. arXiv: 1305.5107 [astro-ph.EP].

Niedzielski, A. and A. Wolszczan (2008). "A HET search for planets around evolved stars". In: *Exoplanets: Detection, Formation and Dynamics*. Ed. by Y.-S. Sun, S. Ferraz-Mello, and J.-L. Zhou. Vol. 249. IAU Symposium, pp. 43–47. DOI: 10.1017/S1743921308016347. arXiv: 0712.2297.

Okaji, M. et al. (1995). "Laser interferometric dilatometer at low temperatures: application to fused silica SRM 739". In: *Cryogenics* 35.12, pp. 887 –891. ISSN: 0011-2275. DOI: https://doi.org/10.1016/0011-2275(95)96887-R. URL: http://www.sciencedirect.com/science/article/pii/001122759596887R.

Ortiz, M. et al. (2016). "Precise radial velocities of giant stars. IX. HD 59686 Ab: a massive circumstellar planet orbiting a giant star in a 13.6 au eccentric binary system". In: 595, A55, A55. DOI: 10.1051/0004-6361/201628791. arXiv: 1608.00963 [astro-ph.EP].

Osterman Steve, Diddams Scott Beasly Matthew Froning Cynthia Hollberg Leo Macqueen Phillip Mbele Vela Weiner Andrew (2007). "A proposed laser frequency comb-based wavelength reference for high-resolution spectroscopy". In: vol. 6693. DOI: 10.1117/12.734193. URL: https://doi.org/10.1117/12.734193.

Pepe, Francesco, David Ehrenreich, and Michael R. Meyer (2014). "Instrumentation for the detection and characterization of exoplanets". In: 513, pp. 358–366. DOI: 10.1038/nature13784. arXiv: 1409.5266 [astro-ph.EP].

Perryman, M. A. C. et al. (1997). "The HIPPARCOS Catalogue". In: 323, pp. L49–L52.

Petigura, Erik A., Andrew W. Howard, and Geoffrey W. Marcy (2013). "Prevalence of Earth-size planets orbiting Sun-like stars". In: *Proceedings of the National Academy of Science* 110, pp. 19273–19278. DOI: 10.1073/pnas.1319909110. arXiv: 1311.6806 [astro-ph.EP].

Queloz, D. et al. (2001). "From CORALIE to HARPS. The way towards 1 m s^{-1} precision Doppler measurements". In: *The Messenger* 105, pp. 1–7.

Quirrenbach, A. et al. (2010). "CARMENES: Calar Alto high-resolution search for M dwarfs with exo-earths with a near-infrared Echelle spectrograph". In: *Ground-based and Airborne Instrumentation for Astronomy III*. Vol. 7735. Society of Photo-Optical Instrumentation Engineers (SPIE) Conference Series, p. 773513. DOI: 10.1117/12.857777.

Quirrenbach, A. et al. (2014). "CARMENES instrument overview". In: *Ground-based and Airborne Instrumentation for Astronomy V*. Vol. 9147. Society of Photo-Optical Instrumentation Engineers (SPIE) Conference Series. DOI: 10.1117/12.2056453.

Quirrenbach, A. et al. (2018). "CARMENES: high-resolution spectra and precise radial velocities in the red and infrared". In: *Ground-based and Airborne Instrumentation for Astronomy VII*. Vol. 10702. Society of Photo-Optical Instrumentation Engineers (SPIE) Conference Series, 107020W. DOI: 10.1117/12.2313689.

Quirrenbach, Andreas et al. (2019). "Precise radial velocities of giant stars - XI. Two brown dwarfs in 6:1 mean motion resonance around the K giant star iuchi". In: *A&A* 624, A18. DOI: 10.1051/0004-6361/201834423. URL: https://doi.org/10.1051/0004-6361/201834423.

Ramsey, L. W. (1988). "Focal ratio degradation in optical fibers of astronomical interest". In: *Fiber Optics in Astronomy*. Ed. by S. C. Barden. Vol. 3. Astronomical Society of the Pacific Conference Series, pp. 26–39.

Redman, S. L., G. Nave, and C. J. Sansonetti (2014). "The Spectrum of Thorium from 250nm to 5500nm: Ritz Wavelengths and Optimized Energy Levels". In: *The Astrophysical Journal Supplement Series* 211.1, p. 4.

Reffert, Sabine et al. (2006). "Precise Radial Velocities of Giant Stars. II. Pollux and Its Planetary Companion". In: *The Astrophysical Journal* 652.1, p. 661. URL: http://stacks.iop.org/0004-637X/652/i=1/a=661.

Reichert, Katja et al. (2019). "Precise radial velocities of giant stars. XII. Evidence against the proposed planet Aldebaran b". In: *arXiv e-prints*, arXiv:1903.09157, arXiv:1903.09157. arXiv: 1903.09157 [astro-ph.SR].

Reiners, A. et al. (2018a). "The CARMENES search for exoplanets around M dwarfs. HD147379 b: A nearby Neptune in the temperate zone of an early-M dwarf". In: 609, L5, p. L5. DOI: 10.1051/0004-6361/201732165. arXiv: 1712.05797 [astro-ph.EP].

Reiners, A. et al. (2018b). "The CARMENES search for exoplanets around M dwarfs. High-resolution optical and near-infrared spectroscopy of 324 survey stars". In: 612, A49, A49. DOI: 10.1051/0004-6361/201732054. arXiv: 1711.06576 [astro-ph.SR].

Riekert, L. (1961). "F. Kohlrausch, Praktische Physik. Herausgegeben von H. Ebert und E. Justi. Band 1: Allgemeines, Mechanik, Akustik, Wärme, Optik. 21. Auflage, 692 Seiten, 420 Abb. 1960 bei Teubner in Stuttgart, Preis: Ln. DM 46,60". In: *Zeitschrift für Elektrochemie, Berichte der Bunsengesellschaft für physikalische Chemie* 65.10, pp. 910–910. DOI: 10.1002/bbpc.19610651018. eprint: https://onlinelibrary.wiley.com/doi/pdf/10.1002/bbpc.19610651018. URL: https://onlinelibrary.wiley.com/doi/abs/10.1002/bbpc.19610651018.

Rosa, M. R. et al. (2003). "FOS Post-Operational Archive and STIS Calibration Enhancement". In: *HST Calibration Workshop : Hubble after the Installation of the ACS and the NICMOS Cooling System*. Ed. by S. Arribas, A. Koekemoer, and B. Whitmore, p. 161.

Saio, H. et al. (2015). "Oscillatory convective modes in red giants: a possible explanation of the long secondary periods". In: 452, pp. 3863–3868. DOI: 10.1093/mnras/stv1587. arXiv: 1507.03430 [astro-ph.SR].

Sarmiento, L. F. et al. (2014). "Characterizing U-Ne hollow cathode lamps at near-IR wavelengths for the CARMENES survey". In: *Ground-based and Airborne Instrumentation for Astronomy V*. Vol. 9147. P. 914754. DOI: 10.1117/12.2056501.

Sato, B. et al. (2007). "A Planetary Companion to the Hyades Giant ϵ Tauri". In: 661, pp. 527–531. DOI: 10.1086/513503.

Sato, B. et al. (2008a). "Planetary Companions around Three Intermediate-Mass G and K Giants: 18 Delphini, ξ Aquilae, and HD 81688". In: 60, pp. 539–550. DOI: 10.1093/pasj/60.3.539. arXiv: 0802.2590.

— (2008b). "Properties of Planets around G, K Giants". In: *Extreme Solar Systems*. Ed. by D. Fischer et al. Vol. 398. Astronomical Society of the Pacific Conference Series, p. 67.

Savitzky, Abraham. and M. J. E. Golay (1964). "Smoothing and Differentiation of Data by Simplified Least Squares Procedures." In: *Analytical Chemistry* 36.8, pp. 1627–1639. DOI: 10.1021/ac60214a047. URL: https://doi.org/10.1021/ac60214a047.

Schwab, C. et al. (2012). "Investigating spectrograph design parameters with the Yale Doppler diagnostic facility". In: *Ground-based and Airborne Instrumentation for Astronomy IV*. Vol. 8446. P. 844695. DOI: 10.1117/12.926357.

Setiawan, J. et al. (2003). "Evidence of a sub-stellar companion around HD 47536". In: 398, pp. L19–L23. DOI: 10.1051/0004-6361:20021846.

Skilling, John (2006). "Nested sampling for general Bayesian computation". In: *Bayesian Anal.* 1.4, pp. 833–859. DOI: 10.1214/06-BA127. URL: https://doi.org/10.1214/06-BA127.

Steinmetz, T. et al. (2009). "Fabry–Pérot filter cavities for wide-spaced frequency combs with large spectral bandwidth". In: *Applied Physics B* 96.2, pp. 251–256. ISSN: 1432-0649. DOI: 10.1007/s00340-009-3374-6. URL: https://doi.org/10.1007/s00340-009-3374-6.

Stock, S., S. Reffert, and A. Quirrenbach (2018). "Precise radial velocities of giant stars. X. Bayesian stellar parameters and evolutionary stages for 372 giant stars from the Lick planet search". In: 616, A33, A33. DOI: 10.1051/0004-6361/201833111. arXiv: 1805.04094 [astro-ph.SR].

Strand, K. A. (1943). "The Triple System ξ Boötis". In: 55, p. 28. DOI: 10.1086/125483.

Struve, O. (1952). "Proposal for a project of high-precision stellar radial velocity work". In: *The Observatory* 72, pp. 199–200.

Stürmer, Julian (2015). "Technologies for improving the precision of radial velo city measurements with high-resolution fibre-fed échelle spectrographs". PhD thesis. Landessternwarte Königstuhl.

Stürmer, Julian (2019). personal communication.

Tal-Or, Lev et al. (2019). "Correcting HIRES/Keck radial velocities for small systematic errors". In: 484.1, pp. L8–L13. DOI: 10.1093/mnrasl/sly227. arXiv: 1810.02986 [astro-ph.EP].

Tala, M. et al. (2016). "A high-resolution spectrograph for the 72cm Waltz Telescope at Landessternwarte, Heidelberg". In: *Ground-based and Airborne Instrumentation for Astronomy VI*. Vol. 9908. Society of Photo-Optical Instrumentation Engineers (SPIE) Conference Series, 99086O. DOI: 10.1117/12.2232730. arXiv: 1608.06090 [astro-ph.IM].

Tala, M. et al. (2017). "Two simple image slicers for high resolution spectroscopy". In: *Experimental Astronomy* 43.2, pp. 167–176. DOI: 10.1007/s10686-017-9526-5.

Tala Pinto, M. et al. (2018). "Physical modeling of echelle spectrographs: the CARMENES case study". In: *Society of Photo-Optical Instrumentation Engineers (SPIE) Conference Series*. Vol. 10705, 107051U. DOI: 10.1117/12.2313211.

Trifonov, T. et al. (2014). "Precise radial velocities of giant stars. VI. A possible 2:1 resonant planet pair around the K giant star η Ceti". In: 568, A64, A64. DOI: 10.1051/0004-6361/201322885. arXiv: 1407.0712 [astro-ph.EP].

Trifonov, T. et al. (2018). "The CARMENES search for exoplanets around M dwarfs . First visual-channel radial-velocity measurements and orbital parameter updates of seven M-dwarf planetary systems". In: 609, A117, A117. DOI: 10.1051/0004-6361/201731442. arXiv: 1710.01595 [astro-ph.EP].

van Leeuwen, F. (2007). "Validation of the new Hipparcos reduction". In: 474, pp. 653–664. DOI: 10.1051/0004-6361:20078357. arXiv: 0708.1752.

Villaver, Eva et al. (2014). "Hot Jupiters and Cool Stars". In: *The Astrophysical Journal* 794.1, p. 3. URL: http://stacks.iop.org/0004-637X/794/i=1/a=3.

Vogt, S. S. (1987). "The Lick Observatory Hamilton Echelle Spectrometer". In: 99, pp. 1214–1228. DOI: 10.1086/132107.

Wildi, F. et al. (2010). "A Fabry-Perot calibrator of the HARPS radial velocity spectrograph: performance report". In: *Ground-based and Airborne Instrumentation for Astronomy III*. Vol. 7735. P. 77354X. DOI: 10.1117/12.857951.

Wittenmyer, R. A. et al. (2011). "The Pan-Pacific Planet Search. I. A Giant Planet Orbiting 7 CMa". In: 743, 184, p. 184. DOI: 10.1088/0004-637X/743/2/184. arXiv: 1111.1007 [astro-ph.EP].

Wittenmyer, R. A. et al. (2016). "The Pan-Pacific Planet Search III: five companions orbiting giant stars". In: 455, pp. 1398–1405. DOI: 10.1093/mnras/stv2396. arXiv: 1510.04343 [astro-ph.EP].

Wolszczan, A. and D. A. Frail (1992). "A planetary system around the millisecond pulsar PSR1257 + 12". In: 355, pp. 145–147. DOI: 10.1038/355145a0.

Wood, P. R. (2015). "The pulsation modes, masses and evolution of luminous red giants". In: 448, pp. 3829–3843. DOI: 10.1093/mnras/stv289. arXiv: 1502.03137 [astro-ph.SR].

Zucker, S. and T. Mazeh (1994). "Study of spectroscopic binaries with TODCOR. 1: A new two-dimensional correlation algorithm to derive the radial velocities of the two components". In: 420, pp. 806–810. DOI: 10.1086/173605.